Application Directed Synthesis of Multifunctional Fullerene Derivatives

Xiangyi Chen

Submitted in accordance with the requirements for the degree of Doctor of Philosophy

School of Chemistry

January 2022

Acknowledgements

Firstly, I would like to express my thanks to my supervisors Dr Thomas Chamberlain and Prof. Michaele Hardie for their support and encouragement throughout the study of my PhD. Special thanks to Tom, his day-to-day guidance paves the way of accomplishing my PhD.

Thanks to Catherine Peake and Toby Maccormack in University of Nottingham for her help in carrying out the redox flow battery cell cycling tests. Thanks to Dr Dongxu Yang in University of Electronic Science and Technology of China for carrying out the lithographic patterning tests.

Thanks to Prof. Malcolm Halcrow, Dr Robert Menzel and Prof. Fiona Meldrum for equipments, Dr Alex Kulak for lab safety supervision and technical help, Dr Mark Howard for his help in the NMR analysis of fullerene derivatives.

Thanks to all the current and past members of Chamberlain group and Hardie group; Ed, Matt, Sarah and Brendan for synthetic and practical support.

Finally, thanks to all of my family, in particular my father and grandmother. Their endless love and support give me faith to overcome all the challenges.

Abstract

This thesis presents work on the synthesis and characterisation of functionalised fullerene derivatives designed specifically for applications in energy storage, supramolecular assembly and lithographic patterning. Chapter 1 provides an introduction to fullerene, fullerene chemistry, the examples of structurally complex fullerene derivatives and their corresponding applications. Chapter 2 describes the synthesis of highly soluble fullerene derivatives as charge carriers for redox flow batteries, achieving a remarkably high solubility of ~336 mM in *o*DCB, and exhibiting a wide potential window, 1.78 V, in an electrolyte consisting of *o*DCB/tetrabutylammonium tetrafluoroborate. The synthesis of a series of tris-fullerene CTG molecules that can be used for developing supramolecular arrays is introduced in Chapter 3, in which a synthetic strategy of using tris-amino acid derivatised CTG as the starting material in a one-pot Prato reaction was proposed and investigated to yield the target molecule. In Chapter 4, a fullerene-platinum complex is explored as a resist material to develop the lithographic pattern, in which a sub-13 nm line width was achieved. The presence of Pt atoms enhances the secondary electron scattering and thus increased the energy deposition efficiency resulting in better lithographic patterning capability. Overall, this thesis acts as a guide to efficient and targeted fullerene derivative synthesis, providing insight and strategy into fullerene functionalisation which will help push forward the exploitation of fullerene as a nanosized building block to be utilised in applied, functional materials in the future.

Abbreviations

C_{60}	Fullerene
PCBM	Phenyl-C_{61}-butyric acid methyl ester
oDCB	Ortho-dichlorobenzene
PPh	Triphenylphosphine
DCM	Dichloromethane
BHJ	Bulk-heterojunction
P3HT	poly(3-hexylthiophene)
LUMO	lowest unoccupied molecular orbital
HOMO	Highest occupied molecular orbital
OTf	Triflate
RFB	Redox flow batteries
EES	Electrical energy storage
BzNSN	2,1,3-Benzothiadiazole
MeCN	Acetonitrile
LiTFSI	Lithium bis(trifluoromethylsulfonyl)imide
DBMMB	2,5-Di-tert-butyl-1-methoxy-4-[2'-methoxyethoxy]benzene
Fc	Ferrocene
TEA	Triethylamine
TLC	Thinlayer chromatography
CS_2	Carbon disulfide
WE	Working electrode
CE	Counter electrode
RE	Reference electrode

TBATFB	Tetrabutylamonium tetrafluoro borate
DMAP	4-Dimethylaminopyridine
oDCB	Ortho dichlorobenzene
NMR	Nuclear magnetic resonance
CV	Cyclic voltammetry
ESI	Election spray ionization
CTG	Cyclotriguaiacylene
CHY	Cyclohexane
MCB	Monochlorobenzene
XPS	X-ray photoelectron spectroscopy
ICP	inductively coupled plasma
HSQ	resist hydrogen silsesquioxane

Table of Contents

List of Figure

good clearance between the lines and vertical resist walls; (i) ~45° tilted and (j) ~85° tilted images of the 40 nm pitch line-space patterns transferred to silicon by ICP etching. 318

List of tables

List of Schemes

Chapter 1 Introduction of fullerene chemistry

1.1 Fullerene, C_{60}

Fullerene is the third allotrope of carbon after the discovery of diamond and the graphite. The 1996 Nobel Prize in Chemistry was awarded to Harold Kroto, Robert Curl and Richard Smalley for their work in the discovery of these carbon cage species.[1] Among the fullerene family, C_{60} is the most abundant species, consisting of 20 hexagons and 12 pentagons, giving a beautiful cage structure with a van der Waals diameter of 1 nm (**Figure 1.1**).[1-3] Due to its abundancy and economical accessibility, C_{60} was selected as the only form of fullerene to be investigated for this project, therefore, the name 'fullerene' is used ubiquitously in all further content and refers to C_{60} unless explicitly stated.

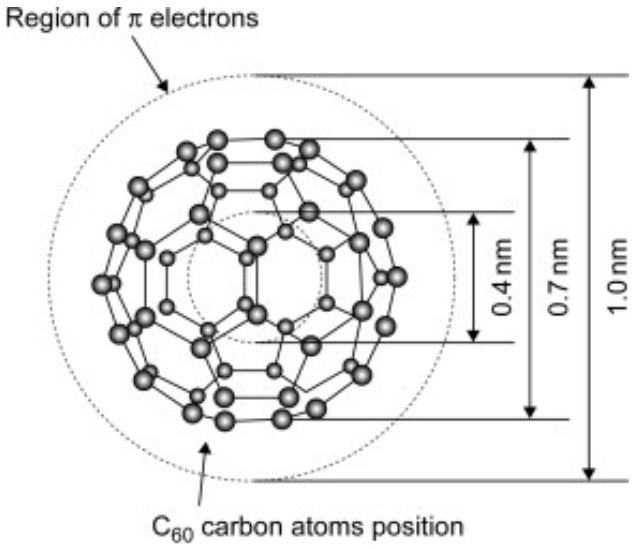

Figure 1.1 The structure of fullerene, C_{60}.

In C_{60}, there are a total of 30 double bonds, however, the fullerene is not a super aromatic structure. As all of the double bonds only exist within the six membered carbon rings (hexagons), this results in poor electron delocalization and makes it behave like a series of isolated electron deficient alkenes. As a result, fullerene tends to react with electron rich species.[2-3] C_{60} is able to reversibly accept 6 electrons,

undergoing a series of 1 electron redox processes and, as a result of its rigid structure, it is one of the fastest electron-accepting species known.[4-6] Meanwhile, it also exhibits photoactivity, being able to absorb light from the ultraviolet to visible region. Due to these interesting properties and the unique nature of its nanosized structure, C_{60} is considered a promising candidate for applications in solar cells,[7-11] energy storage,[12-13] catalysis[14] and pharmaceuticals. [15-17]

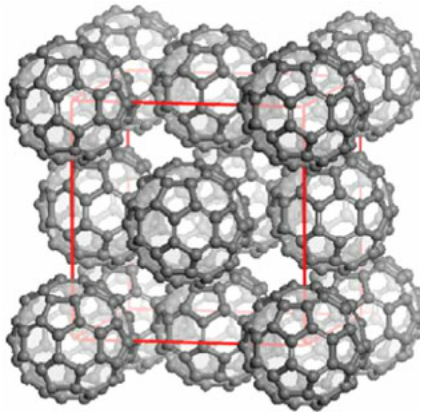

Figure 1.2 Diagram showing the hexagonally close packed structure of fullerene molecules.

However, due to the smooth surface and high level of symmetry, fullerene molecules very readily and tightly pack with each other (**Figure 1.2**). This results in pure fullerene molecules being notoriously insoluble in common solvents, impeding their usage in practical applications and hindering the fabrication of fullerene-based devices. To make fullerenes easier to manipulate, the best and most common method is to functionalize the fullerene by adding different organic groups across the [6,6] junctions (bond length = 1.38 Å), i.e. between two hexagons of the cage, or the [5,6] junctions (bond length = 1.45 Å) i.e. between a pentagon and a hexagon of the cage (**Figure 1.3**).[2-3] This not only solves the problem of solubility efficiently but also dramatically expands the chemical versatility of the resultant fullerene species.

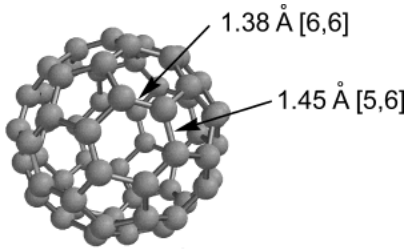

Figure 1.3 Different bond length of C_{60}.

1.2 Reactions used to functionalize fullerene

Since the discovery of fullerene, the research based around fullerene functionalisation has never stopped. A wide variety of reaction types have been tested, including reactions with radicals, halogens and bases, which enable access to functionalized fullerenes in a relatively short time (reaction time up to 1 hour)[18] and decent yield (more than 70%).[19] However, the reaction types mentioned above are not stereo-selective, resulting in a lack of control of the final structure and thus limiting its application in more sophisticated areas like pharmaceuticals and energy storage. Therefore, reaction types with higher degrees of control over the final structure have been introduced and utilized extensively to synthesise functionalized fullerene derivatives. These include, the Bingel reaction (1,3-cyclopropanation), the Prato reaction (1,3-dipolar cycloaddition) and the Diels-Alder reaction ([4+2] cycloaddition), which are introduced in the following sections.

1.2.1 Bingel reaction

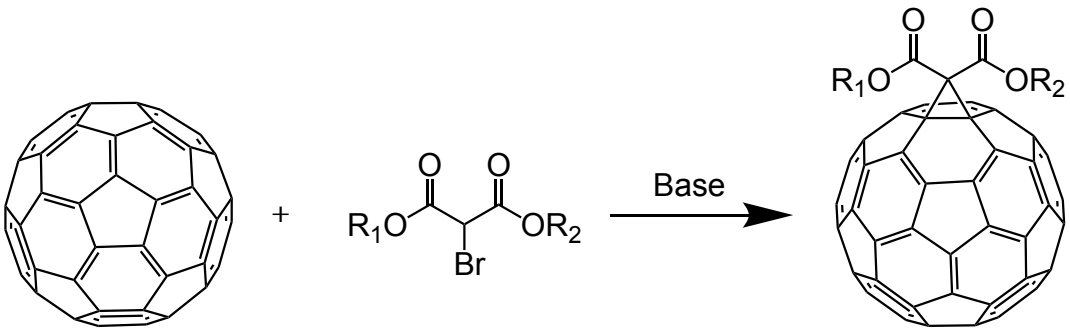

C_{60} Bromonated malonate Methanofullerene

Scheme 1.1 A model Bingel reaction.

The Bingel reaction is also referred to in the literature as a fullerene cyclopropanation reaction, which methanofullerene as the product containing a three membered ring on the [6,6] junction of the cage (**Scheme 1.1**).[20] It was first reported by C. Bingel, who used a brominated diethyl malonate to react with fullerene in the presence of a strong base (**Figure 1.4**). After deprotonation of the malonate derivative, the carbon with the bromine group attached forms a carbon anion that subsequently attacks the double bond of the [6,6] junction of C_{60}. The negative charge is transferred to the carbon on the opposite side of the double bond, followed by attack of this carbon on the malonate and expulsion of the bromine as a leaving group, resulting in methanofullerene as the product. The Bingel reaction is the most extensively used reaction in fullerene chemistry, thousands of methanofullerene derivatives have been synthesized for a diverse range of different applications, such as the famous commercially available solar cell charge carrier, phenyl-C_{61}-butyric acid methyl ester (PCBM). In comparison to the Prato reaction, the Bingel reaction is more energy efficient, it can be performed at or below room temperature (at as low as 0 °C in some cases). This low reaction temperature means that the Bingel reaction is suitable for appending highly reactive functionalities, like azide groups. Malonate derivatives starting materials are very easy

to synthesize and decorate, which facilitates a diversity in the potential molecular designs with a wide variety of different structures and groups for different applications explored. However, the Bingel reaction gives a product with closed, three membered rings, which means strong bond strain is also created so the products suffer from issues with stability and, therefore, are not suitable for some applications which have harsh operating conditions.

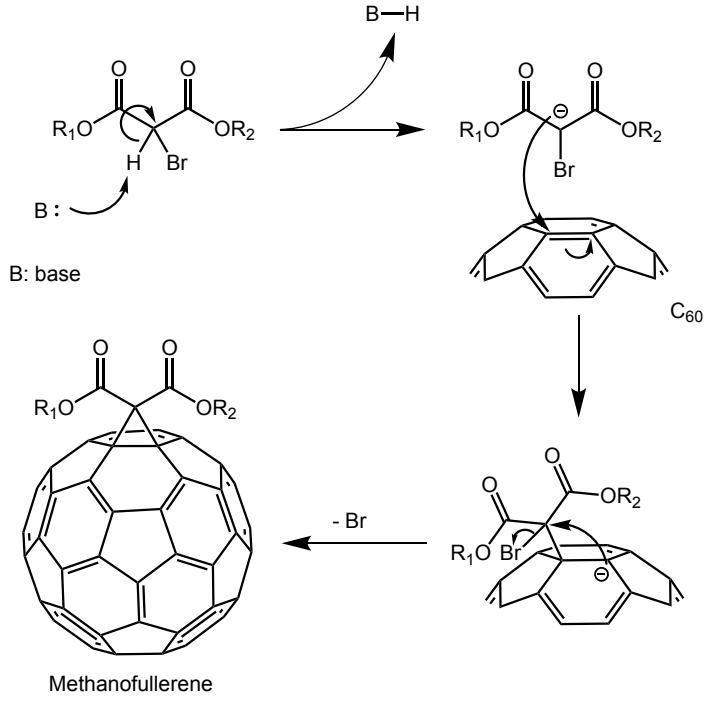

Figure 1.4 Mechanism of the Bingel reaction.

1.2.2 Prato reaction

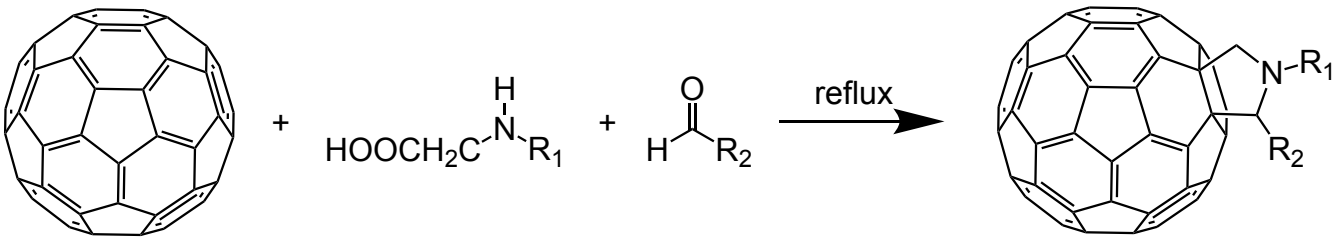

Scheme 1.2 A model Prato reaction.

The Prato reaction is a 1,3-dipolar cycloaddition, which occurs between an azomethine and an olefin, forming a pyrrolidine ring product (**Scheme 1.2**).[21-22] This reaction was first reported by Otohiko Tsuge for azomethine ylide chemistry, then Maurizio Prato first applied this reaction to fullerene, hence the name, the Prato reaction. The Prato reaction uses amino acid and aldehyde as starting materials, which form a reactive ylide intermediate in situ that can react with the double bond of the [6,6] junction of the fullerene forming a five membered ring product, fulleropyrrolidine (**Figure 1.5**). The Prato reaction is very efficient, which enables chemists to add multiple functionalities sequentially to the carbon cage in one pot reactions, facilitating the fabrication of fullerene based multifunctional nanomaterials. Importantly, the Prato reaction forms a closed five membered ring, pyrrolidine, as a product, which is more stable than the methanofullerene obtained from the Bingel reaction due to five membered rings having less bond strain than three membered rings. This makes fulleropyrrolidine derivatives better candidates for applications which need to operate under harsh conditions, like high temperature and higher voltages. Unlike the Bingel reaction, which can happen at room temperature, the Prato reaction requires higher reaction temperatures to occur, and thus is normally performed under toluene reflux conditions or *o*DCB reflux conditions. This high reaction temperature consumes more energy and crucially constrains the functional groups which can be added to the cage, e.g. some highly reactive starting materials that can react with double bond of fullerene e.g. azide derivatives or primary amine, cannot be tolerated. The variety of amino acids and aldehydes used for the Prato reaction is also very limited, which further restricts the utilisation of the Prato reaction. These disadvantages explain why Bingel reactions dominates the literature over Prato reactions in terms of the number of examples utilizing each reaction type in synthetic routes to functionalised fullerenes.

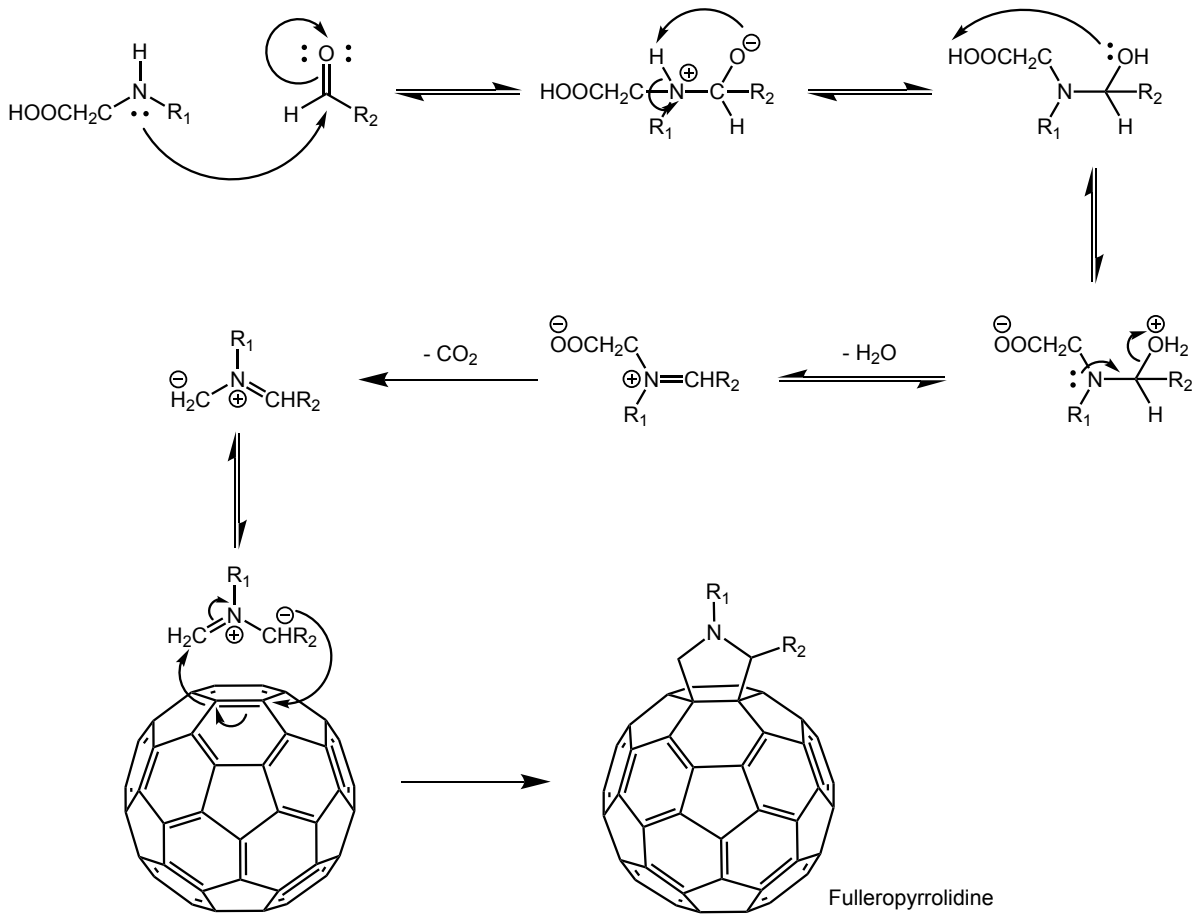

Figure 1.5 The mechanism of the Prato reaction.

1.2.3 Diels-Alder reaction

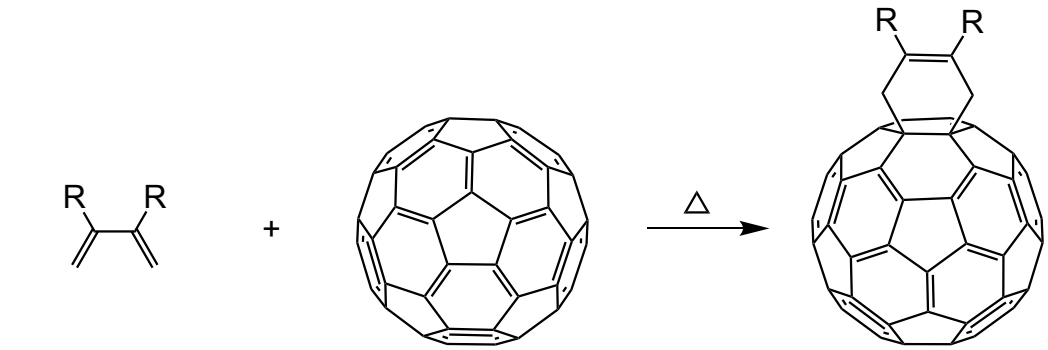

Diene derivative C_{60}

Scheme 1.3 Diels-Alder model reaction.

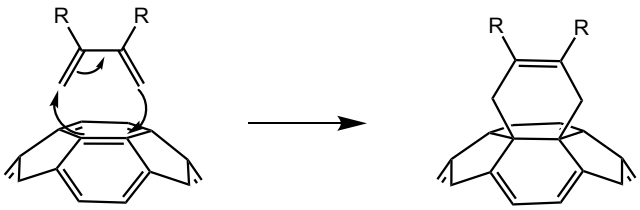

Figure 1.6 Mechanism of Diels-Alder reaction.

The Diels-Alder reaction occurs between a conjugated diene and a substituted alkene giving a substituted cyclohexene derivative as a product. This reaction is governed by the interaction between 4π electrons from the diene and 2π electrons from the alkene. The Nobel prize in Chemistry was awarded to Otto Diels and Kurt Alder for their discovery of this reaction in 1928.[23-24] The Diels-Alder reaction is a powerful and versatile tool to synthesise natural products and new materials with complicated structures. This reaction was applied successfully to fullerenes, due to the electron deficient nature of fullerene, specifically the double bond in the [6,6] junction which acts as a 2π electron electrophile. This facilitates the Diels-Alder reaction by electron transportation with diene derivatives forming two new C-C bonds (see **Figure 1.6**).[25] The product formed from the reaction has a six-membered ring, which is called [6,6]cyclohexene adduct (see **Scheme 1.3**). However, this reaction reverses due to the nature of the negative change in entropy and enthalpy. Upon heating, the fullerene [6,6]cyclohexene adduct can decompose by undergoing a retro-Diels-Alder reaction. At the same time, the synthesis of dienes can be tricky due to difficulties in controlling the stereochemistry. These two drawbacks constrain the Diels-Alder reaction in the context of functionalised fullerene chemistry, making it the third most popular option after the Bingel and Prato reactions. However, the Diels-Alder reaction still plays an important role in the synthesis of fullerene-based charge carriers and as a tool to support the Bingel reaction and Prato reactions in terms of poly-adduct synthesis.

1.3 Functionalised fullerene material

1.3.1 C_{60} mono-adduct

Fullerene mono-adducts are easier to synthesise and isolate with well-defined structures than higher adducts of fullerene due to the lack of complexity caused by the presence of the regioisomers. A lot of theoretical studies have been carried out based on mono-adducts, beside the fullerene-based charge carriers for solar cells, the synthesis of electron donor-acceptor nanohybrid and condition (such as light, pH and redox) responsive nanomaterials are the most popular direction that chemists are interested in. Two examples are giving here, more examples can be found in the literature.[26-29]

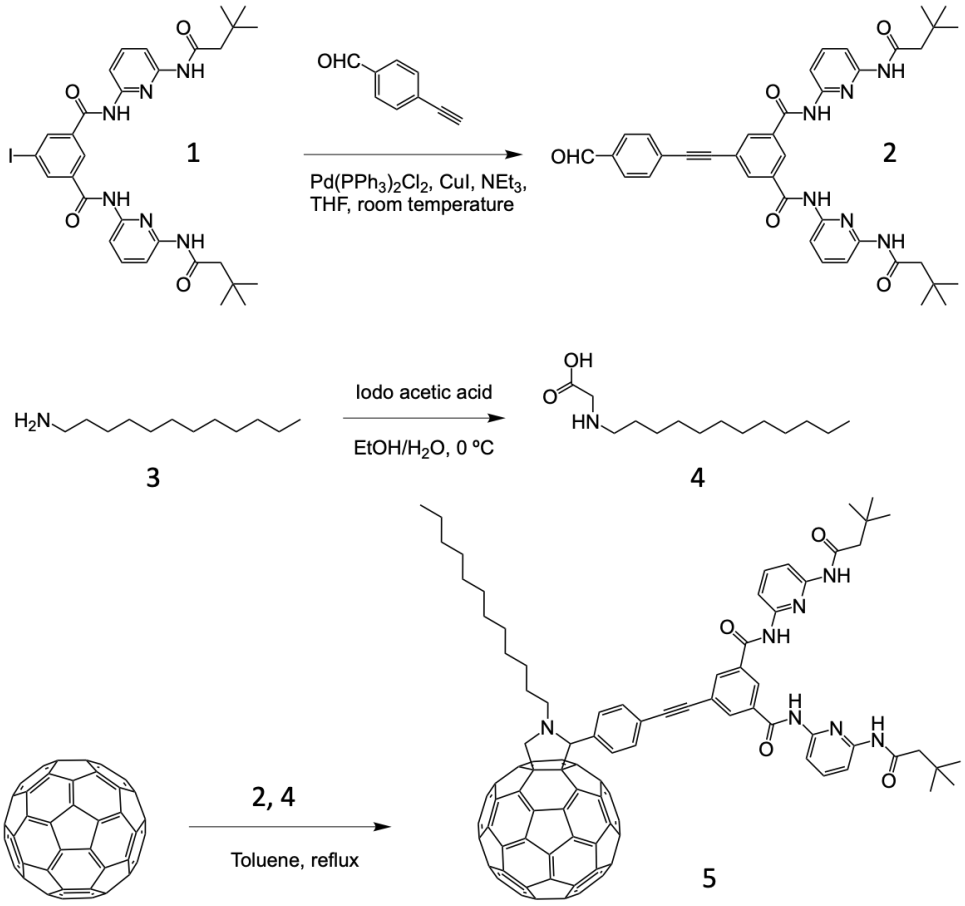

Scheme 1.4 Route to synthesise the Hamilton receptor functionalised fullerene mono-adduct, **5**.

Florian *et al*. reported a study, which fabricated a series of electron donor-acceptor nanohybrids based on a fullerene mono-adduct.[30] In comparison with traditional donor-acceptor systems, in which the two electron active moieties are linked by a covalent bond, the authors introduced a supramolecular porphyrin/fullerene hybrid that was assembled together by the hydrogen bonds between Hamilton receptor and cyanuric acid donor derivatives. In this system, the metalloporphyrin moiety acts as the light harvesting unit, undergoing photoexcitation to give electrons, which are transferred through the conjugated spacer to the fullerene forming a charge separated state. In the synthesis of the fullerene mono-adduct (see **Scheme 1.4**), an iodo

molecule **1**, which contains a Hamilton receptor groups, was reacted with 4-ethynylbenzaldehyde in the presence of $Pd(PPh_3)_2Cl_2$ as catalyst giving aldehyde **2** as a the product, which is one of the starting material for the subsequent fullerene Prato reaction. Separately, dececylamine, **3**, was added to iodoacetic acid at 0 ºC to synthesise the N-dodecyl glycine with a long alkyl chain to improve the solubility of the fullerene derivative. The C_{60}, and compounds **2** and **4** were added together in toluene under reflux conditions to perform the Prato reaction, obtaining the Hamilton functionalised mono-adduct, **5**. Subsequently, molecule **5** was added to the DCM solution of cyanuric acid derivative, **6**, which contained a metalloporphyrin moiety, the Hamilton receptor group and cyanuric acid group self-assembled, giving the fullerene/porphyrin hybrid, **7**, as the product (see **Scheme 1.5**). The self-assembly was characterised by ^1H NMR spectroscopy and fluorescence assays, revealing strong 6-fold hydrogen bonding resulting in a fast equilibrium with the binding constant in the order of 10^4 M^{-1}. At the same time, a fast electron transfer with the value of 3.1 x 10^9 s^{-1} was also achieved benefitting from the rigid spacer between the fullerene and metalloporphyrin.

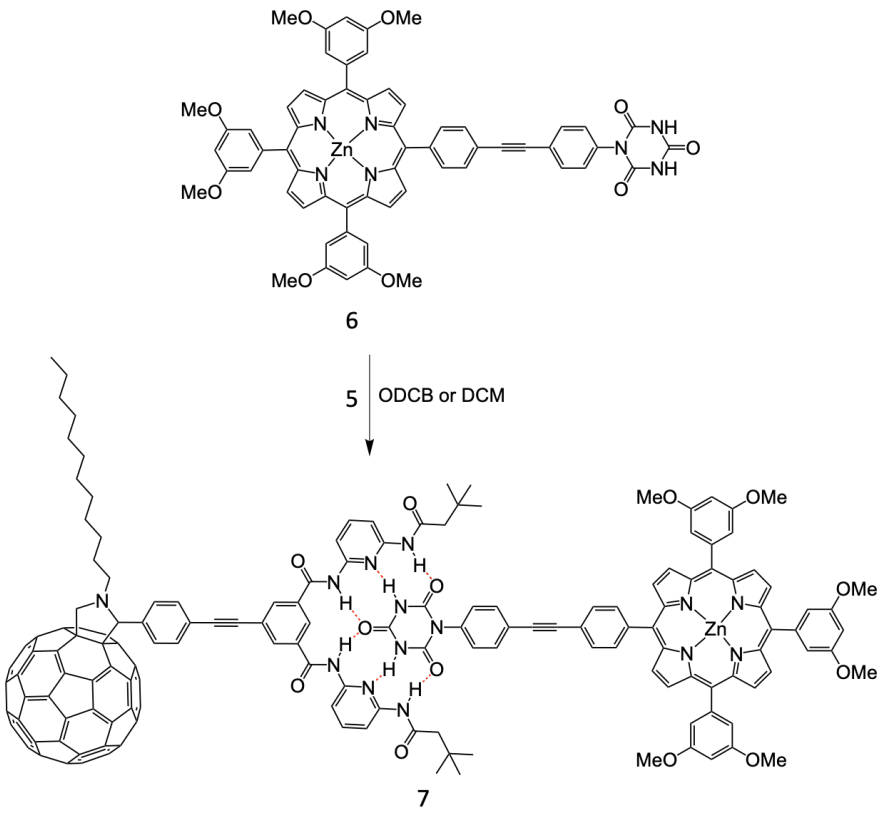

Scheme 1.5 Route to synthesise fullerene/metalloporphyrin hybrid, **7**.

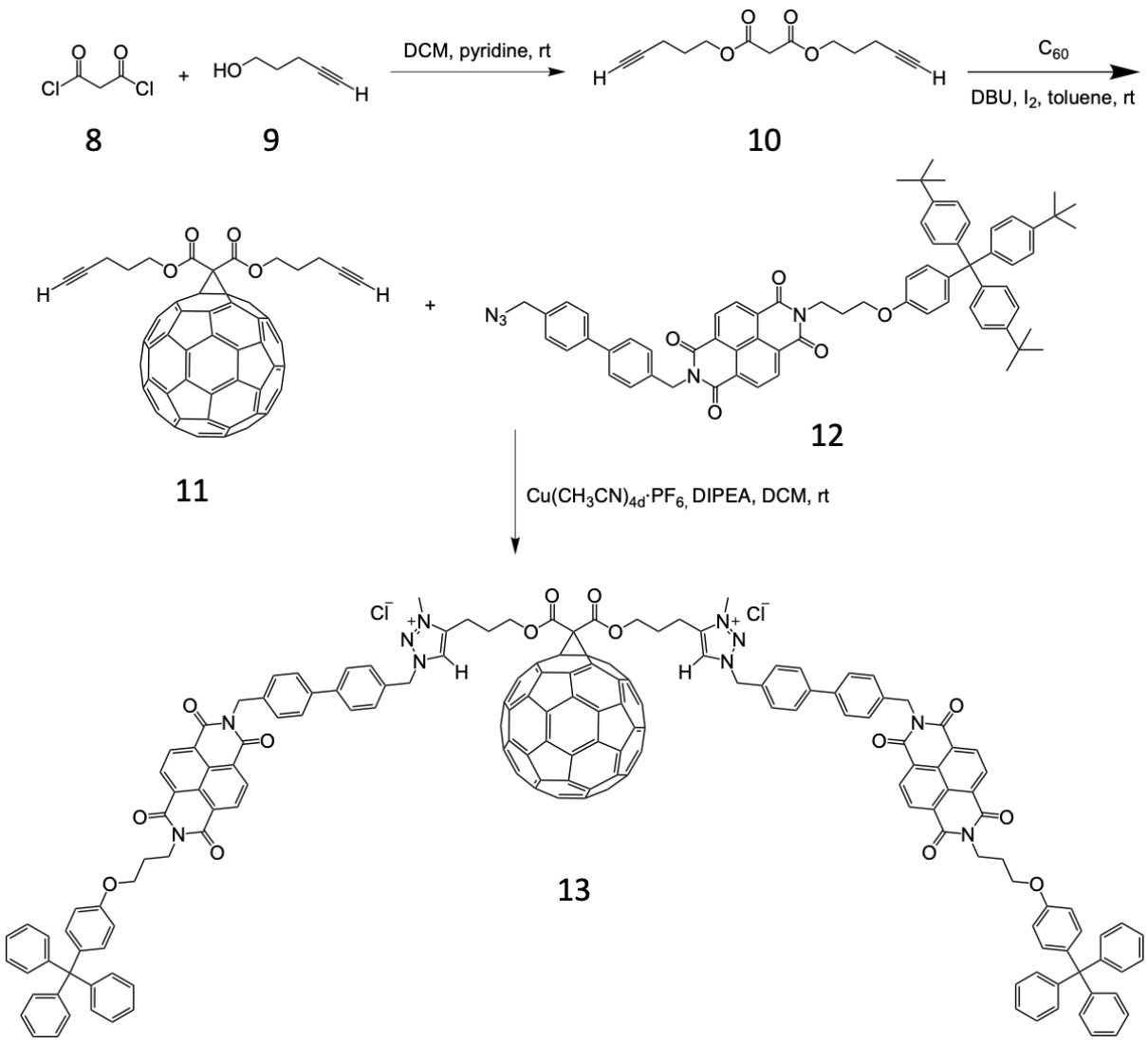

Scheme 1.6 Route to synthesise fullerene mono-adduct, **13**, with two naphthalene dimide groups and two triazolium groups.

Timothy *et al*. recently reported a novel rotaxane system, which used a fullerene mono-adduct as a building block in which the fullerene cage served as a sterically bulky stopper unit as well.[31] Interestingly, an anion mediated molecular motion of the rotaxane was observed, with the subsequent discovery of an unprecedented switchable fluorescence quenching behavior that is induced by the rotaxane motion. The synthesis of the fullerene building block was performed via a Bingel reaction (see **Scheme 1.6**). First, a commercially accessible malonyl dichloride, **8**, was reacted with

4-pentyn-1-ol ,**9**, in the presence of pyridine to obtain malonate **10** with two alkyne groups. This was subsequently used to react with fullerene in the presence of DBU as base under Bingel conditions giving fullerene mono-adduct, **11**. Subsequently, compound **11** was reacted with azide derivative **12** with two naphthalene dimide (NDI) groups via copper-catalyzed azide-alkyene cycloaddition, which forms two triazolium groups, yielding the fullerene based axle, **13**, as the product. For the rotaxane formation (see **Scheme 1.7**), the synthesis was carried out using a chloride anion template-based clipping of two bis-vinyl-functionalised ferrocenyl macrocycle precursors, **14**, giving the rotaxane, **15**·(Cl_2), as the product. After adding Amberlite resin, the bis-chloride salt version of **15**·(Cl_2) underwent an anion exchange, forming a bis-hexafluorophosphate salt, **15**·(PF_6). The two trityl ends and the fullerene in the middle serve the function of stoppers, which restrict the motion of the macrocycle in the middle of them. The formation and the configuration of each version of the rotaxanes were characterised by ^{1}H, ^{13}C, ^{1}H ROESY NMR spectroscopy as well as MALDI mass spectrometry. Fluorescence spectroscopy indicated that anion-exchange not only changed the relative position of the macrocycle in relation to the fullerene axle but also induced a strong emission response (see **Figure 1.7**). In its chloride salt form, the ferrocenyl functionalised macrocycles stay at the position of the triazolium, which exposes the NDI groups and negates the electron transfer between the ferrocene groups and NDI groups, resulting in the active emission from the NDI fluorophore. In the hexafluorophosphate salt, the macrocycles shifted to the position of NDI groups, quenching the NDI emission due to the formation of a charge separated state with NDI the moieties.

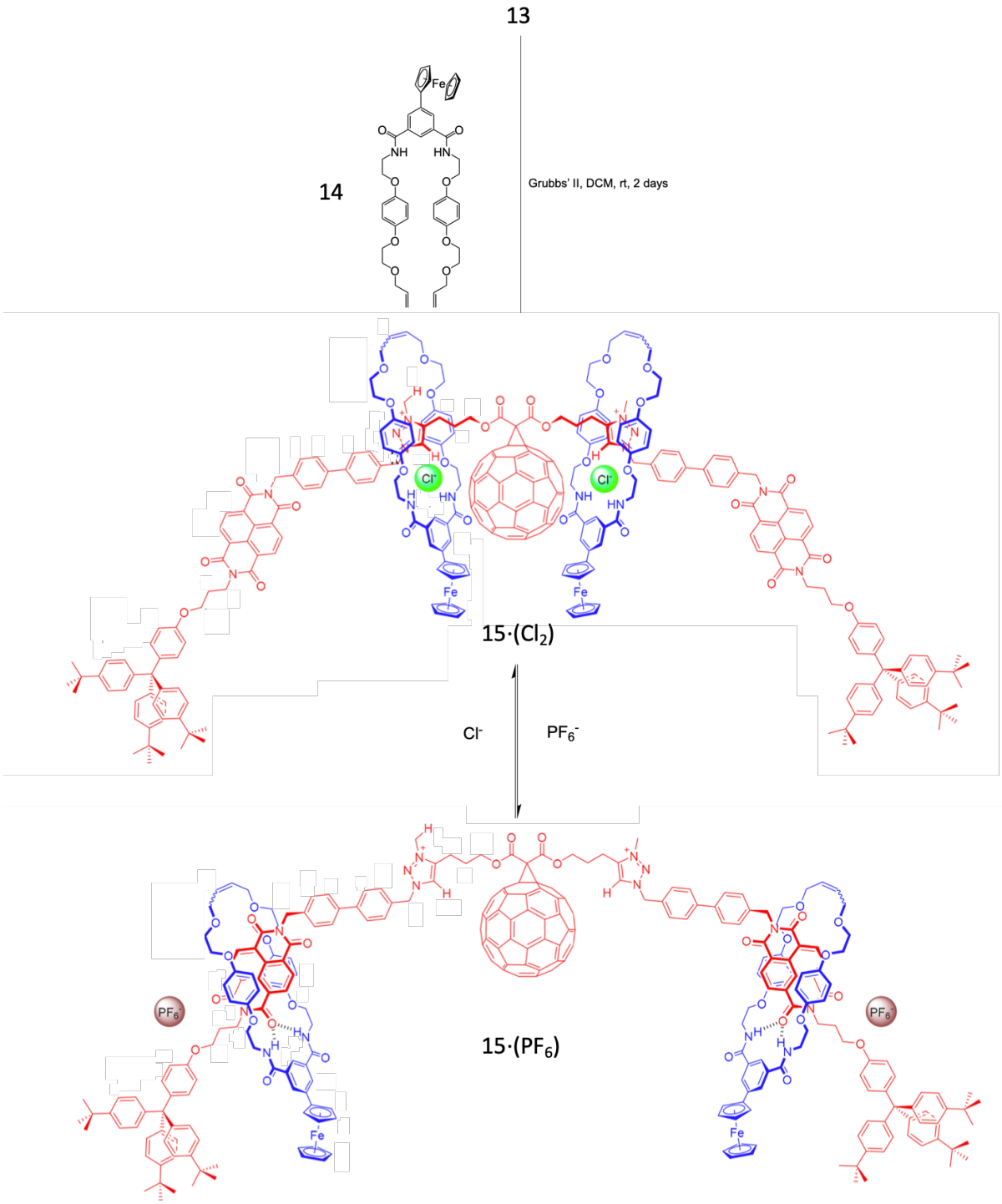

Scheme 1.7 Route to synthesise rotaxanes **15**·(Cl_2) and **15**·(PF_6).

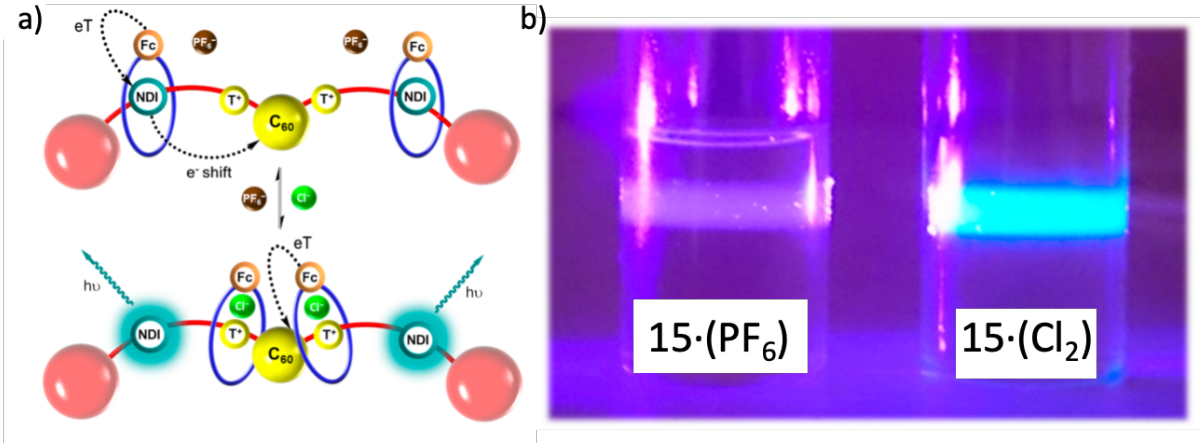

Figure 1.7 a) Diagram of fullerene base rotaxane and its anion induced molecular motion. b) A comparison of the response of **15**·(Cl_2) and **15**·(PF_6) to fluorescence in distinct.

1.3.2 Fullerene poly-adducts

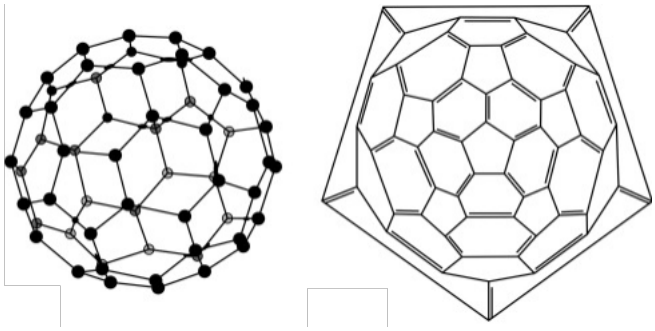

Figure 1.8 Chemical structure of C_{60} fullerene (left) and the corresponding Schlegel diagram (right).

There are 30 double bonds in fullerene (**Figure 1.8**), and up to six functionalities can be added to the cage to form poly-adducts. The spherical structure of fullerene is a promising scaffold for the construction of multifunctional nanomaterials and a wide variety of different reactions and substitution patterns are possible (**Table 1.1**). In particular, the hexakis T_h octahedral addition pattern has found applications in metal organic frameworks. Exploitation of poly-functionalised fullerene derivatives with

interesting electrochemical and structural properties has always been a core topic in fullerene research, and as such is comprehensively studied and reviewed in the literature.[32-35] The electron accepting, multivalence and UV-Vis absorbing properties of functionalized fullerenes make them promising candidates for a variety of potential applications, such as electron acceptors for photovoltaic solar cells, charge carriers for energy storage, sensitizers for photodynamic therapy, inhibitors for antiviral usage and components for building up C60-polymer hybrid materials.

Table 1.1 Examples for substitution patterns of fullerene

Substitution	Symmetry
Bis	I_h, C_1, C_2, C_s
Tris	C_2, C_{2v}
Tetrakis	D_{2h}, C_{2v}
Pentakis	C_{2v}, C_s, C_5, C_{5v}
Hexakis	D_2, T_h, T

In the past few decades, the Bingel cyclopropanation, Prato 1,3-dipolar addition, and the Diels-Alder reactions have been extensively used for fullerene functionalization, which have been optimized and comprehensively characterized to yield poly-adducts for molecular architectures and multifunctional devices.

The development of this area over the past decade is briefly reviewed below in terms of the structure, properties and potential application is reviewed below, for a comprehensive review of fullerene derivatives reported before this period see references.[36-38] The radical and atom addiction to C_{60} of species such as H, O, F, Cl, Br and I gives references.[39] However, I have excluded these examples from this review

due to the non-steroselective nature of these reactions and thus the reduction in interest in recent years.

1.3.2.1 Fullerene bis-adduct

Fullerene bis-adducts are the most widely reported fullerene poly-adduct species and are commonly used as electron acceptors for photoelectronic device, due to the high yielding and flexible synthesis routes available.

He *et al*. synthesized indene-C_{60}-bis-adduct (ICBA), **16**, via a one-pot reaction with a decent yield of 34% in trichlorobenzene (**Scheme 1.8**).[40] In comparison to phenyl-C_{61}-butyric acid methyl ester (PCBM, it is known as one of the most efficient electron acceptors for bulk-heterojunction (BHJ) solar cell), compound **16** showed a high LUMO level (0.17 eV) and better solubility in common solvents (90 mg/mL in chloroform). It was blended with electron donating polymer to form a P3HT (poly(3-hexylthiophene))/ICBA BHJ solar cell, which showed good performance, with a 0.9% higher PCE compared to the P3HT/PCBM system.

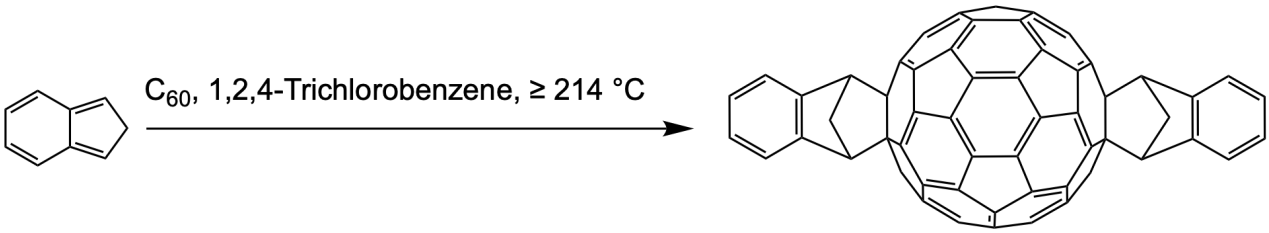

Scheme 1.8 Route to synthesise **ICBA**.

Grag *et al*. reported a bis functionalized fullerene system that serves as an artificial photosynthetic reaction centre (**Scheme 1.9**).[41] Two porphyrin moieties were appended to C_{60} using 1,3-dipolar cycloaddition, using N-methylglycine (sarcosine) and a hexaphenylbenzene derivative with two aldehyde functionalized porphyrin arms as starting materials. The resulting product **17** has a rigid structure and C_2-symmetry

addition pattern, which are provided by the hexaphenylbenzene fragment. The system showed very fast photoinduced electron transfer and a long-lived charge separated state. When compared with its single porphyrin analogue, a higher quantum yield of charge separation was also achieved due the doubled absorption cross section.

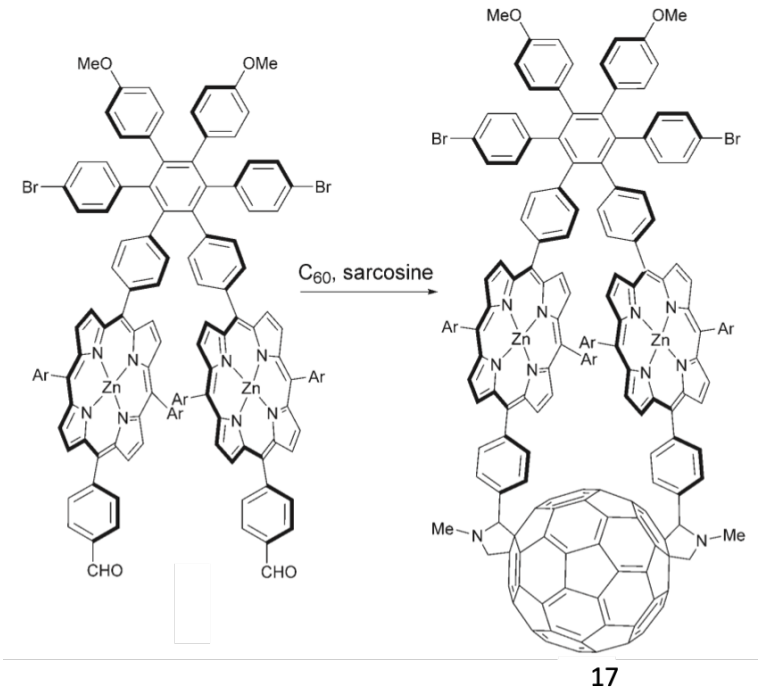

Scheme 1.9 Route to synthesise diporphyrin functionalized fullerene, **17**, with C_2 symmetry.

Sigwalt *et al*. reported two fullerene bis-malonate molecules with two different ring sizes (**Scheme 1.10**).[42] Using a modified reaction procedure, C_{60} reacted with cyclic bis-malonate **18**, obtaining D_{2h} isomer **19** and C_2 isomer **20** in 8% and 18% yield respectively. The formation of both of the products was confirmed by ^{1}H and ^{13}C NMR, UV-Vis, and IR spectroscopes and MALDI-ToF spectrometry. The trans-1 addition pattern of **19** was proven by single crystal XRD. UV-Vis spectroscopy was also used to confirm the trans-3 addition pattern of compound **20**. This reaction showed good stereo-selectivity with no further isomers formed. Computational work was also

performed, indicating that **20** was a lower energy isomer than **19**, which explains the high yield of the trans-3 product. Molecule **19** can be used as the precursors for novel nanomaterials with two malonate functionalities appended, resulting in C_{60} tetrakis-adducts with four substituents located in the equatorial belt of the fullerene.

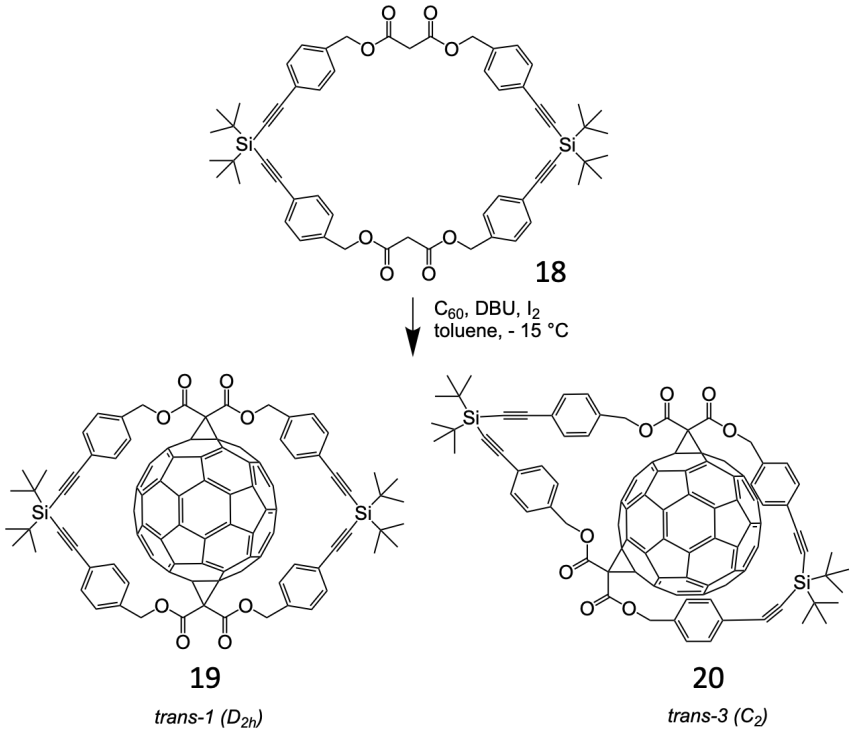

Scheme 1.10 Route to synthesise two bis-fulleromalonates, **19** and **20** with different addition patterns.

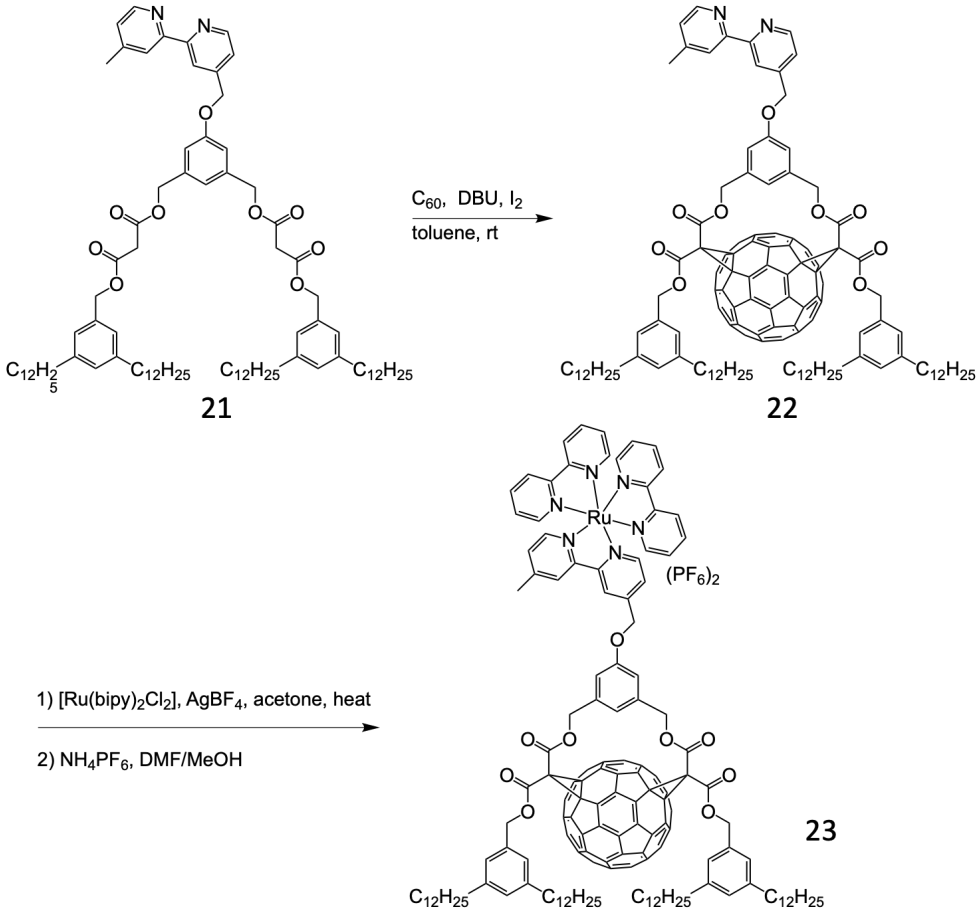

Scheme 1.11 Route to synthesise the amphiphilic C_{60}-bipy-Ru complex, **23**.

In terms of fullerene bis-malonate derivatives, the Nierengarten group reported an amphiphilic fullerene-ruthenium complex, which showed the properties of metal to fullerene charge transfer properties and the ability to form Langmuir films.[43] 2,2'-Bipyridine derivative **21**, with two tethered bis-malonate groups and four long alkyl chains were used as the starting material and reacted with C_{60} via a double Bingel cyclopropanation to give fullerene-bipyridine ligand **22**. After complexation with $[Ru(bipy)_2Cl_2]$, fullerene-Ru complex **23** was formed. In UV-Vis spectroscopy revealed a strong quenching of the luminescence emission of the tris(2,2'-bipyridine)ruthenium(II) complex, providing evidence of photoinduced charge transfer from the Ru complex moiety to the fullerene cage. The Langmuir film of compound **23**

is formed successfully due to the presence of the four long alkyl chains which prevented the disordered aggregation of the fullerene moieties.

Bis-adducts are a flourishing species and being widely investigated as charge carriers in bulk heterojunction organic polymer solar cells. Theoretical studies into the charge separation properties and inter- and intra-molecular interactions between functionalities and the fullerene cage, have also been well performed. More information regarding fullerene bis-adducts can be found in the following references with some key examples listed below (**Figure 1.9**).

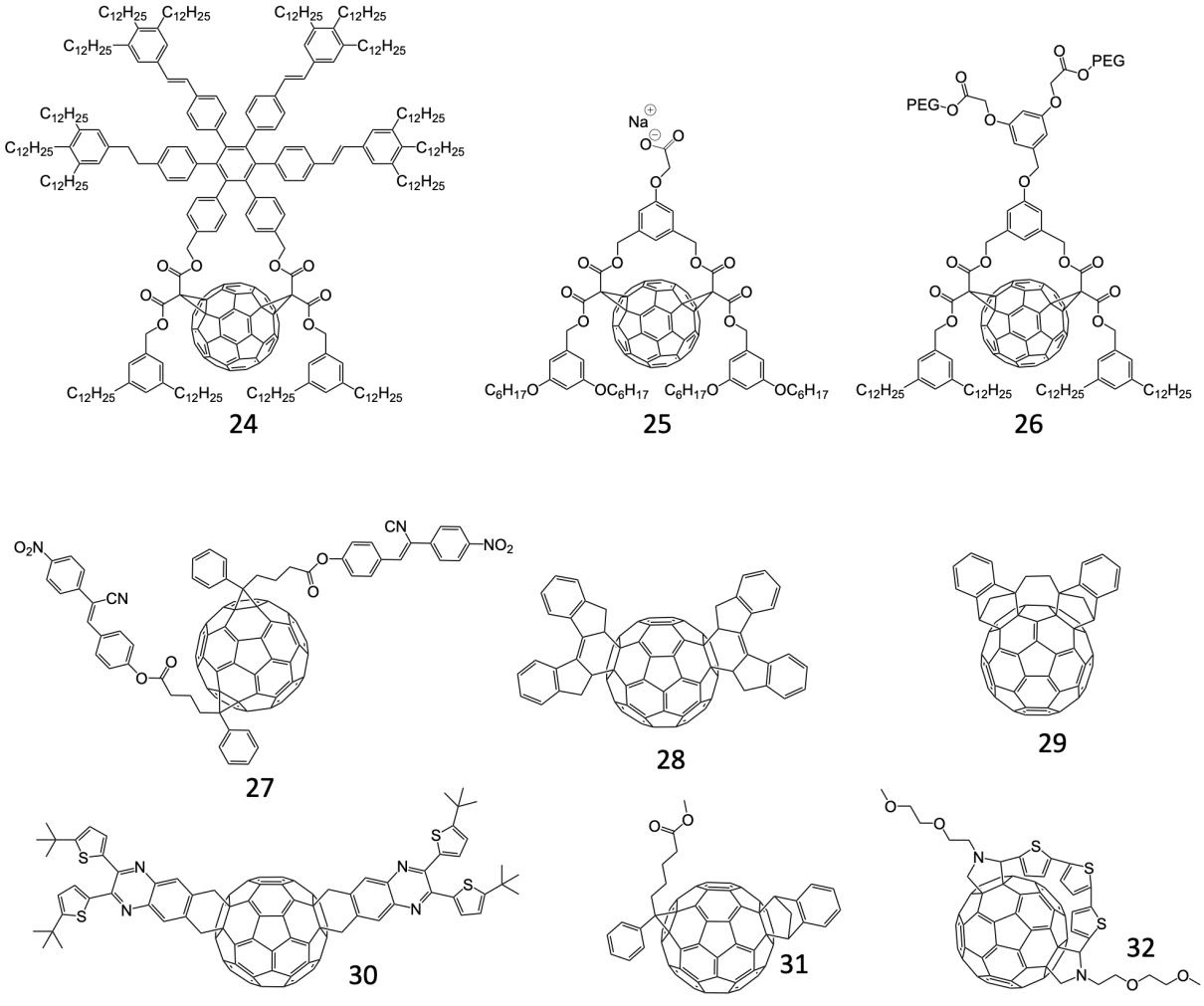

Figure 1.9 Examples of recently reported fullerene bis-adducts, **24**,[44] **25**,[45] **26**,[46] **27**,[47] **28**,[48] **29**,[49] **30**,[50] **31**[51] and **32**.[52]

1.3.2.2 Fullerene tris-adducts

Theoretically, the addition of three groups over the [6,6] junction of the fullerene cage can give up to 46 different regioisomers. Preorganisation of the starting material is crucial to synthesise pure isomers, which are essential if the fullerenes are to be subsequently used as building blocks for well-defined nanomaterials. In 2013, Sigwalt *et al*. reported a route to synthesise a fullerene tris-adduct via threefold cyclopropanation between C_{60} and tert-butyl(trialkoxy)silane-based tris-malonates, giving molecule **33** in a yield of 26% (see **Scheme 1.12**).[53] The silane moiety serves as a tether for holding three malonate groups into the *e*,*e*,*e*-addtion pattern. After deprotection of the tert-butyl silane end with BF_3•EtO_2 in a CH_2Cl_2/CH_3CN mixture, molecule **34**, with three hydroxy groups was obtained in a quantitative yield.

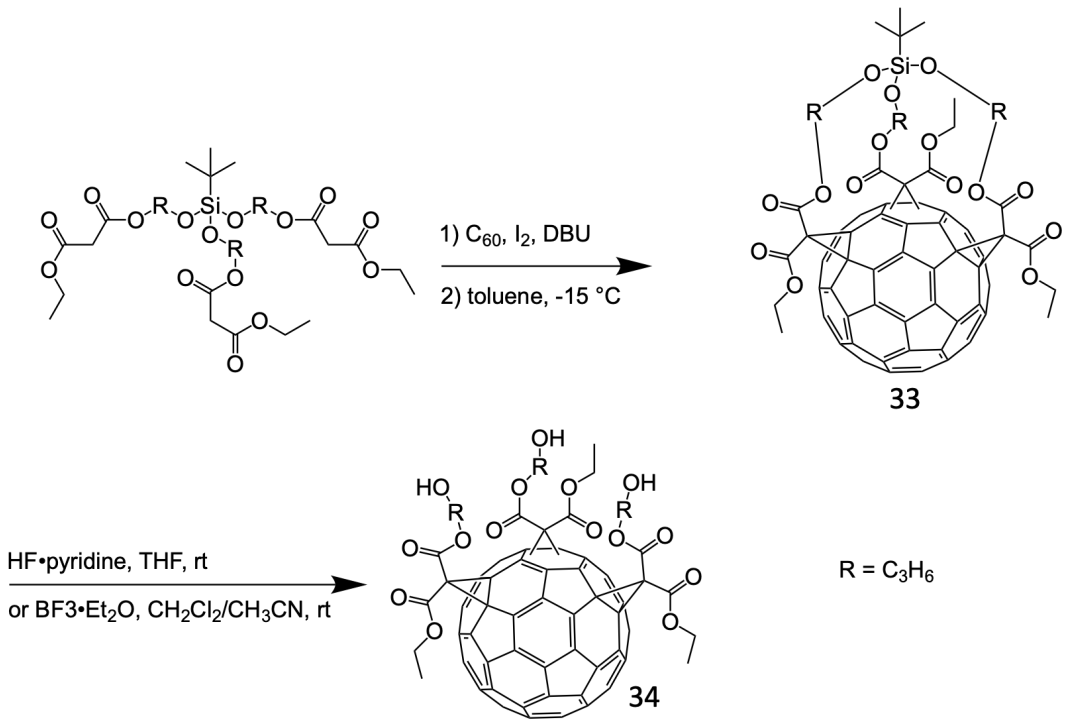

Scheme 1.12 Route to synthesise fullerene tris-malonate with three pendant hydroxy groups, **34**.

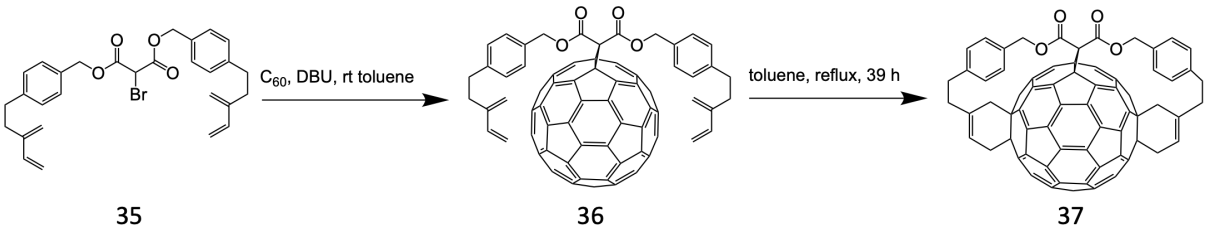

Scheme 1.13 Route to synthesise fullerene tris-adducts, **37**, with an e,e,trans-1 (C_{2v}) addition pattern.

In terms of synthesizing fullerene tris-adducts with stereo-selectivity, F. Diederich *et al*. reported a route to synthesise an e,e,trans-1 fullerene isomer by adopting combinations of a Bingel reactions and a Diels-Alder [4 + 2] cycloaddiciton.[54] Specifically, a tethered bis(1,3-butadienyl)malonate derivative, **35**, was prepared, followed by reaction with C_{60}, giving a fullerene malonate monoadduct **36** with two reactive end groups. The solution of **36** was heated for 39 hours to give a fullerene C_{2v} symmetrical tris-adducts, **37**, in a yield of 60%.

Tethered threefold addition to the fullerene cage provides a path to generate chemicals with well-defined structures, which can be translated into more advance nanomaterials. Beside the synthesis of tris-adducts with certain addition patterns, the preparation of tris-adducts prepared as mixtures of isomers is also wildly exploited, principally serving as a charge carrier in solar cells. More information regarding fullerene tris-adducts can be found in the following references with some key examples listed below (**Figure 1.10**).

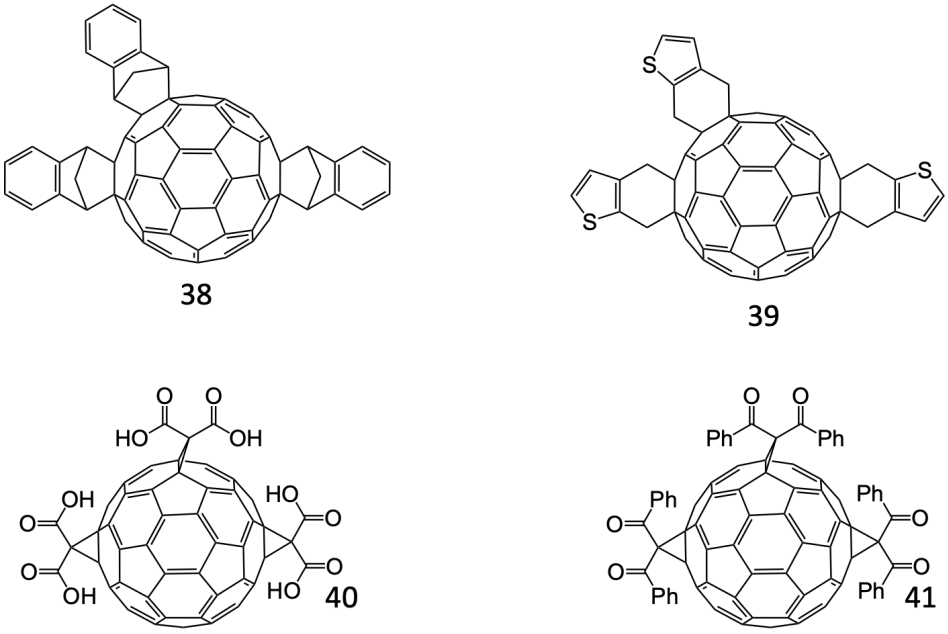

Figure 1.10 Recently reported fullerene tris-adducts, **38**,[55] **39**,[56] **40**[57] and **41**.[58]

1.3.2.3 Fullerene tetrakis-adducts

In comparison to the poly-adducts discussed above, fullerene tetrakis-adduct adduct systems are less developed and studied as a result of how difficult the regioselective synthesis is. Nevertheless, they can still play an important role as precursors for fabricating more complicated hexakis-adducts. The Diederich groups reported a route to synthesise a malonate tetrakis-adduct with four functionalities arranged along the equatorial belt of the fullerene cage (**Scheme 1.14**).[59] The tris-adduct, **37**, was reacted with excessive ethylmalonate in a Bingel reaction to give mixed hexakis-adducts **42**. Then under irradiation with a Hg lamp in the presence of O_2, **43**, with two alcohol groups was formed, followed by conversion into **44**. Subsequently, the cleavage under the basic conditions gave the symmetric tetrakis-adducts, **45**. The molecular structure was confirmed by X-ray crystallography (**Figure 1.11**), revealing that the four groups were positioned along the equatorial belt of the fullerene cage.

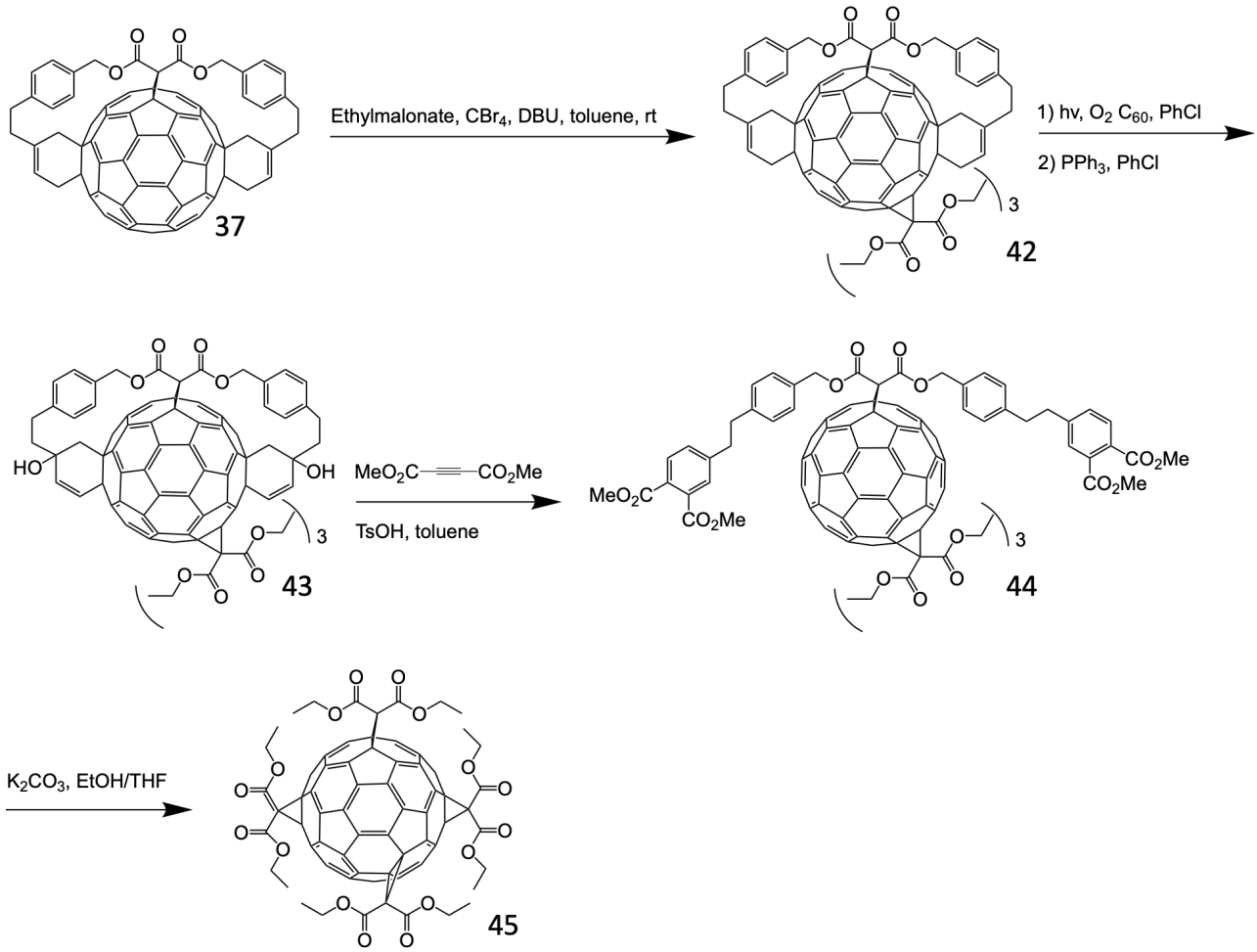

Scheme 1.14 Route to synthesise fullerene tetrakis-adduct, **45**.

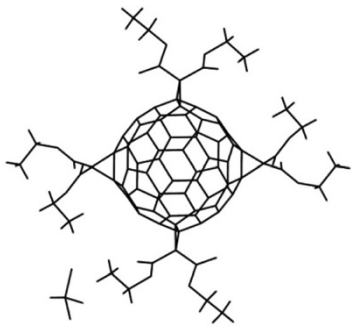

Figure 1.11 XRD structure of **45**.

1.3.2.4 Fullerene pentakis-adducts

Very few reports of route to synthesise fullerene pentakis-adducts synthesised via Bingel reaction, Prato [1 + 3] cycloaddiction, and Diels-Alder [4 + 2] cycloaddiction

have been published in recent years. Routes to synthesise pentakis-adducts mainly focused on pentahaptofullerene and its metal complexes. The electronic properties and intramolecular interactions of these species are interesting to both chemists and physicists. Several examples are listed below with references provided (**Figure 1.12**). As this type of species is not relevant to my research interests, the specific details of fullerene pentakis-adduct synthesis are not elaborated on in this review.

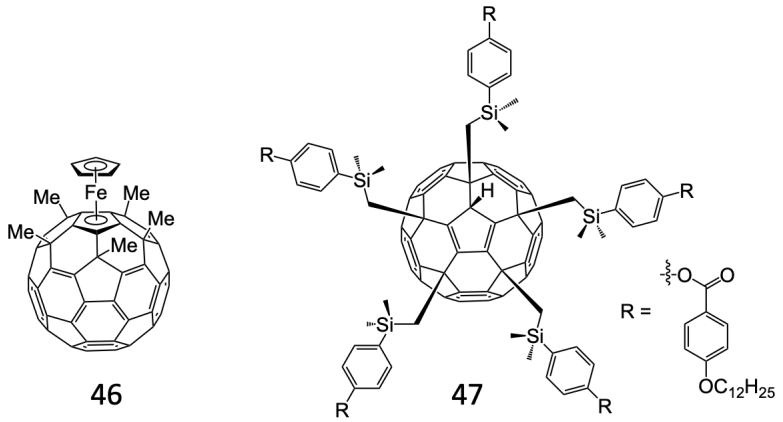

Figure 1.12 Examples of recent fullerene pentakis-adducts, **46** [60]and **47**.[61]

1.3.2.5 Fullerene hexakis-adducts

Synthesising fullerene hexakis-adducts with a highly symmetrical octahedral addition pattern has received a lot of attention from researchers focused on fabricating novel fullerene-based nanomaterials. The Bingel reaction is the most dominant reaction type used for hexakis-adduct synthesis due to its mild reaction conditions and easily accessible starting materials.

At an early stage, Hirsch *et al*. reported work in which they synthesised a fullerene hexakis-adduct in stepwise fashion via Bingel reaction.[62] First, the C_s-symmetrical tetrakis adduct was synthesized, followed by adding another group on to the cage to form the C_{2v}-symmtric pentakis-adduct and finally the T_h-symmetric hexakis-adduct.

However, this method used laborious and small scale HPLC purification, resulting in an incredibly low final yield of 0.2%.

In order to improve the yield and prepare more versatile hexakis-adducts, different groups have reported a variety of routes that make simple fullerene hexakis-malonate derivatives with one or two reactive end groups in one step. This approach enables further functionalization to then be applied by coupling other groups on the reactive ends. Nierengarten *et al*. reported a route to synthesise a fullerene hexakis-adduct with twelve azide groups, which enabled the further functionalization via 1,3-dipolar cycloaddition click reaction with alkynes moieties to form 1,2,3-triazole rings.[63] Firstly, a bis-azide malonate, **48**, was synthesized via reaction between malonyl chloride and 3-bromopropan-1-ol followed by subsequently treatment with sodium azide. Hexakis-adduct, **49**, was obtained from the reaction between C_{60} and **48** with DBU as the base in ODCB for three days in yield of 62%. The twelve azide groups in **49** were then used in a click chemistry, and depending on the aryl acetylene derivatives used, various octahedral hexakis-adducts were synthesized. After this work, they reported a route that synthesized the hexakis-adduct with twelve trimethylsilyl-protected alkene groups followed by deprotection and reaction with orgainic azide derivatives, to give a highly functionalized hexakis-adduct.[64] They also proved the possibility of synthesising fullerene hexakis-adducts in a stepwise approach. A fullerene mono-adduct with two trimethylsilyl-protected alkene groups was synthesised at first, followed by reaction with bis-azidemalonate giving the hexakis-adduct as the product. Further functionalization can then be performed on this molecule as above. A lot of products based on these routes were obtained, more examples can be found in the following references.[65-66]

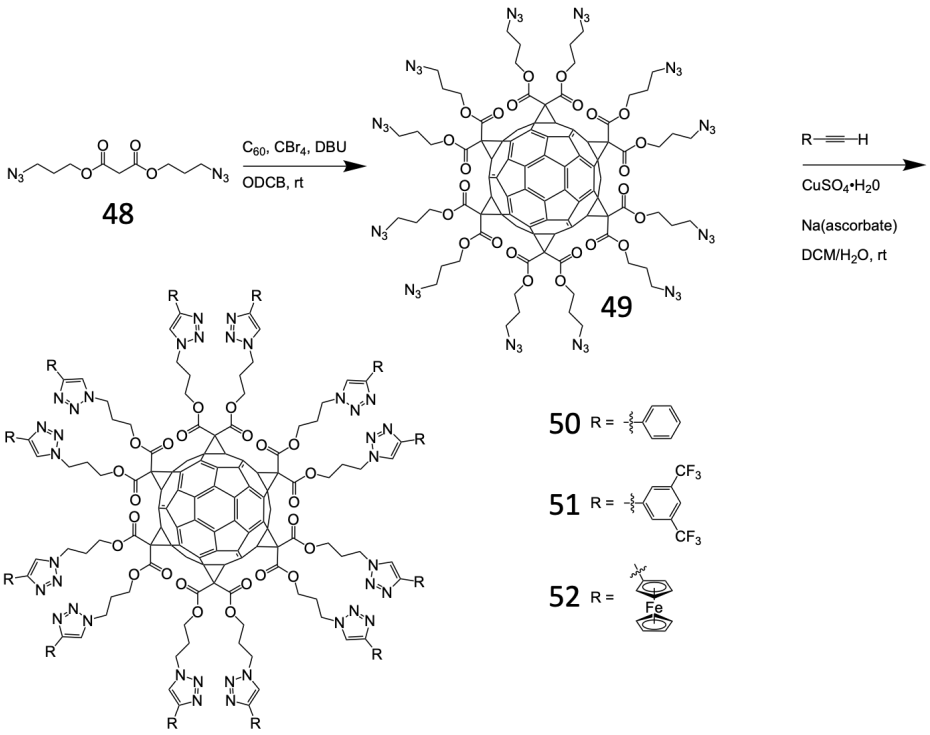

Scheme 1.15 Route to synthesise fullerene hexakis-adduct, **49**, with 12 azide groups, and further functionalised derivatives obtained via click chemistry, **50**-**52**.

In terms of synthesising fullerene hexakis-adducts in a step-wise fashion with different malonates, Brettreich *et al*. reported a route to prepare globular amphiphiles, see **Scheme 1.16**. First, malonate, **53**, with two tertbutyl group protected carboxylic groups was reacted with fullerene in a Bingel cyclopropanation, giving mono-adduct **54** as the product.[67] Then, **54** was reacted with bis-alkylmalonate in a DMA-templated 5-fold cyclopropanation to give a C_{2v} symmetry octahedral hexakis-adduct **55** in a yield of 40%. The two tertbutyl groups were removed to expose the carboxylic acid groups, which were subsequently reacted with the amide dendron **56** in the presence of DCC and HOBt to give the tertbutyl group protected intermediate. After deprotection with TFA, the amphiphilic hexakis-adduct, **57**, was formed with ten alkyl chain groups and 18 carboxylic groups. It shows the ability to form the vesicles with a size range of 100-400 nm, which is comparable to those formed from common phospholipids.

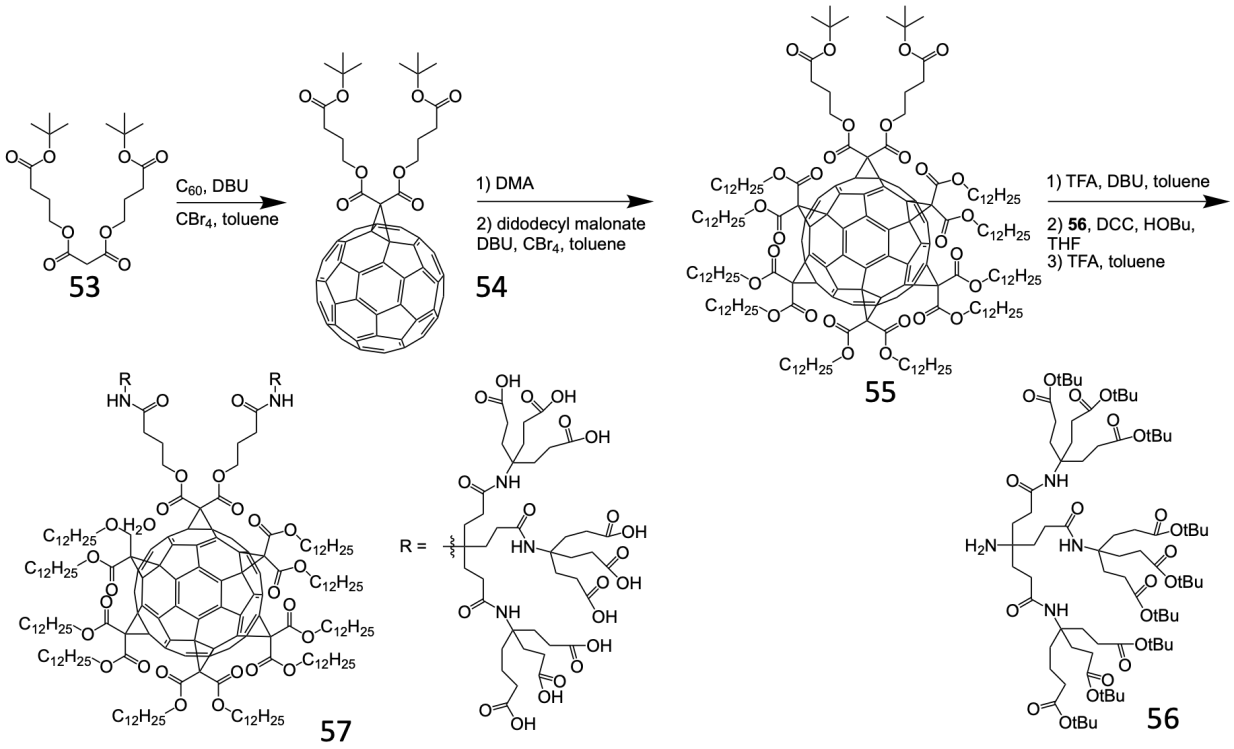

Scheme 1.16 Route to synthesise amphiphilic hexakis-adduct, **57**.

Synthesisng hexakis-adducts with normal malonate gives dodeca-substituted products, which are not suitable for material science applications which require octahedral building blocks, e.g. cubic metal-organic frameworks. To tackle this problem, Pierrat *et al*. reported a route to synthesise a hexakis-adduct with six end groups (see **Scheme 1.17**).[68] First, malonate-isophthalate oxyethylene macrocycles, **58a**-**d**, were synthesized with halide, pyridine and azide end groups. After reacting with C_{60} in a 6-fold Bingel reaction, octahedral hexakis-adduct species, **59a**-**d**, were synthesized. Depending on the different end groups, a variety of further functionalisation can be performed, such as click reactions, Sonogashira reactions, Suzuki reactions and Heck reactions. Derivative **59a** with six pyridine ends, is a good candidate for fabricating octahedral metal-organic frameworks.

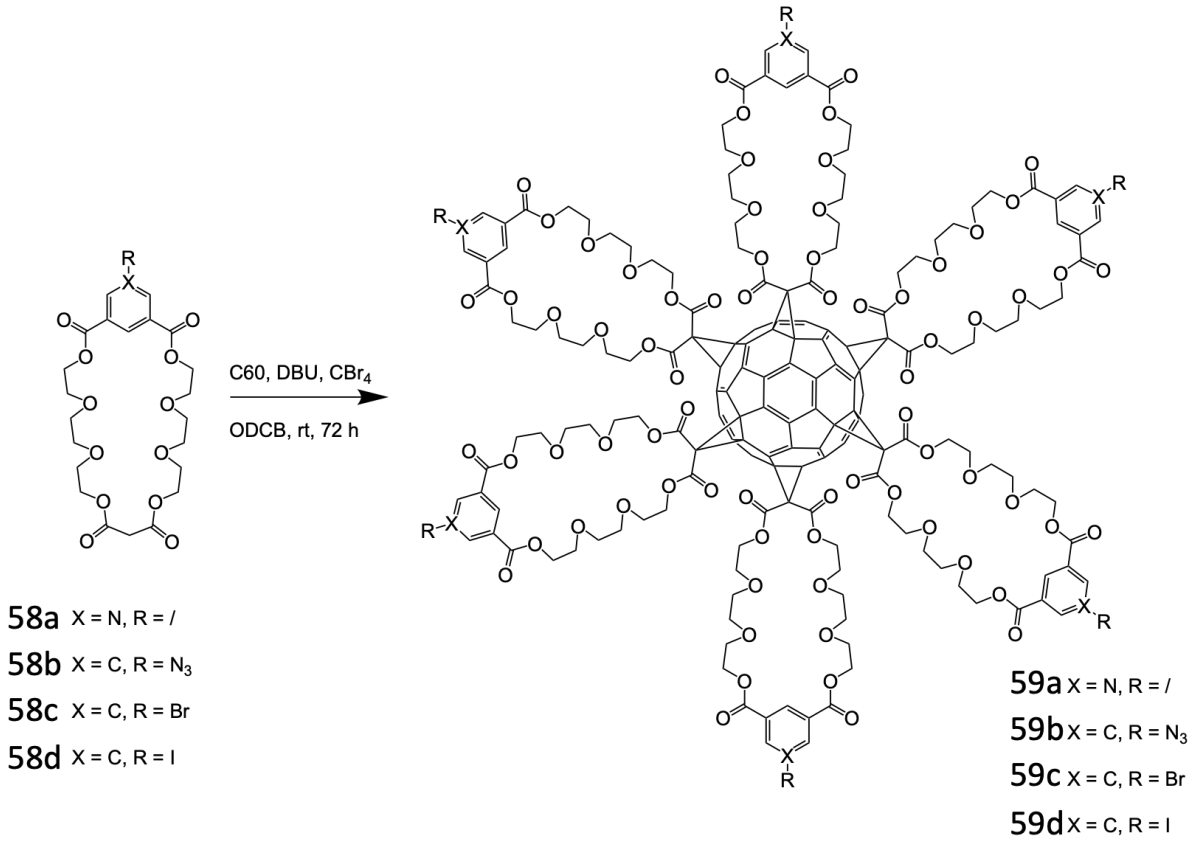

Scheme 1.17 Route to synthesise fullerene hexakis-adducts with a variety of different end groups.

1.3.3 Multi-fullerene systems

Synthesis of multi-fullerene systems, i.e. molecules containing more than one cages, is a rapidly evolving research direction, which combines the synthesis of mono- and poly-adducts. It requires, high levels of regiochemical control, the correct selection of starting material and advanced analysis of the structure of the products. Depending on the different bonds or forces used to link the fullerenes together, systems are classified as, 1, covalently linked system, e.g. fullerene dendrimer, and 2, supramolecularly linked system, e.g. fullerene-based metal-organic frameworks and coordination polymers, which are introduced in this section.

1.3.3.1 Covalently linked multi-fullerene systems

Hörmann *et al*. reported a route to prepare a fullerene dimer system (**Scheme 1.18**), which involved the synthesis of an innovative C_{2v} symmetry pentakis-adduct.[69] First, the authors synthesised an isoxazolinofullerene, **60**, in which the isoxazoline group acts as a protecting group that can be removed via retro-cycloaddition. The remaining octahedral positions of **60** were functionalized with malonate derivatives in a five-fold Bingel reaction, giving hexakis-adduct **61a**-**b**. The deprotection of the isoxazoline group was carried out by irradiation in the presence of maleic anhydride, resulting in the formation of pentakis-adduct **62a**-**b**, in which **62a** was reacted with cyclic bismalonate **63** giving **64** as the product. Fullerene **64** has a reactive malonate end group, which was used to react with another pentakis-adduct **62b** to give the final fullerene dimer **65**. In this work, authors proposed an isooxazoline protection deprotection strategy to synthesise C_{2v} symmetrical pentakis-adducts, which has a variety of choices of in terms of functionalities. Then these highly functionalized pentakis-adducts can be used as good building block to fabricate more advanced multi-fullerene systems.

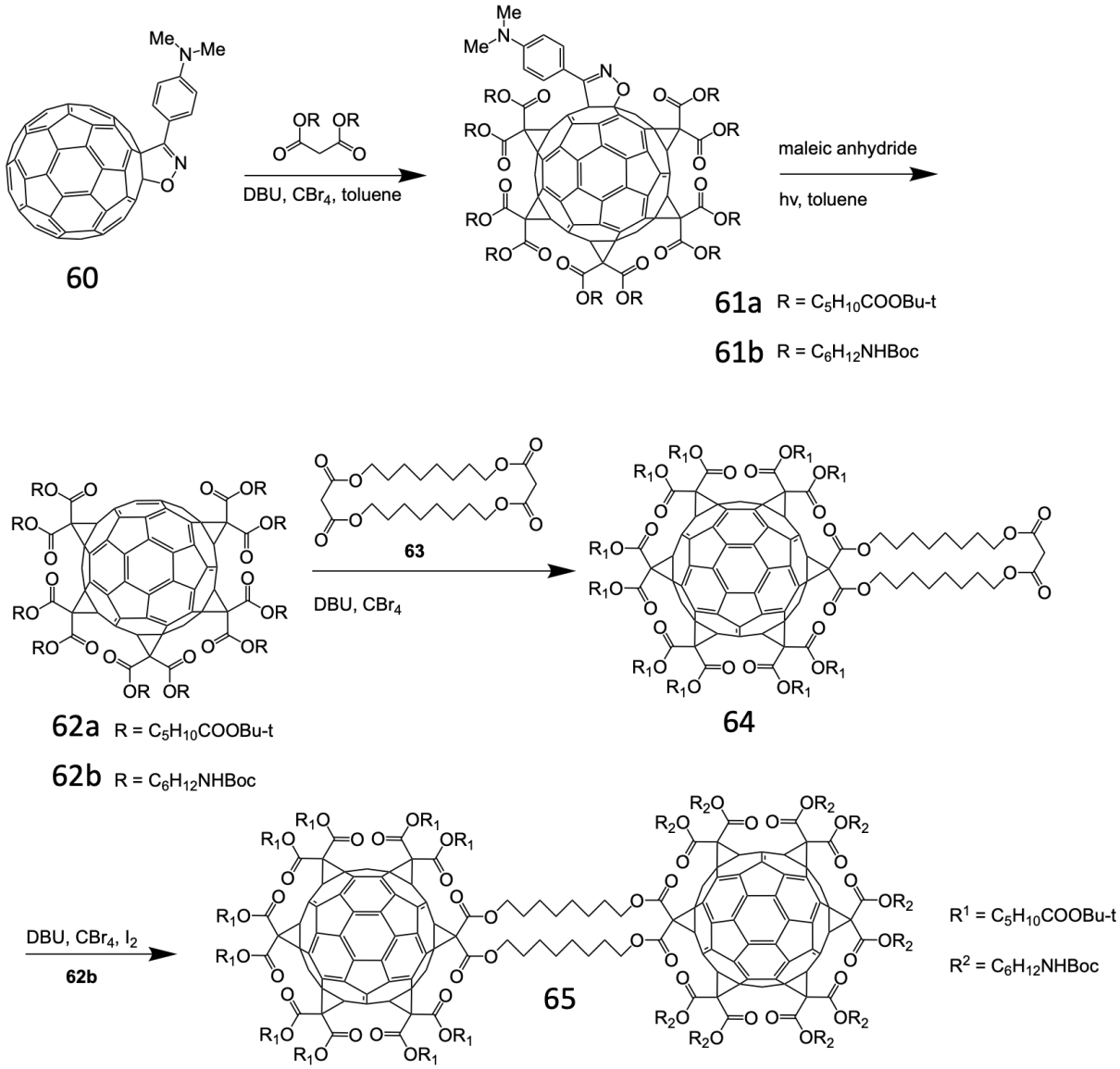

Scheme 1.18 Route to synthesise fullerene dimer, **65**.

Wasserthal *et al*. reported a route to synthesise a fullerene-based dendrimer, which involves the pentakis-adduct synthesised from the isooxazoline protection deprotection route (**Scheme 1.19**).[70] First, a chloride functionalized cyclic bismalonate, **66**, that was synthesized from reaction of **63** and sulfuryl dichloride, was reacted with fullerene in the presence of DBU through a 9,10-dimethylanthracene (DMA) templated Bingel reaction, resulting in the octahedral hexakis-adduct, **67**. Next, compound **67** was reacted with excess pentakis-adduct **68** that was prepared via the isooxazoline

protection-deprotection method in the presence of tert-butylimino tri(pyrrolidino)phosphorane as base, resulting in the final target molecule **69** in a yield of 43%. Detailed analysis, including ESI and MALDI MS and UV-Vis spectrometry were carried out to characterize the molecule **69**. Depending on which of the different core hexakis-adducts that were used, various dendrimer systems have been synthesized. Martín *et al*. reported several 13-fullerene systems using hexakis-adduct with 12 alkene groups or 12 azide groups as the core molecule to incorporate another 12 fullerene moieties via click chemistry, giving a giant globular multivalent fullerenes species for antivirus applications (**Figure 1.13**).[71]

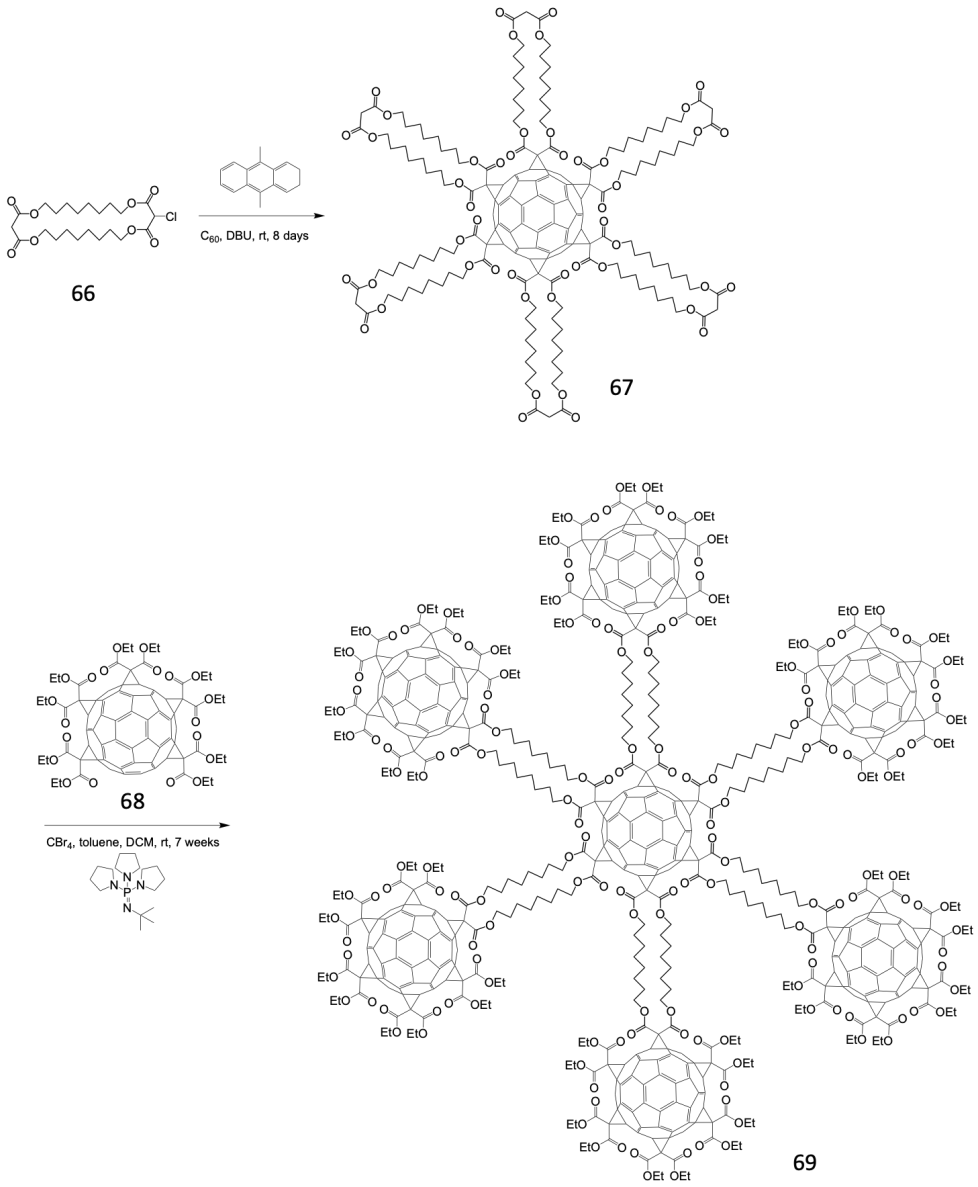

Scheme 1.19 Route to synthesise heptafullerene, **69**.

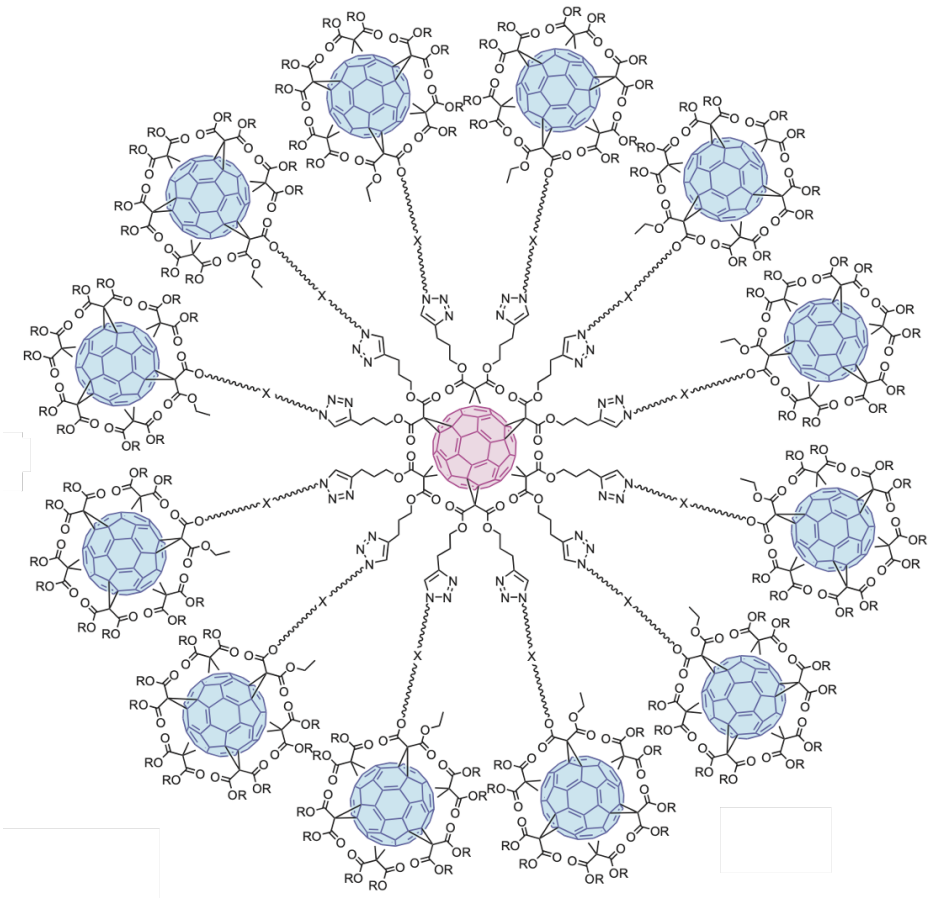

Figure 1.13 The giant globular multivalent fullerenes containing macromolecule, obtained via click chemistry.

Recently, Xu *et al*. reported a fullerene trimer system, in which a macrocyclic ring is used to serve as a template (**Scheme 1.20**).[72] The previously mentioned molecule, **68**, was synthesised as a stopper and reacted with **63** to give the hexakis-adduct **70** via Bingel reaction in the presence of DBU and CBr_4. At the same time, a brominated cyclic bismalonate, **71**, was synthesised from **63** and bromine, which was subsequently reacted with **68** to give hexakis-adduct, **72**. Fullerene dimer, **73**, was synthesized via reaction between **70** and fullerene using BTTP as base, in which the second fullerene moiety can be incorporated with a macrocyclic ring [10]CCP to form a pseudorotaxane supramolecule, **74**. Fullerene **72** was reacted with **74** in the presence of BTTP, giving a fullerene based rotaxane structure, **75**, in which two

hexakis-adducts act as stopper to lock the [10]CCP in the middle of the structure. Due to the existence of the [10]CCP moiety, the addition position of the middle fullerene was limited, resulting in only trans-2 and trans-3 regioisomers, which were isolated by HPLC and characterised by ^{1}H, ^{13}C NMR and MALDI MS.

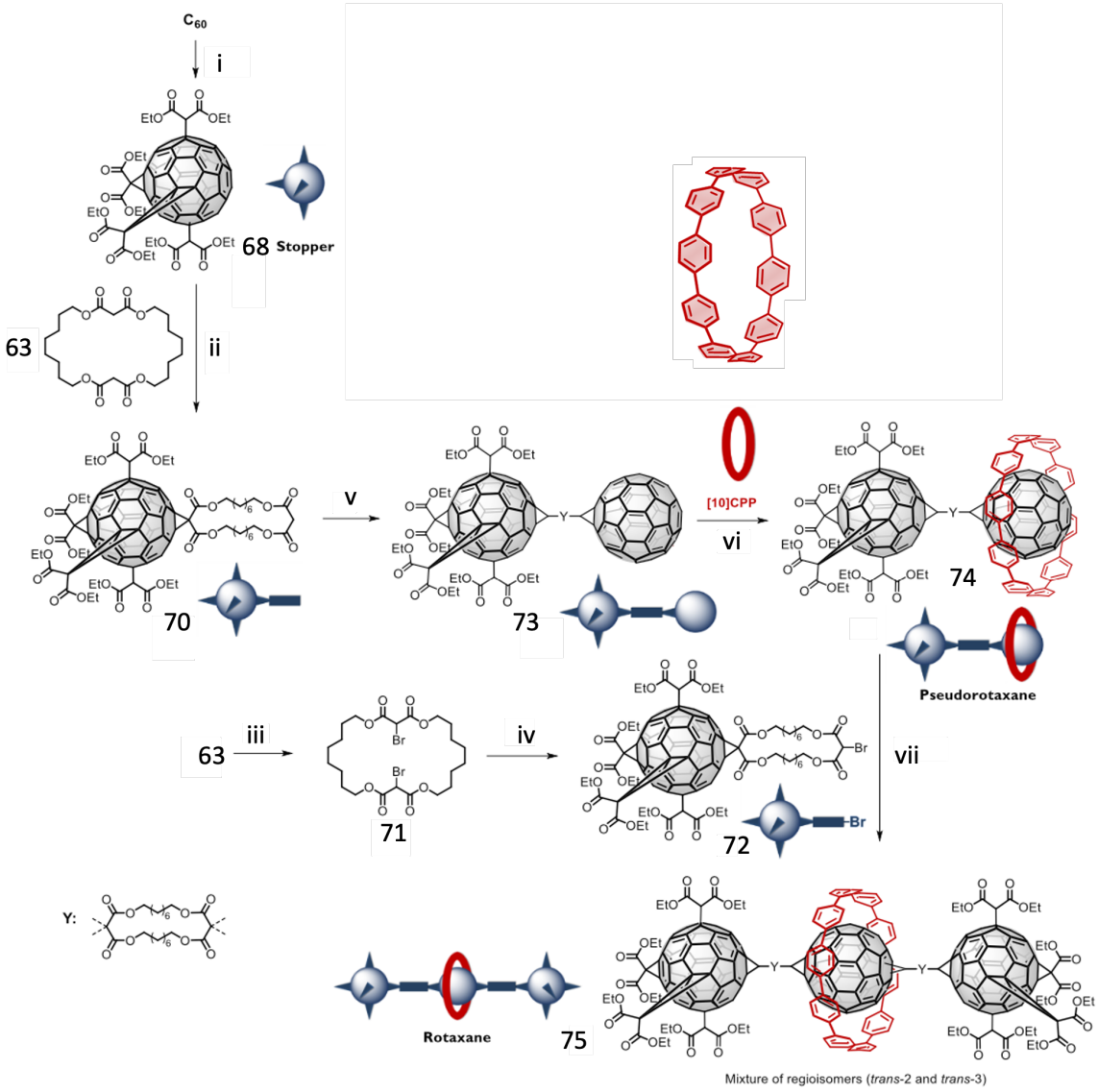

Scheme 1.20 Route to synthesisethe three fullerene containing rotaxane system, **75**.

1.3.3.2 Supramolecularly linked multi-fullerene systems

Beside covalently linked fullerene derivatives, fullerene derivatives can also be linked together by intermolecular interactions. In comparison with covalent bonds, the strength of supramolecular bonds or intermolecular interactions are typically lower. The advantage is the reversibility of such interactions, which facilitates the formation of complicated structures over large domains enabling greater flexibility in how the properties of the resultant structures can be tuned. The inherently spherical structure, high degree of symmetry and ability to poly-functionalise the cage make fullerene derivatives promising candidates to generate supramolecular assemblies. As a result, numerous fullerene derivatives have been fabricated into well-defined supramolecular arrays (metal organic frameworks, coordination polymer) and random aggregate, showing the potential of such systems in the applications for catalysis, drug delivery, energy storage and nonlinear optics.

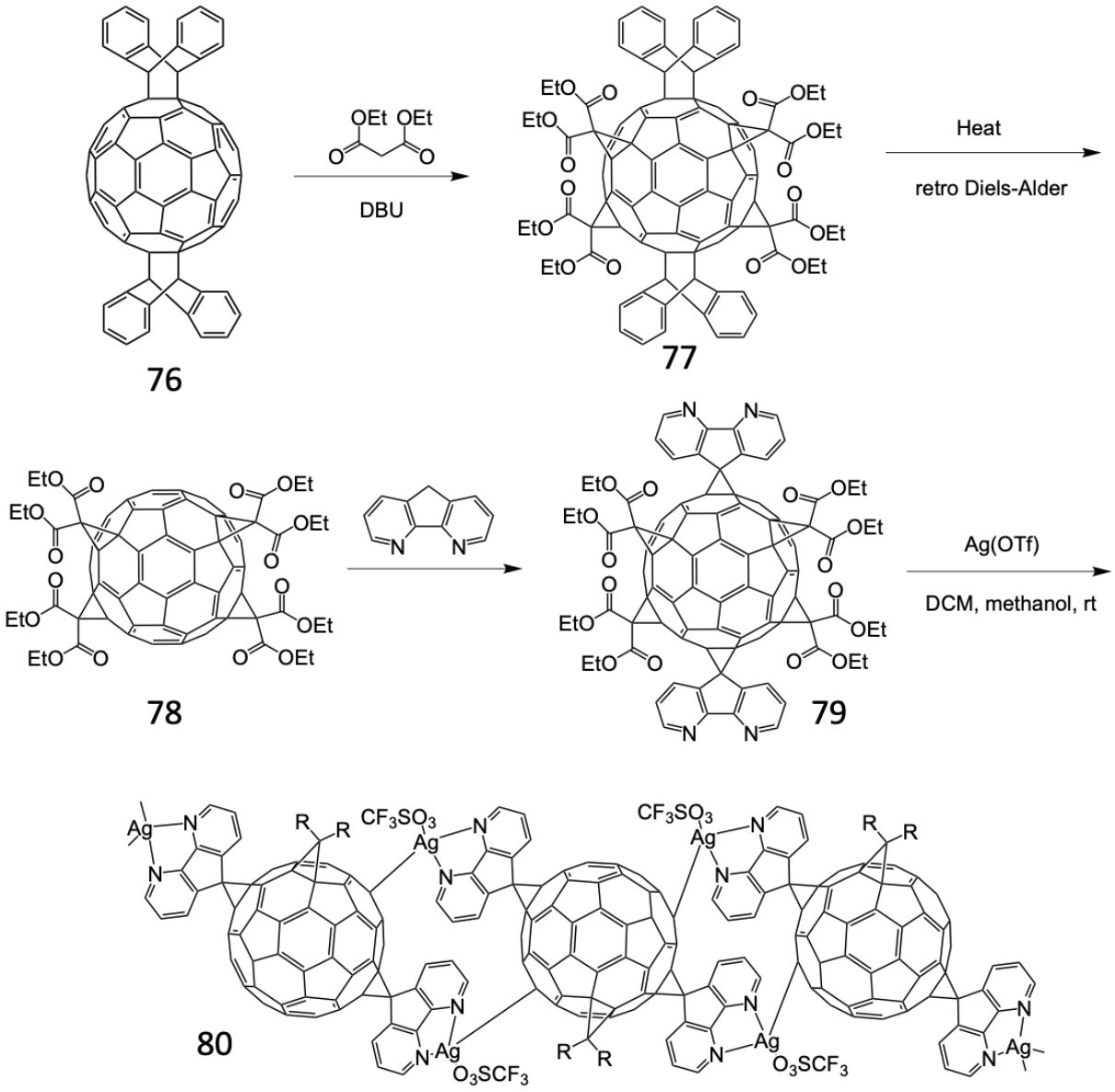

Scheme 1.21 Route to synthesise fullerene-based coordination polymer, **80**.

Peng *et al*. reported a supramolecular array, which introduced a novel fullerene ligand forming a linear coordination polymer by silver complexation (see **Scheme 1.21**).[73] They synthesized a fullerene hexakis-adduct mono-unit with two 4,5-diazafluorene groups in a trans conformation, in which the 4,5-diazafluorene group is considered as a good ligand for metal coordination and it can be added to fullerene efficiently via Bingel reaction. The mono-units were then reacted with silver triflate to form a linear metal-organic coordination polymer. Firstly, a fullerene bis-adduct, **76**, with two

anthracene protecting groups in the trans positions was synthesized, followed by addition of four diethyl malonate groups in the equatorial positions to form hexakis-adduct, **77**. The anthracene groups were deprotected through a thermally induced retro Diels-Alder reaction forming tretrakis adduct, **78**, in which the remaining two empty trans positions were subsequently functionalised with 4,5-diazafluorene groups via a Bingel reaction giving hexakis-adduct, **79**, as the mono-unit in a yield a of 91%. Interestingly, the planar 4,5-diazafluorene group is ideally orientated perpendicular to the fullerene surface, with making the two bipyridine groups parallel to each other, which makes **79** a promising linker for other systems, e.g. MOFs. Eventually, a yellow-green crystal of the coordination polymer, **80**, was formed by slow diffusion of silver triflate in methanol into a solution of **79** in DCM followed by the addition of toluene. The structure of this crystal was characterized by X-ray crystal structure analysis (see **Figure 1.14**), which indicated no intermolecular interaction between fullerene units due to the existence of the four ethyl malonate groups on each C_{60} cage. Each fullerene unit was coordinated to two silver ions with the silver ions bound to the carbon atoms of adjacent fullerenes. The π–π stacking of diazafluorene rings from neighboring fullerene unit was also observed, see **Figure 1.14**.

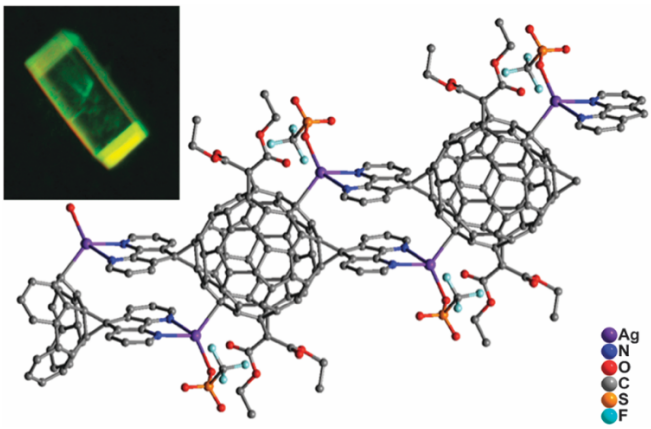

Figure 1.14 A fragment of the 1D coordination polymer, **80**. In which π–π stacking interaction between neighbouring diazafluorene rings was observed. A picture of crystal is inset.

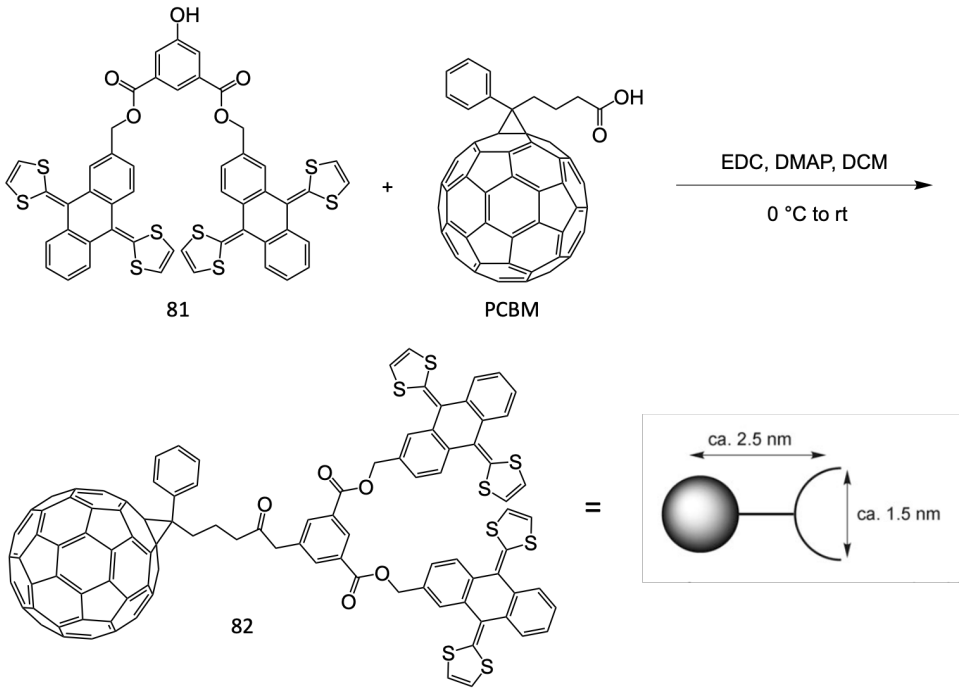

Scheme 1.22 Route to synthesise fullerene monomer, **82**.

Gustavo *et al*. also reported a fullerene-based supramolecular polymer, in which the monomers were linked together by π–π aromatic interactions.[74] They used π extended tetrathiafulvalene (exTTF) groups as a recognizing motif to bind the convex

surface of C_{60}. First, two exTTFs were coupled with an isophthalic diester forming a tethered tweezer shaped molecule, **81**. This was used as a starting material that was subsequently reacted with a PCBM molecule, due to its high solubility to obtain the fullerene monomer, **82** (see **Scheme 1.22**). This molecule can assemble together in a head to tail fashion, resulting in 1D linear array (**Figure 1.15**). The authors used ^{1}H NMR to analyse the **82** in $CDCl_3$ in different concentrations. They found increasing the concentration of **82** induced a shielding effect of the resonances, which indicated the formation of the assembly. UV-Vis spectrometry and cyclic voltammetry studies were also carried out to provide more evidence. After drop-casting solutions of **82** in DCM onto mica, AFM was used to give further evidence of prove the formation of a linear structure (see **Figure 1.15**).

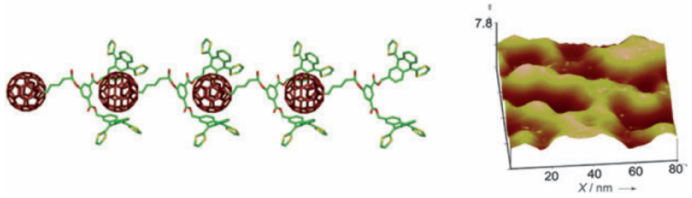

Figure 1.15 (left) Schematic of supramolecular polymer fragment, (**82**)$_4$ and (right) AFM image (tapping mode, air, 298 K) of a dropcast of a dichloromethane solution of **82.**

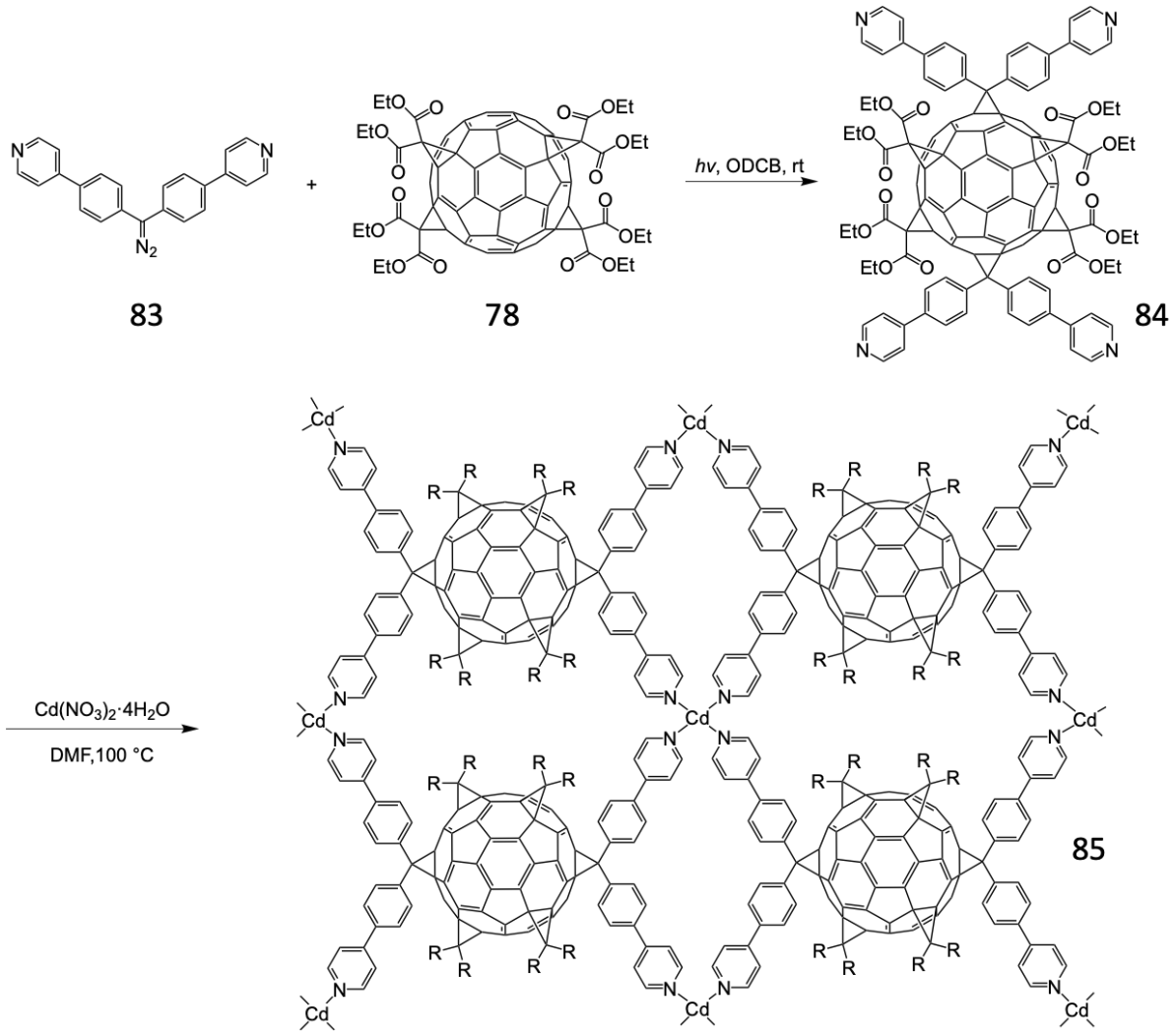

Scheme 1.23 Route to synthesise 2D fullerene-based MOF, **85**.

Peng *et al*. reported a two-dimensional (2D) fullerene-based MOF using a fullerene hexakis-adduct with four pyridyl groups as the mono-unit, in which four nitrogen atoms are orientated in a rectangle.[75] The crystal structure shows the 2D layers packed together with isolated mono-units located between layers forming a complicated three dimensional structure. First, 4,4'-(4,4'-(diazomethylene)bis(4,1-phenylene))dipyridine, **83**, was synthesized, followed by bonding to the trans position of the previously mentioned fullerene tetrakis-adduct, **78**, giving fullerene hexakis-adduct as product **84**, as product, with four pyridine nitrogens in the trans position forming a planar rectangle (**Scheme 1.23**). Pyridine groups are favored ligands to coordinate metal centres to

synthesise supramolecular MOF, while the second phenyl groups serves as a spacer, which help to increase the reach of the ligand and reduce the steric hindrance. The final 2D MOF was formed by reacting **84** with $Cd(NO_3)_2 \cdot 4H_2O$ in DMF at 100 °C overnight. The reaction mixture was allowed to cool down to room temperature, followed by adding methanol to form a layer on the top of the solution. Yellow crystals, **85**, were obtained after several weeks. The MOF structure was characterized by single crystal XRD, which indicated each fullerene coordinates four cadmium ions forming two different sized pores (**Figure 1.16a**). Interestingly, isolated fullerene mono-units fit in the space between the 2D layers at the centers of the two pore-I structures (**Figure 1.16b**). The interaction between ethyl malonate groups of isolated fullerene mono-unit and the phenyl pyridine moieties of the 2D MOF layer was also observed, which linked the 2D networks together into a 3D structure (**Figure 1.16c**).

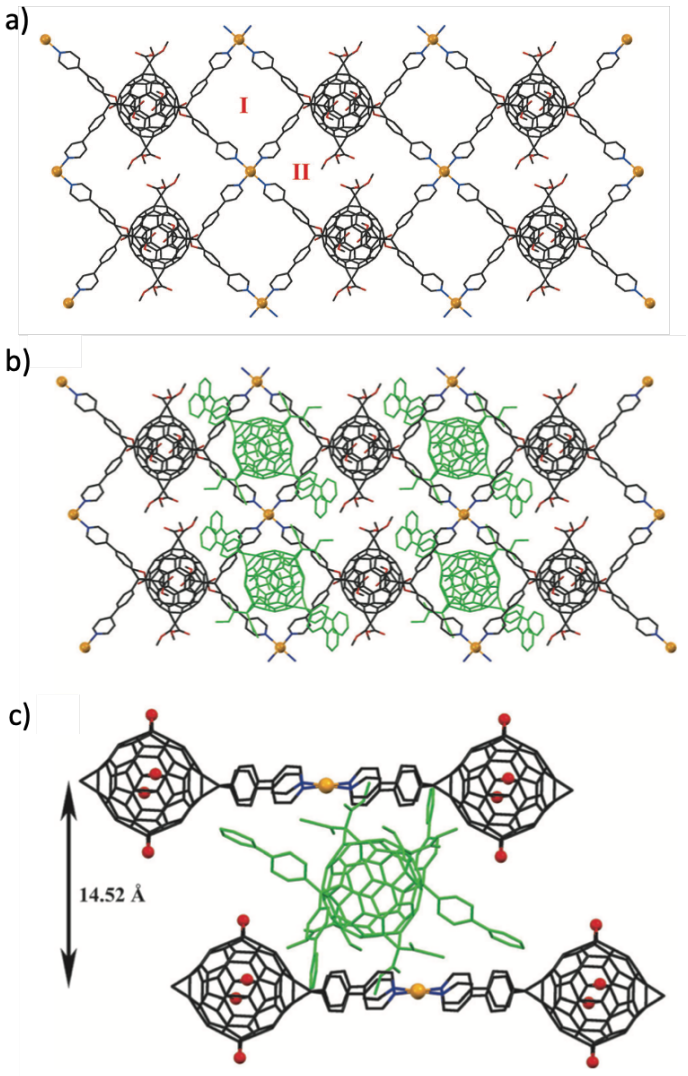

Figure 1.16 Diagrams of fullerene-based MOF, **85**, showing; a) the 2D layer of fullerene-based MOF contains two pores-I and II; b) isolated fullerene monomers, **84**, accommodated in the pore-I; and c) two MOF layers are linked together by pore-I accommodated fullerene monomer, **84**, forming the 3D structure.

Multi-fullerene systems have shown the potential to be used in applications such as anti-virus treatments, catalysis, energy storage and etc. However, due to the complicated nature and poor scalability of the synthesis and separation of fullerene species and the complexity of the resultant analysis, this research direction is less developed.

1.4 Conclusion

In summary, fullerene functionalisation has been well exploited over the past few decades, with many C_{60} based materials synthesised for applications and even more advanced structures have been proposed. However, there still remains the potential to achieve further advances, especially in terms of designing fullerene building blocks for multifunctional nanomaterials. Multifunctional nanomaterials, such as carbon nanotubes, is another underdeveloped approach which could be exploited to form novel hybrid nanocarbon systems. This improved molecular design also needs evolution of methods/control of the conditions to direct fullerene derivatives into arrays such as MOFs, COFs and supramolecular polymers, if fullerene-based materials are to be developed to meet the future challenges, such as fossil fuel deficit, global warming and environmental pollution from chemical production process. Fullerene can accept electrons quickly, stably and reversibly. After proper functionalisation, fullerene derivatives can perform as charge carriers for the sustainable energy production and storage, accelerating the replacement of traditional fossil fuel. At the same time, the fullerene can be functionalised with multi functionalities, which could act as scaffold for fabricating material for highly efficient catalyst when coordinating to metal, biosensor and medicine when biomolecule binding groups are added.

The aim of this project is to design and synthesise the fullerene derivatives as i) charge carriers for redox flow batteries, ii) scaffold for developing supramolecular arrays and iii) photo resist material for lithography nanopatterning. **Chapter 2** presents the work of highly soluble fullerene charge carriers for symmetrical redox flow batteries, in which ferrocene group that can quickly, stably and reversibly give electron is appended to fullerene cage forming a type of molecule that can be positively or negatively charged

and enabling these molecules to work in both side of the cell (catholyte and anolyte). Beside ferrocene group, a family of molecules with different solubilising groups, electron- donating and withdrawing groups were synthesised to study their contributions to solubility and electrochemical property. A rule of molecular design for improving solubility and achieving bespoke potential window is summarised, which could lead fullerene-based charge carriers to further advances.

The supramolecular assembly is common in living cells, such as protein-protein assembly, lipid-lipid assembly and etc, which are essential and important to maintain functions of biology system. However, the supramolecular assembly behavior in living system is yet to be fully understand due to its complicated nature. The study of the artificial supramolecular assembly can provide the hint to scientist for further pushing the understanding of this subject. Due to the nanosized spherical structure and the π electron rich nature of fullerene, it has been studied a lot in fabricating supramolecular assemblies as the guest molecule to bind with the other host molecules, e.g. cyclodextrin, cyclotricatechylene and extra, relying on the π-π stacking, Van der Waals interaction and shape complementation (concave-convex). After covalently appending the fullerene to the scaffold molecule with multi reactive functionalities to form the multi-fullerene armed scaffold, then the fullerene moiety can further bind the other host molecules to develop the supramolecular arrays. Depending on the type of the scaffold and the host-molecule used, 2D and 3D supramolecular arrays can be achieved. **Chapter 3** is presented for developing synthetic routes to synthesising a fullerene trimer by appending the three fullerene cages to a cyclotriguaiacylene (CTG) molecule. Cyclotriguaiacylene is a cyclic trimer of guaiacol. It has one hydroxy group and one methoxy group on each benzene ring. The hydroxy group on the CTG is functionalised with desired groups to react with either fullerene derivatives or C_{60} on its

unfunctionalised form, resulting the three-fullerene armed CTG molecule, in which fullerene can subsequently bind the other host molecules to develop supramolecular assembly.

Nanoscale patterning is considered as a fundamental step in various of advanced solid-state devices for example integrated electronics, chemical and biological sensors. In **Chapter 4**, fullerene-platinum complex for lithographically developping the carbon-based nanopattern is present. Fullerene is initially functionalised with bipyridine ligand and solubilising group, giving a non-metal fullerene derivative, which is able to coordinate Pt to form a fullerene-Pt complex. The non-methal fullerene derivatives and fullerene-Pt complex are both used to develop the lithographic nano-pattern and making the comparison with each other. The C_{60}-Pt complex is expected to have higher sensitivity to electron beam that non-metal fullerene derivatives, as the presence of the Pt metal center can enhance the secondary electron scattering and thus increase energy deposition efficiency.

1.5 References

1. Kroto, H. W.; Heath, J. R.; O'Brien, S. C.; Curl, R. F.; Smalley, R. E., C60: Buckminsterfullerene. *Nature* **1985,** *318* (6042), 162-163.
2. Hirsch, A.; Brettreich, M., *Fullerenes: chemistry and reactions*. John Wiley & Sons: 2006.
3. Kadish, K. M.; Ruoff, R. S., *Fullerenes: chemistry, physics, and technology*. John Wiley & Sons: 2000.
4. Xie, Q.; Perez-Cordero, E.; Echegoyen, L., Electrochemical detection of C606- and C706-: Enhanced stability of fullerides in solution. *Journal of the American Chemical Society* **1992,** *114* (10), 3978-3980.
5. Echegoyen, L.; Echegoyen, L. E., Electrochemistry of fullerenes and their derivatives. *Accounts of chemical research* **1998,** *31* (9), 593-601.
6. Dubois, D.; Kadish, K. M.; Flanagan, S.; Wilson, L. J., Electrochemical detection of fulleronium and highly reduced fulleride (C605-) ions in solution. *Journal of the American Chemical Society* **1991,** *113* (20), 7773-7774.
7. Brabec, C. J.; Gowrisanker, S.; Halls, J. J.; Laird, D.; Jia, S.; Williams, S. P., Polymer–fullerene bulk-heterojunction solar cells. *Advanced Materials* **2010,** *22* (34), 3839-3856.
8. Li, G.; Shrotriya, V.; Huang, J.; Yao, Y.; Moriarty, T.; Emery, K.; Yang, Y., High-efficiency solution processable polymer photovoltaic cells by self-organization of polymer blends. In *Materials For Sustainable Energy: A Collection of Peer-Reviewed Research and Review Articles from Nature Publishing Group*, World Scientific: 2011; pp 80-84.
9. Yang, C.; Kim, J. Y.; Cho, S.; Lee, J. K.; Heeger, A. J.; Wudl, F., Functionalized methanofullerenes used as n-type materials in bulk-heterojunction polymer

solar cells and in field-effect transistors. *Journal of the American Chemical Society* **2008,** *130* (20), 6444-6450.

10. He, Y.; Chen, H.-Y.; Hou, J.; Li, Y., Indene− C60 bisadduct: a new acceptor for high-performance polymer solar cells. *Journal of the American Chemical Society* **2010,** *132* (4), 1377-1382.
11. Zhao, G.; He, Y.; Li, Y., 6.5% efficiency of polymer solar cells based on poly (3‐hexylthiophene) and indene‐C60 bisadduct by device optimization. *Advanced Materials* **2010,** *22* (39), 4355-4358.
12. Pupysheva, O. V.; Farajian, A. A.; Yakobson, B. I., Fullerene nanocage capacity for hydrogen storage. *Nano Letters* **2008,** *8* (3), 767-774.
13. Friedl, J.; Lebedeva, M. A.; Porfyrakis, K.; Stimming, U.; Chamberlain, T. W., All-fullerene-based cells for nonaqueous redox flow batteries. *Journal of the American Chemical Society* **2018,** *140* (1), 401-405.
14. Coq, B.; Planeix, J. M.; Brotons, V., Fullerene-based materials as new support media in heterogeneous catalysis by metals. *Applied Catalysis A: General* **1998,** *173* (2), 175-183.
15. Martinez, Z. S.; Castro, E.; Seong, C.-S.; Cerón, M. R.; Echegoyen, L.; Llano, M., Fullerene derivatives strongly inhibit HIV-1 replication by affecting virus maturation without impairing protease activity. *Antimicrobial agents and chemotherapy* **2016,** *60* (10), 5731-5741.
16. Khakina, E. A.; Ol'ga, A. K.; Popova, M. L.; Peregudov, A. S.; Troyanov, S. I.; Chernyak, A. V.; Martynenko, V. M.; Kulikov, A. V.; Schols, D.; Troshin, P. A., Synthesis of different types of alkoxy fullerene derivatives from chlorofullerene C 60 Cl 6. *Organic & biomolecular chemistry* **2017,** *15* (4), 773-777.

17. Yu, C.; Avci, P.; Canteenwala, T.; Chiang, L. Y.; Chen, B. J.; Hamblin, M. R., Photodynamic therapy with hexa (sulfo-n-butyl)[60] fullerene against sarcoma in vitro and in vivo. *Journal of nanoscience and nanotechnology* **2016,** *16* (1), 171-181.

18. Lebedeva, M. A.; Chamberlain, T. W.; Schröder, M.; Khlobystov, A. N., An efficient route to the synthesis of symmetric and asymmetric diastereomerically pure fullerene triads. *Tetrahedron* **2012,** *68* (25), 4976-4985.

19. Zhang, Y.; Matsuo, Y.; Li, C.-Z.; Tanaka, H.; Nakamura, E., A scalable synthesis of methano [60] fullerene and congeners by the oxidative cyclopropanation reaction of silylmethylfullerene. *Journal of the American Chemical Society* **2011,** *133* (21), 8086-8089.

20. Bingel, C., Cyclopropanierung von fullerenen. *Chemische Berichte* **1993,** *126* (8), 1957-1959.

21. Tsuge, O.; Kanemasa, S., Recent advances in azomethine ylide chemistry. In *Advances in heterocyclic chemistry*, Elsevier: 1989; Vol. 45, pp 231-349.

22. Maggini, M.; Scorrano, G.; Prato, M., Addition of azomethine ylides to C60: synthesis, characterization, and functionalization of fullerene pyrrolidines. *Journal of the American Chemical Society* **1993,** *115* (21), 9798-9799.

23. Whiting, A.; Windsor, C. M., What makes a neutral imino dieneophile undergo a thermal, non-catalysed, Diels-Alder reaction? *Tetrahedron* **1998,** *54* (22), 6035-6050.

24. Holmes, H., The D iels‐A lder Reaction Ethylenic and Acetylenic Dienophiles. *Organic Reactions* **2004,** *4*, 60-173.

25. Martin, N.; Martinez-Grau, A.; Sanchez, L.; Seoane, C.; Torres, M., The First Hetero-Diels− Alder Reaction of C60 with 1-Azadienes. Synthesis of

Tetrahydropyrido [2 ‘, 3 ‘: 1, 2][60] fullerene Derivatives. *The Journal of Organic Chemistry* **1998,** *63* (22), 8074-8076.

26. Schuster, D. I.; MacMahon, S.; Guldi, D. M.; Echegoyen, L.; Braslavsky, S. E., Synthesis and photophysics of porphyrin–fullerene donor–acceptor dyads with conformationally flexible linkers. *Tetrahedron* **2006,** *62* (9), 1928-1936.
27. Guldi, D. M.; Maggini, M.; Scorrano, G.; Prato, M., Intramolecular electron transfer in fullerene/ferrocene based donor− bridge− acceptor dyads. *Journal of the American Chemical Society* **1997,** *119* (5), 974-980.
28. Langa, F.; de la Cruz, P.; Espíldora, E.; González-Cortés, A.; de la Hoz, A.; López-Arza, V., Synthesis and Properties of Isoxazolo [60] fullerene− Donor Dyads. *The Journal of organic chemistry* **2000,** *65* (25), 8675-8684.
29. Guldi, D. M.; Zilbermann, I.; Gouloumis, A.; Vazquez, P.; Torres, T., Metallophthalocyanines: versatile electron-donating building blocks for fullerene dyads. *The Journal of Physical Chemistry B* **2004,** *108* (48), 18485-18494.
30. Wessendorf, F.; Grimm, B.; Guldi, D. M.; Hirsch, A., Pairing fullerenes and porphyrins: Supramolecular wires that exhibit charge transfer activity. *Journal of the American Chemical Society* **2010,** *132* (31), 10786-10795.
31. Barendt, T. A.; Rašović, I.; Lebedeva, M. A.; Farrow, G. A.; Auty, A.; Chekulaev, D.; Sazanovich, I. V.; Weinstein, J. A.; Porfyrakis, K.; Beer, P. D., Anion-mediated photophysical behavior in a C60 fullerene [3] rotaxane shuttle. *Journal of the American Chemical Society* **2018,** *140* (5), 1924-1936.
32. Da Ros, T., Twenty years of promises: fullerene in medicinal chemistry. In *Medicinal Chemistry and Pharmacological Potential of Fullerenes and Carbon Nanotubes*, Springer: 2008; pp 1-21.

33. Guldi, D. M.; Prato, M., Excited-state properties of C60 fullerene derivatives. *Accounts of chemical research* **2000,** *33* (10), 695-703.

34. Bendikov, M.; Wudl, F.; Perepichka, D. F., Tetrathiafulvalenes, oligoacenenes, and their buckminsterfullerene derivatives: the brick and mortar of organic electronics. *Chemical reviews* **2004,** *104* (11), 4891-4946.

35. Nakamura, E.; Isobe, H., Functionalized fullerenes in water. The first 10 years of their chemistry, biology, and nanoscience. *Accounts of chemical research* **2003,** *36* (11), 807-815.

36. Yan, W.; Seifermann, S. M.; Pierrat, P.; Bräse, S., Synthesis of highly functionalized C 60 fullerene derivatives and their applications in material and life sciences. *Organic & Biomolecular Chemistry* **2015,** *13* (1), 25-54.

37. Guerra, S.; Iehl, J.; Holler, M.; Peterca, M.; Wilson, D. A.; Partridge, B. E.; Zhang, S.; Deschenaux, R.; Nierengarten, J.-F.; Percec, V., Self-organisation of dodeca-dendronized fullerene into supramolecular discs and helical columns containing a nanowire-like core. *Chemical Science* **2015,** *6* (6), 3393-3401.

38. Rice, A. M.; Dolgopolova, E. A.; Shustova, N. B., Fulleretic Materials: Buckyball- and Buckybowl-Based Crystalline Frameworks. *Chemistry of Materials* **2017,** *29* (17), 7054-7061.

39. Singh, H.; Srivastava, M., Fullerenes: Synthesis, Separation, Characterization, Reaction Chemistry, and Applications—A Review. *Energy Sources* **1995,** *17* (6), 615-640.

40. He, Y.; Chen, H.-Y.; Hou, J.; Li, Y., Indene−C60 Bisadduct: A New Acceptor for High-Performance Polymer Solar Cells. *Journal of the American Chemical Society* **2010,** *132* (15), 5532-5532.

41. Garg, V.; Kodis, G.; Chachisvilis, M.; Hambourger, M.; Moore, A. L.; Moore, T. A.; Gust, D., Conformationally Constrained Macrocyclic Diporphyrin−Fullerene Artificial Photosynthetic Reaction Center. *Journal of the American Chemical Society* **2011,** *133* (9), 2944-2954.

42. Sigwalt, D.; Holler, M.; Nierengarten, J.-F., A rigid macrocyclic bis-malonate for the regioselective preparation of trans-1 and trans-3 fullerene bis-adducts. *Tetrahedron Letters* **2013,** *54* (24), 3160-3163.

43. Cardinali, F.; Gallani, J.-L.; Schergna, S.; Maggini, M.; Nierengarten, J.-F., An amphiphilic C60 derivative with a tris(2,2′-bipyridine)ruthenium(II) polar head group: synthesis and incorporation in Langmuir films. *Tetrahedron Letters* **2005,** *46* (17), 2969-2972.

44. Figueira-Duarte, T. M.; Clifford, J.; Amendola, V.; Gégout, A.; Olivier, J.; Cardinali, F.; Meneghetti, M.; Armaroli, N.; Nierengarten, J.-F., Synthesis and excited state properties of a [60]fullerene derivative bearing a star-shaped multi-photon absorption chromophore. *Chemical Communications* **2006,** (19), 2054-2056.

45. van de Coevering, R.; Kreiter, R.; Cardinali, F.; van Koten, G.; Nierengarten, J.-F.; Klein Gebbink, R. J. M., An octa-cationic core-shell dendrimer as a molecular template for the assembly of anionic fullerene derivatives. *Tetrahedron Letters* **2005,** *46* (19), 3353-3356.

46. Gutiérrez Nava, M.; Setayesh, S.; Rameau, A.; Masson, P.; Nierengarten, J.-F., Fullerene-functionalized polyesters: synthesis, characterization and incorporation in photovoltaic cells. *New Journal of Chemistry* **2002,** *26* (11), 1584-1589.

47. Kim, B.; Yeom, H. R.; Choi, W.-Y.; Kim, J. Y.; Yang, C., Synthesis and characterization of a bis-methanofullerene-4-nitro-α-cyanostilbene dyad as a potential acceptor for high-performance polymer solar cells. *Tetrahedron* **2012,** *68* (33), 6696-6700.

48. He, Y.; Chen, H.-Y.; Zhao, G.; Hou, J.; Li, Y., Biindene-C60 adducts for the application as acceptor in polymer solar cells with higher open-circuit-voltage. *Solar Energy Materials and Solar Cells* **2011,** *95* (3), 899-903.

49. Tao, R.; Umeyama, T.; Higashino, T.; Koganezawa, T.; Imahori, H., A single cis-2 regioisomer of ethylene-tethered indene dimer–fullerene adduct as an electron-acceptor in polymer solar cells. *Chemical Communications* **2015,** *51* (39), 8233-8236.

50. Chen, W.; Salim, T.; Fan, H.; James, L.; Lam, Y. M.; Zhang, Q., Quinoxaline-functionalized C60 derivatives as electron acceptors in organic solar cells. *RSC Advances* **2014,** *4* (48), 25291-25301.

51. He, Y.; Peng, B.; Zhao, G.; Zou, Y.; Li, Y., Indene Addition of [6,6]-Phenyl-C61-butyric Acid Methyl Ester for High-Performance Acceptor in Polymer Solar Cells. *The Journal of Physical Chemistry C* **2011,** *115* (10), 4340-4344.

52. Yoshimura, K.; Matsumoto, K.; Uetani, Y.; Sakumichi, S.; Hayase, S.; Kawatsura, M.; Itoh, T., Thiophene-substituted fulleropyrrolidine derivatives as acceptor molecules in a thin film organic solar cell. *Tetrahedron* **2012,** *68* (18), 3605-3610.

53. Sigwalt, D.; Schillinger, F.; Guerra, S.; Holler, M.; Berville, M.; Nierengarten, J.-F., An expeditious regioselective synthesis of [60]fullerene e,e,e tris-adduct building blocks. *Tetrahedron Letters* **2013,** *54* (32), 4241-4244.

54. Isaacs, L.; Diederich, F.; Haldimann, R. F., Multiple Adducts of C60 by Tether-Directed Remote Functionalization and synthesis of soluble derivatives of new carbon allotropes Cn(60+5). *Helvetica Chimica Acta* **1997,** *80* (2), 317-342.

55. Kang, H.; Cho, C.-H.; Cho, H.-H.; Kang, T. E.; Kim, H. J.; Kim, K.-H.; Yoon, S. C.; Kim, B. J., Controlling Number of Indene Solubilizing Groups in Multiadduct Fullerenes for Tuning Optoelectronic Properties and Open-Circuit Voltage in Organic Solar Cells. *ACS Applied Materials & Interfaces* **2012,** *4* (1), 110-116.

56. Chen, S.; Ye, G.; Xiao, Z.; Ding, L., Efficient and thermally stable polymer solar cells based on a 54π-electron fullerene acceptor. *Journal of Materials Chemistry A* **2013,** *1* (18), 5562-5566.

57. Guerra, S.; Schillinger, F.; Sigwalt, D.; Holler, M.; Nierengarten, J.-F., Synthesis of optically pure [60]fullerene e,e,e-tris adducts. *Chemical Communications* **2013,** *49* (42), 4752-4754.

58. Giovannitti, A.; Seifermann, S. M.; Bihlmeier, A.; Muller, T.; Topic, F.; Rissanen, K.; Nieger, M.; Klopper, W.; Bräse, S., Single and Multiple Additions of Dibenzoylmethane onto Buckminsterfullerene. *European Journal of Organic Chemistry* **2013,** *2013* (35), 7907-7913.

59. Cardullo, F.; Seiler, P.; Isaacs, L.; Nierengarten, J.-F.; Haldimann, R. F.; Diederich, F.; Mordasini-Denti, T.; Thiel, W.; Boudon, C.; Gisselhrccht, J.-P.; Gross, M., Bis- through Tetrakis-Adducts of C60 by Reversible Tether-Directed Remote Functionalization and systematic investigation of the changes in fullerene properties as a function of degree, pattern, and nature of functionalization. *Helvetica Chimica Acta* **1997,** *80* (2), 343-371.

60. Sawamura, M.; Kuninobu, Y.; Toganoh, M.; Matsuo, Y.; Yamanaka, M.; Nakamura, E., Hybrid of Ferrocene and Fullerene. *Journal of the American Chemical Society* **2002,** *124* (32), 9354-9355.

61. Matsuo, Y.; Muramatsu, A.; Hamasaki, R.; Mizoshita, N.; Kato, T.; Nakamura, E., Stacking of Molecules Possessing a Fullerene Apex and a Cup-Shaped Cavity Connected by a Silicon Connection. *Journal of the American Chemical Society* **2004,** *126* (2), 432-433.

62. Hirsch, A.; Lamparth, I.; Karfunkel, H. R., Fullerene Chemistry in Three Dimensions: Isolation of Seven Regioisomeric Bisadducts and Chiral Trisadducts of C60 and Di(ethoxycarbonyl)methylene. *Angewandte Chemie International Edition in English* **1994,** *33* (4), 437-438.

63. Iehl, J.; de Freitas, R. P.; Delavaux-Nicot, B.; Nierengarten, J.-F., Click chemistry for the efficient preparation of functionalized [60] fullerene hexakis-adducts. *Chemical communications* **2008,** (21), 2450-2452.

64. Iehl, J.; Nierengarten, J. F., A Click–Click Approach for the Preparation of Functionalized [5: 1]-Hexaadducts of C60. *Chemistry–A European Journal* **2009,** *15* (30), 7306-7309.

65. Nierengarten, J.-F.; Iehl, J.; Oerthel, V.; Holler, M.; Illescas, B. M.; Muñoz, A.; Martín, N.; Rojo, J.; Sánchez-Navarro, M.; Cecioni, S., Fullerene sugar balls. *Chemical communications* **2010,** *46* (22), 3860-3862.

66. Lallana, E.; Sousa-Herves, A.; Fernandez-Trillo, F.; Riguera, R.; Fernandez-Megia, E., Click chemistry for drug delivery nanosystems. *Pharmaceutical research* **2012,** *29* (1), 1-34.

67. Brettreich, M.; Burghardt, S.; Böttcher, C.; Bayerl, T.; Bayerl, S.; Hirsch, A., Globular Amphiphiles: Membrane-Forming Hexaadducts of C60. *Angewandte Chemie International Edition* **2000,** *39* (10), 1845-1848.

68. Pierrat, P.; Vanderheiden, S.; Muller, T.; Bräse, S., Functionalization of hexakis methanofullerene malonate crown-ethers: promising octahedral building blocks for molecular networks. *Chemical communications* **2009,** (13), 1748-1750.

69. Hörmann, F.; Donaubauer, W.; Hampel, F.; Hirsch, A., Efficient Synthesis of C2v-Symmetrical Pentakisadducts of C60 as Versatile Building Blocks for Fullerene Architectures that Involve a Mixed Octahedral Addition Pattern. *Chemistry–A European Journal* **2012,** *18* (11), 3329-3337.

70. Wasserthal, L. K.; Kratzer, A.; Hirsch, A., Sequential Fullerenylation of Bis-malonates–Efficient Access to Oligoclusters with Different Fullerene Building Blocks. *European Journal of Organic Chemistry* **2013,** *2013* (12), 2355-2361.

71. Ramos-Soriano, J.; Reina, J. J.; Illescas, B. M.; de la Cruz, N.; Rodríguez-Pérez, L.; Lasala, F.; Rojo, J.; Delgado, R.; Martín, N., Synthesis of Highly Efficient Multivalent Disaccharide/[60]Fullerene Nanoballs for Emergent Viruses. *Journal of the American Chemical Society* **2019,** *141* (38), 15403-15412.

72. Xu, Y.; Kaur, R.; Wang, B.; Minameyer, M. B.; Gsänger, S.; Meyer, B.; Drewello, T.; Guldi, D. M.; von Delius, M., Concave–Convex π–π Template Approach Enables the Synthesis of [10]Cycloparaphenylene–Fullerene [2]Rotaxanes. *Journal of the American Chemical Society* **2018,** *140* (41), 13413-13420.

73. Peng, P.; Li, F.-F.; Bowles, F. L.; Neti, V. S. P. K.; Metta-Magana, A. J.; Olmstead, M. M.; Balch, A. L.; Echegoyen, L., High yield synthesis of a new

fullerene linker and its use in the formation of a linear coordination polymer by silver complexation. *Chemical Communications* **2013,** *49* (31), 3209-3211.

74. Fernández, G.; Pérez, E. M.; Sánchez, L.; Martín, N., Self-Organization of Electroactive Materials: A Head-to-Tail Donor–Acceptor Supramolecular Polymer. *Angewandte Chemie* **2008,** *120* (6), 1110-1113.

75. Peng, P.; Li, F. F.; Neti, V. S. P. K.; Metta-Magana, A. J.; Echegoyen, L., Design, Synthesis, and X-Ray Crystal Structure of a Fullerene-Linked Metal–Organic Framework. *Angewandte Chemie International Edition* **2014,** *53* (1), 160-163.

Chapter 2 Highly soluble fullerene-based charge carriers for redox flow batteries

2.1 Background

Electricity has become the dominant form of energy to maintain the development of human societies (40 % of all used energy in US).[1–3] The volume of electricity generated worldwide is estimated to be almost 20 tetrawatt hours, which is massively reliant on fossil fuels (68% of the total generated). With the speed at which the industrial world is booming the demand for electricity is predicted to be doubled by 2050 and tripled by 2100.[1–3] However, the depletion of fossil fuels cannot supply this vast increase in electricity demand. On the other hand, every kWh of electricity generated produces 1 kg of CO_2, which is considered as the trigger for the global warming effect, resulting in detrimental long-term environmental and biological problems. Recently, many EU countries have adopted the carbon emission regulation to monitor and control industry, which benefits the progress of more eco-friendly companies.[1] All of these concerns push the energy transition from fossil fuel based to renewable energy sources.

Among all the renewable energy sources, solar and wind are the most abundant, potentially efficient and accessible forms of energy.[1,2] One hour of the solar irradiation received by the earth is enough to maintain the worldwide energy usage for 1 year. Capturing a small amount of the total wind energy available would also readily meet the world energy demand. These sustainable sources are increasing quickly all over the world, for example wind derived energy is expected to reach 474 GW by 2020 and photovoltaic cell installation is increasing by ~40 % yearly. However, these energies are intermittent. For example, wind energy is only operational when the wind is blowing, a study found that wind power peaks at midnight when energy demand is low. Whilst

solar energy only works well when the sun-light irradiation can be captured properly, which depends on both the weather and time of day (i.e. not at night). At the same time, the renewable power plants are normally based far away from cities. The variable natures of these renewable energy sources cause the poor consistency and reliability of the energy supply, which could endanger the stability of the conventional electric grid when the contribution from renewable energy exceeds 20%.[1–3]

To solve the problem caused by the intermittency of renewable energy, electrical energy storage (EES) has been proposed as the answer. It is hoped to facilitate the growth of a smart energy grid, which is expected to integrate a large amount of energy from renewable sources. In the conventional grid, the temporary mismatch between generation and demand is solved by bringing a large excess of generators online in response to fluctuations, which causes extreme energy waste. EES can be perfectly employed to shift the electricity generated by renewable sources during off-peak periods to peak period of use. The electrical energy will be stored when it is produced with lower value (low demand periods) and released to the load at high-value times (high demand period). Depending on the different storing mechanisms of electrical energy, EES technologies can be classified into two groups. The first group is storing electricity in electrical charges, such as capacitors and supercapacitors, which has the advantage of high efficiency (almost 100%) but suffers from operating at a low energy density and quick discharging times. The second group converts the electrical energy into other forms of energy, such as potential (compressed air energy storage, pumping water up hill), kinetic (flywheels) and chemical energy (redox flow batteries, Li-ion batteries and other battery systems).[1–3] In comparison with kinetic and potential forms of storage using chemical energy has the merits of high efficiency, quick response, easy modular design and less geographical requirements. In this chapter,

development of redox flow batteries (RFBs) is briefly reviewed followed by the introduction of a novel fullerene based RFB system.

2.1.2 Introduction of RFB

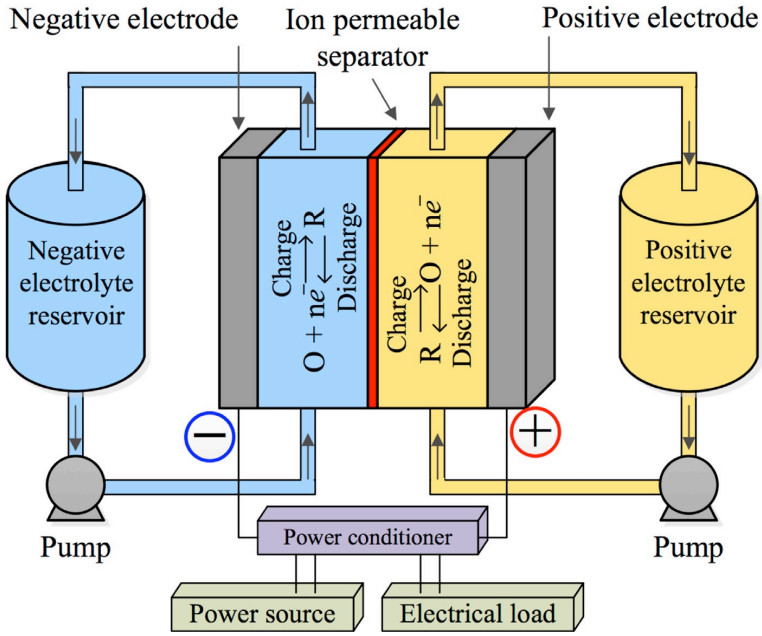

Figure 2.1 A diagram of a traditional RFB system.

Redox flow batteries are a rechargeable form of battery, which stores the electrical energy in the form of electrochemical energy, typically in two soluble reversible redox couples, which are dissolved in flowing electrolytes.[1–4] In charging mode (as show in **Figure 2.1**), oxidised species are generated at the cathode, whilst reduced species are formed at the anode. An ion permeable separator exists in the middle of the cell serving the function of dividing the differently charged species and selectively enabling the transportation of non-active ions (such as H^+ and Cl^-) to neutralise the electrons formed and balance the electrolyte. Depending on the electrolytes reacting with the cathode or anode, they are named catholyte and anolyte respectively, and are circulated to external electrolyte reservoirs sized in accordance with the demands of

different applications. In discharging mode, the electrolytes are pumped back to the cell reacting with the specific electrode, releasing charge to generate an electrical load. RFBs as one of the newest EES technologies are well suited for medium and large electricity storage. The main advantage is that the power capacity and energy capacity are independent of each other. The power capacity is controlled by the size of the electrode and the number of stacks of the cell, whilst the energy capacity depends on the concentration of the active species and the volume of the external tanks. With this feature, an essentially unlimited energy capacity can be achieved by employing large enough tanks. Also, the intimate contact between electrode and liquid electrolyte gives a quick response. This simple exchange mechanism also negates the physical and chemical degradation of the expensive electrodes, lowering maintenance costs. Working at ambient working temperature and separated active materials provide the necessary safety features for large scale application. The flowing electrolytes can also carry the heat formed from the redox reaction away, reducing the possibility of some serious consequences of heat building up, such as explosions. Unlike some solid-state batteries like Li-ion, RFBs are constructed of less active material (such as binders, additives), providing higher scalability.

However, the number of existing practically available systems are still very limited, with vanadium RFBs being the only ones available/used at scale currently. The RFBs are commonly considered as low energy density system due to the low cell operation voltages and poor solubility of the active material in the electrolyte solutions. The high cost of materials (such as the active species, the ion-permeable membrane and the electrode) also challenges the prosperity of RBF development. Efforts in both fundamental chemical research, looking at aspects such as redox couples, electrolyte and etc., and engineering research, for example better cell design and materials, are

required to find a more promising system. In the following part, some existing RFBs systems are introduced and discussed.

2.1.3 Types of RFBs system

The modern RFBs system was invented by National Aerounautics and Space Administration (NASA) scientist Lawrence Thaller in the 1970s.[5] Since then, various systems have been proposed and researched, such as Fe/Cr, all vanadium, polysulphide/bromine and etc.[5–19] Depending on the solvent that the redox couples are dissolved in, the RFBs are classified as aqueous based systems and non-aqueous based systems. Depending on the type of charge carries used in the catholyte and anolyte sides of the RFBs, they are classified as asymmetrical RFBs and symmetrical RFBs (see **Figure 2.2**). The former uses different types of charge carrier in the catholyte and anolyte, which has the advantages of flexibility in the choice of the chemicals and tunability depending on different application requirements and thus the possibility of increasing cell voltage and energy density.[20–22] However, due to its asymmetrical nature the catholyte/anolyte charge carriers if the catholyte/anolyte migratse to the opposite side of the cell, known as membrane crossover, this results in severe and irreversible capacity fade.[23,24] On the contrary, symmetrical system uses the same type of charge carrier in both catholyte and anolyte on account of the fact that the charge carrier can undergo both reduction and oxidation processes, which negates the problem of membrane crossover thus facilitating long-term cyclability. The disadvantage is that there is limited flexibility in the choice of the chemical species. Examples of aqueous and non-aqueous RFBs are given with both asymmetrical and symmetrical designs in this section.

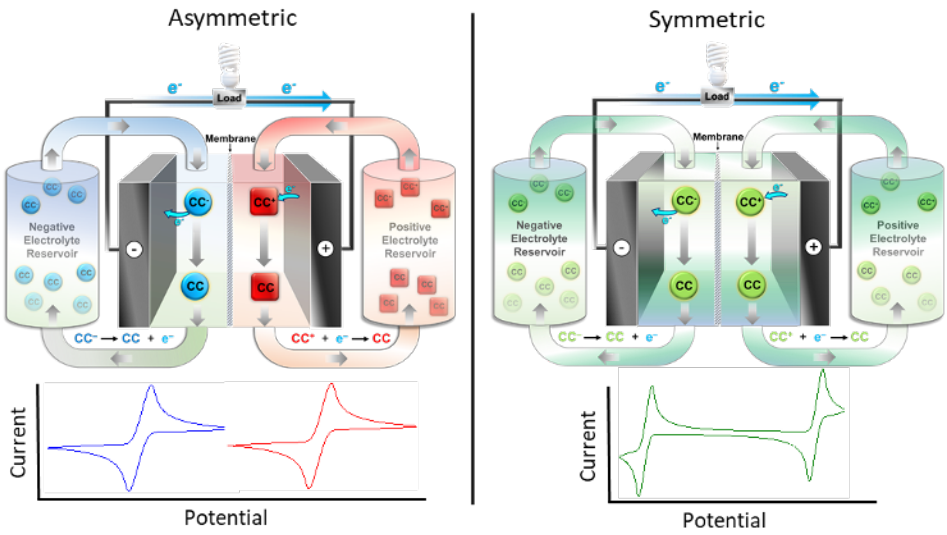

Figure 2.2 Schematic of (left) asymmetrical (right) symmetrical RFB setup and their corresponded cyclic voltammograms of charge carriers.

2.1.3.1 Aqueous based system

Many aqueous systems with both asymmetrical and symmetrical designs have been proposed and investigated (see **Table 2.1**). Vanadium systems act as a benchmark of this area as they have high efficiency, capability and high solubility in water (2 M - 5 M). This has led to them being commercially available, with plants established for storing intermittent energy generated by sustainable sources across the world. Maria Skyllas-kazacos and co-workers introduced all-vanadium RFBs, in which the V^{2+}/V^{3+} redox couple serves at the anode (**Figure 2.3b**) and the V^{4+}/V^{5+} redox couple works at the positive electrode in the form of VO^{2+}/VO_2^{+} (**Figure 2.3a**).[8,9] When different oxidizing states of vanadium crossover the membrane, the efficiency is reduced, but the electrolyte can be converted back to the correct form of each side by electrochemistry without the loss of the expensive charge carriers. This significantly reduces the time and cost of system maintenance. However, vanadium is not earth abundant, the high price of the vanadium based redox couple has stalled it use to

some extent. Another problem is the vanadium active material has a narrow working temperature around 10 - 40 °C, causing precipitation when the temperature is in the outside the range.

a) $VO^{2+} + H_2O \underset{\text{discharge}}{\overset{\text{charge}}{\rightleftharpoons}} VO_2^+ + e^- + 2H^+ \quad U^0 = 1.00\ V$

b) $V^{2+} \underset{\text{charge}}{\overset{\text{discharge}}{\rightleftharpoons}} V^{3+} + e^- \quad U^0 = -0.26\ V$

Figure 2.3 The redox reaction of all-vanadium RFBs, a) catholyte redox reaction; b) anolyte redox reaction. This system achieves a potential window of 1.26 V.

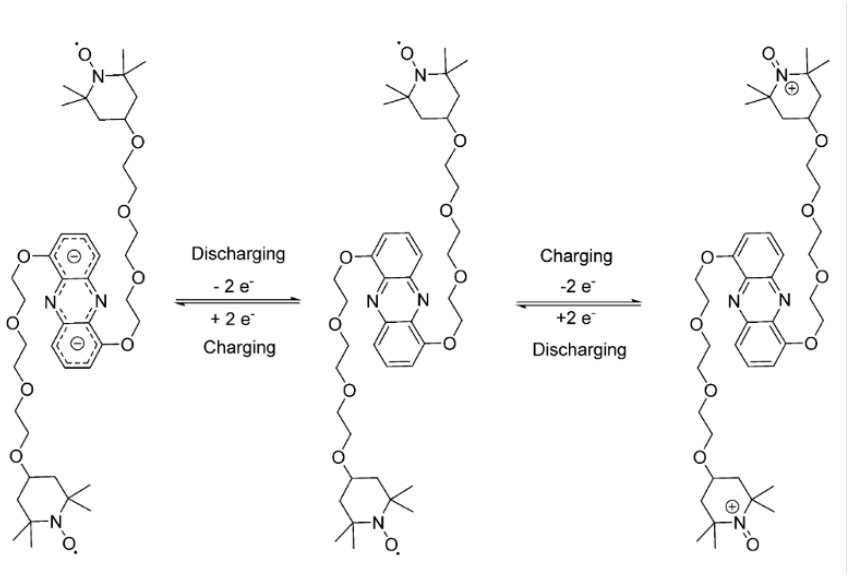

Figure 2.4 Schematic of the redox mechanism of the combi-Tempo/phenazine charge carrier.

Jan Winsberg and co-workers reported a symmetrical aqueous RBF using an organic combi-molecule, a Tempo/phenazine derivatives, as the charge carriers (see **Figure 2.4**).[25] Two Tempo moieties were covalently attached to a phenazine group via triethylene glycol to improve the water solubility. In this molecule, two Tempo groups conduct 1 electron oxidation reactions, which serve as the catholyte active moieties in the cell, whereas the phenazine group undergoes a two-electron reduction, which

serves as the anolyte active moiety in the cell. The setup can achieve a redox potential of 1.2 V, which is within the potential window of water, avoiding unwanted the water electrolysis.

The aqueous based systems are still recognised as low power and energy density systems due to the low potential window available due to water electrolysis and the low solubility of active materials. The most popular vanadium-based systems have multiple disadvantages; high cost, large environmental impact and poor temperature stability, which hamper their use on a large scale and thus worldwide adoption. Therefore, exploration of new, cheap and sustainable charge carriers is still highly required.

Table 2.1 Examples of aqueous based RFBs

Redox couple	**Electrolyte**	**Solubility, M**	**Potential window, V**	**Power density, mW cm^{-2}**	**Energy density, Wh L**	**Ref.**
VO^{+2}/V^{3}	2.5M H_2SO_4/6M HCl	2.5	1.26	N/A	25-35	[26]
$FeCl_2/FeCl_3$	1M TEOA/1.5M NaOH	0.2/0.2	1.34	160	N/A	[27]
RIBOTEMPO	1.5 M NaCl	1.22	1.23	N/A	26	[28]
TEMPTMA/MA	N/A	3.2/2.5	1.4	N/A	38	[29]
BQDS/AQDS	1M H_2SO_4	1.5/4	1.04	25	N/A	[30]

DHBQ/ $K_4Fe(CN)_6$	2M/1M KOH	4.31	1.21	300	N/A	[31]
BHPC/ $K_4Fe(CN)_6$	1M KOH	1.55	1.27	430	N/A	[32]
DHPS/ $K_4Fe(CN)_6$	1M NaOH	1.8	1.4	N/A	N/A	[33]

3.1.3.2 Non-aqueous based systems

The primary advantage of non-aqueous based systems is the wider available potential window than aqueous systems, allowing high-energy density systems. Also, in organic solvents there is more choice of redox couples, with possibility to use cheaper species. In addition, multi-electron transfer redox reactions can be adopted to further expand the energy density.[22,24,34–37] More positive aspects laso include higher solubility and stability of active, organic material in organic solvents.

The study of organic based system is in a preliminary stage. To date, some organic systems have achieved the higher operating potentials than aqueous systems with the values above 2.0 V. However, the solubility of most reported redox couples is currently lower than aqueous systems such as the vanadium system (> 2 M). The viscosity of the organic solvents is also higher than water, which could result in the high pressure endangering the safety. Also, other issues exist, including; smaller current densities, poor voltage and energy efficiencies and degradation of active materials, have been encountered in most of the systems reported to date, which has limited the development of the organic solvent based system. Many fundamental studies have focused on the innovation of redox couples and probing the compatibility of supporting electrolytes, which is required to fully understand the problem and find the solutions.

In the following section, the state of the art in organic based systems is reviewed and a recently reported fullerene system is explored as a potentially promising candidate. Wentao Duan and co-workers reported a non-aqueous asymmetrical RFB system using the organic molecule, 2,1,3-benzothiadiazole (BzNSN) as the anolyte, which has a low redox potential, fast electrochemical kinetics and high solubility in organic solvents, as high as 5.7 M in acetonitrile (MeCN) and 2.1 M in lithium bis(trifluoromethylsulfonyl)imide (LiTFSI).[20] A cell using BzNSN as the anolyte and 2,5-di-tert-butyl-1-methoxy-4-[2'-methoxyethoxy]benzene (DBMMB) as the catholyte was constructed in the presence of LiTFSI/MeCN as electrolyte, with a high cell potential of 2.36 V reported (**Figure 2.5**).

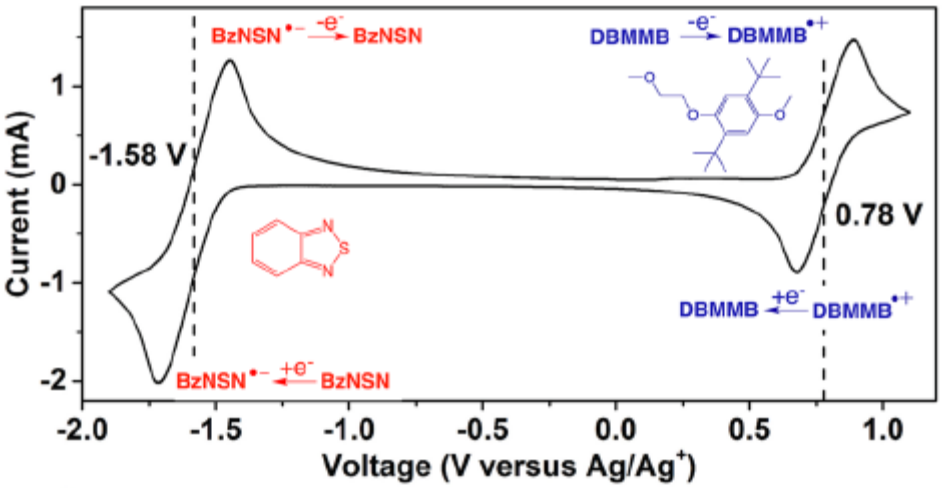

Figure 2.5 The cyclic voltammetry results of the BzNSN/DBMMB RFB system. The redox processes of BzNSN and DBMMB are displayed. A cell potential of 2.36 V is achieved using these redox couples.

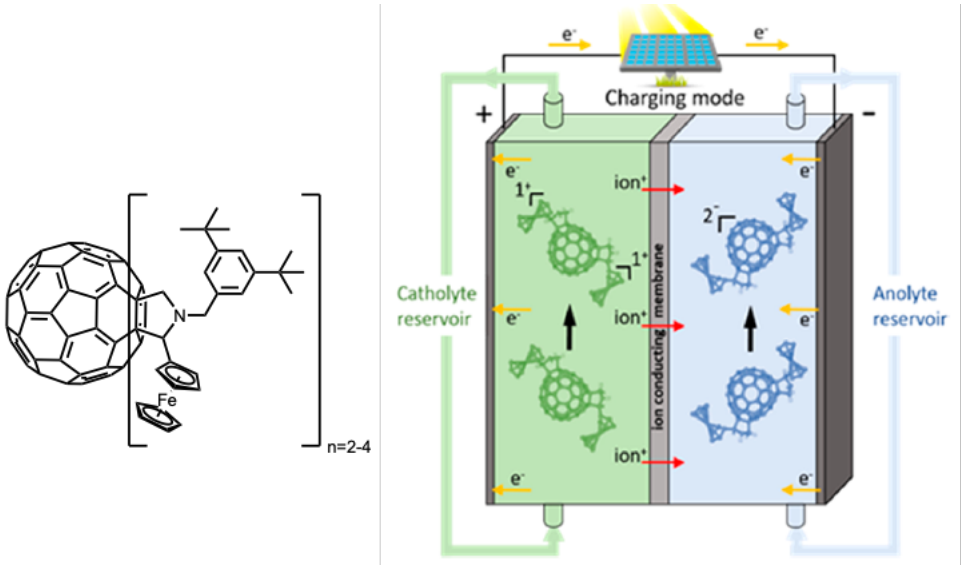

Figure 2.6 (left) Chemical structure of ferrocene-C_{60} molecules, where the number of (n) denoted the number of ferrocene groups appended on each fullerene cage; (right) diagram of the symmetrical fullerene based RFB, which used a fullerene-ferrocene bis-adduct as both catholyte and anolyte.

In 2018, Jochen Friedl and co-workers reported a non-aqueous system utilising functionalised fullerene derivatives as redox couples.[38] In this work (**Figure 2.6**), ferrocene groups were appended to the cage, acting as the catholyte active moiety, whilst the fullerene cage itself accepts electron as the anolyte active moiety. The ditertbutylphenyl groups were appended to increase the solubility of the molecule, and thus increase the energy density of the system, in *o*-DCB, which was selected as it is a typical and excellent solvent for fullerene derivatives. By using ferrocene-C60 bis-adducts in both catholyte and anolyte, a symmetrical RFB system was constructed to negate the problems of membrane crossover, achieving a potential window of 1.64 V. It also used the combination of ferrocene-C60 bis-adducts and ICBA to build up several asymmetrical system, which used ferrocene-C60 in the catholyte and ICBA in the anolyte, resulting in a potential window of 1.49 V, a theoretical current density of

1.2 A cm^{-2} and theoretical energy densities of 80 W h $mol^{-1}L$, which is better than the benchmark vanadium RFB (0.07 A cm^{-2} and 17 W h $mol^{-1}L$ respectively). This innovative work provided a new idea to find the promising system using functionalised fullerene as redox couples, which has excellent electrochemical properties and earth abundant, sustainable elements (only consists of C, N, Fe). With further work, fullerene based RFBs have huge potential to revolutionize the EES industrial and find application as the solution to harnessing renewable energy sources more effectively.

In summary, the non-aqueous based RFBs still require extensive development on both the fundamental and engineering research to compete with the aqueous systems such as all vanadium system. The organic solvent can potentially expand the solubility of the redox couples and the wider potential window can result in higher energy densities. However, the instability of the active material in organic solvent was observed in several cases after cycling, which is necessary to understand and subsequently address. More examples are listed in **Table 2.2**.

Table 2.2 Examples of non-aqueous based RFBs.

Redox couple	**Solvent/ electrolyte**	**Solubility, M**	**Potential window, V**	**Power density, mW cm^{-2}**	**Energy density, Wh L**	**Ref.**
$V(acac)_3$	0.5 M $TEABF_4$ in CH_3CN	1	2.2	N/A	N/A	[39]

$Ru(acac)_3$	1 M $TEABF_4$ in CH_3CN	0.05	1.3	N/A	N/A	[40]
$[Ru(bpy)_3](FB_4)_2$	0.1 M $TEABF_4$ in CH_3CN	0.2	2.6	N/A	N/A	[41]
TEMPO/*N*-Methylphthalimide	1M $NaClO_4$ in CH_3CN	N/A	1.6	70	N/A	[42]
TEMPO/$LiPF_6$	2M $LiPF_6$ in mixture of EC/PC/EMC	5.2	3.5	N/A	126	[43]
BCF3EPT/TMeQ	0.2 M $LiBF_4$ in PC	1.2/0.37	1.4	N/A	N/A	[44]
PAF/PAE	0.1 M $LiBF_4$ in CH_3CN	1	0.95	N/A	N/A	[45]
B(MEEO)EPT	0.5 M TEATFSI in ACN	0.5	0.59	N/A	N/A	[46]

2.2 Aims and Objectives

2.2.1 General approach

This project is inspired by the reported fullerene based RFB system, which was mentioned above. The aim of this project is to synthesise highly soluble, stable and electrochemically active fullerene derivatives for RFBs application. This will be achieved via the following objectives:

1. A variety of solubility imparting groups will be appended to the fullerene cage, initially to study how different groups contribute to the solubility of species in *o*-DCB.
2. Ferrocene groups and solubility imparting groups will be appended to the fullerene cage simultaneously to study the influence of the ferrocene group on the solubility.
3. All the molecules synthesised will be tested by cyclic voltammetry to study the redox properties.
4. Selected molecules with the best solubility in *o*-DCB will be used for cell performance tests.

3.2.2 Synthetic strategy

2.2.2.1 C_{60} charge carrier synthetic route 1: two step; Prato reaction, Nucleophilic Substitution

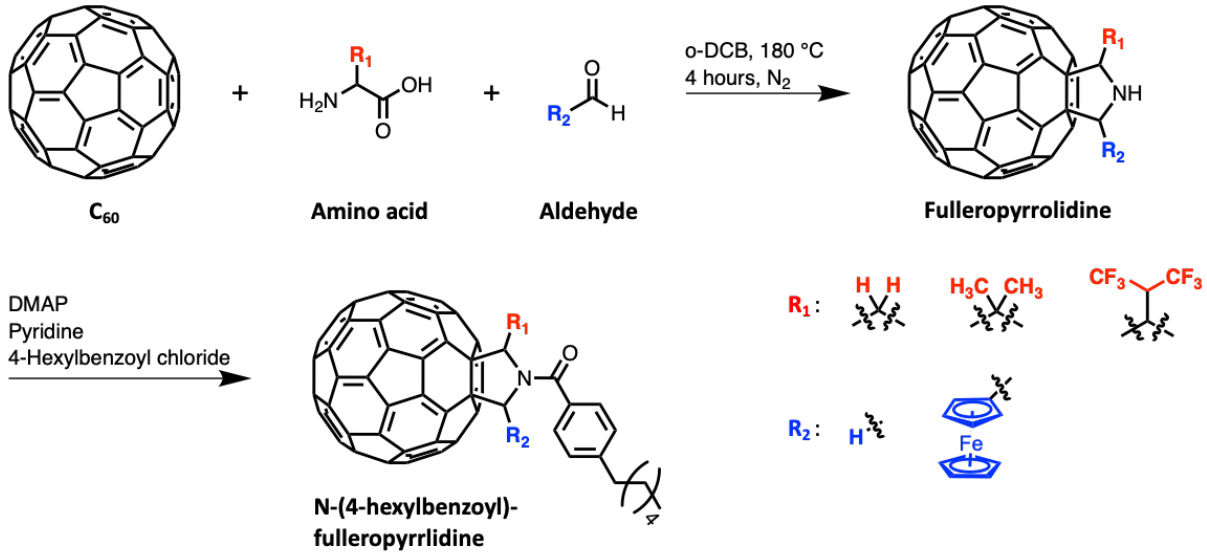

Figure 2.7 Synthetic route for preparation of highly soluble fullerene derivatives, fulleropyrrolidines are made initially via Prato reaction, followed by nucleophilic substitution giving the corresponding N-(4-hexylbenzoyl)-fulleropyrrolidine. N.B. When R_1 and R_2 of fulleropyrrolidine are all protons, the aminoacid used is amine protected, N-trityl glycine.

As seen in **Figure 2.7**, a two-step synthetic route that combines the Prato reaction and nucleophilic substitution was proposed, in which the Prato reaction was the crucial step that appended different $\mathbf{R_1}$ and $\mathbf{R_2}$ groups in the fulleropyrrolidine simultaneously. Three amino acids with different substituents; two protons, two methyl groups and a 1,1,1,3,3,3-hexafluoro propyl group, in the *α* carbons and two aldehydes; formaldehyde and ferrocenecarboxaldehyde were used. The formaldehyde was used with three amino acids as starting materials for Prato reaction to solely study the solubility changes along with the $\mathbf{R_1}$ groups in the fulleropyrrolidine. When

ferrocenecarboxaldehyde was used, the purpose was to both form molecules that undergo both reduction and oxidation and study how ferrocene influences the solubility. DMAP as a base was used to deprotonate the fullleropyrrolidine forming the nucleophile to react with 4-hexylbenzoyl chloride, giving the N-(4-hexylbenzoyl)-fulleropyrrolidine as product, in which the hexylbenzene group can further increase the solubility in non-polar solvent, e.g. *o*-DCB. Pyridine was used to mop the HCl generated from the reaction.

2.2.2.2 C_{60} charge carriers synthetic route 2: one-pot Prato reaction

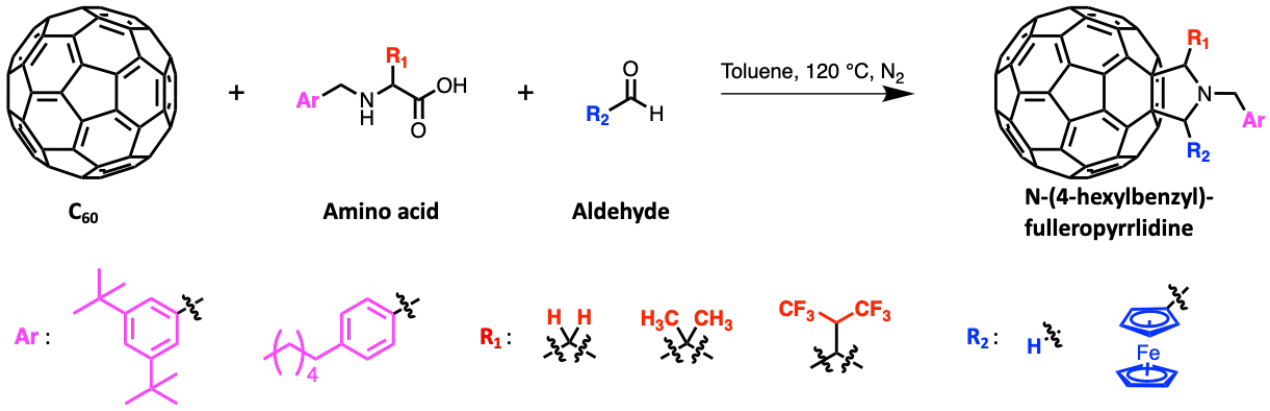

Figure 2.8 Synthetic route for preparation of highly soluble fullerene charge carrier through a one-pot Prato reaction.

As seen in **Figure 2.8**, a one-pot Prato reaction was also proposed, in which a group of functionalised amino acids that contain two different aromatic groups and the same $\mathbf{R_1}$ groups as in route 1 in the *α* carbons positions were used as the starting materials. To compare with the route 1, this route can add functionalities in three positions of two pyrrolidine ring carbons and N at the same time, and thus is expected to result in improved efficiencies and yields. As the ditertbutylphenyl group was used for imparting solubility to the fullerene-ferrocene molecule in the literature, the hexylphenyl group is introduced to act as a straight alkyl chain alternative to prove the effects on the

solubility. At the same time, different aromatic groups have the potential to impact the redox properties of the fullerene derivatives. By comparing them, some valuable design rules are expected to be obtained to exploit in future molecular design of C_{60} RFB charge carriers. More importantly, this route replaces the carbonyl linker between the porrolidine ring and aromatic groups in route 1 with a methylene, and thus reduces the steric hindrance of the species. This is hoped to avoid steric hindrance in the formation of bulky and rigid molecules when **R_1**, **R_2** and **Ar** groups are 1,1,1,3,3,3-hexafluoro propyl, ferrocene and ditertbutyl group respectively, which has been proved and will be discussed in the following section.

3.2.2.3 Synthetic route for the amino acids for C_{60} charge carrier synthetic route 2

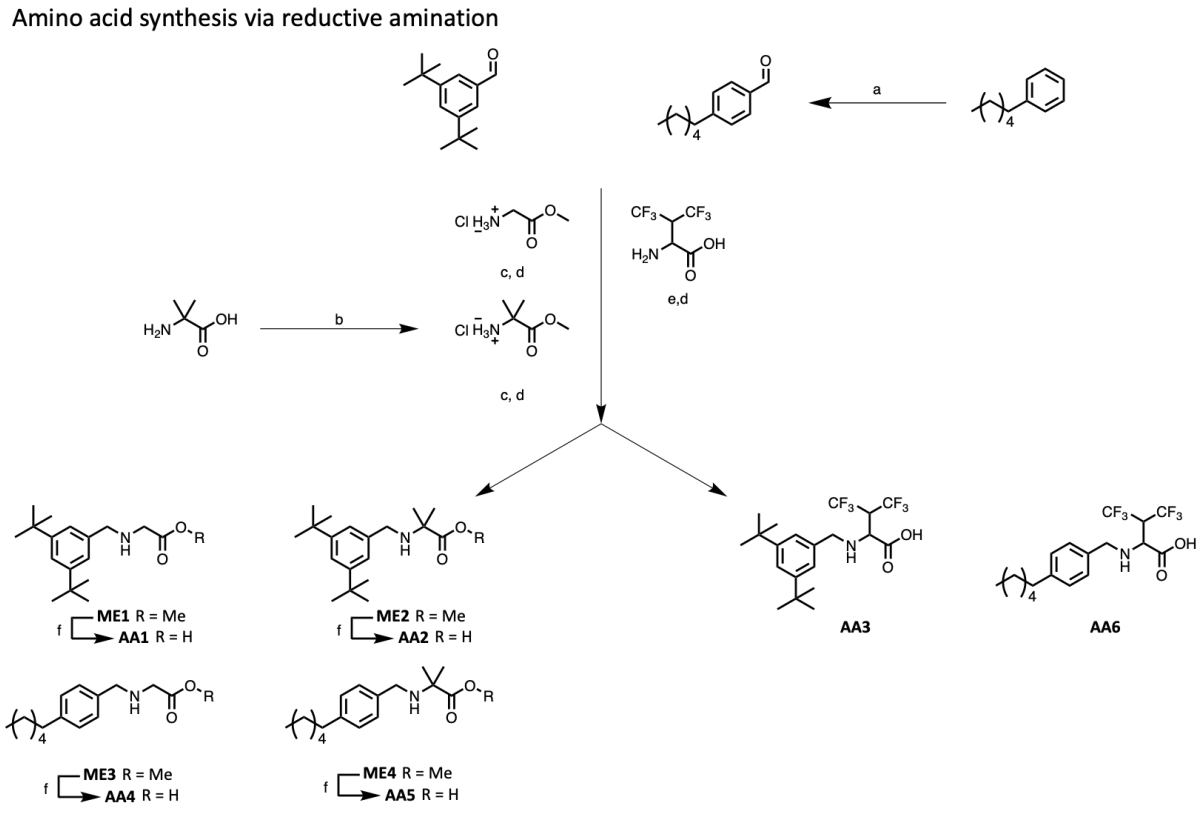

Figure 2.9 Synthetic routes to synthesise amino acids, **AA1**-**6**. Reagents and conditions: (a) hexamethylenetetramine, TFA, 80 °C, 17 hours; (b) $SOCl_2$, MeOH,

0°C to rt, 24 hours; (c) TEA, 4 Å molecular sieves, anhydrous DCM, rt, 17 hours; (d) $NaBH(OAc)_3$, anhydrous DCM, rt, 17 hours; (e) 4 Å molecular sieves, anhydrous MeOH, rt, 24 hours; (f) NaOH, methanol, rt, 72 hours.

The implementation of route 2 requires the six different amino acids, and thus the synthetic routes in **Figure 2.9** was proposed. Hexylbenzaldehyde and 2,2 dimethyl glycine methyl ester hydrochloride were made in advance according to the reported procedures. Benzaldehyde reacts separately with glycine methyl ester and 2,2 dimethyl glycine methyl ester hydrochloride accordingly via reductive amination, giving their corresponding methyl protected amino acids, **ME1,2** and **ME3,4**, followed by hydrolysis under basic conditions, giving the corresponding amino acids, **AA1,2** and **AA3,4**. Due to the scarcity of a commercial source of the protected version of the hexafluoro DL valine, **AA5** and **AA6** are synthesised directly via the reactive amination with benzaldehyde, each with different purification procedures.

2.3 Results and Discussion

2.3.1 C_{60} charge carrier synthesised from route

Table 2.3 Fulleropyrrolidines, **1** and **2**, and the corresponding N-(4-hexylbenzoyl) fulleropyrroldines, **3** and **4**, synthesised via route 1.

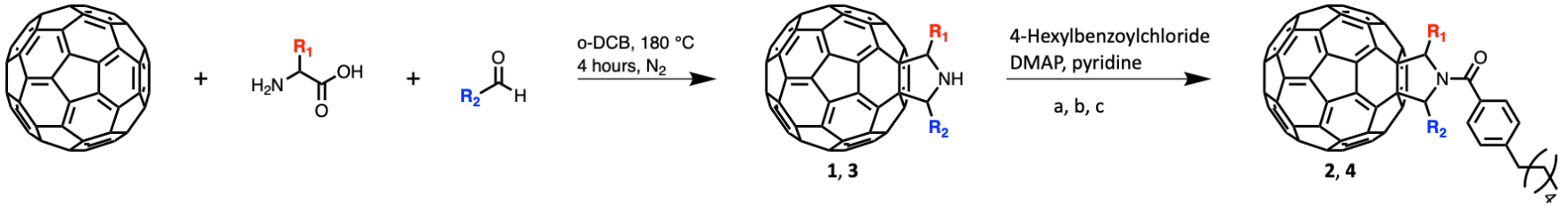

	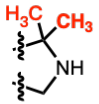	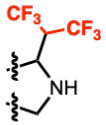	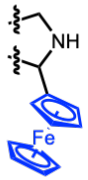	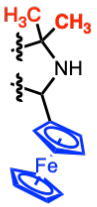	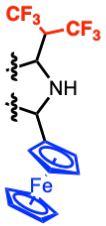	
1a 40%	**1b** 21%	**1c** 30%	**3a** 49%	**3b** 32%	**3c** 39%	
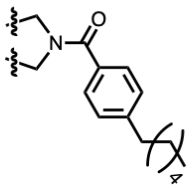	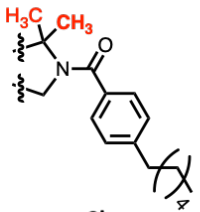	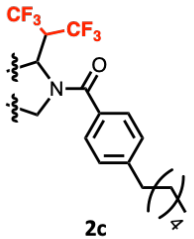	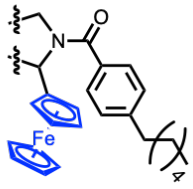	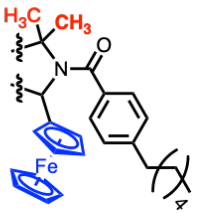	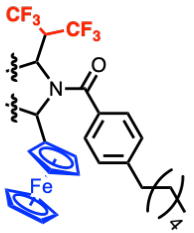	
2a 23% 9% to C_{60}	**2b** 25% 5% to C_{60}	**2c** 19% 6% to C_{60}	**4a** 57% 28% to C_{60}	**4b** 0 %	**4c** 0%	

* In the preparation of the **1a**, amine protected amino acid, N-trityl glycine was used as starting material, giving N-trityl fulleropyrroldine as product, the trityl groups was then deprotected by trifluoromethanesulfonic acid in DCM at room temperature for 1 hour, giving **1a** in quantitative yield, which was not demonstrated in the table for clarity. Conditions of nucleophilic substitution: a) **2a** and **2b** were synthesised in anhydrous DCM, rt, 17 hours, b) **2c** was synthesised in toluene, 110 °C, 17 hours, c) **4a** was synthesised in toluene, rt, 17 hours.

The preparation of fullerene derivatives via route 1 is illustrated in **Table 2.3** (full details can be found in the experimental section). Fulleropyrrolidines with only solubility imparting groups, **1a**,**b**,**c**, were successfully synthesised via Prato reaction, which was subsequently treated with DMAP to form a nucleophile that replaced the chloride of 4-hexylbenzyl chloride forming **2a**,**b**,**c** successfully. Fulleropyrrolidines with both solubility imparting groups and redox active ferrocene groups, **3a**,**b**,**c** were also synthesised successfully. However, the following nucleophilic reaction only demonstrated the formation of **4a**. Different reagents and conditions were attempted, but no trace of formation of **4b** and **4c** was detected. It was concluded that there must be a large amount of steric hindrance in the reaction making the formation impossible. Molecules were purified by column chromatography and characterised by ^{1}H and ^{13}C NMR spectroscopy, FT-IR spectroscopy, UV-Vis spectroscopy and matrix assisted laser desportion/ionisation (MALDI) time of flight mass MALDI ToF MS spectroscopy.

2.3.1.1 Synthesis of 1a

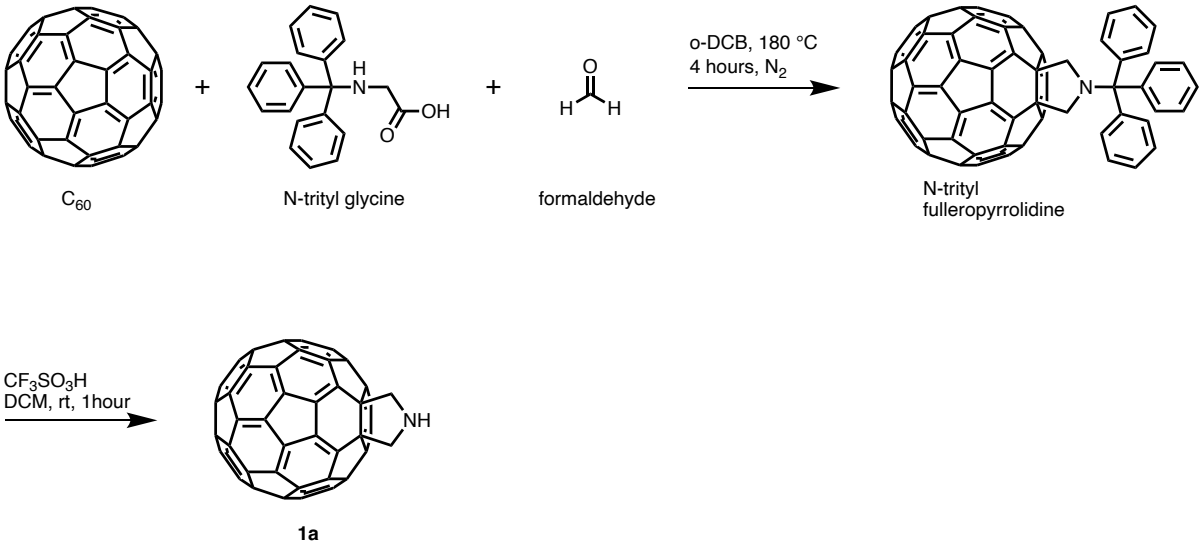

Scheme 2.1 Route to synthesise N-trityl fulleropyrrolidine and **1a**.

N-Tritylfulleropyrrolidine and **1a** were synthesised following the previously reported procedures,[47] in which C_{60}, N-trityl glycine and formaldehyde were used as the starting materials to make the amine protected fulleropyrrolidine, N-trityl fulleropyrrolidine in a 40% yield, and was subsequently deprotected using the strong acid (trifluoromethane sulfonic acid), giving **1a** in a 100% yield. The reaction to synthesise N-trityl fulleropyrrolidine was monitored by TLC (CS_2), in which the spot with Rf = 0.85 was determined to be the N-trityl fulleropyrrolidine. All of the characterisation data agreed with the literature. In the ^{1}H NMR spectrum (see **Figure 2.10**), three aromatic peaks with δ = 7.9, 7.42 and 7.29 ppm corresponded to the trityl protons, and a singlet with δ = 4.17 was also detected corresponding to the four fulleropyrrolidine protons. In MALDI ToF mass (negative mode) data (Figure 2.11), a peak with m/z = 1005 was shown, which matches the m/z of the N-trityl fulleropyrrolidine $[M]^-$ ion. After the deprotection, **1a** was characterised by MALDI ToF mass (positive mode) spectrometry, in which a peak with m/z = 763.8 was detected matching the $[\mathbf{1a}+H]^+$ ion.

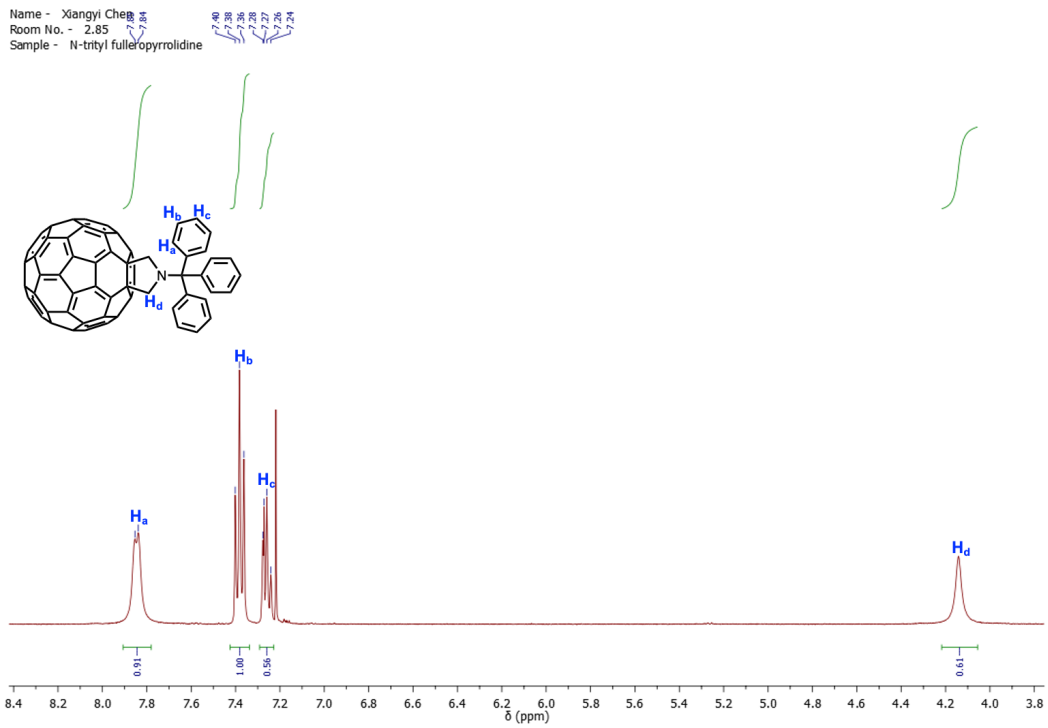

Figure 2.10 ^{1}H NMR (400 MHz, $CDCl_3$, *δ*, ppm) spectrum of N-trityl fulleropyrrolidine with three aromatic proton environment peaks and 1 pyrrolidine proton environment peak detected.

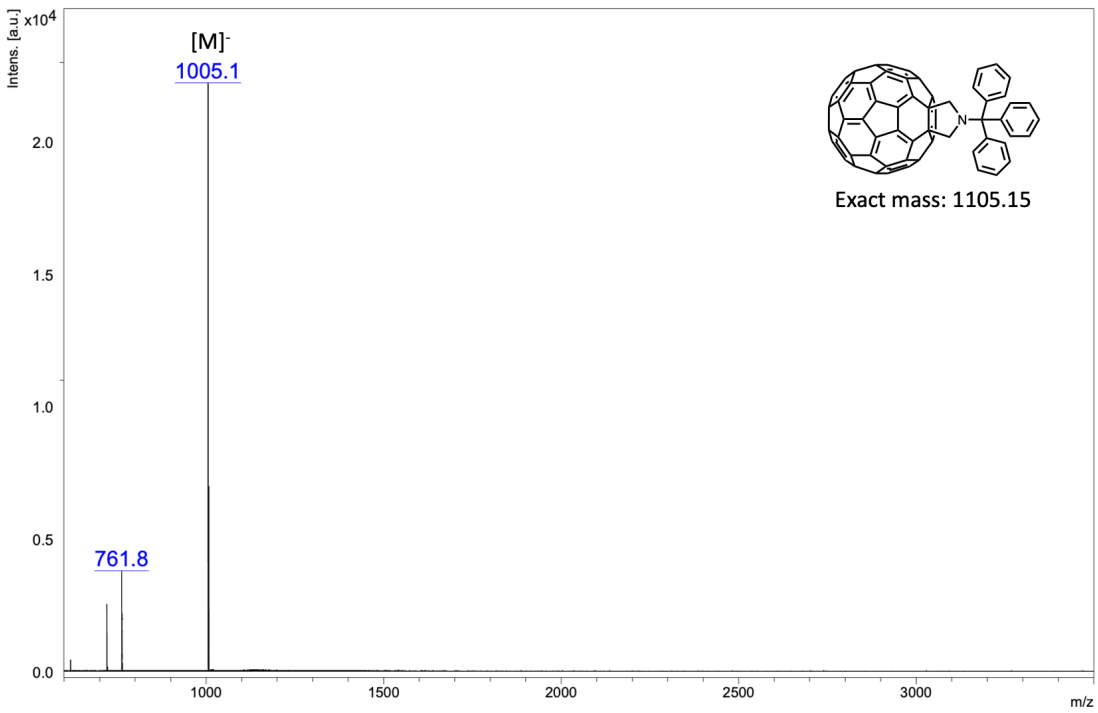

Figure 2.11 MALDI ToF mass spectrum (negative mode) of N-trityl fulleropyrrolidine, in which the peak with m/z = 1005.1 matches the calculated mass of the $[M]^-$ ion.

2.3.1.2 Synthesis of 1b

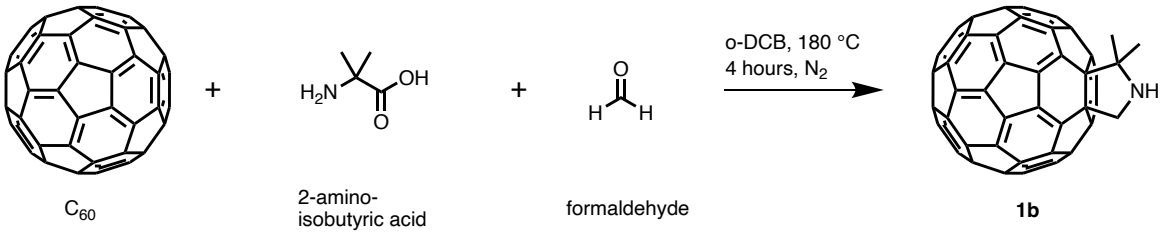

Scheme 2.2 Route to synthesise 1b.

Fulleropyrrolidine **1b** (**Scheme 2.2**) with two methyl groups in pyrrolidine was synthesised following the previously reported method,[47] using C_{60}, 2-aminoisobutyric acid and aldehyde as starting materials. The reaction was monitored by TLC (toluene/ethyl acetate 9/1), where the spot with R_f = 0.3 was determined to be **1b**, and the crude product was purified via column chromatography giving **1b** as a black solid

in a 21% yield. The ^{1}H NMR spectrum (**Figure 2.12-top**), shows two singlets with δ = 4.83 and 2.09 ppm which corresponding to pyrrolidine protons and dimethyl protons respectively. In the ^{13}C NMR spectrum (**Figure 2.12-bottom**), the C_{60} C peaks, the four pyrrolidine C peaks and one methyl C peak are observed and are consistent with the literature. Peaks with m/z = 791.01 and 719.97 were found in the MALDI ToF data (**Figure 2.13**), and are related to [**1b**]$^{-}$ and $[C_{60}]^{-}$ ions respectively.

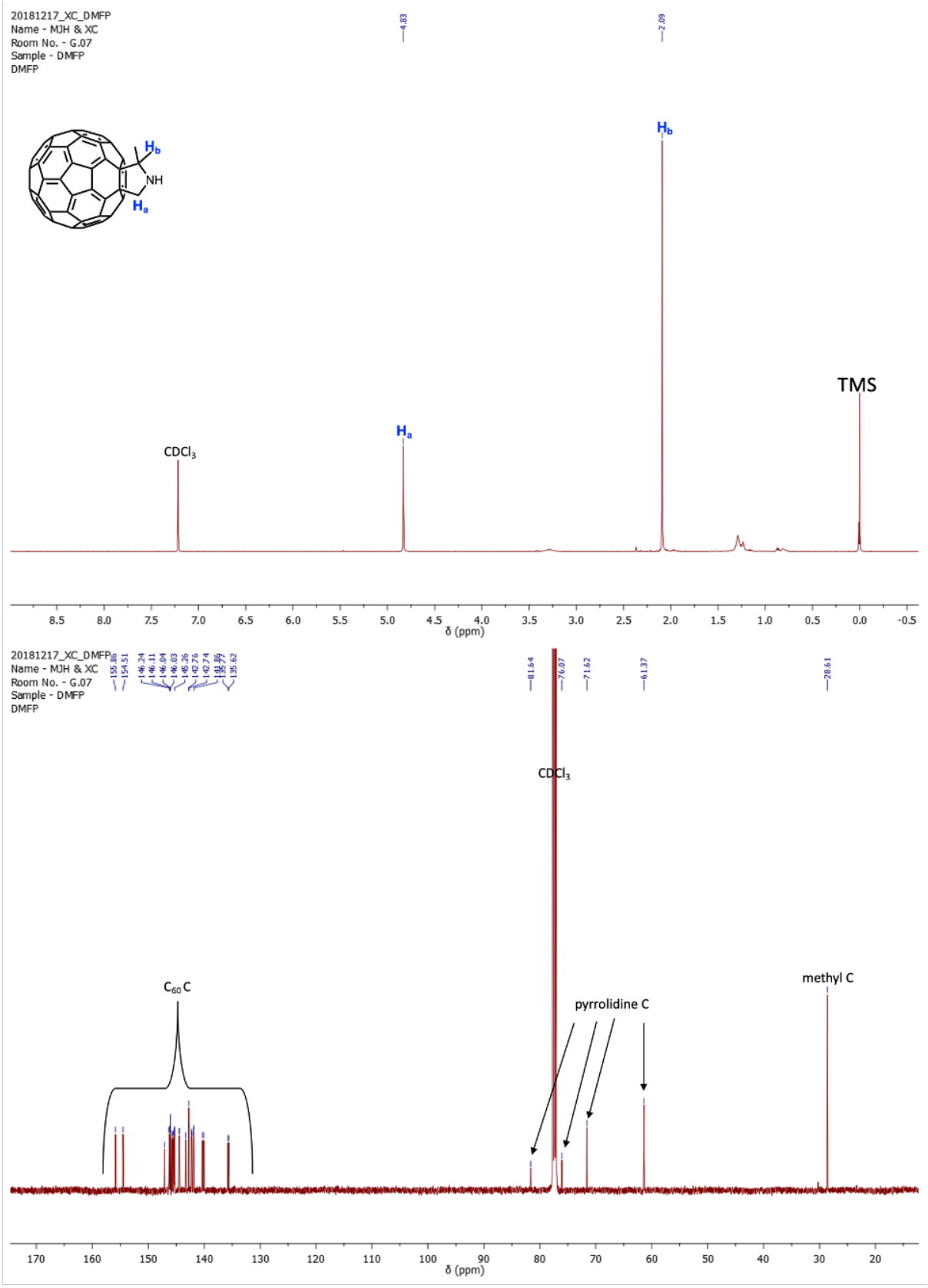

Figure 2.12 ^{1}H (top) and $^{13}C\{^{1}H\}$ NMR (bottom) (400 MHz, $CDCl_3$, δ, ppm) spectrum of **1b**.

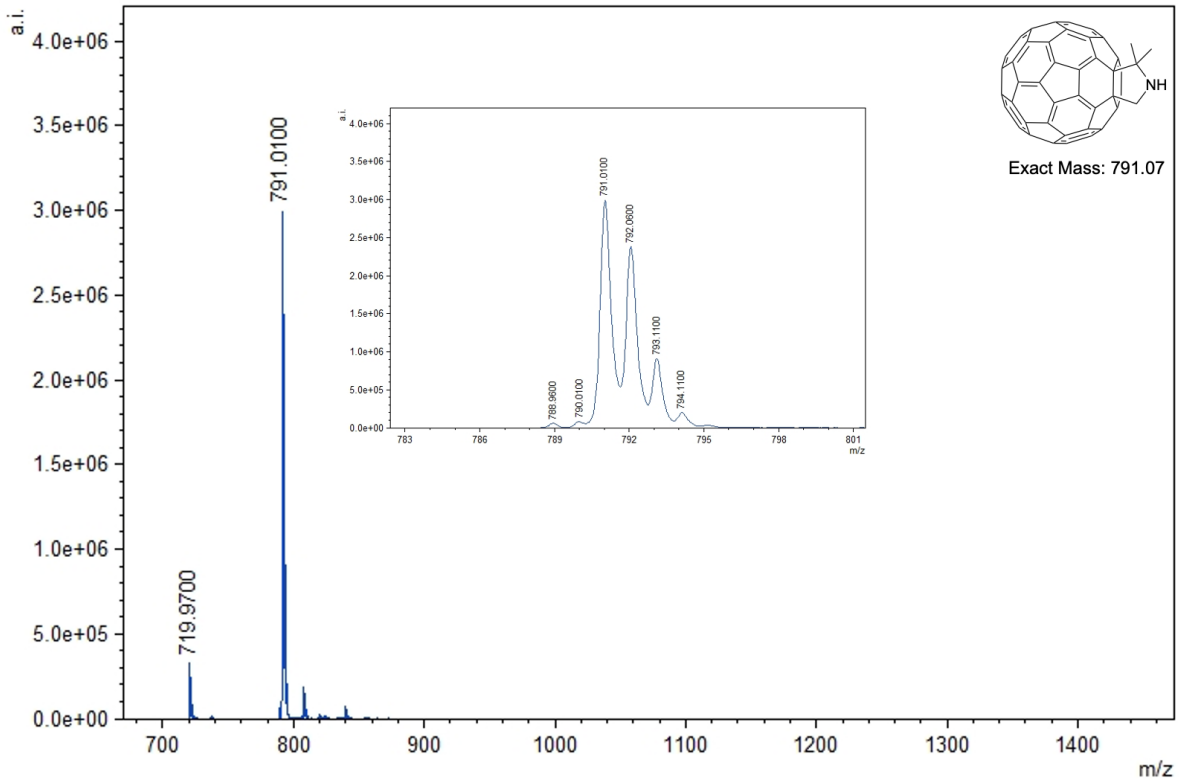

Figure 2.13 MALDI ToF mass spectrometry data (negative mode) of 1b. Inset shows the isotopic distribution of **1b**.

2.3.1.3 Synthesis of 1c

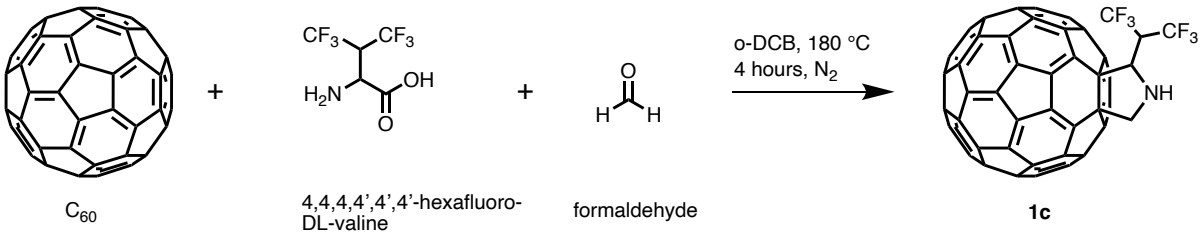

Scheme 2.3 Route to synthesise **1c**.

Fulleropyrrolidine **1c** with a hexafluoroisopropanyl group on the pyrrolidine was synthesised using C_{60}, 4,4,4,4',4',4'-hexafluoro-DL-valine and formaldehyde as starting materials (**Scheme 2.3**). The reaction was monitored by TLC (toluene), with the spot with R_f = 0.78 was determined to be **1c**. The reaction mixture was purified by

column chromatography (silica gel, toluene), giving the pure product in a 30% yield. In ^{1}H NMR spectrum (**Figure 2.14**), a diagnostic multiplet at δ = 4.38 ppm was found corresponding to CH between two trifluoromethyl groups. MALDI ToF mass spectrometry data was also used to confirm the successful synthesis of **1c** (**Figure 2.15**), where the peak at m/z = 912.91 was found to correlate to the [**1c**]$^-$ ion.

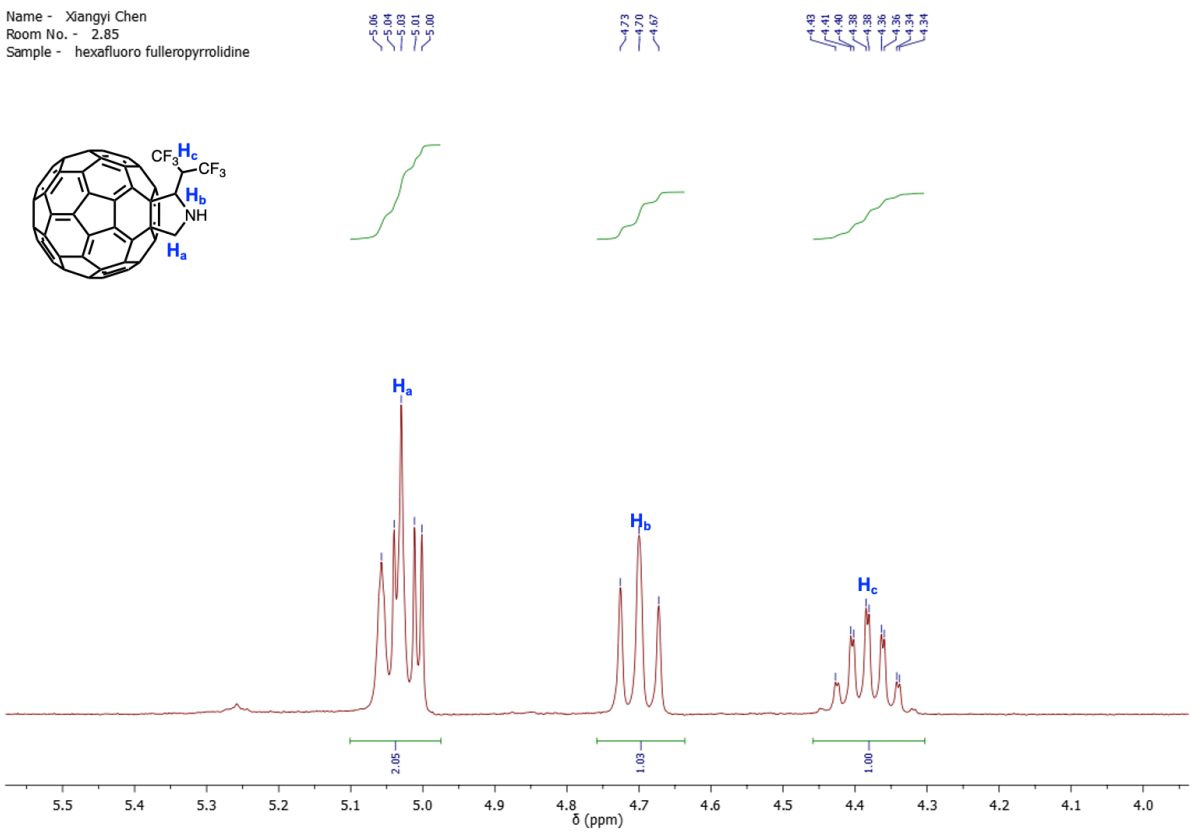

Figure 2.14 ^{1}H NMR (400 MHz, $CDCl_3$, δ, ppm) spectrum of **1c**.

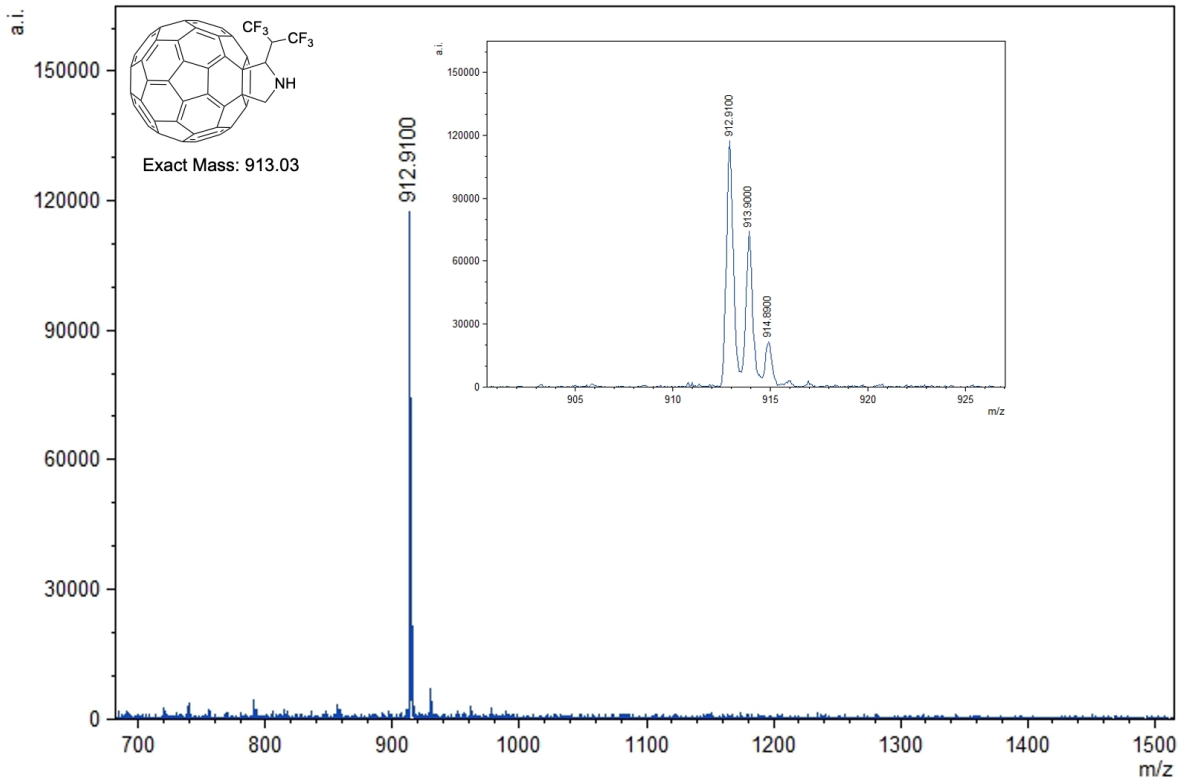

Figure 2.15 MALDI ToF ms (negative mode) spectrum of **3c**. Inset shows the isotopic distribution of **3c**.

2.3.1.4 Synthesis of 2a

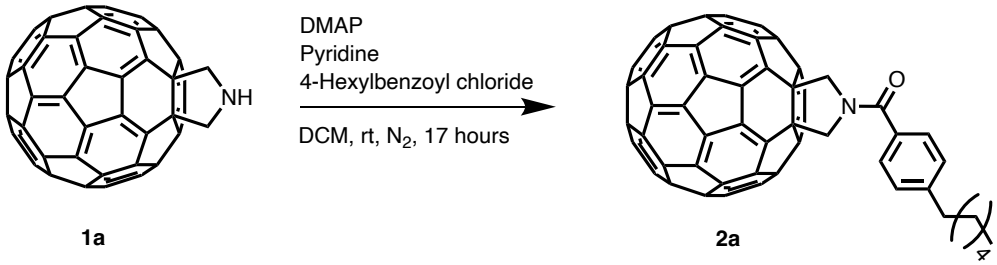

Scheme 2.4 Route to synthesise molecule **2a**.

The reaction mixture used to synthesise synthesise **2a** (**Scheme 2.4**) was monitored by TLC (toluene), with a spot found at a R_f = 0.3. The reaction mixture was purified by column chromatography (silica gel, toluene), giving pure product in a 23% yield. In the ^{1}H NMR spectrum (see **Figure 2.16**), the diagnostic pyrrolidine singlet, δ = 5.52, and

two aromatic doublets, δ = 7.76 and 7.33 ppm, were both detected, which indicated the success of the coupling reaction. Evidence for the formation of **2a** was also provided by MALDI ToF mass spectrometry (see **Figure 2.17**) with the peak at m/z = 950.73 corresponding to the $[M]^-$ ion. In the FT-IR spectrum, a distinct peak with a wavenumber of 1639 cm^{-1} was found and interpreted as being a result of the carbonyl group.

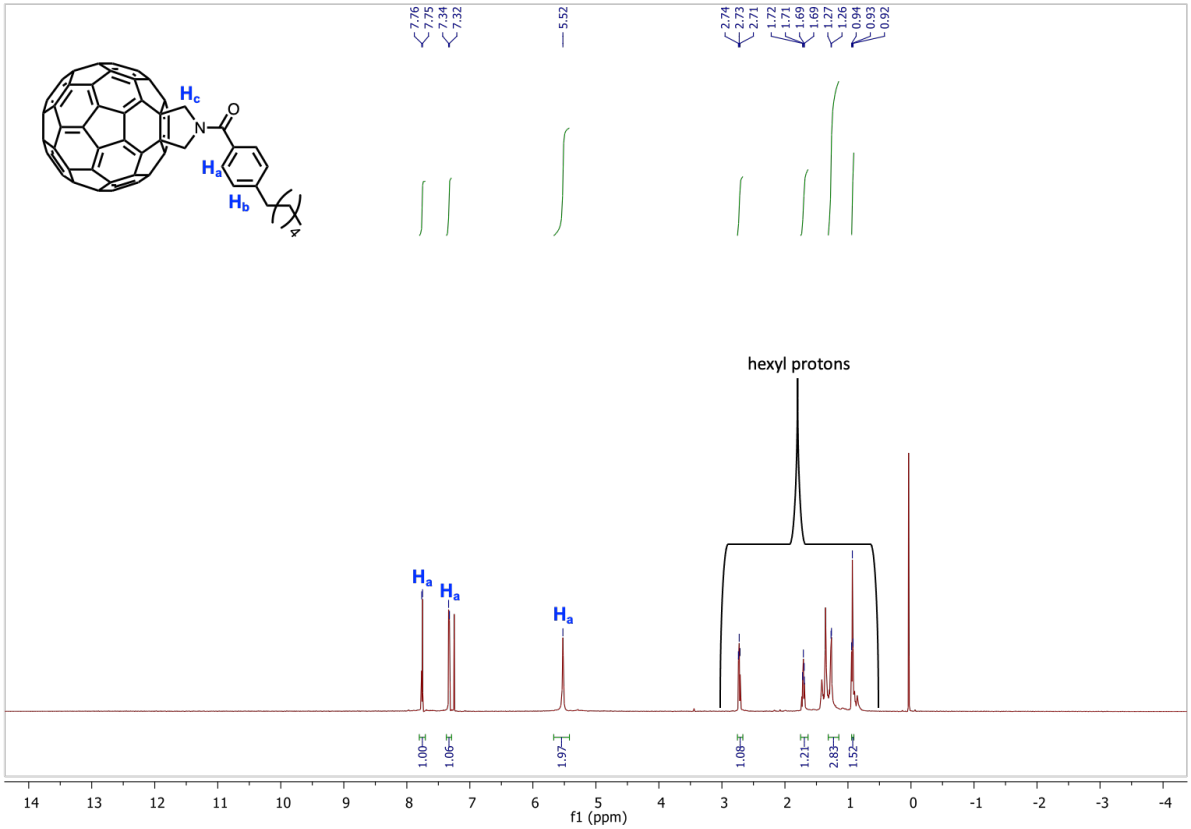

Figure 2.16 ^{1}H NMR (400 MHz, $CDCl_3$, δ, ppm) spectrum of **2a**.

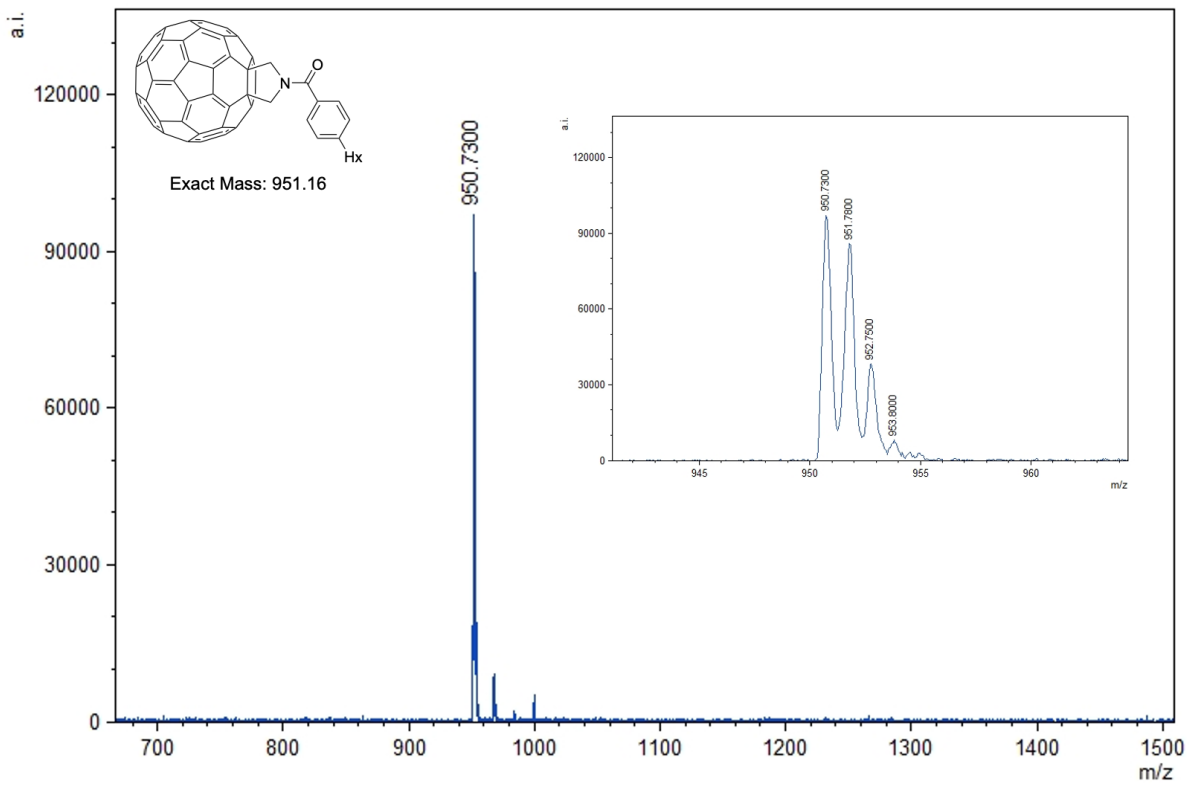

Figure 2.17 MALDI ToF mass spectrometry data (negative mode) of **2a**. The inset shows the isotopic distribution of **2a**.

2.3.1.5 Synthesis of 2b

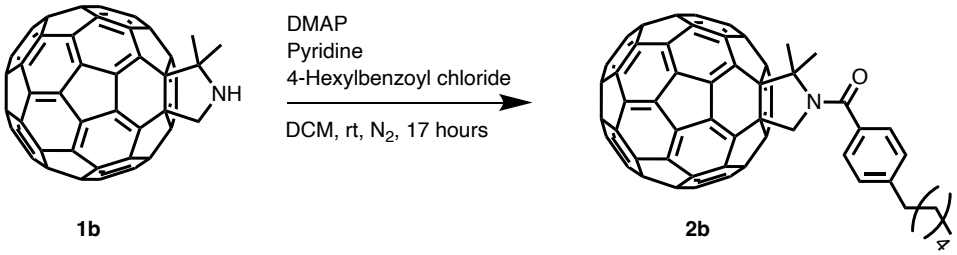

Scheme 2.5 Route to synthesise **2b**.

The reaction mixture used to synthesise **2b** (**Scheme 2.5**) was monitored by diagnostic TLC (*o*-DCB), with a spot on TLC plate appearing at R_f = 0.875. The reaction mixture was purified by silica gel column chromatography (*o*-DCB) to give the material in a 25% yield. The formation of **2b** was confirmed by ^{1}H NMR, MALDI-TOF

mass and FT-IR (**Figure 2.18**). In the ^{1}H NMR spectrum, characteristic peaks for the two aromatic doublets at δ = 8.05 and 7.80 ppm, a singlet for pyrrolidine at 5.40 ppm and one dimethyl singlet at δ = 1.32 ppm were detected to confirm the formation of the **2b**. The molecular ion peak at 978.62 m/z in the MALDI ToF mass spectrometry data was found corelating to [**M**]$^{-}$ ion of **2b**. A carbonyl peak with wavenumber of 1649 cm^{-1} was found in the FT-IR spectrum.

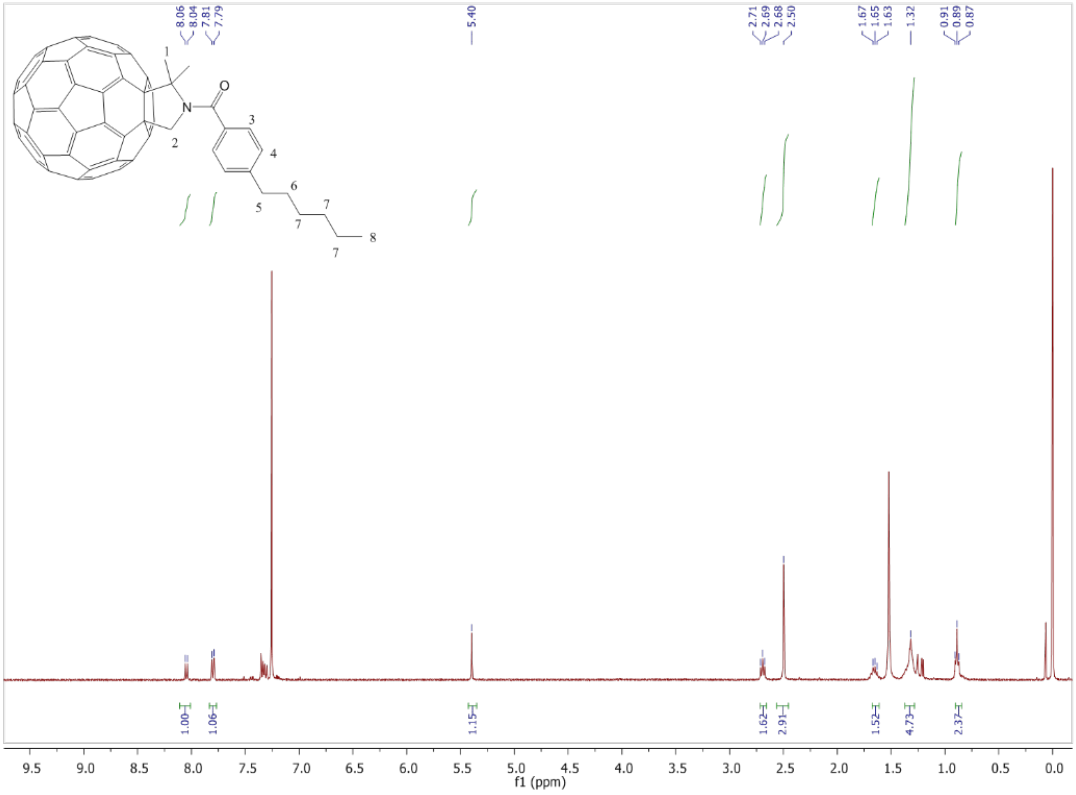

Figure 2.18 ^{1}H NMR (400 MHz, $CDCl_3$, δ, ppm) spectrum of **2b**.

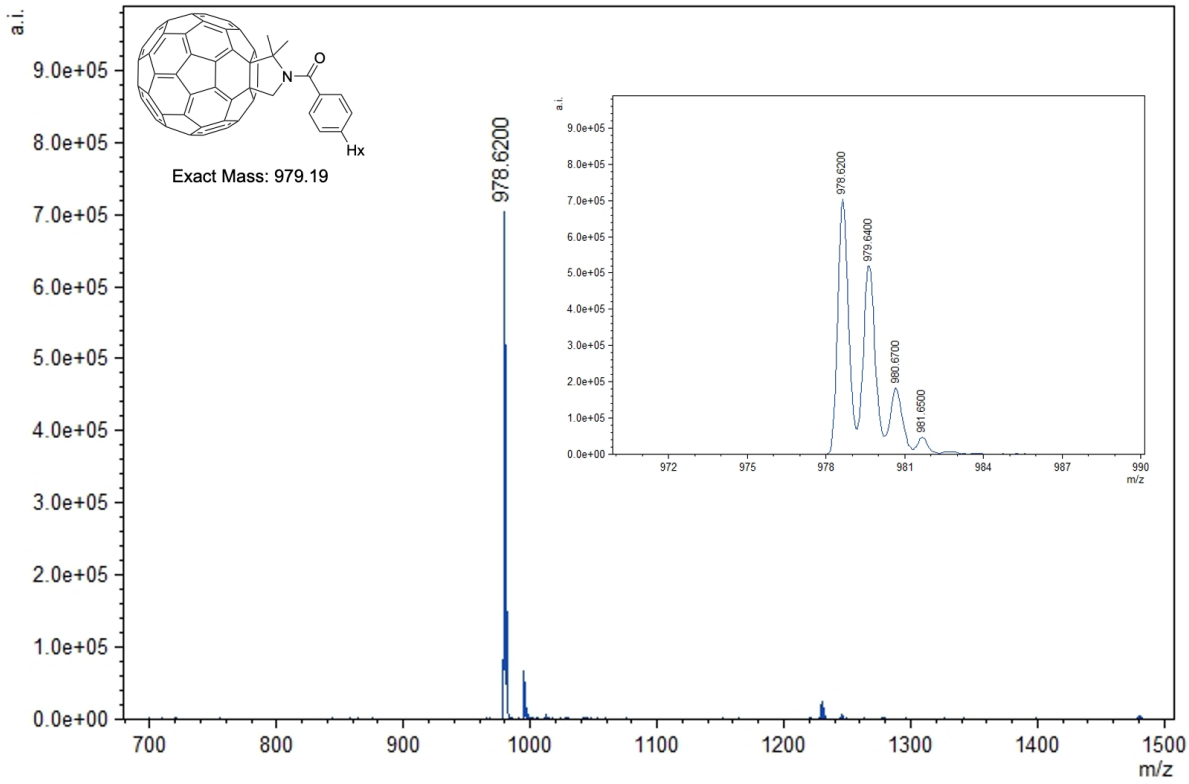

Figure 2.19 MALDI ToF mass spectrometry data (negative mode) of **2b**. The inset shows the isotopic distribution of **2b**.

2.3.1.6 Synthesis of 2c

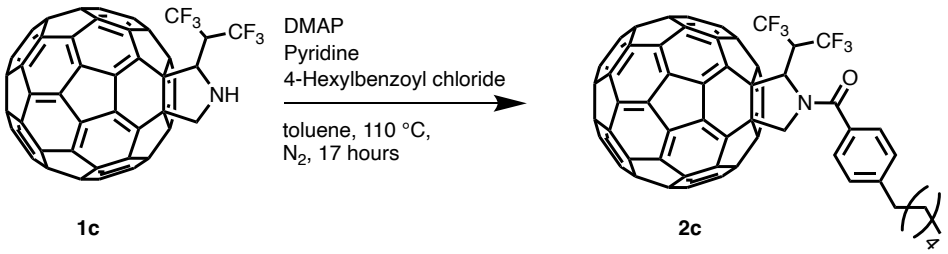

Scheme 2.6 Route to synthesise **2c**.

Fulleropyrrolidine **1c** was used directly to synthesise **2c** by coupling with 4-hexylbenzoyl chloride (**Scheme 2.6**). The reaction was initially performed in DCM at room temperature for 3 days, which was monitored by TLC, however, no formation of **2c** was observed. The reaction was then attempted in DCM under reflux conditions,

but the product was still not observed via TLC. This is probably caused by the strong electron-withdrawing group on the pyrrolidine ring resulting in a slow reaction rate for the coupling reaction or providing the steric hindrance to the bulky group attacking the nitrogen atom. Therefore, more energy is required to facilitate the formation of **2c**. Finally, the reaction was performed in toluene heated to 110 °C for overnight. A spot, corresponding to the formation of **2c**, was observed in TLC with a R_f = 0.19. The reaction mixture was purified by silica gel column chromatography (CS_2/toluene 9/1 v/v), giving **2c** in a 19% in yield. The MALDI ToF mass spectrum provided the evidence of the formation of **2c**, where a molecular ion peak appeared at m/z = 1100.47, which was assigned to the [**M**]$^-$ ion of **2c**. Further analysis was carried out by IR spectrometry, which showed a carbonyl peak at 1655 cm[1].

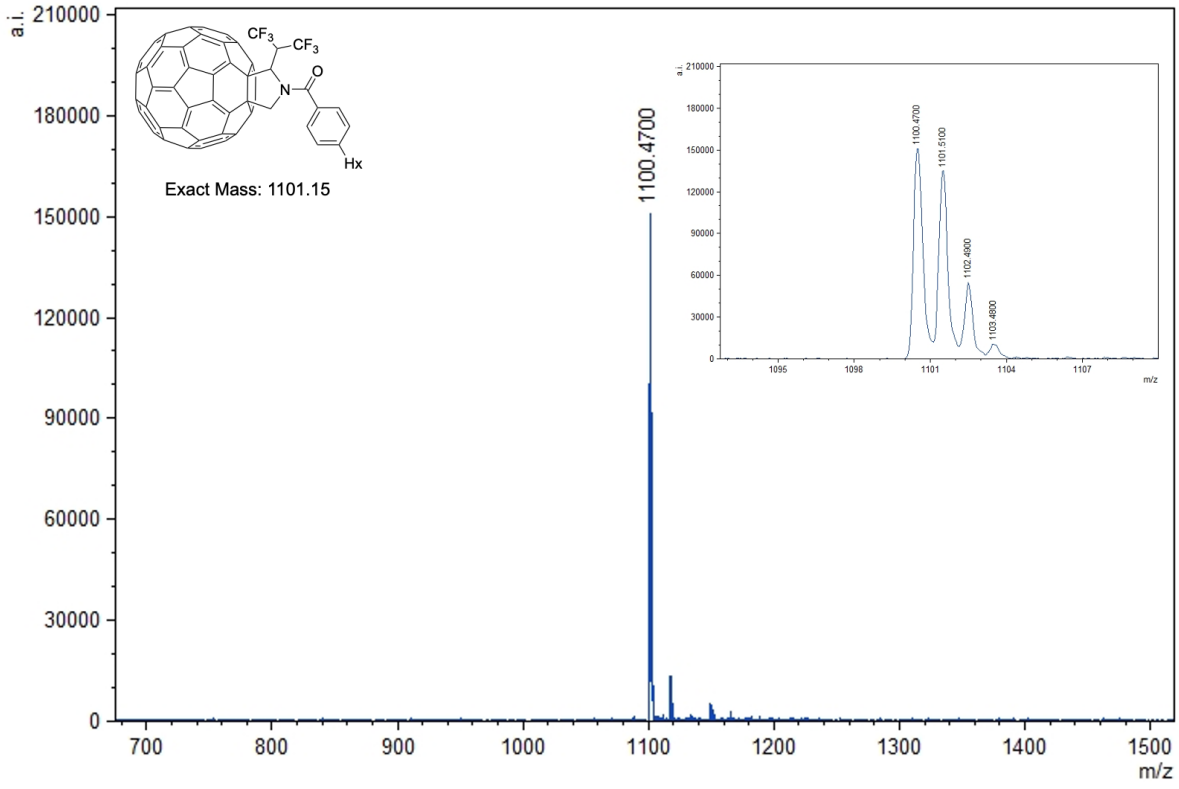

Figure 2.20 MALDI ToF mass spectrometry data (negative mode) of **2c**. The inset indicates the isotopic distribution.

2.3.1.7 Synthesis of 3a

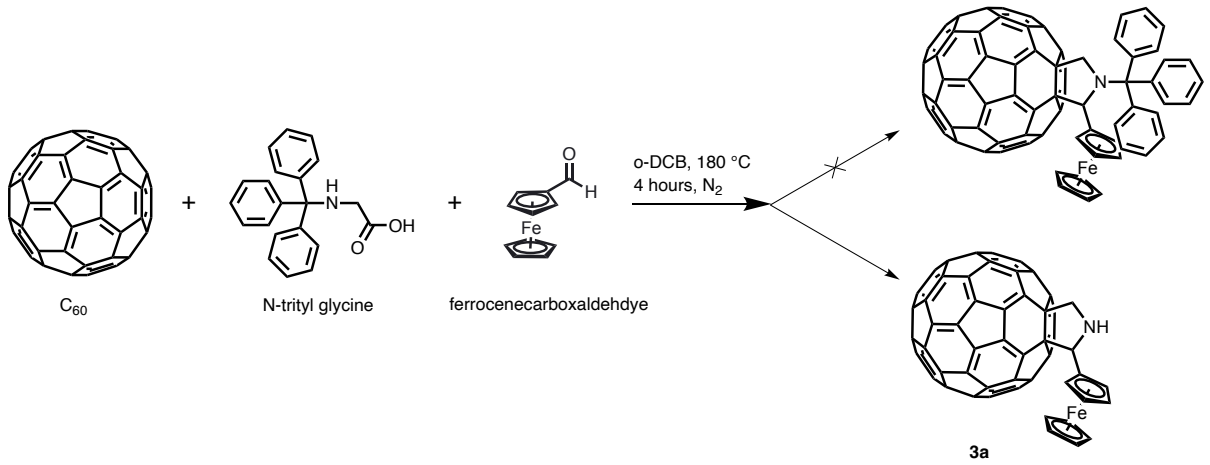

Scheme 2.7 Route to synthesise molecule **3a**. The **3a** was synthesised directed instead of the trityl protected fulleropyrrolidine.

Using N-trityl glycine as starting material was expected to form N-trityl-2-ferrocenyl fulleropyrrolidine. The reaction was performed and monitored by TLC (toluene), which showed a new spot with R_f = 0.37. The column chromatography (SiO_2, toluene) was used to isolate the new band, followed by characterising with NMR and MALDI ToF mass spectroscopy, indicating the direct formation of **3a** instead of N-trityl-2-ferrocenyl fulleropyrrolidine. In ^1H NMR spectrum (see **Figure 2.21**), ferrocene proton peaks (labelled as H_{Fc}) and a pyrrolidine proton peaks (labelled as H_a and H_b) were detected. The addition of the ferrocene group induced the imbalanced magnetic effect in the H_b, in which two protons coupled with each other giving two doublets at δ = 5.02 and 4.88 ppm with J = 15 Hz. The MALDI ToF mASs data (**Figure 2.22**) showed a peak with m/z = 946.44 which matched the [**3a**]$^-$. As a result, a separate deprotection step to remove the trityl group was not required. After adding a ferrocene group into the 2' position of the pyrrolidine ring, compared to the case when formaldehyde is used, the N position of the ring is quit sterically hindered. The presumption is probably that the

N-trityl-2-ferrocenyl fulleropyrrolidine formed at first, but the bulky tertiary carbon of the trityl group is quickly kicked out, forming the molecule **3a** directly to release this sterically induced strain. This same phenomena in terms of increase steric strain was also observed during the synthesis of molecule **4a**-**c**. A more thorough investigation, e.g. computational modelling of the conformation of transition states, is required to explain this fully.

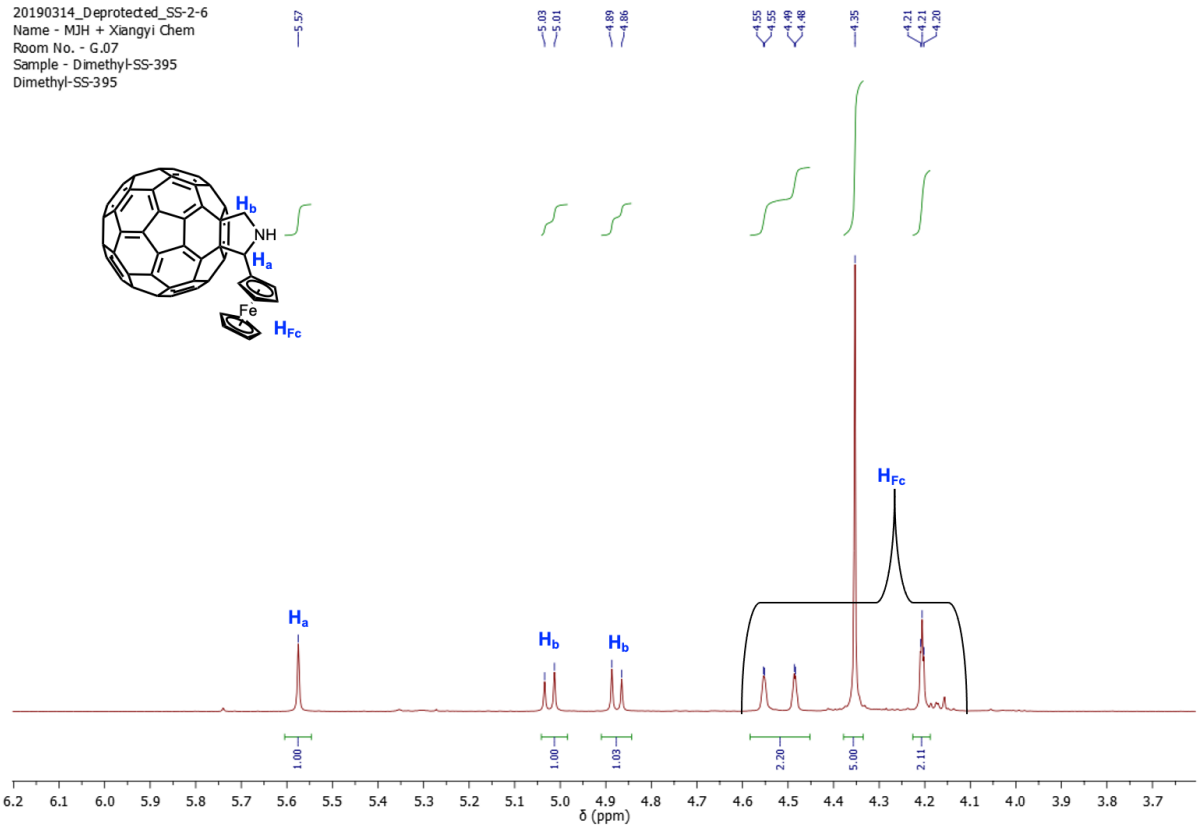

Figure 2.21 ^{1}H NMR spectra (500 MHz, $CDCl_3/CS_2$, δ, ppm) of the isolated band from the column with R_f = 0.37, which indicated molecule **3a** instead of N-trityl-2-ferrocenyl fulleropyrrolidine was formed.

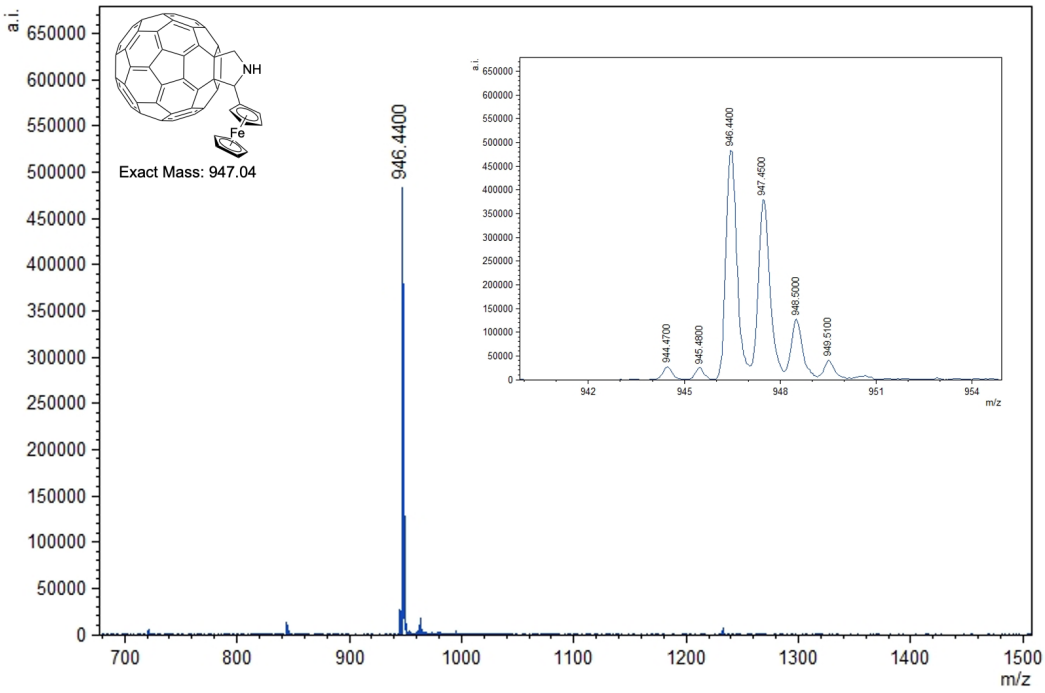

Figure 2.22 MALDI ToF mass (negative mode) spectrum of **3a**. The inset shoes the isotopic distribution of **3a**.

2.3.1.8 Synthesis of 3b

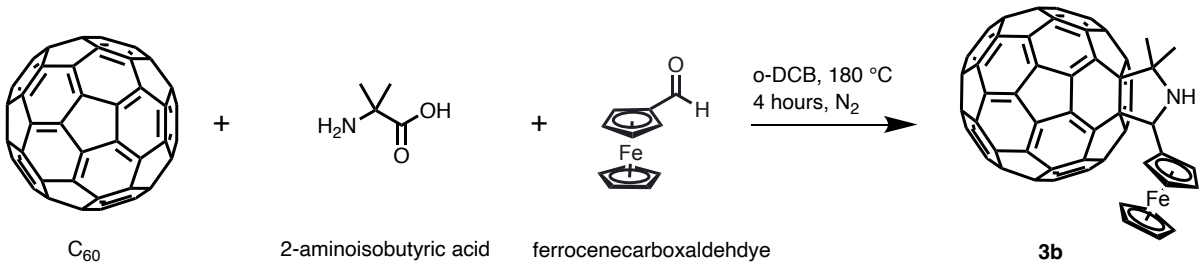

Scheme 2.8 Route to synthesise **3b**.

The reaction to synthesise molecule **3b** (**Scheme 2.8**) was monitored by TLC (toluene), with a spot with R_f = 0.43 observed. The reaction mixture was purified by column chromatography (toluene), giving the product in a 32.2% yield. Due to the addition of the ferrocene group, the two methyl groups on the opposite side of the pyrrolidine ring became unequal and thus gave two singlets with 2.29 ppm and 2.15 ppm (labelled as

H_b and H_c in **Figure 2.23**). Pyrrolidine proton on ferrocene side was also detected as a singlet with 5.86 ppm (labelled as H_a). In MALDI ToF mass data (**Figure 2.24**), a peak with m/z = 944.78 was found, which matches the value of [**3b**]$^-$.

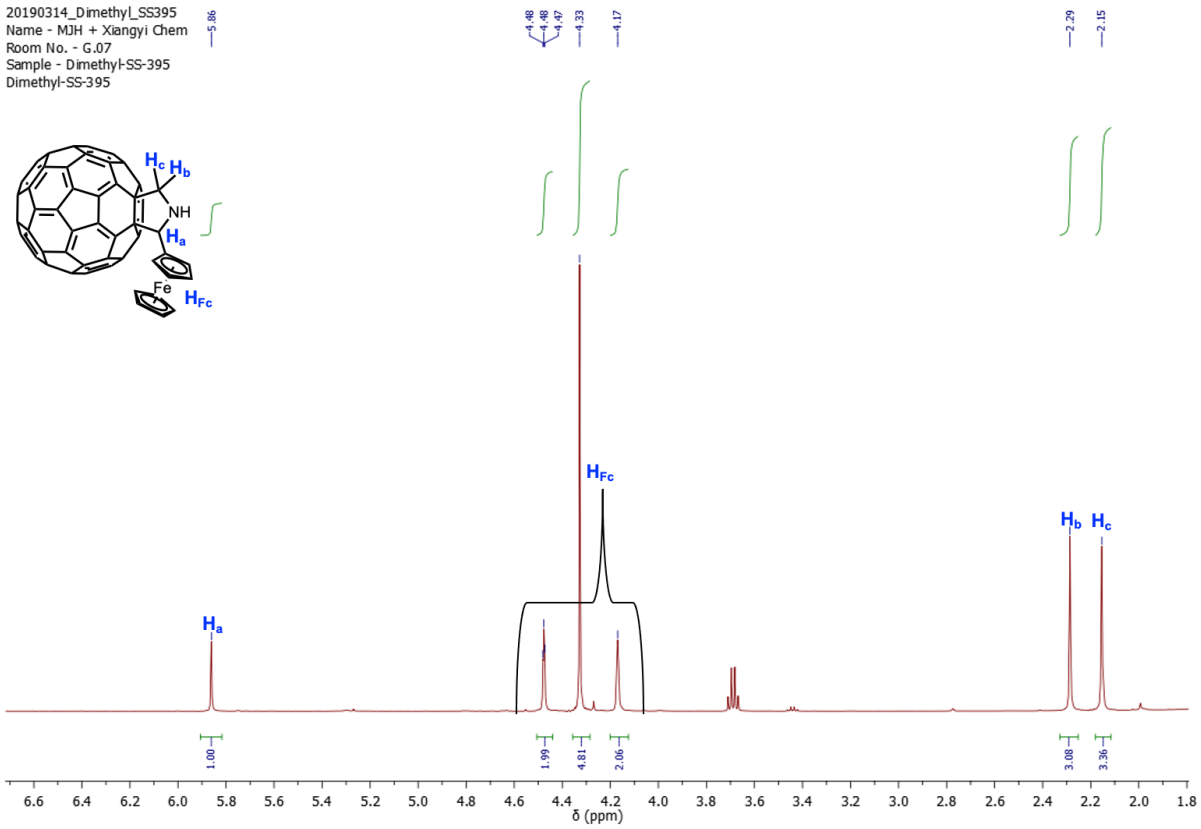

Figure 2.23 ^{1}H NMR (500 MHz, $CDCl_3/CS_2$, δ, ppm) spectrum of **3b**.

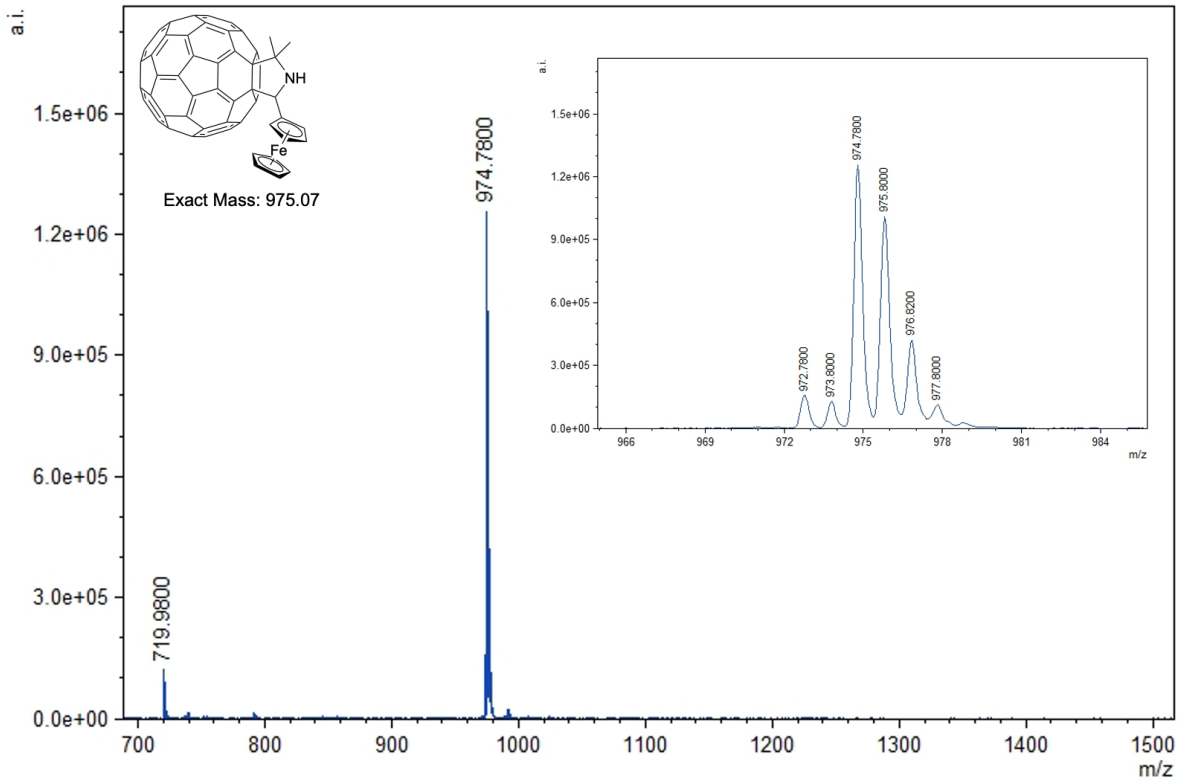

Figure 2.24 MALDI ToF mass (negative mode) data of **3b**. The inset shoes the isotopic distribution of **3b**.

2.3.1.9 Synthesis of 3c

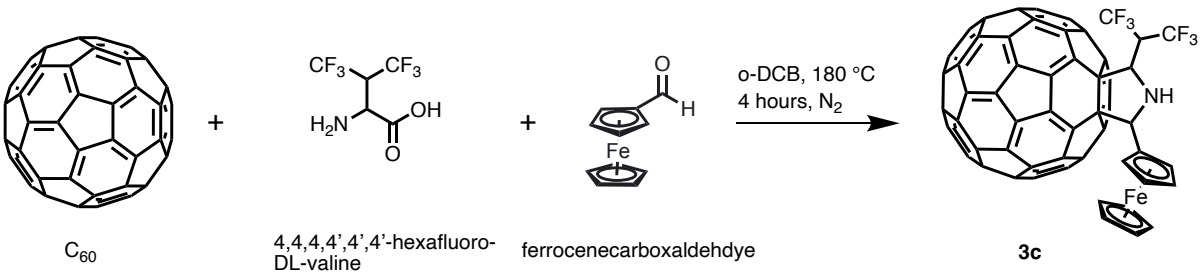

C_{60} 4,4,4,4',4',4'-hexafluoro-DL-valine ferrocenecarboxaldehdye **3c**

Scheme 2.9 Route to synthesise **3c**.

The reaction conditions to synthesise molecule **3c** were shown in ***Scheme 9***. The reaction was monitored by TLC (CS_2), and a new spot with R_f = 0.85 observed. The product was isolated by column chromatography (CS_2), obtaining the product as a black powder in a 39.1% yield. The formation of molecule **3c** was confirmed by ^1H

NMR (**Figure 3.26**) and MALDI ToF mass (negative mode, **Figure 3.27**). In this molecule, both pyrrolidine carbons are chiral. In ^{1}H NMR spectrum, pyrrolidine proton on ferrocene side gave a doublet at 5.58 ppm (labelled as H_a), whereas the pyrrolidine proton on hexafluoro side gave a peak at 5.31 ppm (labelled as H_b). The methine proton between two trifluoromethyl groups gave a multiplet at 4.46 ppm (labelled as H_c) which overlapped with one of the ferrocene peaks. In MALDI ToF mass data, a peak with m/z = 1097.72 was found, corresponding to the [**3c**]$^-$.

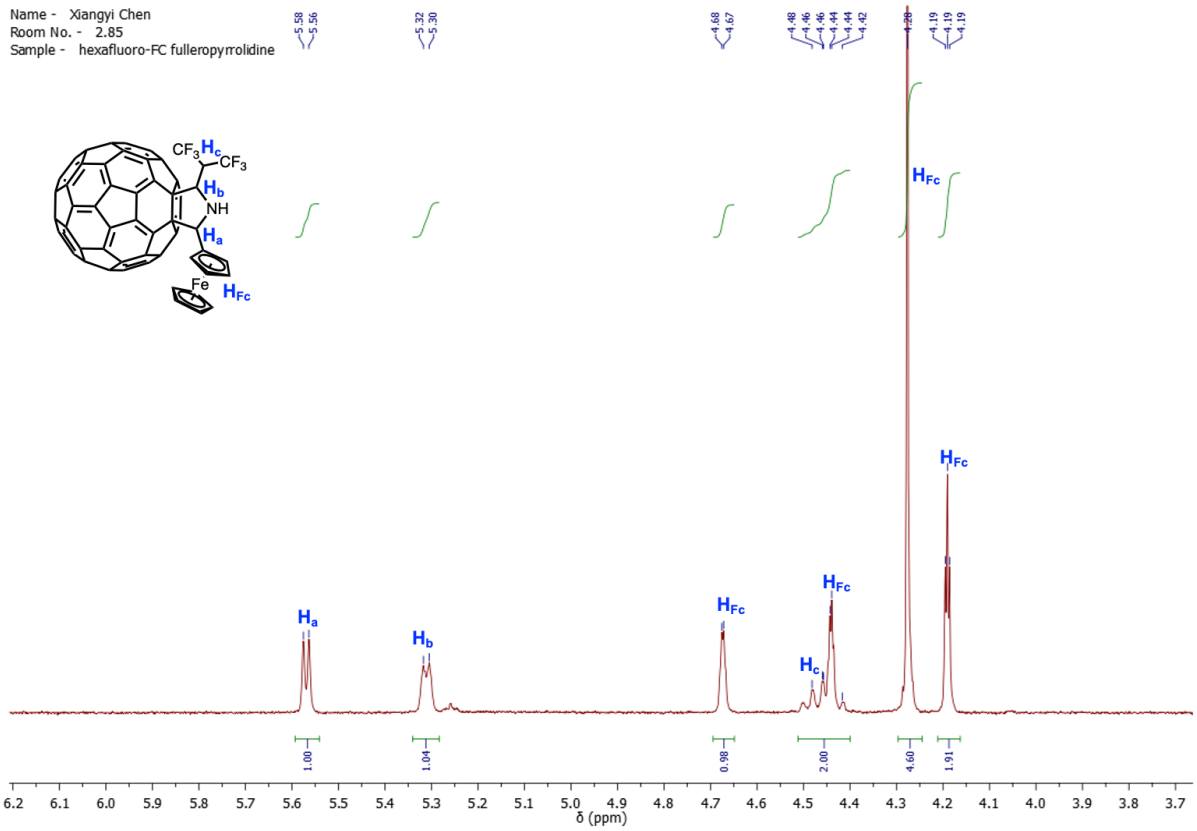

Figure 2.25 ^{1}H NMR (400 MHz, $CDCl_3/CS_2$, δ, ppm) spectrum of molecule **3c**.

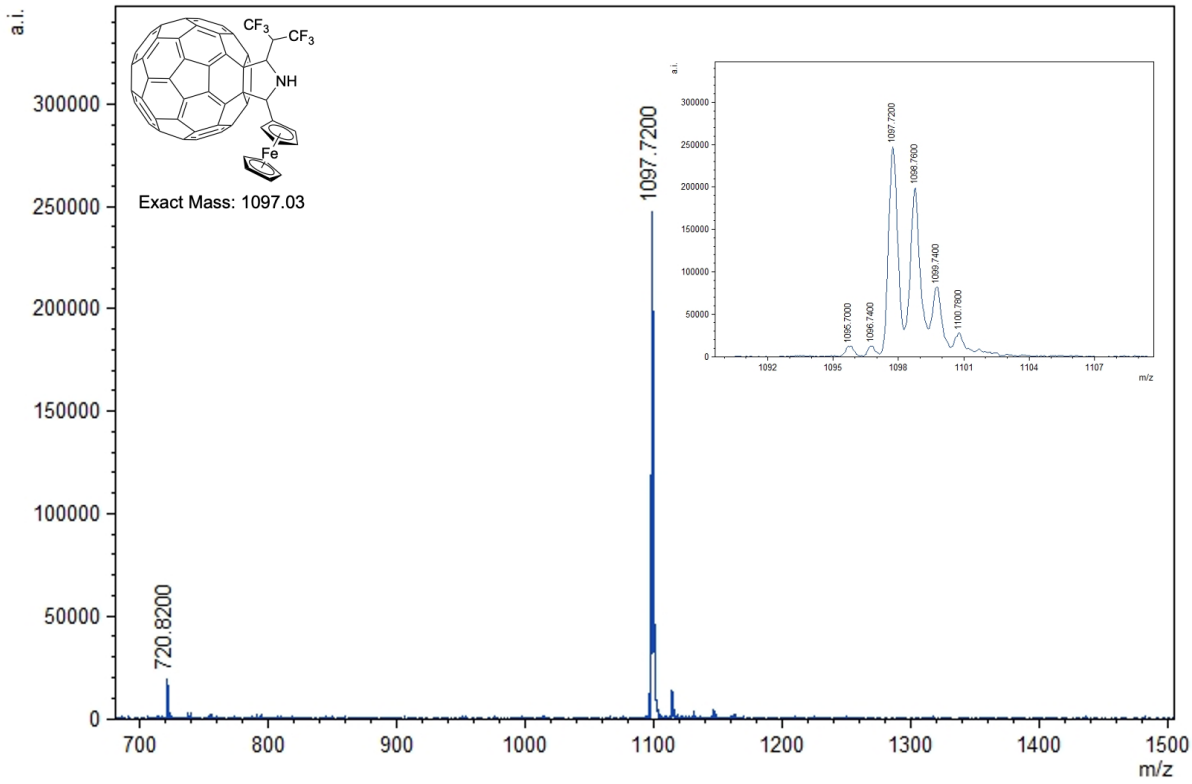

Figure 2.26 MALDI ToF mass (negative mode) data of **3c**. The inset shows the isotopic distribution of the **3c**.

2.3.1.10 Synthesis of ferrocene and solubilising groups appended fullerene derivatives, 6a-c

Ferrocene group appended fulleropyrrolidine derivatives, **5a**-**c**, were designed as the starting material for coupling with a solubilising alkyl chain group, forming **6a**-**c** as products. Similar to the preparation of **4a**-**c**, DMAP was used as a base to deprotonate the fulleropyrrolidines **5a**-**c**, which subsequently reacted with 4-hexylbenzoyl chloride to give molecule **6a**-**c**. However, only **6a** formed, with reactions to form **6b** and **6c** failing. The details and explanation are outlined below.

2.3.1.10a Synthesis of molecule **6a**.

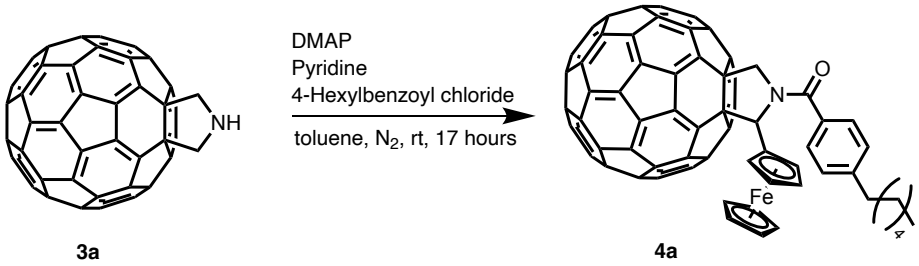

Scheme 2.10 Route to synthesise **4a**.

Several reaction conditions were tried to synthesise **4a** (**Scheme 3.10**), including i) DCM, rt, N_2, 18 h to 7 days; ii) DCM, reflux, N_2, 18 h to 7 days; iii) toluene, rt, N_2, 18 h to 7 days, with reaction mixture monitored by TLC (toluene) in each case. The poor solubility of **3a** in DCM impeded the formation of **4a** in DMC. Only the third set of conditions (toluene, rt) worked, and 17 hours was enough to form the product **4a**, which was purified by column chromatography (SiO_2, toluene) giving **4a** in the yield of 57%. In the ^1H NMR spectrum, diagnostic alkyl proton peaks were observed at chemical shift = 2.72, 1.70 1.32 and 0.9 ppm, whilst the ferrocene proton peaks were also observed at chemical shift = 4.32-4.73 ppm. A peak with m/z = 1135.80 was found in MALDI ToF mass data, matching the m/z of [**4a**]$^-$. The reason why the reaction did not happen in DCM is that the solubility of the **4a** in DCM is very poor, impeding the reaction.

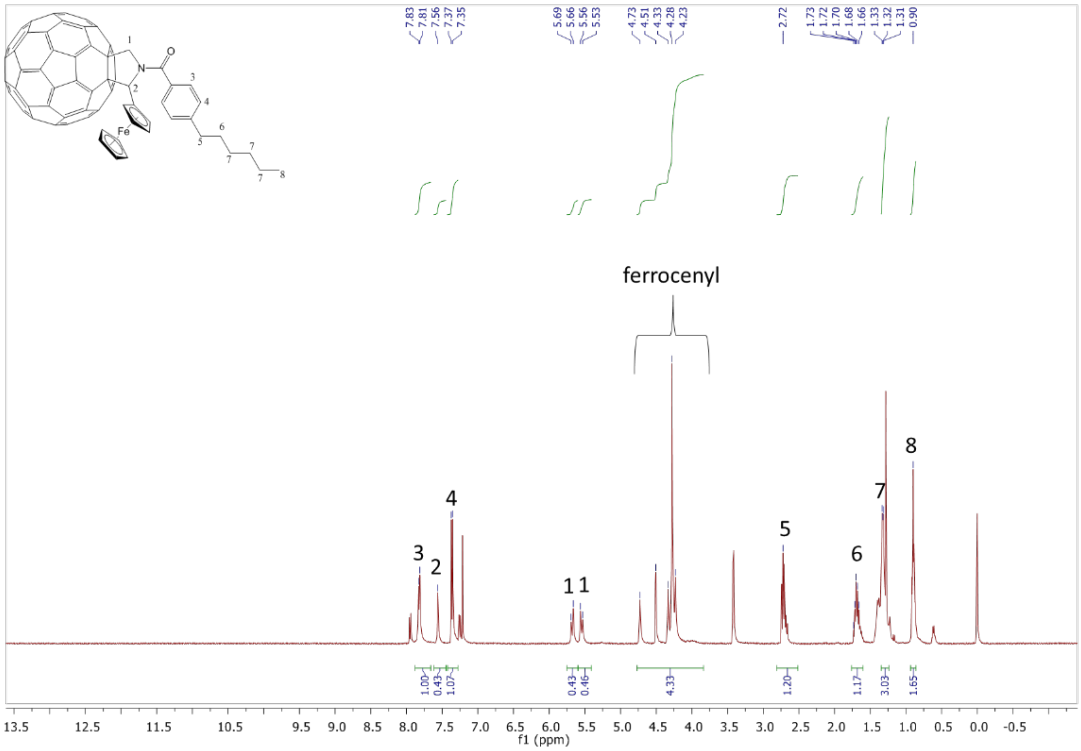

Figure 2.27 ^{1}H NMR spectrum of molecule **4a** (recorded at 500 MHz in $CDCl_3/CS_2$).

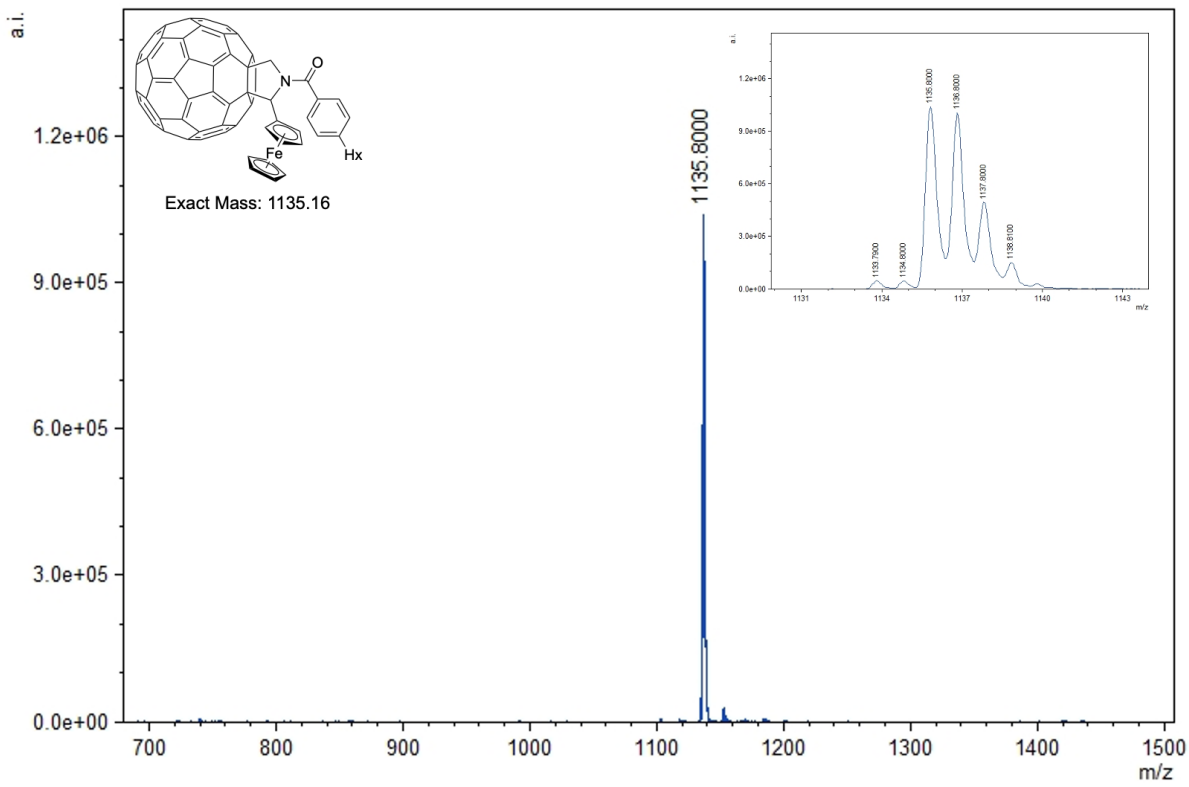

Figure 2.28 MALDI ToF mass (negative mode) spectrum of **4a**. The inset shows isotopic distribution of **4a**.

2.3.1.10b Synthesis of **4b**

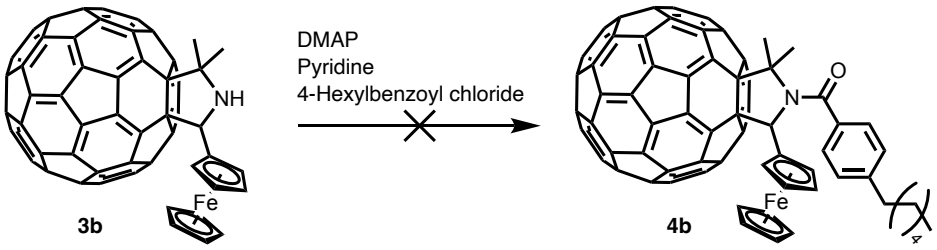

Scheme 2.11 Route to synthesise **4b**.

Several reaction conditions were attempted in order to synthesise molecule **4b**, including; i) DCM, rt, N_2, 18 h to 7 days ; ii) DCM, reflux, N_2, 18 h to 7 days; iii) toluene, rt, N_2, 18 h to 7 days; iv) toluene, reflux, N_2, 18 h to 7 days; v) ODCB, rt, N_2, 18 h to 7 days. Different solvents were used, moving from DCM to toluene then to ODCB in

order to find a solvent which dissolved fullerene precursor **3b** as good as possible. Different temperatures were also tried, from rt to reflux, to give more energy to activate the reaction to form **4b**. However, in all case no new spots were observed by TLC (toluene). The reaction mixtures were also analysed by MALDI ToF ms (**Figure 2.29**), with no peaks matching the mass of **4b** (calculated m/z = 1163), and only the starting material **3b** observed in all cases. A stronger base DBU (pKa = 13.5 whereas DMAP is 9.7) was also tested, but again there was no sign of the product being formed. It is concluded that the main reason of failure is that the steric hindrance. To compare with **3a**, **3b** is more sterically hindered than **3a** due to the extra two methyl groups in the pyrrolidine ring. After the deprotonation of **3b**, the formed nucleophile is too hindered to attack the carbonyl of the 4-hexylbenzoyl chloride. This situation also happened on the reaction to synthesise **4c**, which was stated below.

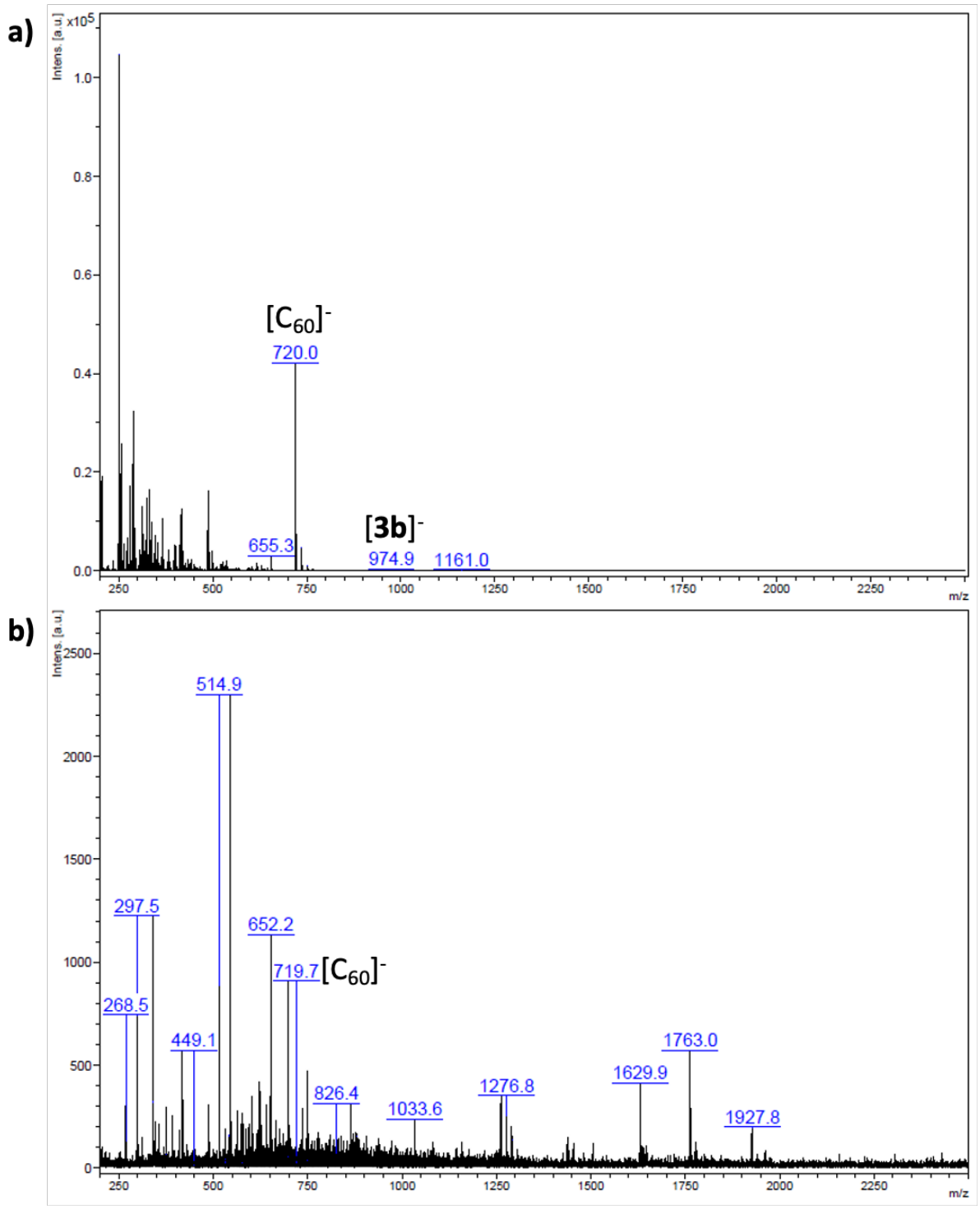

Figure 2.29 MALDI ToF ms data of the reaction mixture to synthesise **4b**; a) negative mode data shows a peak corresponding to fullerene along with the starting material **3b**; b) positive mode data shows a peak corresponding to fullerene.

2.3.1.10c Synthesis of **4c**.

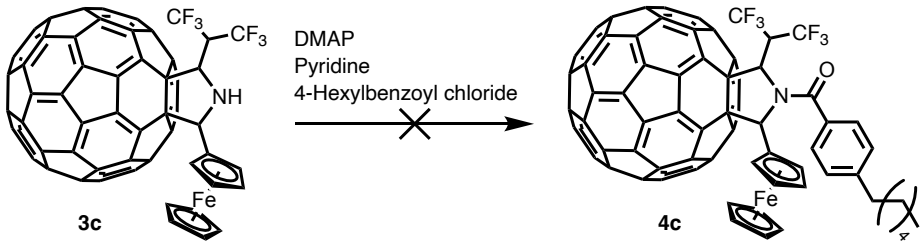

Scheme 2.12 Route to synthesise **4c**.

The reactions to synthesise **6c** were performed several times with different condition (**Scheme 2.12**) including; i) DCM, rt, N_2, 18 h to 7 days; ii) DCM, reflux, N_2, 18 h to 7 days; iii) toluene, rt, N_2, 18 h to 7 days; iv) toluene, reflux, N_2, 18 h to 7 days. The reaction mixture was monitored by TLC (toluene) and analysed by MALDI ToF ms (negative mode, **Figure 2.30**), which only detected the fullerene and unreacted starting material **3c**. It is proposed that the reaction failed for possible two reasons; 1) the existence of the hexafluoroisopropanyl group in **3c** means that once the nucleophile is formed by the deprotonation process it is too hindered to react with the 4-hexylbenzoyl chloride as in the case of **3b**; and 2) the hexafluoroisopropanyl is a strong electron withdrawing group, which reduces the reactivity of the nucleophile formed from **3c**.

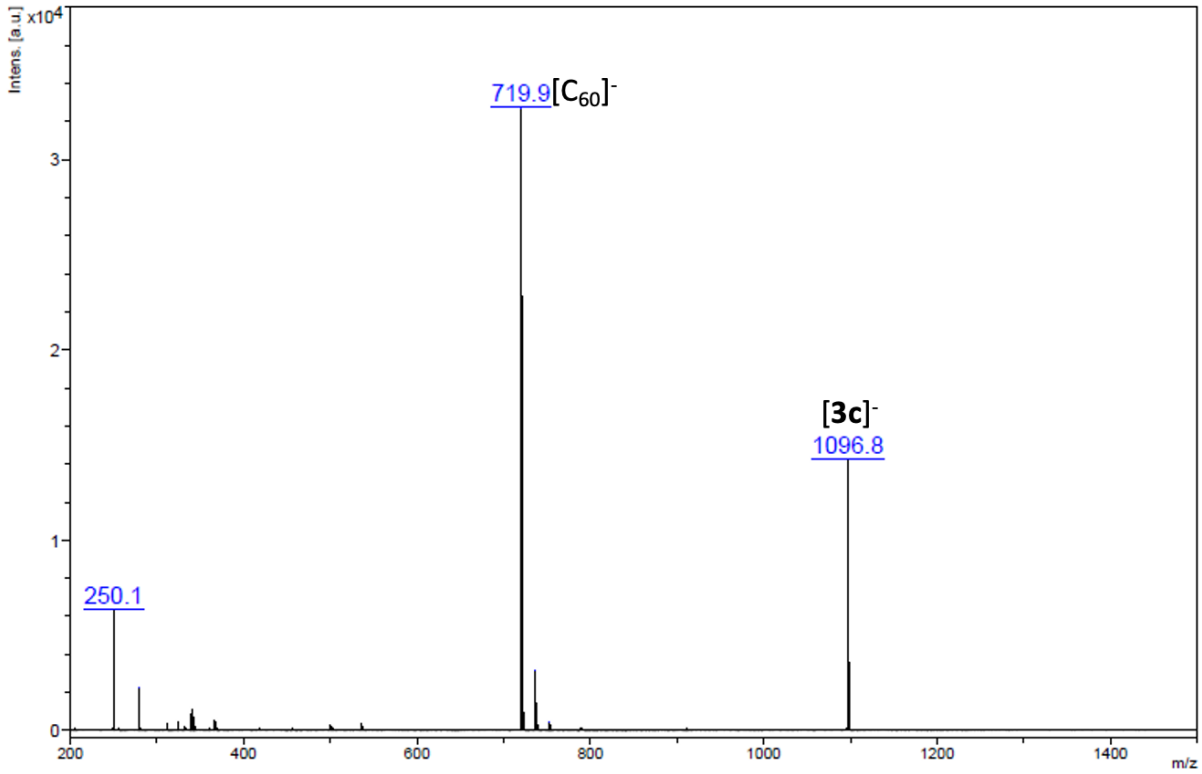

Figure 2.30 MALDI ToF mass (negative mode) data of the reaction mixture used to synthesise **4c**, with only peaks corresponding to fullerene and unreacted starting material **3c** detected.

2.3.2 Synthesis of N-substituted valine amino acids, AA1-6

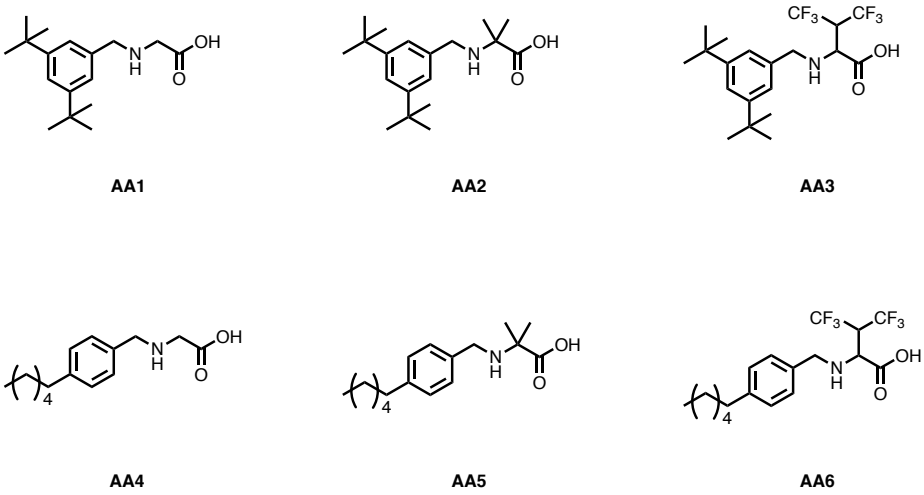

Figure 2.31 Target N-substituted valine amino acids **AA1-6**.

The amino acids used in C_{60} charge carrier synthetic route 2 requires two functional groups to perform the one-pot Prato reaction: 1) either a N-ditertbutylbenzyl or N-hexylbenzyl group and 2) either two protons, two methyl groups or a hexafluoropropanyl on the *α* carbon. Methyl esters, **ME1,2,4** and **5**, were synthesised initially, followed by hydrolysis to give the corresponding amino acids **AA1,2,4** and **5**, whilst **AA3 and 6** were synthesised directly. All the materials were characterised by ^{1}H, ^{13}C NMR chromatography, LC-MS spectroscopy and FT-IR spectroscopy.

2.3.2.1 Synthesis of N-((3,5-Di-tert-butylphenyl)methyl)glycine, AA1.

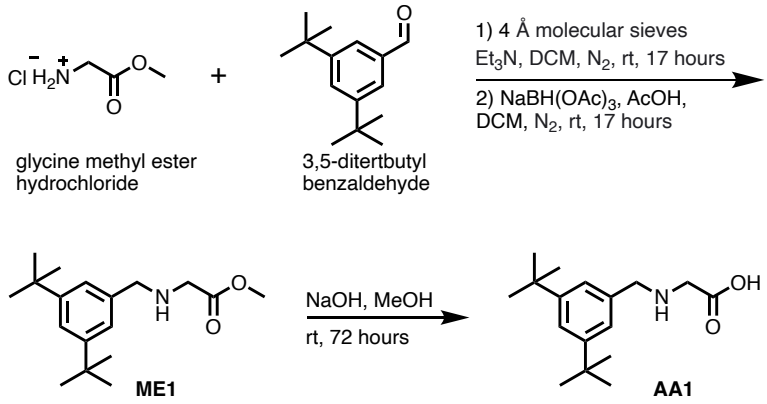

Scheme 2.13 Route to synthesise **AA1**.

Following the previously reported experimental method to synthesise **AA1**,[48] a reductive amination between glycine methyl ester hydrochloride and 3,5-ditertbutylbenzaldhyde was performed, in which triethylamine was used to mop up the hydrochloride and expose the lone pair of the amine group so it can react with the aldehyde group. 4 Å molecular sieves were used to remove the water by-product, pushing the reaction kinetics to the imine intermediate, followed by reducing the imine with $NaBH(OAc)_3$ giving the 2° amine product. After the pre-workup (see Experimental section for full details), the crude product was purified by column chromatography (SiO_2, petroleum ether/ethyl acetate v/v 10/1->10/2), giving **ME1** in a 35% yield. The

product was characterised with the ^{1}H NMR spectroscopy showing two diagnostic methylene singlets (**Figure 2.32top**), with δ = 3.79 and 3.45 ppm, and an ester methyl singlet, with δ = 3.79 ppm, were found indicating the formation of **ME1**. In LC-MS data (**Figure 2.32bottom**), a peak at m/z = 292.22 was found, which matched the m/z value of [**ME1**+H]$^{+}$. Compound **ME1** was subsequently hydrolyzed under basic condition to give the corresponding sodium carboxylate, followed by titration using HCl (1M) to pH = 6.7 giving the target molecule **AA1** in the yield of 66%. NMR spectroscopy, LS-MS were used to characterise **AA1**. In the ^{1}H NMR spectrum of **AA1** (**Figure 2.33top**), the ester methyl singlet disappeared due to the hydrolysis, whilst the two methylene singlets remained. In LS-MS (**Figure 2.33bottom**), a peak at m/z = 276.16 was found corresponding to [**AA1**-H]$^{-}$ ion.

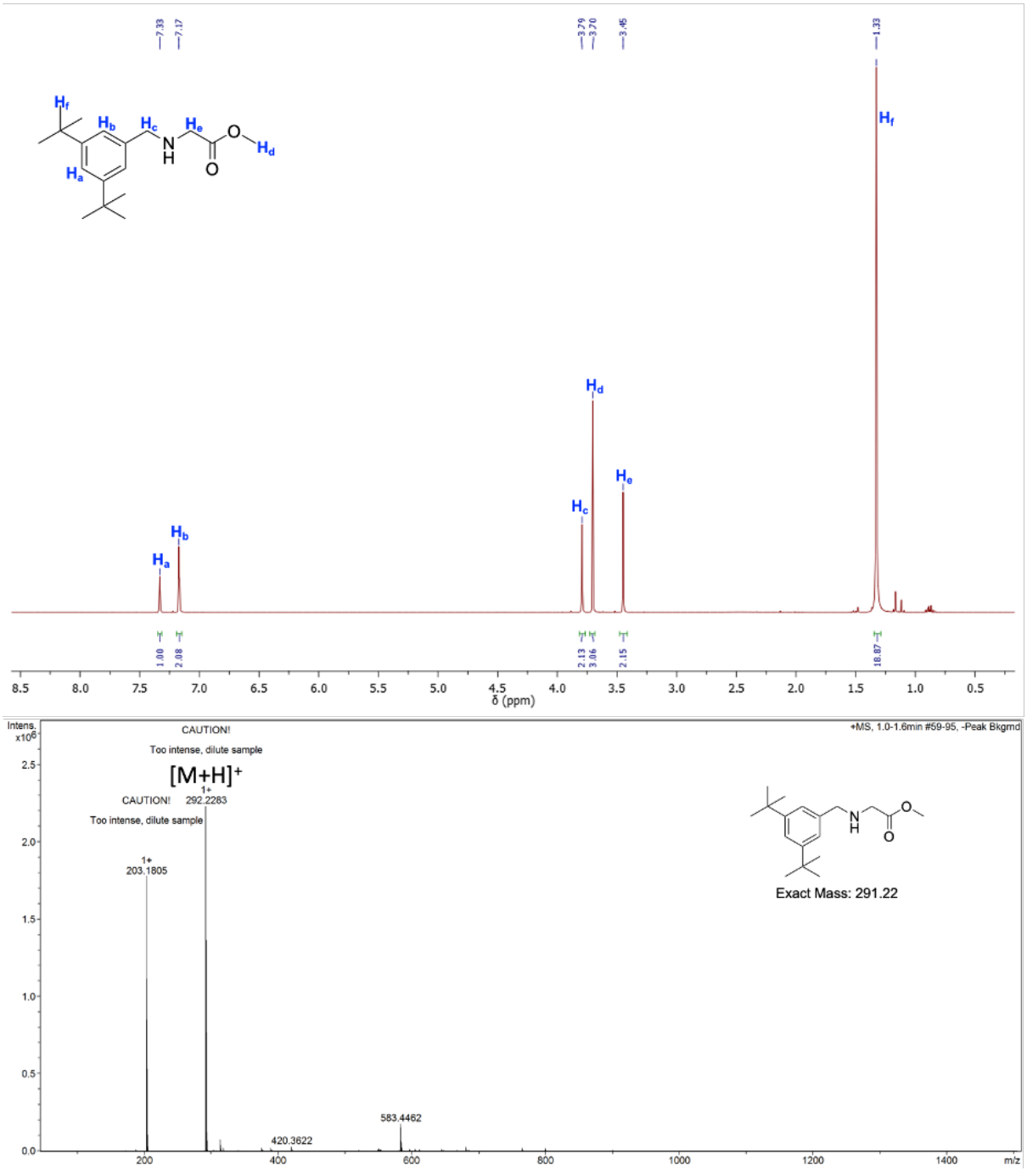

Figure 2.32 (top) ^{1}H NMR (400 MHz, $CDCl_3$, δ, ppm) spectrum of **ME1**; (bottom) LC-MS data of **ME1** shows $[M+H]^+$ peak with m/z = 292.22.

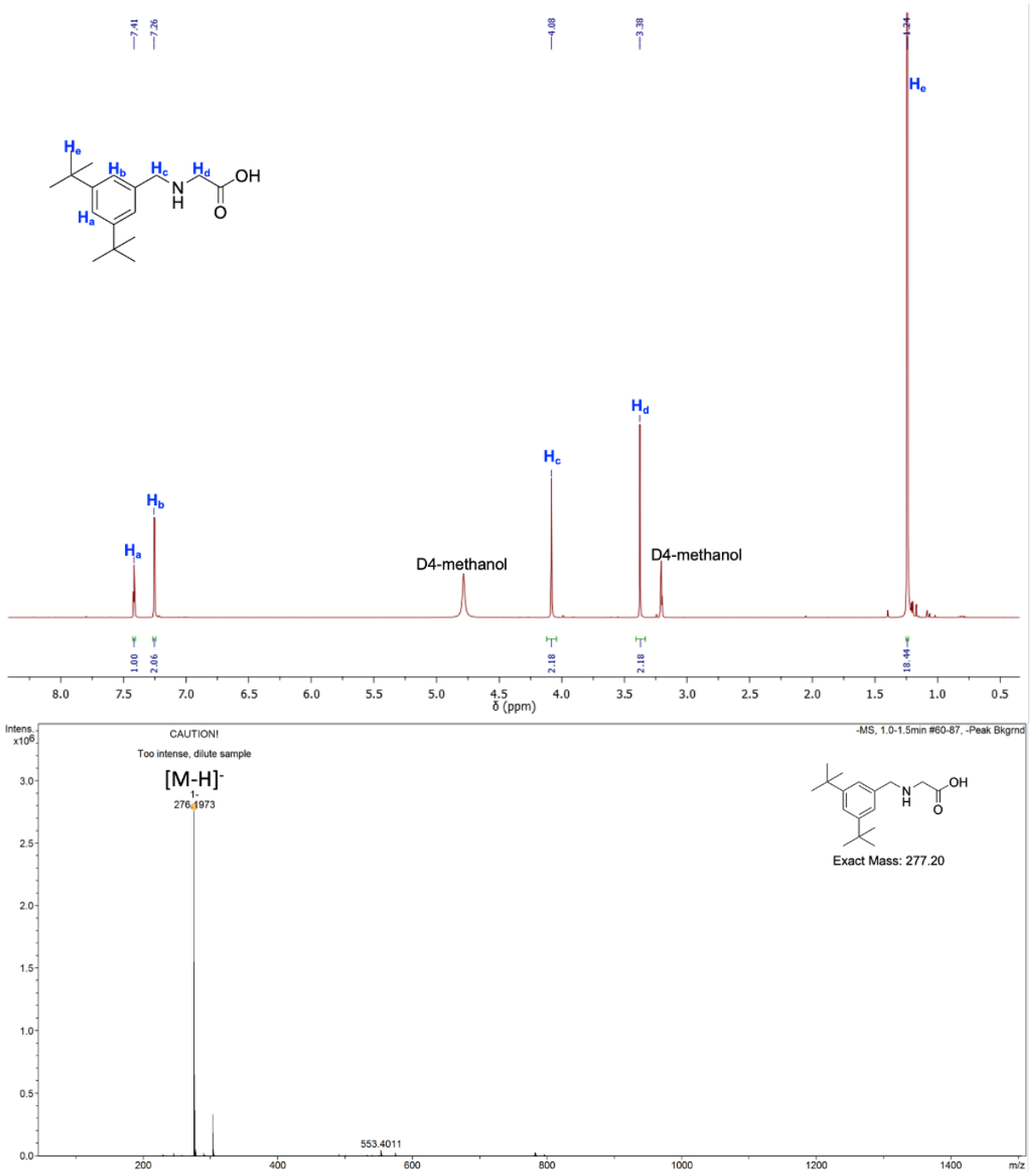

Figure 2.33 (top) ^{1}H NMR (400 MHz, D4-methanol, δ, ppm) spectrum of **AA1**; (bottom) LC-MS data of **AA1** shows $[M-H]^-$ peak with m/z = 276.19.

2.3.2.2 Synthesis of N-((3,5-di-tertbutylphenyl)methyl)-2,2-dimethyl glycine, AA2

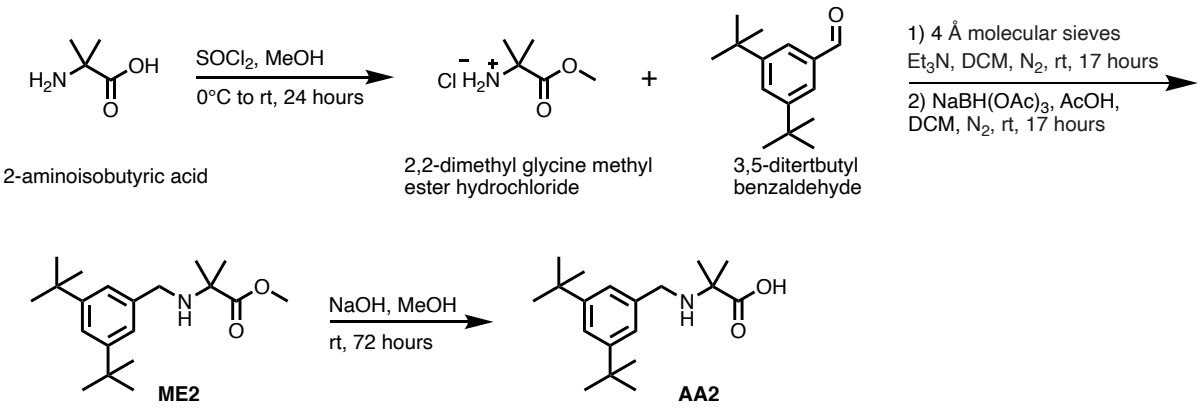

Scheme 2.14 Route to synthesise **AA2**.

2,2-Dimethyl glycine methyl ester hydrochloride was synthesised in a 67% yield following the previously reported procedures. In comparison with the starting material, 2-aminoisobutyric acid, a new singlet with δ = 3.81 ppm showed up in ^{1}H NMR spectrum indicating the that the carboxylic acid group was protected with a methyl group. Subsequently, methyl ester, **ME2**, was synthesised successfully in a 22% yield using 2,2-dimethyl glycine methyl ester hydrochloride and ditertbutylbenzaldehyde as starting materials. The formation of the ME1 was confirmed by ^{1}H NMR spectroscopy, in which two characteristic singlets with δ = 3.53 and 1.30 ppm were found corresponding to the methylene protons and dimethyl protons repectively. In LC-MS data, peak at m/z = 320.25 was found to match the [**ME2**+H]$^+$ ion. After the methyl group deprotection, **AA2** was synthesised successfully in a 80% yield, which was characterised by ^{1}H NMR and LC-MS. In the ^{1}H NMR spectrum, the disappearance of the ester methyl group was observed. In the LC-MS data, a peak at m/z = 304.22 was found to match the value of the [**AA2**-H]$^-$ ion.

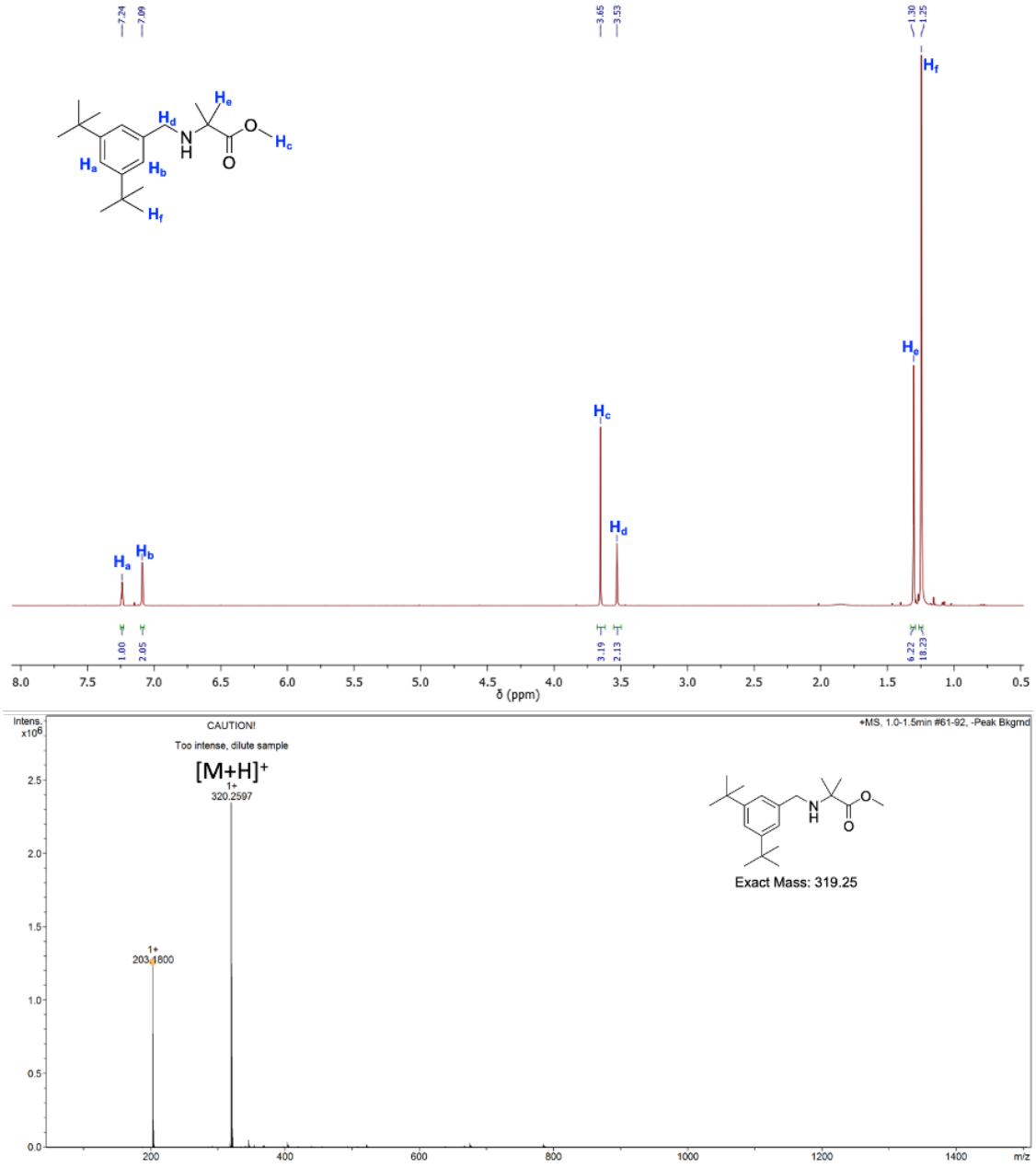

Figure 2.34 (top) ^{1}H NMR (400 MHz, $CDCl_3$, δ, ppm) spectrum of **ME2**; (bottom) LC-MS data of **ME2** shows $[M+H]^+$ peak with m/z = 320.25.

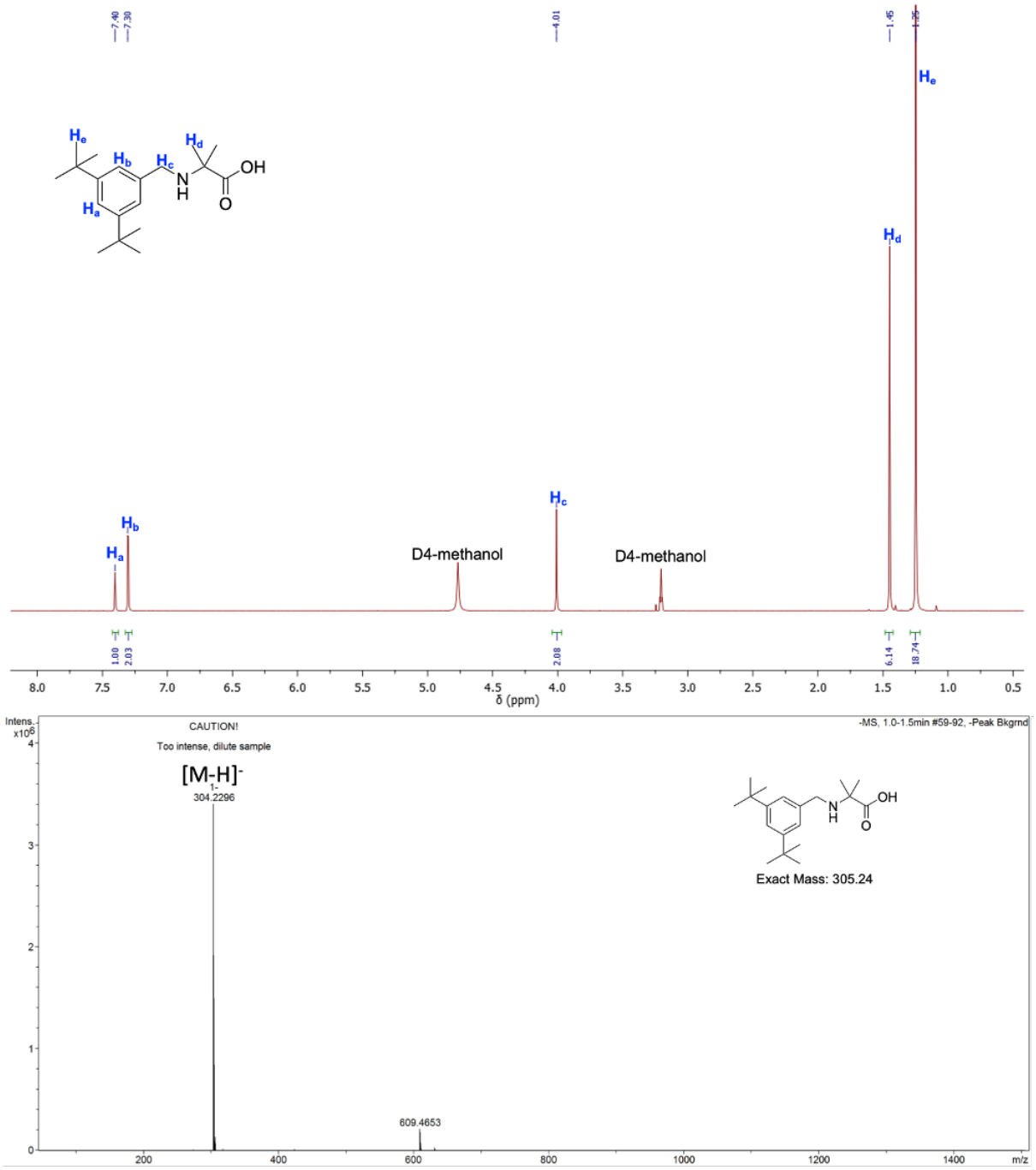

Figure 2.35 (top) ^{1}H NMR (400 MHz, D4-methanol, *δ*, ppm) spectrum of **AA2**; (bottom) LC-MS data of **AA2** shows $[M-H]^-$ peak with m/z = 304.22.

2.3.2.3 Synthesis of N-((3,5-di-tertbutylphenyl)methyl)-4,4,4,4',4',4'-DL-valine, AA3

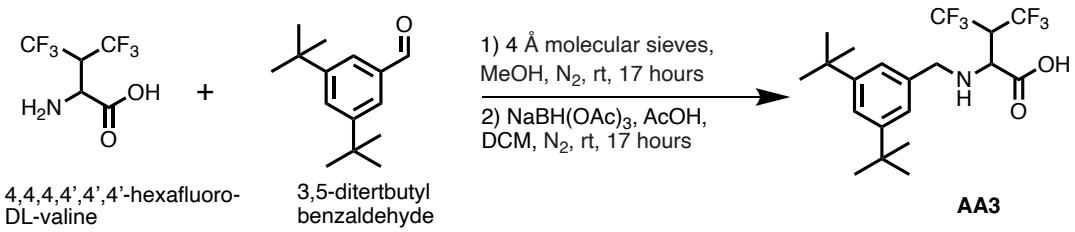

Scheme 2.15 Route to synthesise **AA3**.

As the methyl protected version of the hexafluoro-DL-valine was not commercially available it had to be made. Several reactions were attempted, initially, reaction using hexafluoro valine and thionyl chloride in methanol/DCM was attempted but failed to give the product. Next, TMS-diazomethane, as a commercially available reagent for the methylation of the corresponding carboxylic acid, was used to successfully synthesise the methyl protected hexafluoro valine, which was used directly for the subsequent reductive amination. However, the decomposition of the hexafluoro methyl ester starting material into the carboxylic acid occurred and no product was observed. There are two reasons for the use of methyl esters as the starting material for the reductive amination step in the previous work: i) it improves the poor solubility of the valine molecule in DCM, and ii) it facilitates the purification of the methyl ester product formed from reductive amination via column chromatography. However, as it was not successful in this case, it was decided that was worth attempting to perform the reaction without protecting the carboxylic acid group of the hexafluoro DL valine. To achieve this it was essential to both determine a solvent that can fully dissolve the carboxylic acid and a new purification procedures that can isolate the final amino acid targe molecule, **AA3**. After tests, methanol was used instead of DCM as the solvent

for the reaction. The reaction was monitored by ^{1}H NMR and LC-MS. In the coupling stage, a characteristic imine proton peak with a chemical shift of 8.34 ppm was detected, whilst a peak with m/z = 426.19 was found in the LC-MS data matching the $[imine+H]^{+}$ ion. In the reduction stage, the imine peaks disappeared in the ^{1}H NMR spectrum. At the same time, a peak at m/z = 459.19 was observed, which was proposed to correspond to the $[\mathbf{AA3}+Na]^{+}$ ion. The reaction mixture was then adjusted to pH = 6.7 using $NaHCO_3$ (1M) to quench the excess $NaBH(OAc)_3$ and avoiding the protonation of the amine group in the product. The crude product was precipitated and purified by filtration and by washing with water followed by DCM, giving the pure product in a 45% yield. The formation of **AA3** was proved by NMR spectroscopy and LC-MS spectrometry. In the ^{1}H NMR spectrum, a multiplet at δ = 4.01 ppm corresponding to the methine proton between two trifluoro methyl groups, two doublets at δ = 4.01 and 3.85 ppm corresponding to methylene protons and a doublet at δ = 3.76 ppm corresponding to the methine proton between the amine group and the carboxylic acid group were found as the evidence for the formation of the **AA3**, whilst a characteristic peak at m/z = 426.18 was found in LC-MS data corresponding to the $[\mathbf{AA3}-H]^{-}$ ion. In the ^{19}F NMR spectrum two peaks with δ = -63.22 ppm and -66.11 ppm were found corresponding to the two non-equivalent trifluoro methyl groups.

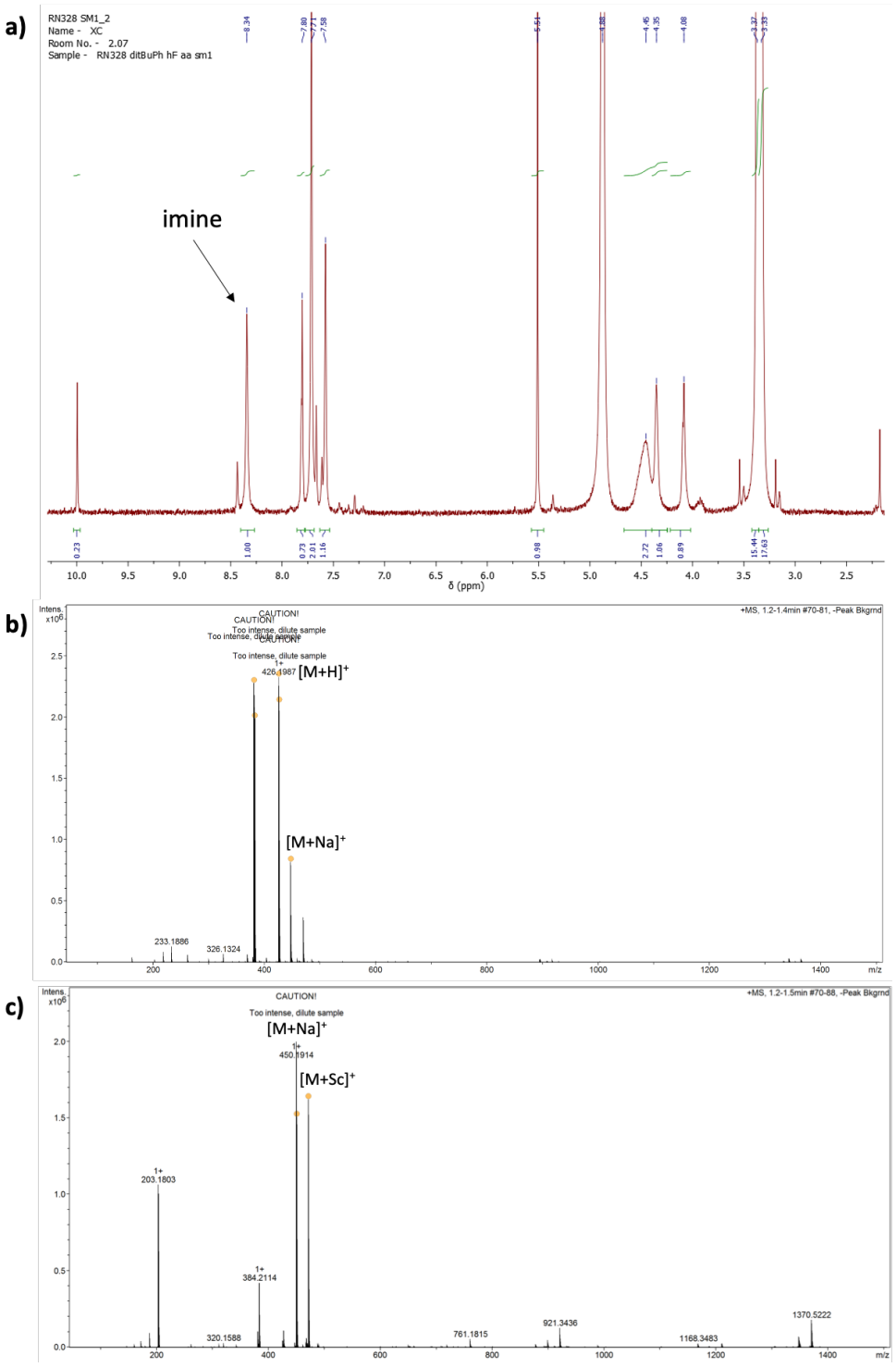

Figure 2.36 Analytical data collected for the reaction mixture used to synthesise **AA3**; a) ^{1}H NMR (400 MHz, D4-methanol, *δ*, ppm) spectrum of the coupling reaction mixture in which the imine peak is observed; LC-MS data of b) the coupling reaction mixture and c) the reduction reaction mixture.

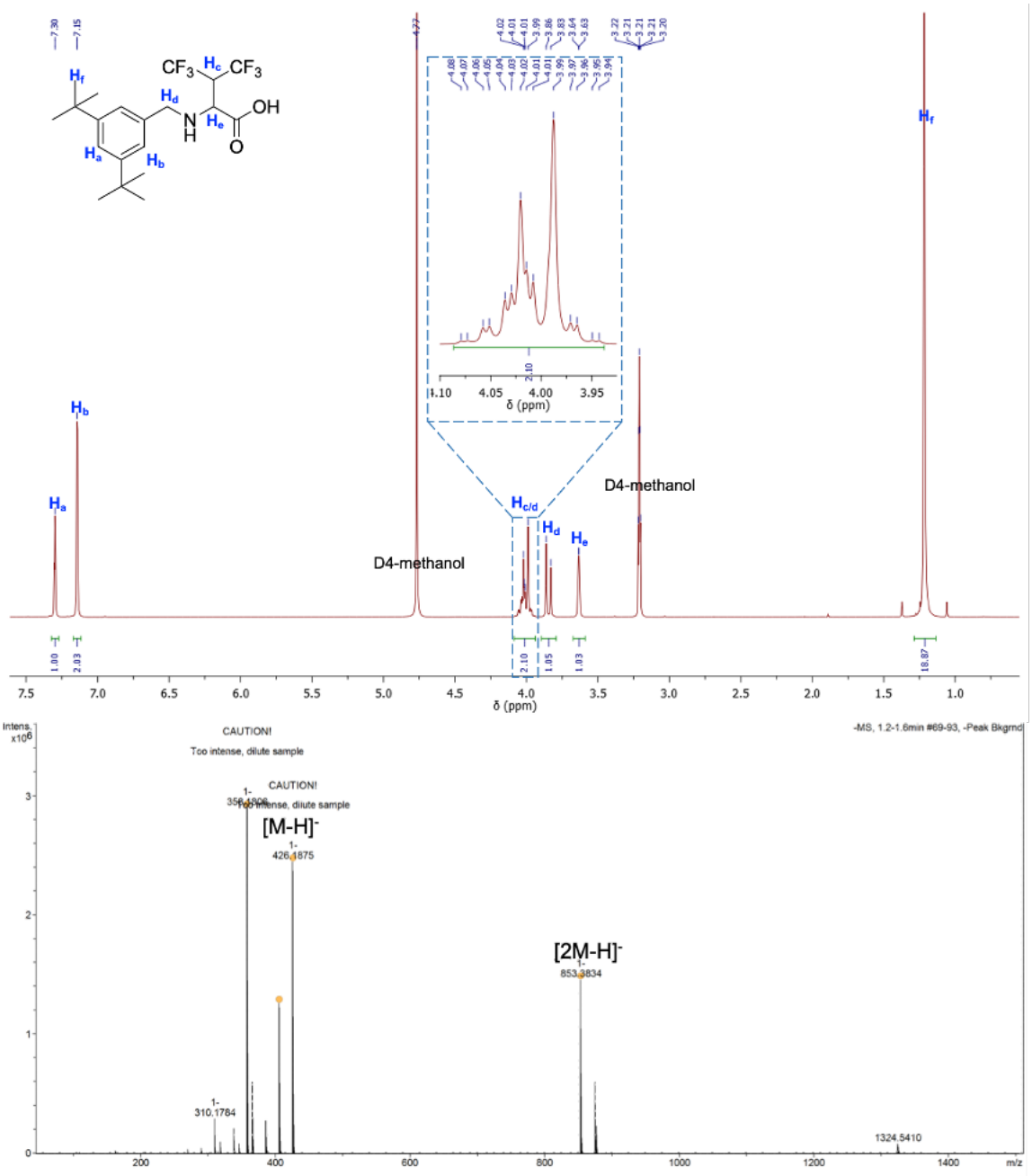

Figure 2.37 (top) ^{1}H NMR (500 MHz, D4-methanol, *δ*, ppm) spectrum of molecule **AA3**; (bottom) LC-MS data of AA3 shows the [M-H]$^{-}$ ion peak with m/z = 426.18.

2.3.2.4 Synthesis of N-((4-Hexylphenyl)methyl)glycine, AA4

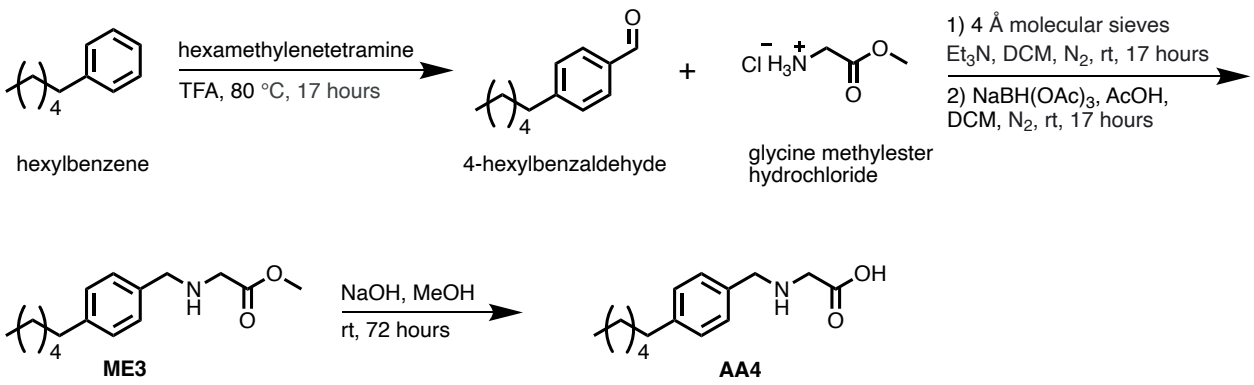

Scheme 2.16 Route to synthesise **AA4**.

Prior to the reductive amination step, the 4-hexylbbenzaldehyde was synthesised using the previously reported procedures. Following the similar procedures to those mentioned above (see Experimental section for full details), **ME3** was successfully synthesised. The product was purified by chromatography (SiO_2, DCM->DCM/methanol v/v 99/1) giving the pure product in a 46% yield. The ^{1}H NMR spectrum shows two diagnostic singlets, interpreted as two methylene groups, were found at δ = 3.75 and 3.40 ppm and a singlet at δ = 3.70 ppm was found corresponding to the ester methyl protons. A peak with m/z = 264.20 was found in LC-MS, which corresponds to the [**ME3**+H]$^+$ ion. Hydrolysis of **ME3** under basic condition was performed to give **AA4** in a 60% yield. Characterisation of **AA4** was carried out by NMR spectroscopy and LC-MS. The peak of the ester methyl proton disappeared in the ^{1}H NMR spectrum, whilst the two peaks of the methylene groups remained. In LC-MS data, a peak at m/z = 276.20 was found corresponding to the [**AA4**-H]$^-$ ion.

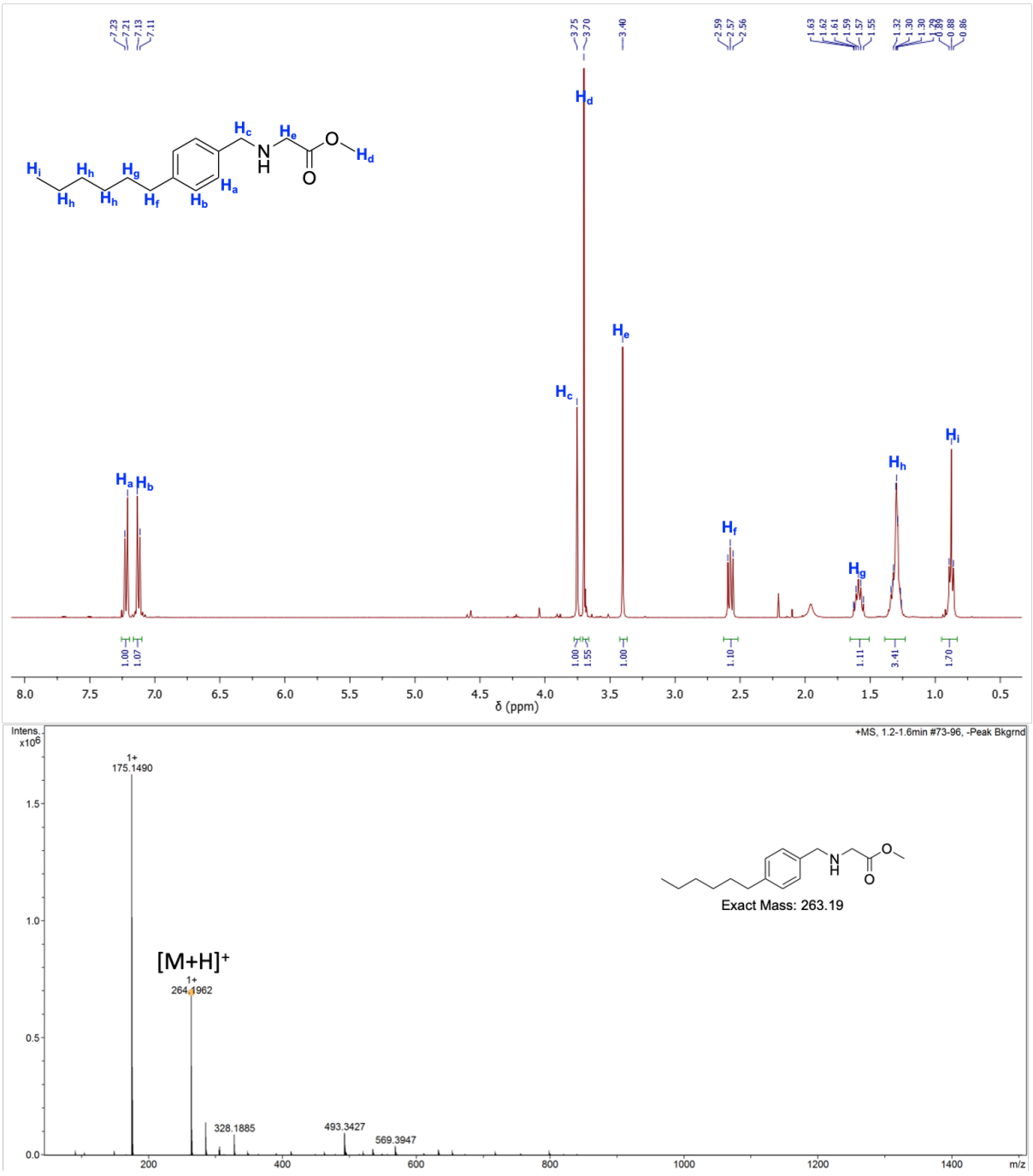

Figure 2.38 (top) ^{1}H NMR (400 MHz, D4-methanol, δ, ppm) spectrum of **ME3**; (bottom) LC-MS data of **ME3** shows the $[M+H]^{+}$ ion peak with m/z = 264.19.

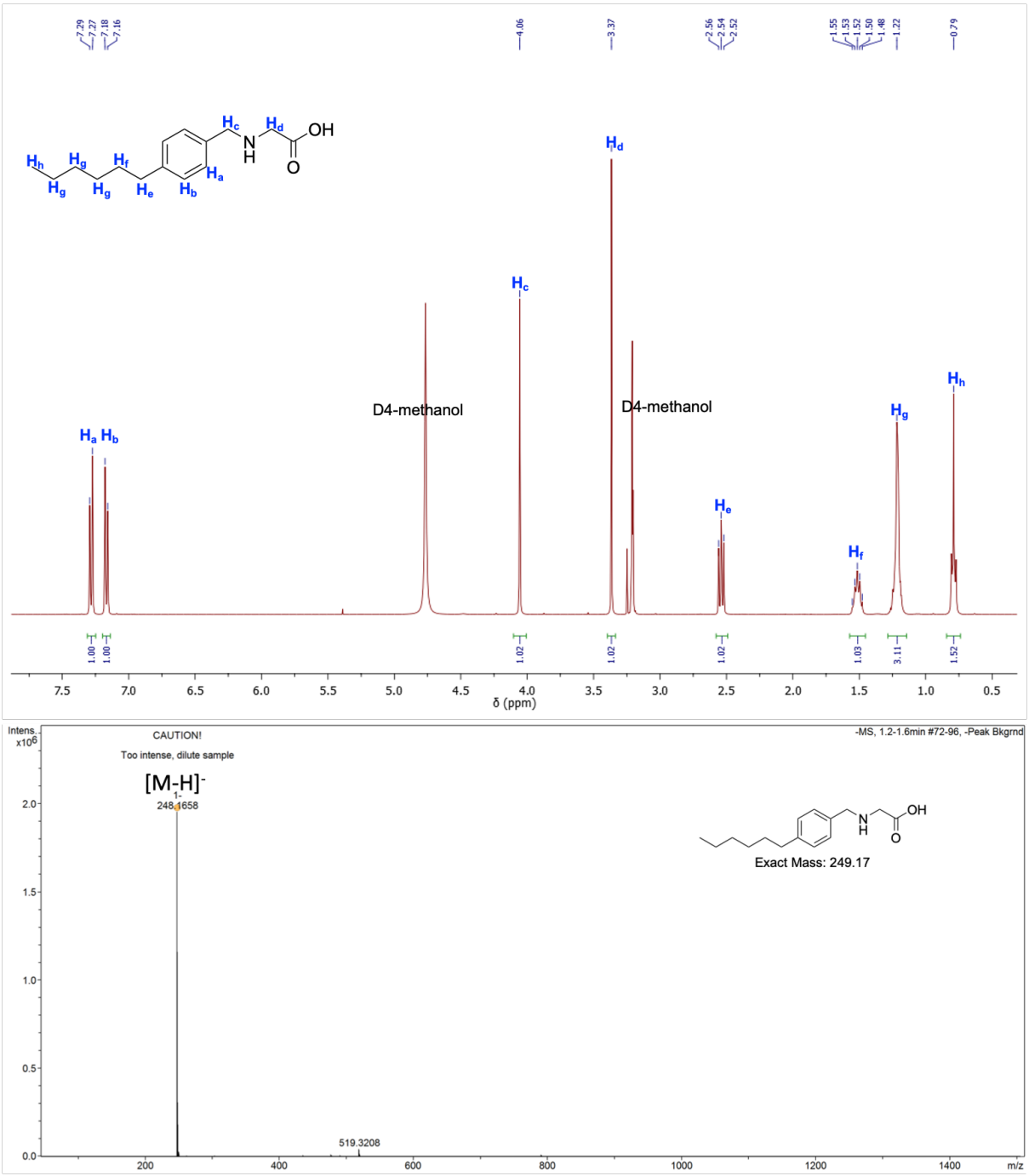

Figure 2.39 (top) ^{1}H NMR (400 MHz, D4-methanol, *δ*, ppm) spectrum of AA4; (bottom) LC-MS data of **AA4** shows the $[M-H]^-$ ion peak with m/z = 248.16.

2.3.2.5 Synthesis of N-((4-Hexylphenyl)methyl)-2,2-dimethyl glycine, AA5

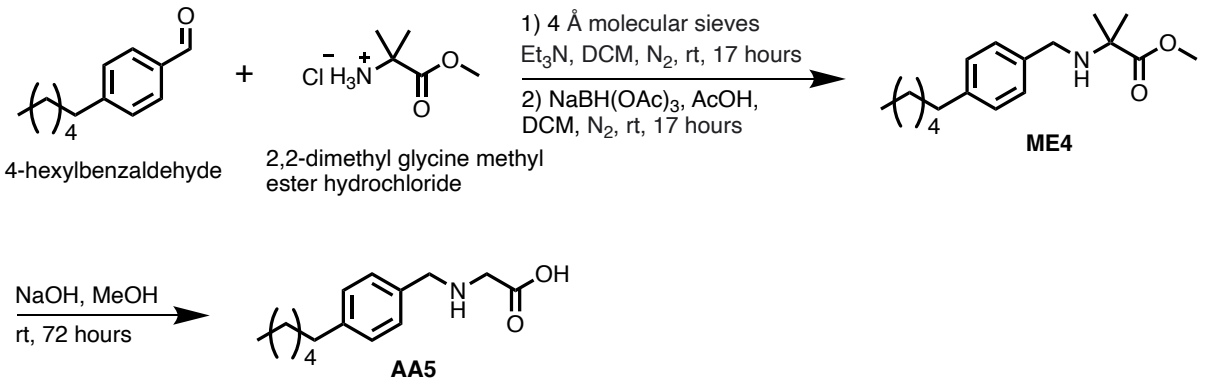

Scheme 2.17 Route to synthesise **AA5**.

ME4 was successfully synthesised via the reductive amination, purified by column chromatography (SiO_2, DCM->DCM/methanol v/v 98/2) giving the pure product in a 43% yield. The NMR spectrum shows a peak from the proton of methylene group at 3.49 ppm, the dimethyl group protons at 1.21 ppm and the ester methyl protons at 3.62 ppm. At the same time a peak with m/z = 292.23 was found in the LC-MS data and taken as the evidence of the formation of **ME4**. Methyl group deprotection yielded **AA5** in a 62% yield. In the ^{1}H NMR spectrum, the peak of the ester methyl protons disappeared, whilst in LC-MS data, a diagnostic peak with m/z = 276.20 matching the value of [**AA5**-H]$^-$ ion was observed.

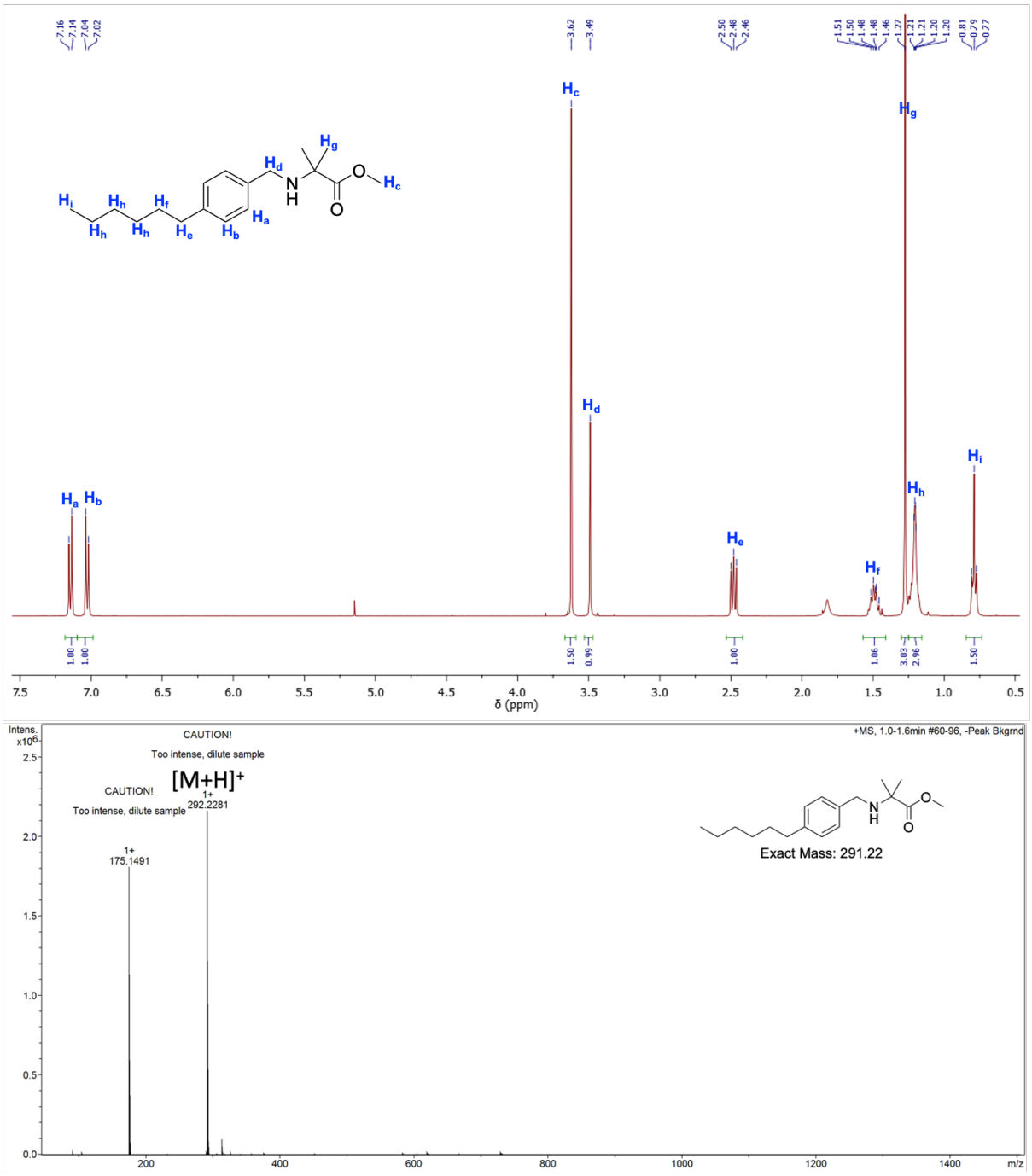

Figure 2.40 (top) ^{1}H NMR (400 MHz, D4-methanol, *δ*, ppm) spectrum of **ME4**; (bottom) LC-MS data of **ME4** shows the [M+H]$^{+}$ ion peak with m/z = 292.22.

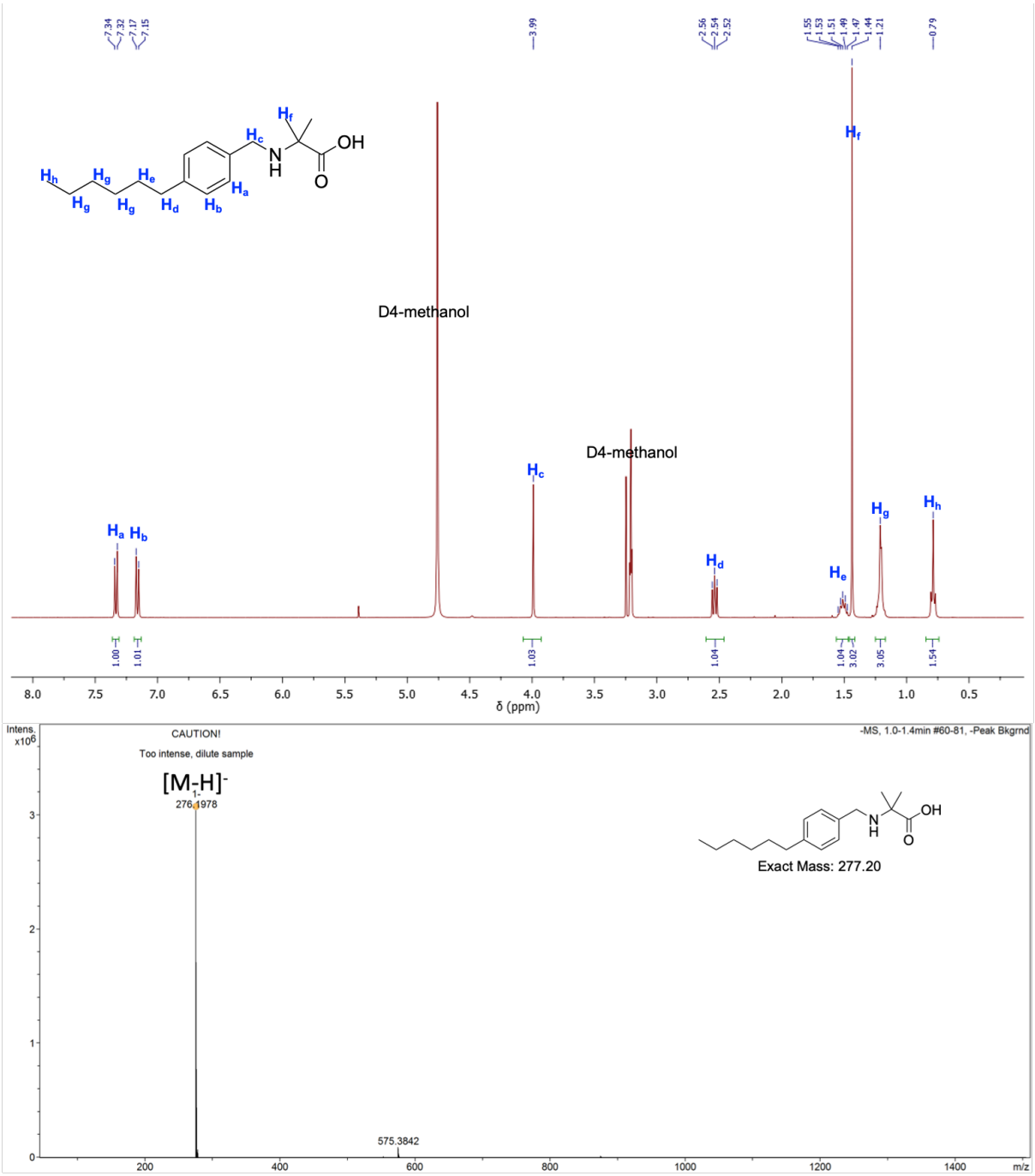

Figure 2.41 (top) ^{1}H NMR (400 MHz, D4-methanol, *δ*, ppm) spectrum of **AA5**; (bottom) LC-MS data of **AA5** shows the $[M-H]^-$ ion peak with m/z = 276.19.

2.3.2.6 Synthesis of N-((4-hexylphenyl)methyl)-4,4,4,4',4',4'-DL-valine, AA6

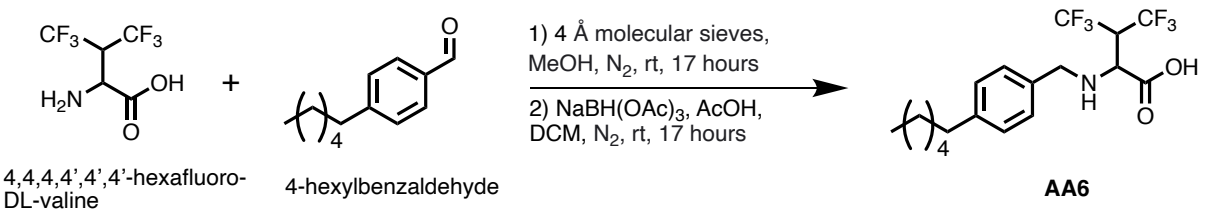

4,4,4,4',4',4'-hexafluoro-DL-valine

4-hexylbenzaldehyde

AA6

Scheme 2.18 Route to synthesise **AA6**.

Using the same procedure, as those used to synthesise **AA3**, **AA6** was synthesised directly via a one pot reaction (see Experimental section for full detials). In the ^{1}H NMR spectrum, a multiplet at δ = 3.99 ppm corresponding to the methine proton between the two trifluoro methyl groups, two doublets at δ = 3.94 and 3.76 ppm corresponding to methylene protons and a doublet at δ = 69 ppm corresponding to methine proton between the amine and carboxylic acid groups were found and taken as the evidence for the formation of the **AA6**. In addition, a characteristic peak with m/z = 398.15 was found in the LC-MS data corresponding to the [**AA6**-H]$^{-}$ ion. In the ^{19}F NMR spectrum two peaks with δ = -63.29 ppm and -66.13 ppm were found corresponding to the two non-equivalent trifluoro methyl groups.

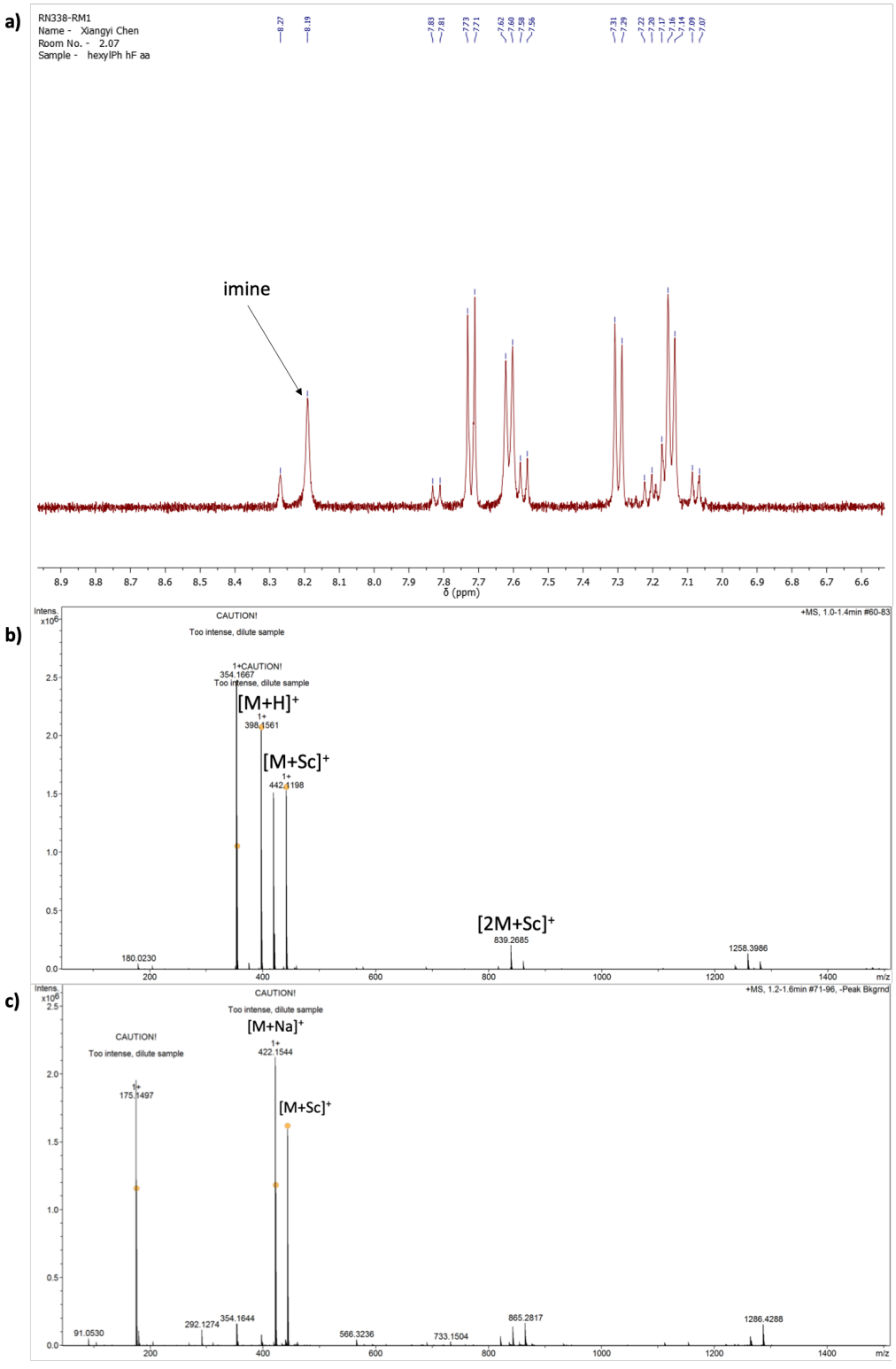

Figure 2.42 Analytical data from the reaction mixture used to synthesise **AA6**; a) ^{1}H NMR (400 MHz, D4-methanol, *δ*, ppm) spectrum of the coupling reaction mixture in which the imine peak was found; LC-MS data of b) the coupling reaction mixture and c) the reduction reaction mixture.

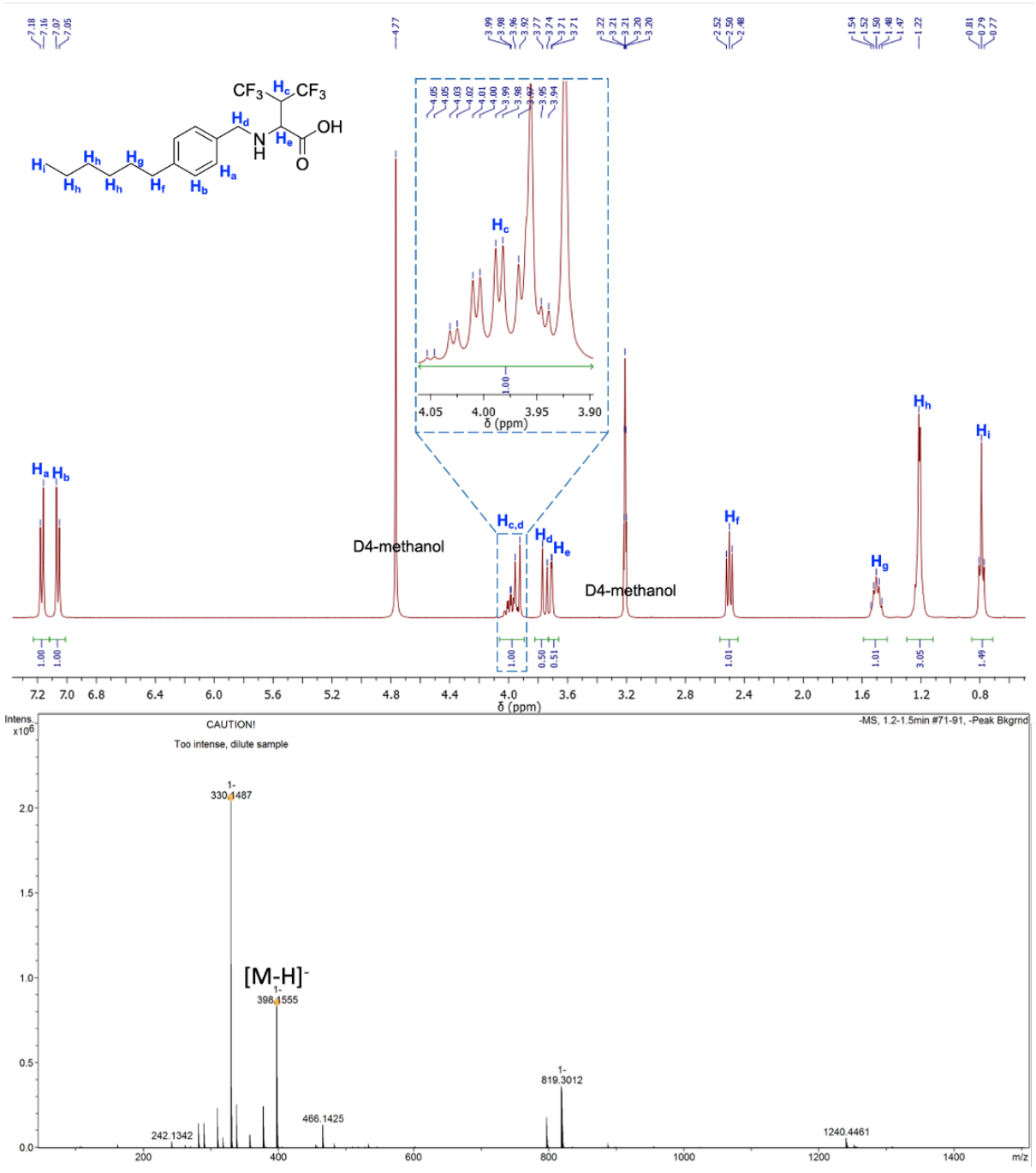

Figure 2.43 (top) ^{1}H NMR (400 MHz, D4-methanol, *δ*, ppm) spectrum of **AA6**; (bottom) LC-MS data of **AA6** shows the $[M-H]^-$ ion peak with m/z = 398.15.

2.3.3 C_{60} charge carriers synthesised via route 2

Table 2.4 Fullerene charge carriers, **5**,**6**,**7** and **8**, synthesised via route 2: one-pot Prato reaction.

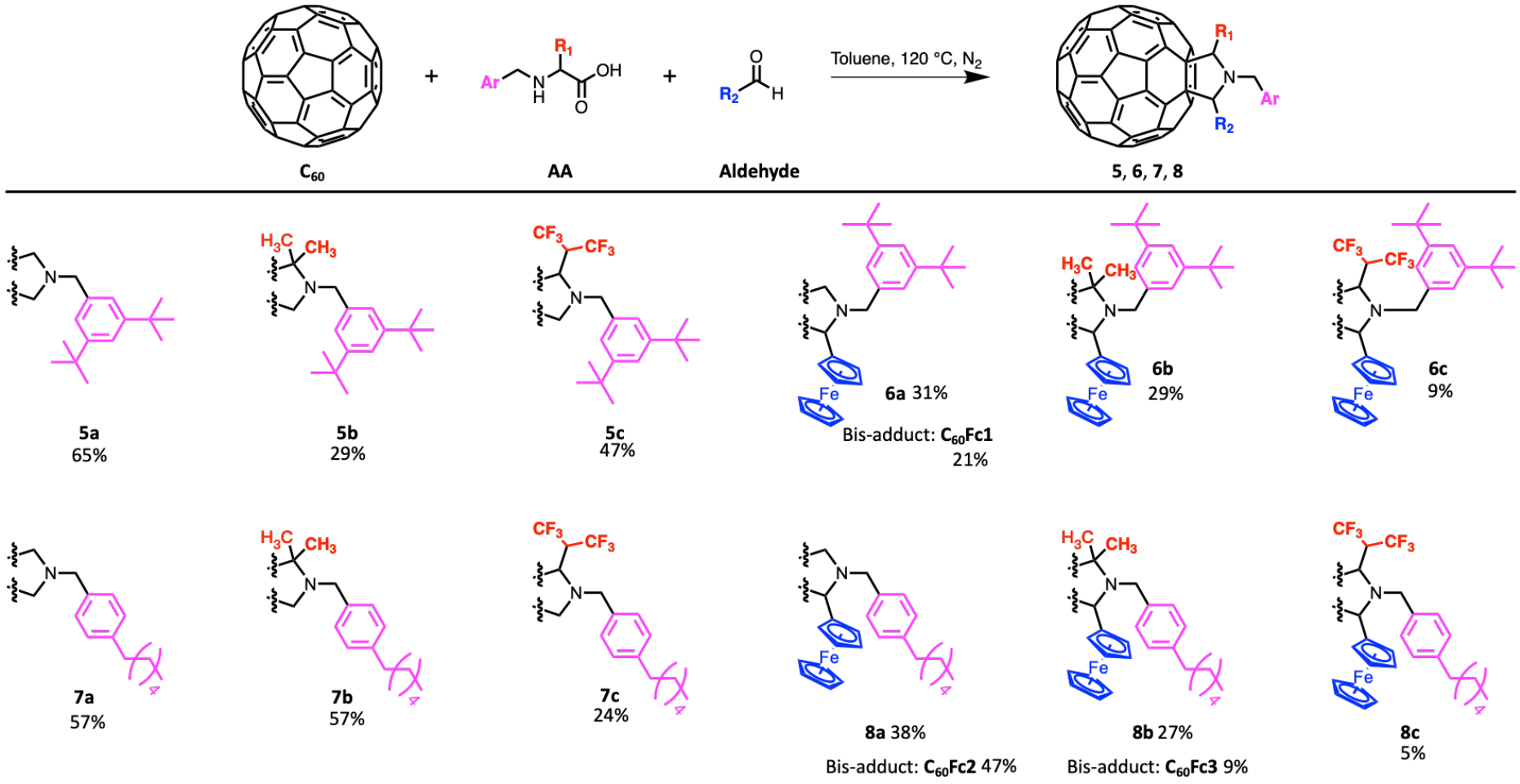

*Reaction time: 4 hours for compound **5**, **7**, **6a**, C_{60}**Fc1**, **8a**, C_{60}**Fc2**; 17 hours for **6b**, **8b**, C_{60}**Fc3**; 24 hours for **6c** and **8c**.

As seen in **Table 2.4**, fullerene derivatives with only solubilising groups, **5** and **7**, and fullerene derivatives with both solubilising groups and ferrocene (electron donating moiety) groups, **6** and **8**, were synthesised synthesised successfully via the synthetic route 2: one-pot Prato reaction. Bis-adducts version of **6a**, **8a** and **8b**, named **C_{60}Fc1**, **C_{60}Fc2** and **C_{60}Fc3** respectively, were also synthesised successfully by using more equivalents of amino acids and aldehydes to C_{60}, which were proposed for RFB cell performance tests due to their good solubility in *o*DCB (see solubility test section). In comparison with the synthetic route 1 that failed to synthesise **4b** and **4c**, molecules, **6b**, **6c**, **8b** and **8c**, with dimethyl or hexafluoro isopropanyl as **R_1**, ferrocene as **R_2** and aromatic N substituents at the same time were synthesised successfully due to the replacement of carbonyl linker between N and aromatic group to methylene. This was concluded that steric hindrance deficiency of methylene linker facilitates the formation of such bulky molecules. All molecules synthesised from synthetic route 2 were characterised by ^{1}H and ^{13}C NMR spectroscopy, MALDI ToF mass scpectroscopy, UV-Vis spectroscopy and FT-IR spectroscopy.

2.3.3.1 Synthesis of N-(3,5-di-tert-butylphenylmethyl)fulleropyrrolidine, 5a.

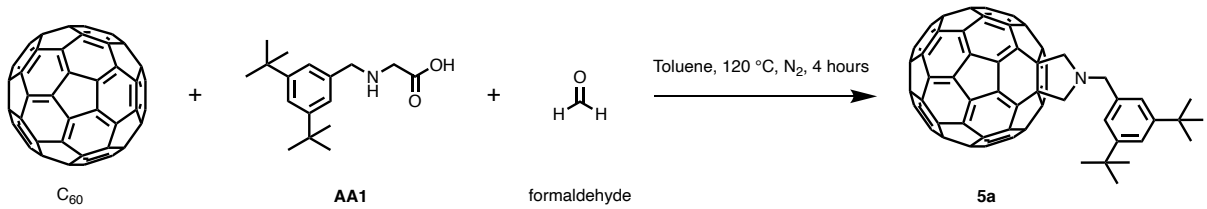

Scheme 2.19 Route to synthesise **5a**.

C_{60}, **AA1** and formaldehyde were used as starting materials to synthesise **5a** under reflux condition for 4 hours in toluene. The reaction mixture was analysed by TLC (toluene), in which a spot with R_f = 0.40 was determined to be **5a**. The reaction mixture was purified by column chromatography (SiO_2, toluene) giving pure product **5a** in a

65% yield. In the ^{1}H NMR spectrum, two singlets at δ = 4.47 and 4.34 ppm were found corresponding to fulleropyrrolidine protons and the protons on methylene linker between N and benzyl groups respectively. MALDI ToF mass spectrometry also provided the evidence for the formation of **5a** with a peak at m/z = 965.39 was found and related to the $[M]^-$ ion of **5a**.

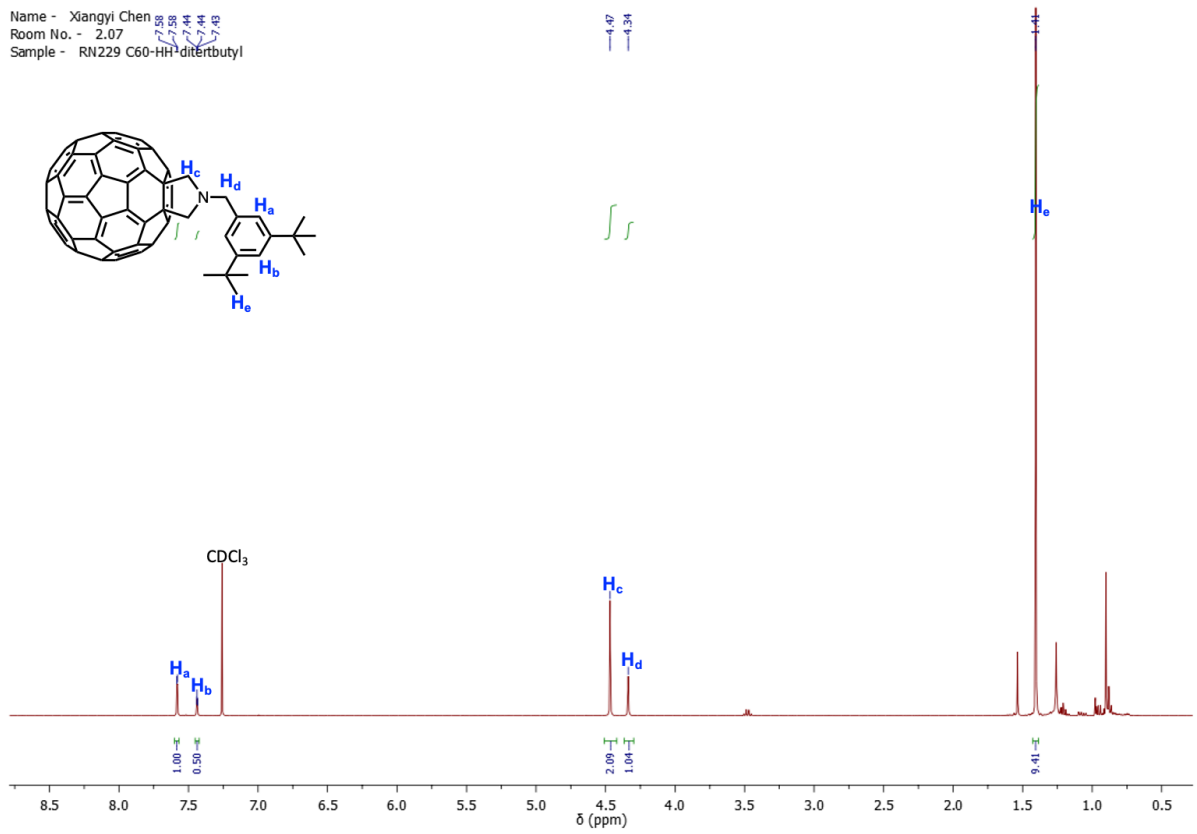

Figure 2.44 ^{1}H NMR (400 MHz, $CDCl_3$, δ, ppm) spectrum of **5a.**

2.3.3.2 Synthesis of N-(3,5-di-tert-butylphenylmethyl)-2,2-dimethyl fulleropyrrolidine, 5b

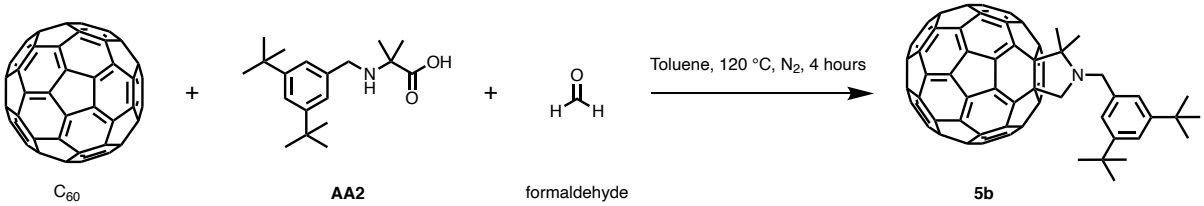

Scheme 2.20 Route to synthesise **5b**.

Using the same conditions to synthesie **5a**, **5b** with dimethyl groups on the pyrrolidine was synthesised using C_{60}, AA2 and formaldehyde as starting materials. The reaction mixture was monitored by TLC (CS_2) with a spot found at a R_f = 0.85, and was subsequently purified by column chromatography (CS_2) giving pure product in a 29% yield. The formation of **5b** was confirmed by ^{1}H NMR spectroscopy and MALDI ToF mass spectrometry. In the ^{1}NMR spectrum, characteristic peaks for the methylene linker at 4.26 ppm, pyrrolidine protons at 4.53 ppm and dimethyl protons at 2.08 ppm were detected. The molecular ion peak at m/z = 993.34 was found in MALDI ToF mass spectrometry data and correlated to the $[M]^-$ ion peak of **5b**.

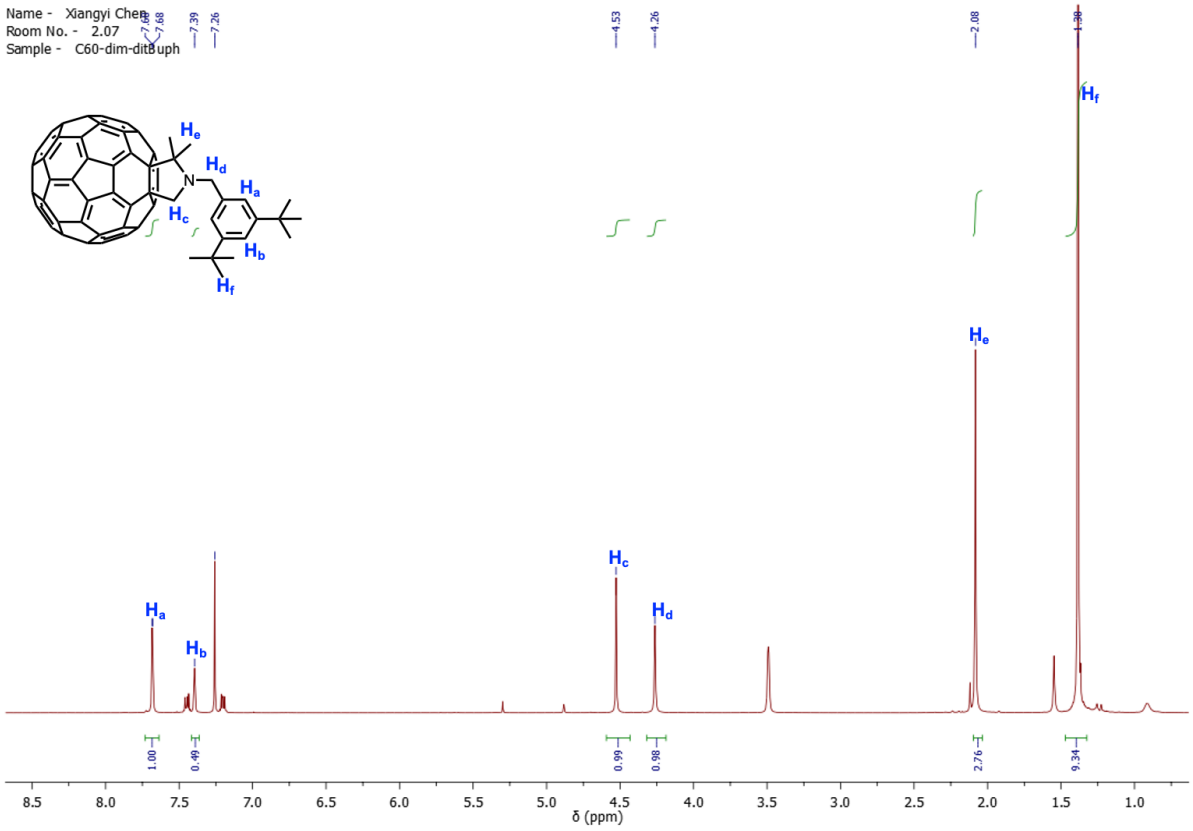

Figure 2.45 ^{1}H NMR (400 MHz, $CDCl_3$, δ, ppm) spectrum of **5b**.

2.3.3.3 Synthesis of N-(3,5-di-tert-butylphenylmethyl)-2-DL-(2,2,2,2',2',2'-hexafluoroisopropyl)fulleropyrrolidine, 5c

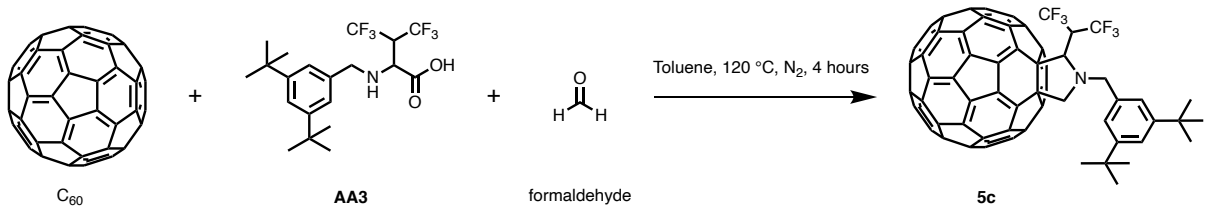

Scheme 2.21 Route to synthesise **5c**.

Following the similar procedures to those mentioned above (see experimental section for full details), **5c** was successfully synthesised. In TLC (CS_2), a new spot with a R_f = was observed and determined to be **5c**. In the ^1H NMR spectrum, a characteristic multipulet at 4.53 ppm corresponding to methine proton between the two trifluoro methyl groups, two doublets at 4.86 and 4.61 ppm corresponding to CH_2 in pyrrolidine and two doublets at 4.96 and 4.56 ppm corresponding to methylene link between N and benzyl groups were found as the evidence of the formation of **5c**. In addition, two peaks with -58.06 ppm and -64.35 ppm were found in the ^{19}F NMR spectrum and were related to the two non-equivalent trifluoro methyl groups. Further evidence for the formation of **5c** was provided by MALDI ToF mass spectrometry, in which a peak at m/z = 1115.09 was found to match the $[M]^-$ ion peak of **5c**.

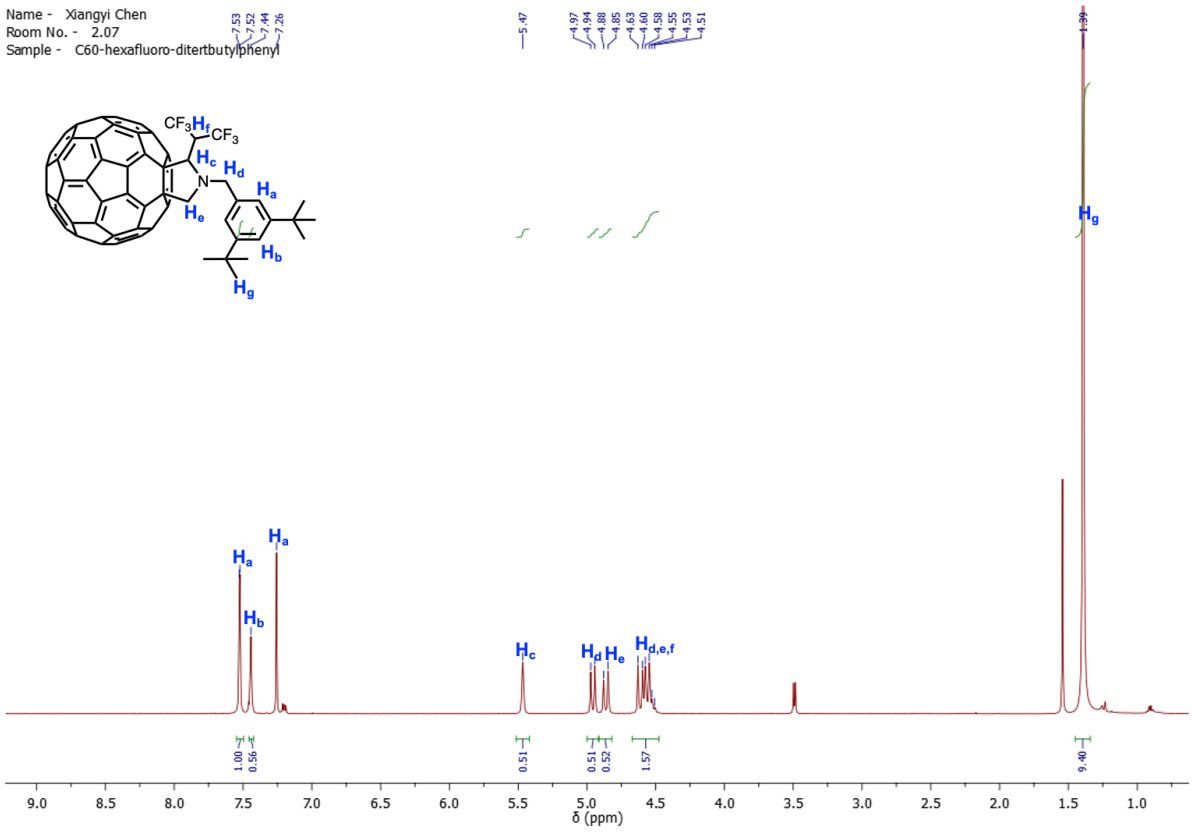

Figure 2.46 ^{1}H NMR (400 MHz, $CDCl_3$, δ, ppm) spectrum of **5c**.

2.3.3.4 Synthesis of N-(3,5-di-tert-butylphenylmethyl)-2-ferrocenyl fulleropyrrolidine, 6a, and corresponding bis-adduct, C60Fc1

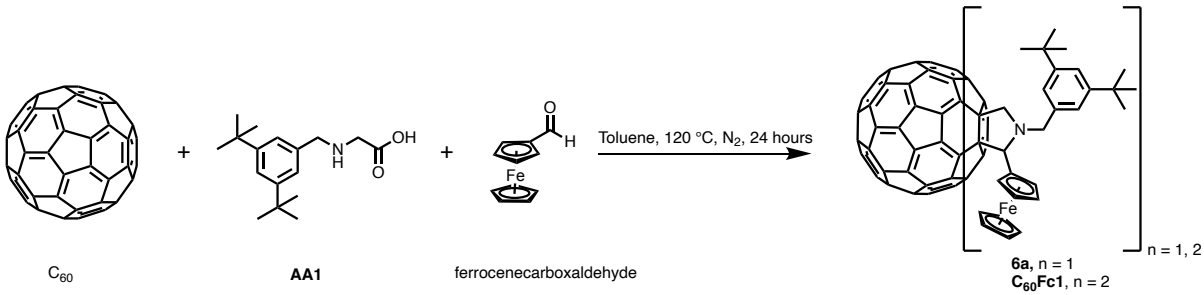

C_{60} **AA1** ferrocenecarboxaldehyde

Scheme 2.22 Route to synthesise 6a, and its corresponding bis-adduct, **C_{60}Fc1**

6a and its bis-adduct **C_{60}Fc1** was reported in the literature. **6a** was proposed to be synthesised for comparing the solubility with the other analogues, whilst **C_{60}Fc1** was

proposed for comparing the cell performance with the other analogues. Following the previously reported procedure, **6a** and its correlated bis-adduct **C_{60}Fc1** were synthesised in a one-pot Prato reaction using C_{60}, **AA1** and ferrocenecarboxaldehyde as starting materials in the equivalent of 1:2:1.2. The reaction mixture was analysed by TLC (CS_2) with two spots found at R_f = and, which were determined to be **6a** and **C_{60}Fc1** respectively, and were subsequently purified by column chromatography (SiO_2) using CS_2 as eluent to give **6a** in a 31% yield then change to CS_2/2%toluene to yield **C_{60}Fc1** in a 21% yield. The ^{1}H NMR spectrum of **6a** shows two doublets at 6.17 and 3.91 ppm interpreted as methylene linker, two doublets at 4.84 and 4.13 ppm interpreted as CH_2 of pyrrolidine and a singlet at 5.23 ppm corresponding to CH of pyrrolidine were found. At the same time, ferrocene peaks at 4.60, 4.33 and 4.26 ppm were also found to confirm the formation of **6a**. The MALDI ToF mass spectrometry data shows a peak with m/z = 1149.12 corresponding to the $[M]^-$ ion of **6a**. Due to the complexity of the fullerene bis-adduct, it is impossible to assign the peak, therefore, it is agreed to use the integral of the protons in different chemical shift region for the characterisation. In the ^{1}H NMR spectrum of **C_{60}Fc1**, the ratio of respective integrations of the aromatic protons, the pyrrolidine with ferrocene and methylene linker protons, and the ditertbutyl protons is [1 / 4.67 / 6], which matches the calculated value of [1 / 4.67 / 6]. MALDI ToF mass spectrometry data also confirmed the formation of the **C_{60}Fc1** by showing a peak at m/z = 1578.85, which matched the $[M]^-$ ion of **C_{60}Fc1**.

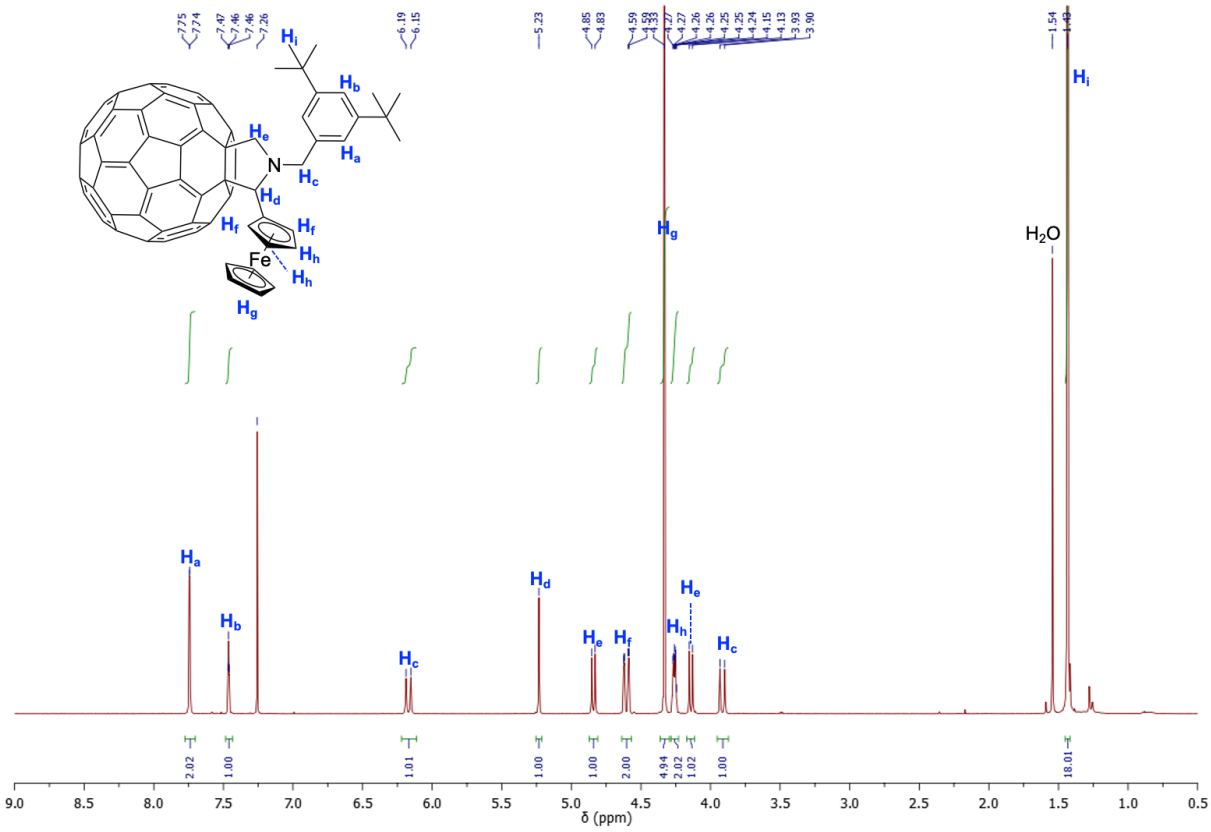

Figure 2.47 ^{1}H NMR (400 MHz, $CDCl_3$, δ, ppm) spectrum of **6a**.

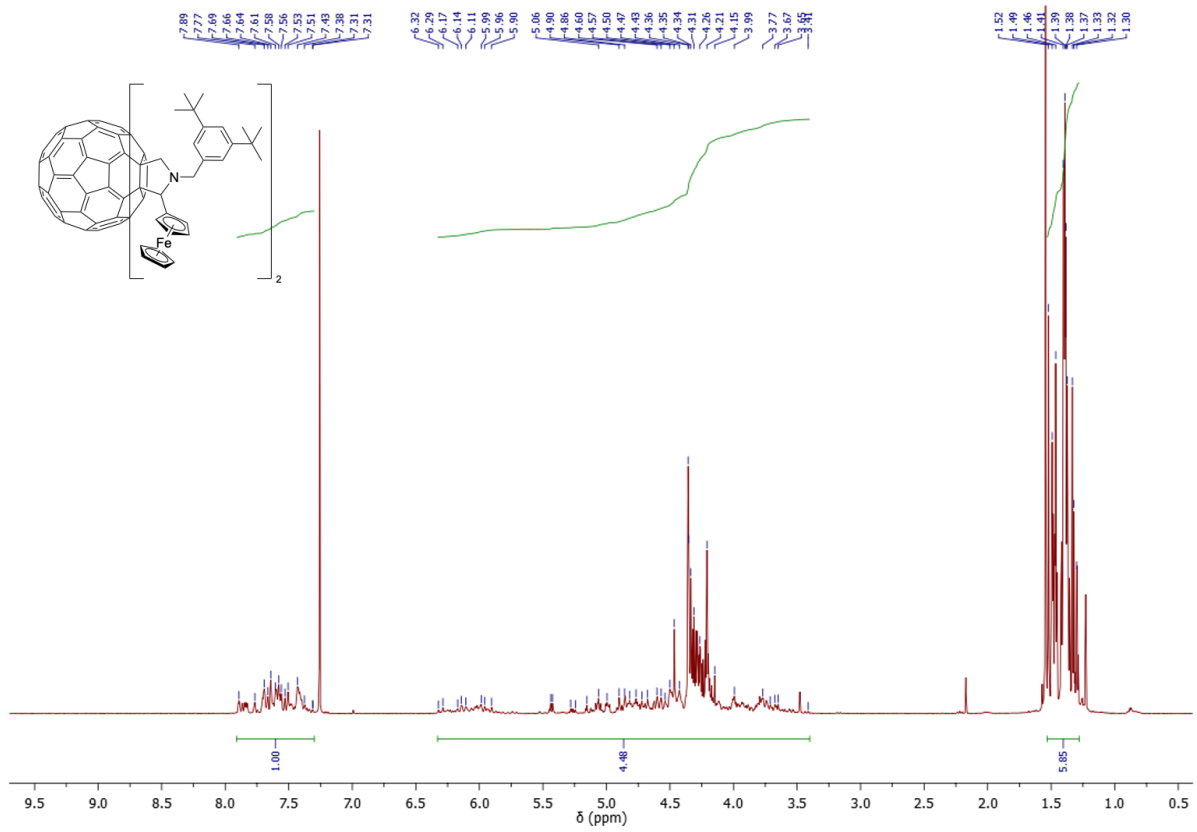

Figure 2.48 ^{1}H NMR (400 MHz, $CDCl_3$, δ, ppm) spectrum of **6a$_{bis}$**.

2.3.3.5 Synthesis of N-(3,5-di-tert-butylphenylmethyl)-2,2-dimethyl-5-ferrocenyl fulleropyrrolidine, 6b

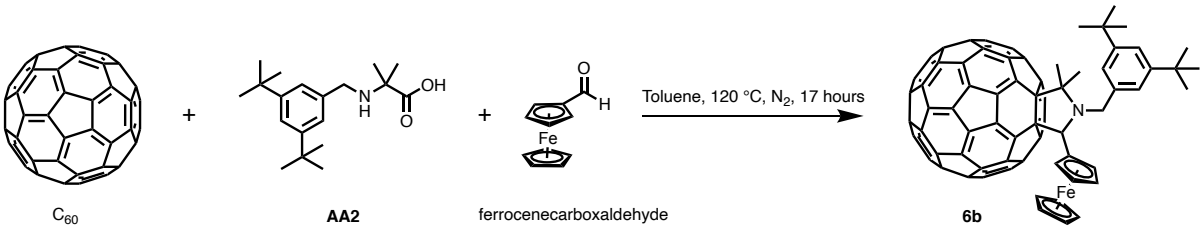

Scheme 2.23 Route to synthesise **6b**.

As seen in **Scheme 2.23**, **6b** was successfully synthesised under the reflux condition in toluene for 17hours, which was monitored by TLC (CS_2) with a new spot found at a R_f = 0.9. The reaction mixture was purifieid by column chromatography (SiO_2, CS_2) yielding **6b** in a 29% yield. In the NMR spectrum, diagnostic doublets at 6.32 and 4.39

ppm corresponding to methylene linker protons, a pyrrolidine methine singlet at 5.78 ppm, a dimethyl singlet at 2.20 ppm were found as the evidence of the formation of the **6b**. The molecular ion peak at m/z= 1177.05 in the MALDI ToF mass spectrometry data was found and correlated to the $[M]^-$ ion of **6b**.

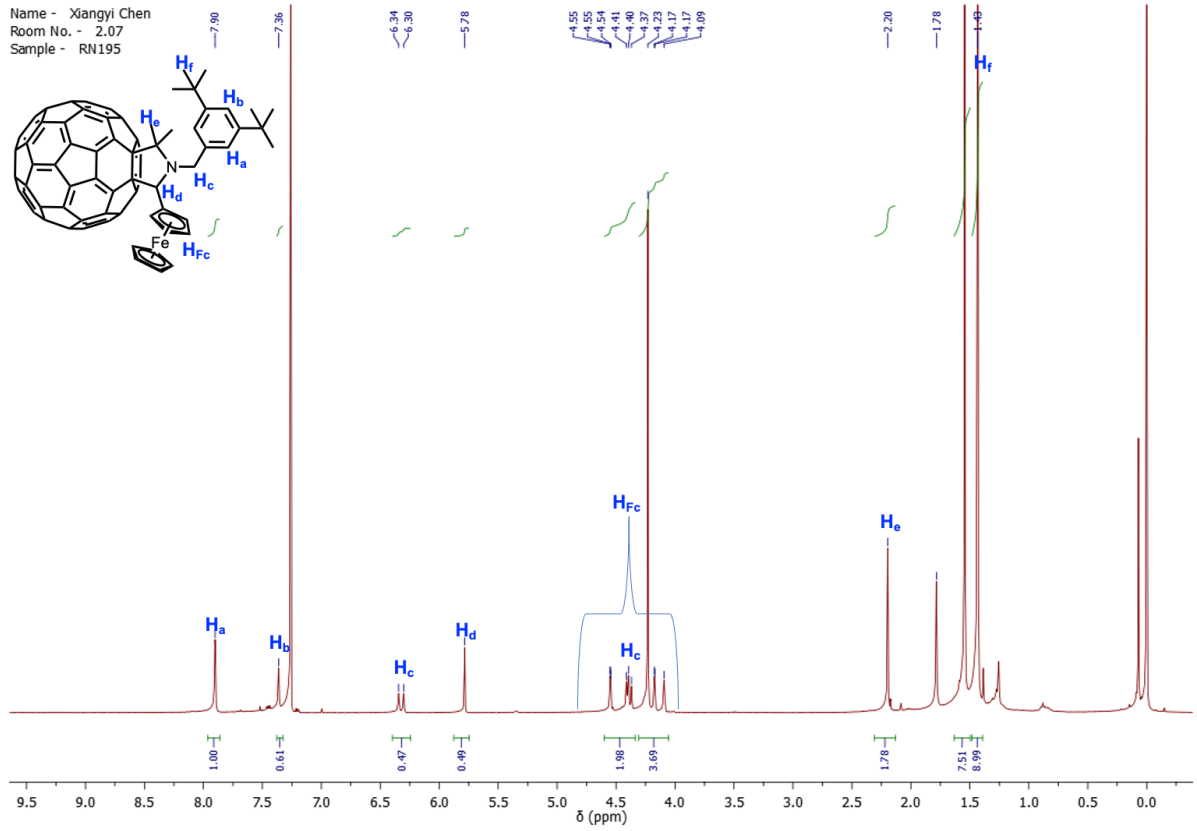

Figure 2.49 ^{1}H NMR (400 MHz, $CDCl_3$, δ, ppm) spectrum of **6b**.

2.3.3.6 Synthesis of N-(3,5-di-tert-butylphenylmethyl)-2-DL-(2,2,2,2',2',2'-hexafluoroisopropyl)-5-ferrocenyl fulleropyrrolidine, 6c

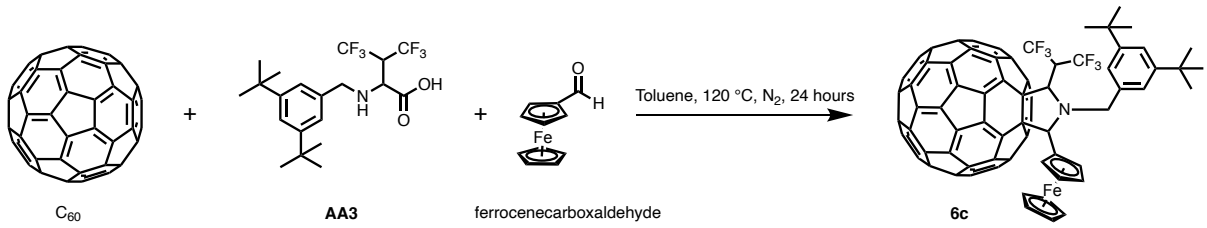

Scheme 2.24 Route to synthesise **6c**.

C_{60}, **AA3** and ferrocenecarboxaldehyde were used as the starting materials to successfully synthesise **6c** via the conditions shown in the **Scheme 2.24**. A new spot at R_f = 0.9 on TLC plate was observed and determined to be **6c**. The reaction mixture was purified by column chromatography (SiO_2, CS_2) giving **6c** in a 9% yield. The formation of the **4b** was confirmed by ^{1}H NMR spectroscopy, in which characteristic peaks for pyrrolidine methine proton next to ferrocene, a singlet at δ = 5.77, methylene linker protons, two doublets at δ = 5.48 and 5.23 ppm, methine proton between two trifluoro methyl groups, a multiplet that overlapped with the ferrocene peaks (δ = 4.42, 4.39 and 4.25 ppm) at δ = 4.36 ppm, and a peak at δ = for methine proton on hexafluoropropanyl side were detected to confirm the formation of **6c**. In the MALDI ToF mass spectrometry data, a peak with m/z = 1299.20 was found and correlated to the $[M]^-$ ion of **6c**.

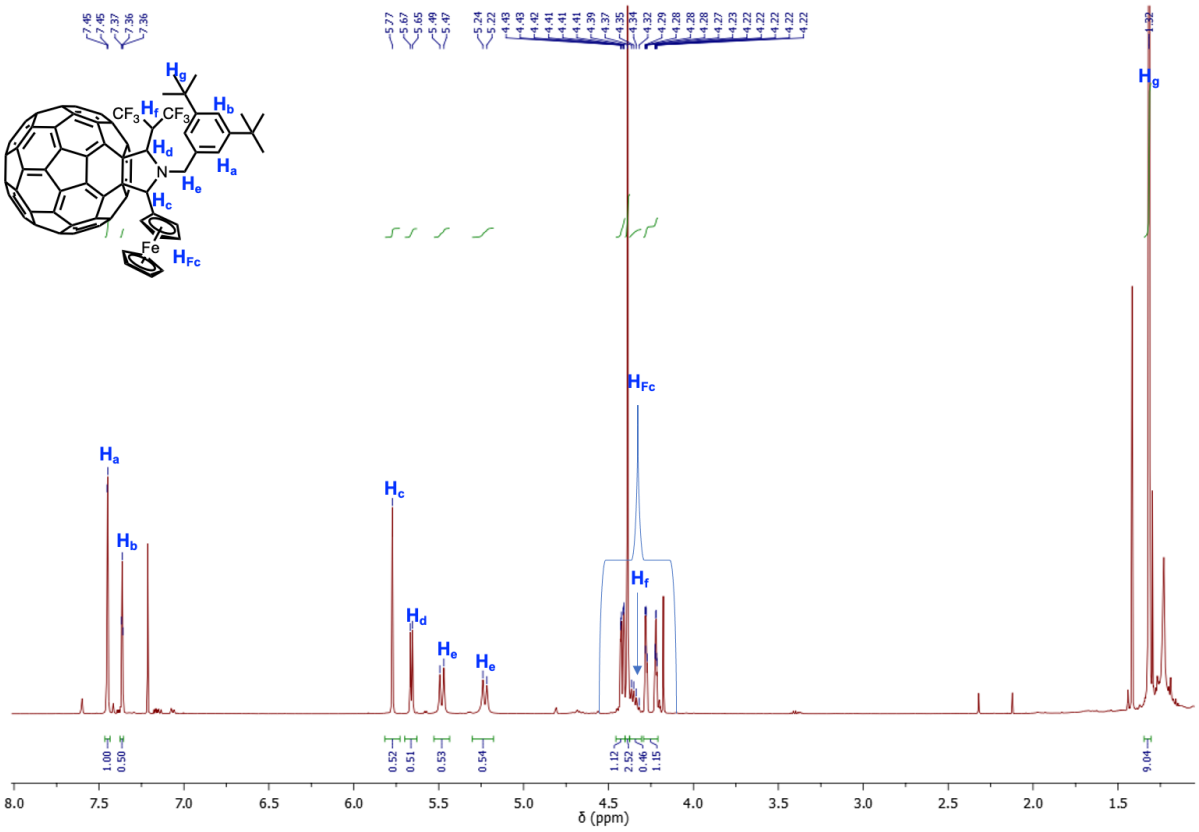

Figure 2.50 ^{1}H NMR (400 MHz, $CDCl_3$, δ, ppm) spectrum of **6c**.

2.3.3.7 Synthesis of N-(4-hexylphenylmethyl)fulleropyrrolidine, 7a

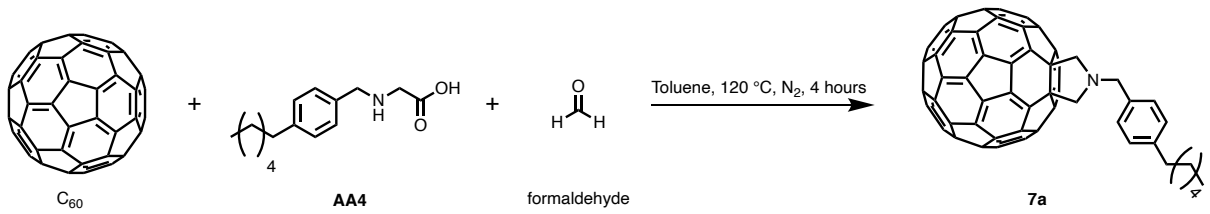

Scheme 2.25 Route to synthesise **7a**.

The reaction mixture used to synthesise **7a** (**Scheme *2.25***) was monitored by TLC (CS_2), a spot found at a R_f = 0.8 The reaction mixture was purified by column chromatography (silica gel, CS_2), giving product in a 57% yield. In the ^1H NMR spectrum, the diagnostic pyrrolidine singlet, δ = 4.43 ppm, and a methylene linker singlet, δ = 4.28 ppm, were detected, which indicated the successful synthesis of **7a**. Evidence for the formation of **7a** was also provided by MALDI ToF mass spectrometry with the peak at m/z = 936.76 corresponding to the $[M]^-$ ion of **7a**.

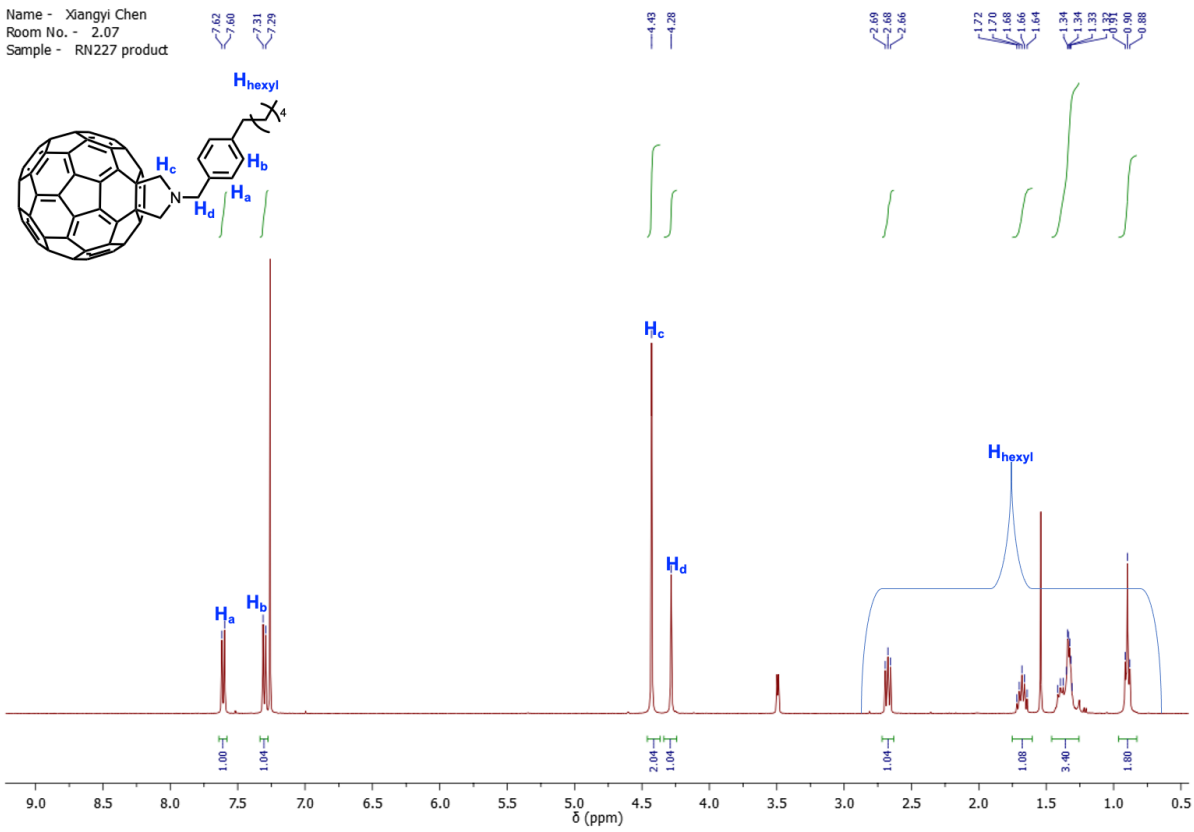

Figure 2.51 ^{1}H NMR (400 MHz, $CDCl_3$, δ, ppm) spectrum of **7a**.

2.3.3.8 Synthesis of N-(4-hexylphenylmethyl)-2,2-dimethyl fulleropyrrolidine, 7b

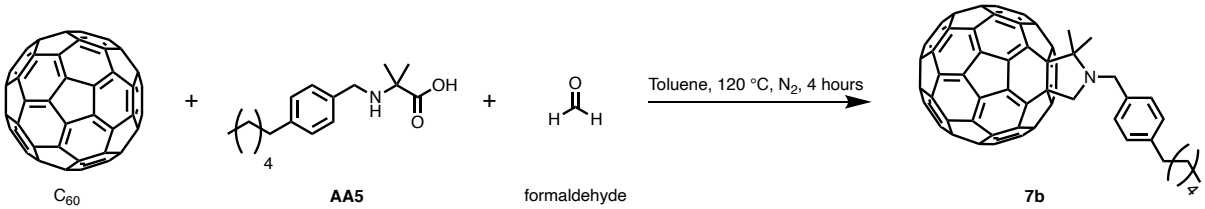

Scheme 2.26 Route to synthesise **7b**.

The reaction mixture used to synthesise **7b** (**Scheme *2.26***) was monitored by diagnostic TLC (CS_2), with a spot on TLC plate appearing at R_f = 0.85. The reaction mixture was purified by silica gel column chromatography (CS_2) to give the material in a 57% yield. The formation of **7b** was confirmed by ^{1}H NMR spectroscopy (**Figure**

2.52) and MALDI-TOF mass spectroscooy. In the ^{1}H NMR spectrum, two characteristic singlets at δ = 4.47 and 4.19 ppm were detected, which were corresponding to the pyrrolidine protons and methylene linker protons, whilst a singlet at δ = 2.07 ppm was also found and correlated to the dimethyl protons. The molecular ion peak at 965.09 m/z in the MALDI ToF mass spectrometry data was found and correlated to the $[M]^{-}$ ion of **7b**.

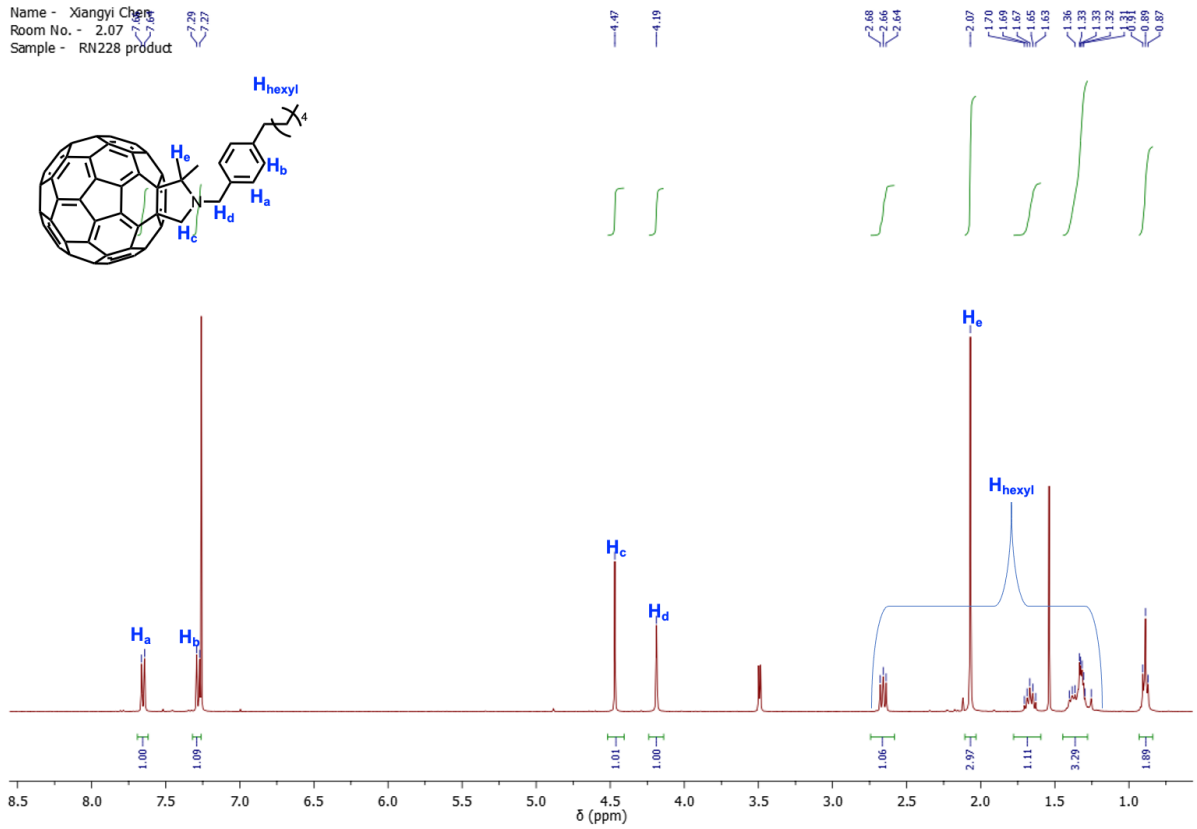

Figure 2.52 ^{1}H NMR (400 MHz, $CDCl_3$, δ, ppm) spectrum of **7b**.

2.3.3.9 Synthesis of N-(4-hexylphenylmethyl)-2-DL-(2,2,2,2',2',2'-hexafluoroisopropyl)fulleropyrrolidine, 7c

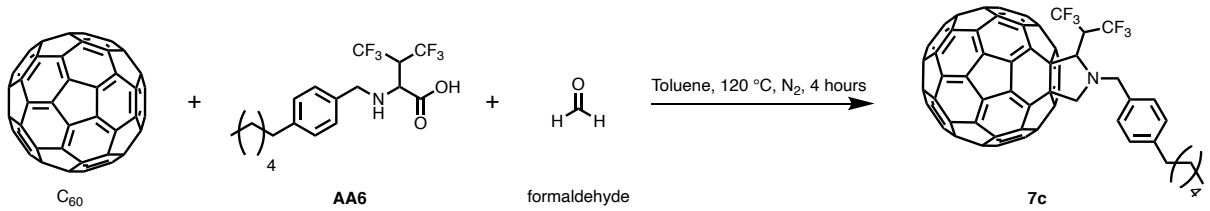

Scheme 2.27 Route to synthesise **7c**.

7c was successfully synthesised via the conditons in **Scheme 2.27**. A spot, corresponding to the formation of **7c**, was observed in TLC with a Rf = 0.9. The reaction mixture was purified by silica gel column chromatography (CS_2), giving **7c** in a 24% yield. The MALDI ToF mass spectrum provides evidence of the formation of **7c**, where a molecular ion peak appears at m/z =1087.31, which was assigned to the [**7c**]$^-$ ion. Due to the existence of the hexafluoroisopropanyl on pyrrolidine carbon, two protons on pyrrolidine CH_2 and methylene linker became non-equivalent, resulting in two set of doublets at δ = 4.87 and 4.42 ppm, and δ = 4.88 and 4.37 ppm respectively in ^{1}H NMR spectrum. In addition, a diagnostic multiplet was also detected at 4.60 ppm, which was corresponded the methine proton of the hexalfuoroisopropanyl.

2.3.3.10 Synthesis of N-(4-hexylphenylmethyl)-2-ferrocenyl fulleropyrrolidine, 8a, and its corresponding bis-adduct, C_{60}Fc2.

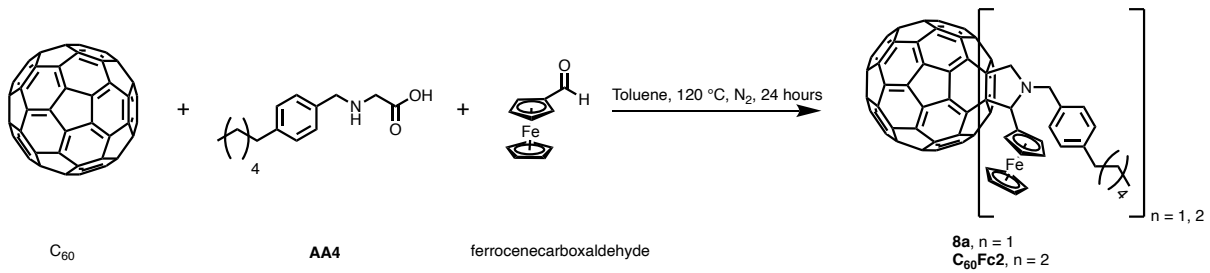

Scheme 2.28 Route to synthesise **8a** and **C_{60}Fc2**.

Following the similar procedures to those mentioned above (see Experimental section for full details), **8a** was successfully synthesised, which was monitored by diagnostic TLC (CS_2), with a spot on TLC plate appearing at R_f = 0.85. ^{1}H NMR spectrum shows two diagnostic doublets, interpreted as the two methylene linker protons, were found at δ = 6.13 and 3.70 ppm and two doublets at δ = 4.74 and 4.04 ppm corresponding to the CH_2 in the pyrrolidine. A peak with m/z = 1121.60 was found in MALDI ToF mass spectrometry data, which corresponded to the [**M**]$^-$ ion of **8a**. And due to the good solubility performance of **8a** in *o*-DCB (see Solubility test section), its bis-adduct was proposed to further expand the solubility in *o*-DCB for conducting RFB cell performance test. Bis-adduct, **C_{60}Fc2**, were synthesised in a one-pot Prato reaction using C_{60}, **AA4** and ferrocenecarboxaldehyde as starting materials in the equivalent of 1:2:1.2. The reaction mixture was analysed by TLC (CS_2) with spots found at R_f = 0.5-0.7 and was determined to be **C_{60}Fc2**, and were subsequently purified by column chromatography (SiO_2, CS_2) yielding **C_{60}Fc2** in a 47% yield. In the ^{1}H NMR spectrum of **C_{60}Fc2**, the ratio of respective integrations of the aromatic protons, the pyrrolidine with ferrocene and methylene linker protons, and the hexyl protons is [1/3.7/3.5], which matches the calculated value of [1 / 3.5 / 3.3]. MALDI ToF mass spectrometry data also confirmed the formation of the **C_{60}Fc2** by showing a peak at m/z = 1522.29, which matched the [M]$^-$ ion of **C_{60}Fc2**.

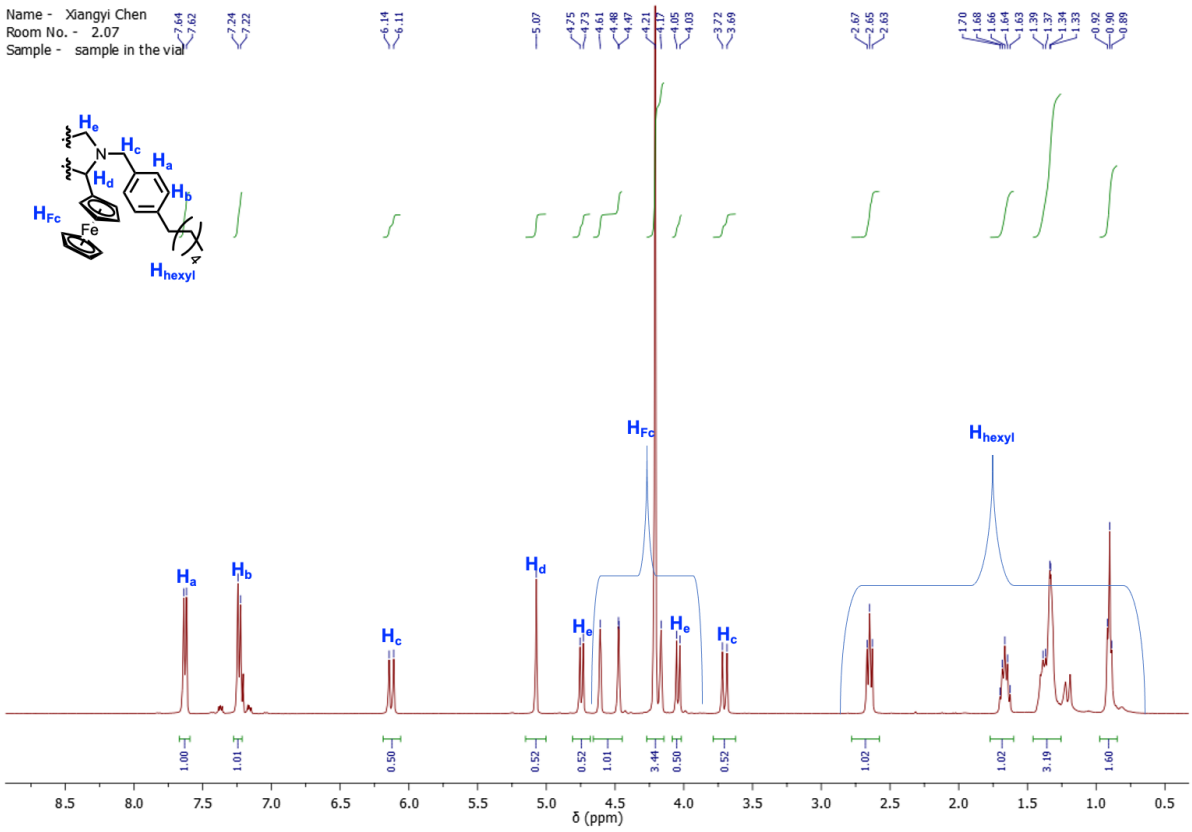

Figure 2.53 ^{1}H NMR (400 MHz, $CDCl_3$, δ, ppm) spectrum of **8a**.

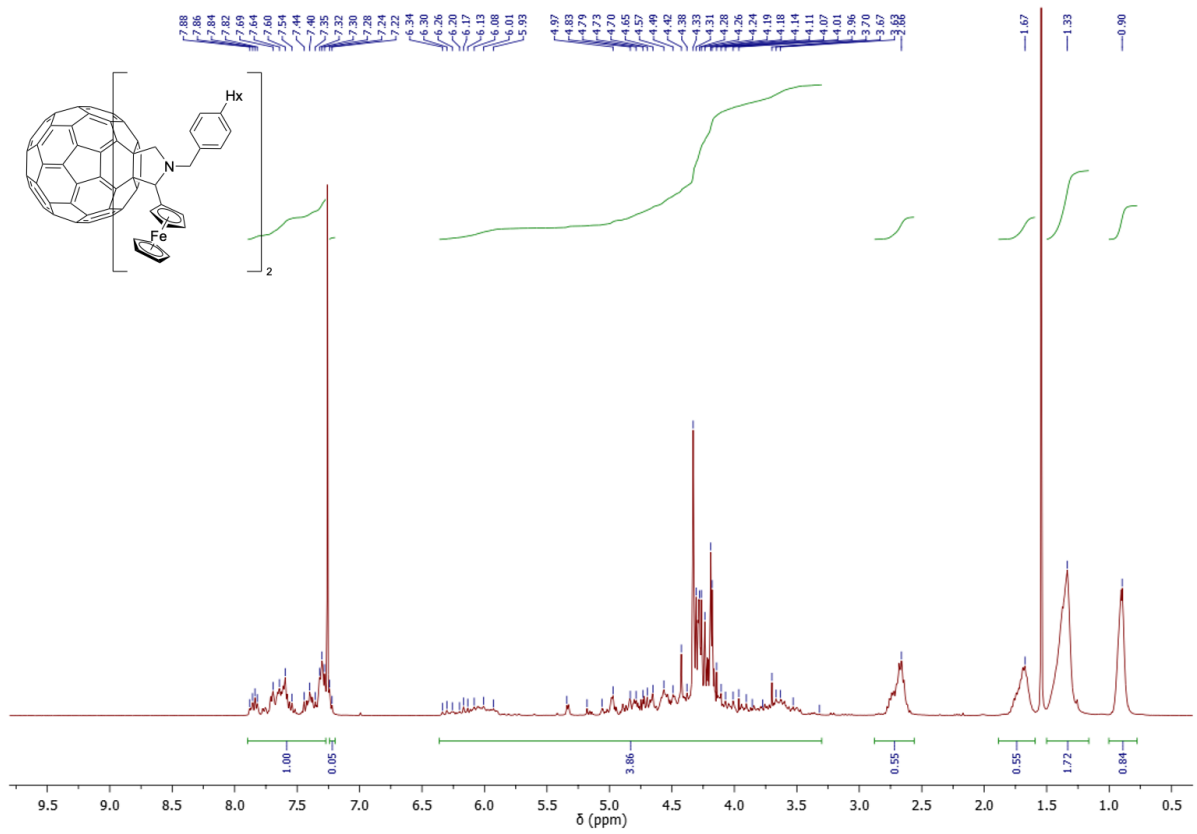

Figure 2.54 ^{1}H NMR (400 MHz, $CDCl_3$, δ, ppm) spectrum of **8a$_{bis}$**.

2.3.3.11 Synthesis of N-(4-hexylphenylmethyl)-2,2-dimethyl-5-ferrocenyl fulleropyrrolidine, 8b, and its corresponding bis-adduct, C60Fc3

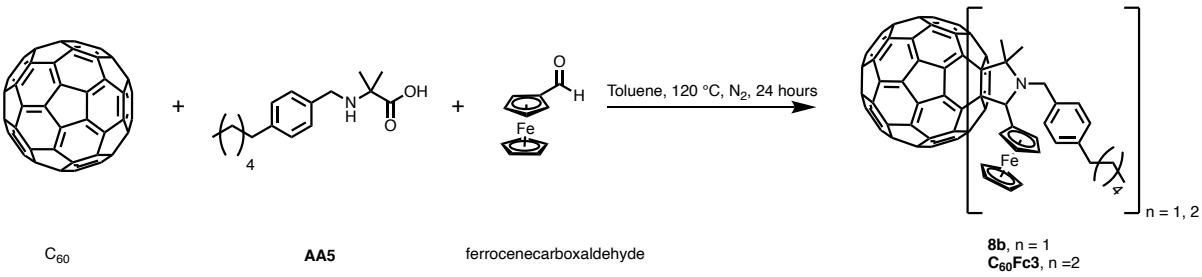

C_{60} **AA5** ferrocenecarboxaldehyde **8b**, n = 1 **C_{60}Fc3**, n =2

Scheme 2.29 Route to synthesise 8b and **C_{60}Fc3**.

8b and its corresponding bis-adduct **C_{60}Fc3** was synthesised following the same procedues of **8b** and **C_{60}Fc3** (see Experimental section for full details). Two spot, corresponding to the formation of **8b** and **C_{60}Fc3**, was observed in TLC (CS_2) with a

Rf = 0.9 and 0.85-0.5 respectively. Column chromatography (SiO_2, CS_2) was used to purify the reaction mixture giving **8b** in a 27% yield and **C_{60}Fc3** in a 9% yield. ^{1}NMR spectroscopy confirmed the formation of **8b**, in which a pyrrolidine singlet at δ = 5.68 ppm, two doublets corresponding to methylene linker at 6.44 and 4.32 ppm and a singlet interpreted as dimethyl group at 2.17 ppm were detected. The MALDI ToF mass spectrometry data shows a peak with m/z = 1149.21 corresponding to the $[M]^-$ ion of **8b**. In the ^{1}H NMR spectrum of **C_{60}Fc3**, the ratio of respective integrations of the aromatic protons, the pyrrolidine with ferrocene and methylene linker protons, and the hexyl protons is [1/2.8/5.5], which matches the calculated value of [1 / 3 / 5.3]. MALDI ToF mass spectrometry data also confirmed the formation of the **C_{60}Fc3** by showing a peak at m/z = 1578.14, which matched the $[M]^-$ ion of **C_{60}Fc3**.

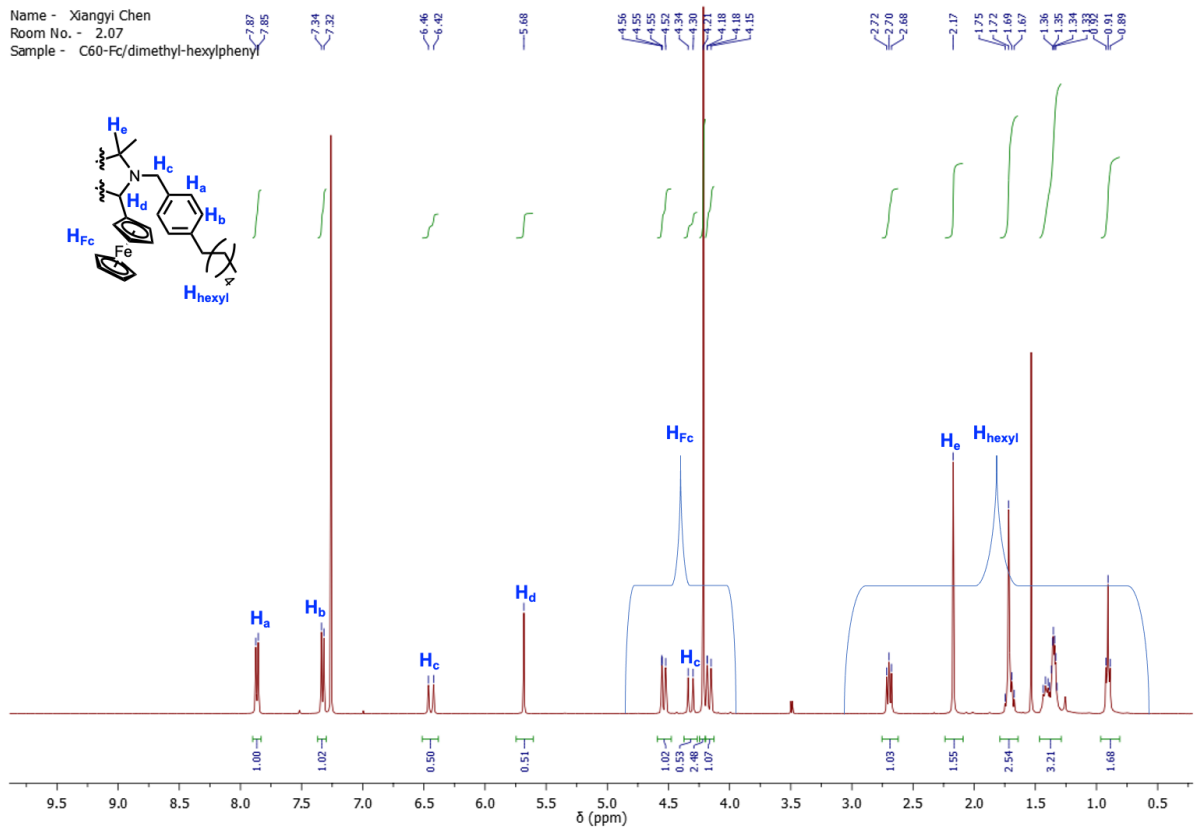

Figure 2.55 ^{1}H NMR (400 MHz, $CDCl_3$, δ, ppm) spectrum of **8b**.

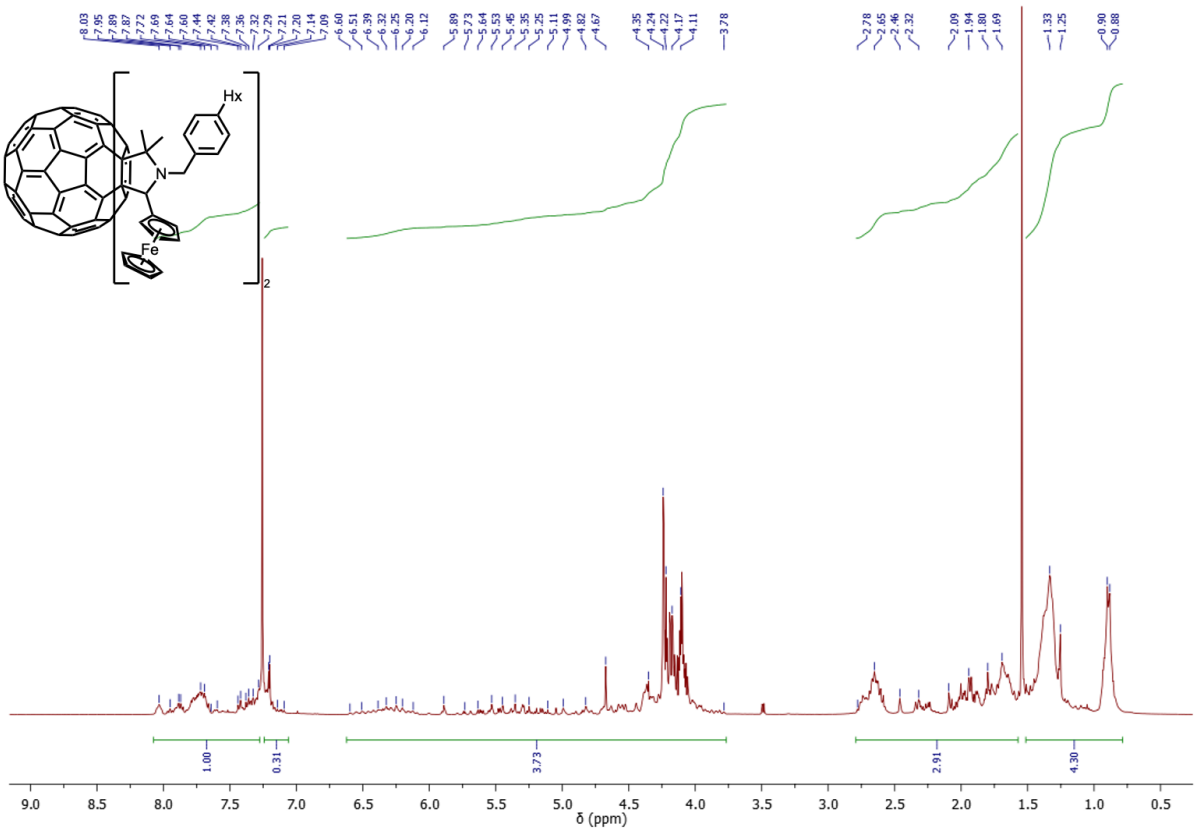

Figure 2.56 ^{1}H NMR (400 MHz, $CDCl_3$, δ, ppm) spectrum of **8b$_{bis}$**.

2.3.3.12 Synthesis of N-(4-hexylphenylmethyl)-2-DL-(2,2,2,2',2',2'-hexafluoroisopropyl)-5-ferrocenyl fulleropyrrolidine, 8c.

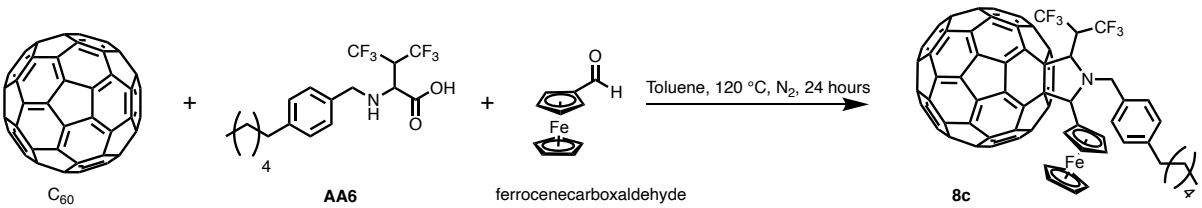

C_{60} **AA6** ferrocenecarboxaldehyde **8c**

Scheme 2.30 Route to synthesise **8c**.

C_{60}, **AA6** and ferrocenecarboxaldehyde were used as the starting materials to successfully synthesise **8c** via the conditions shown in the ***Scheme 2.30***. A new spot

at R_f = 0.9 on TLC plate was observed and determined to be **8c**. The reaction mixture was purified by column chromatography (SiO_2, CS_2) giving **8c** in a 8% yield. The formation of the **8c** was confirmed by ^1H NMR spectroscopy, in which characteristic peaks for pyrrolidine methine proton next to ferrocene, a singlet at δ = 5.84 ppm, methylene linker protons, two doublets at δ = 5.51 and 5.04 ppm, methine proton between two trifluoro methyl groups, a multiplet that overlapped with the ferrocene peak (δ = 4.43, 4.31 and 4.25 ppm) at δ = 4.38 ppm, and a peak at δ = 5.84 ppm for methine proton on hexafluoropropanyl side were detected to confirm the formation of **8c**. In the MALDI ToF mass spectrometry data, a peak with m/z = 1271.26 was found and correlated to the $[M]^-$ ion of **8c**.

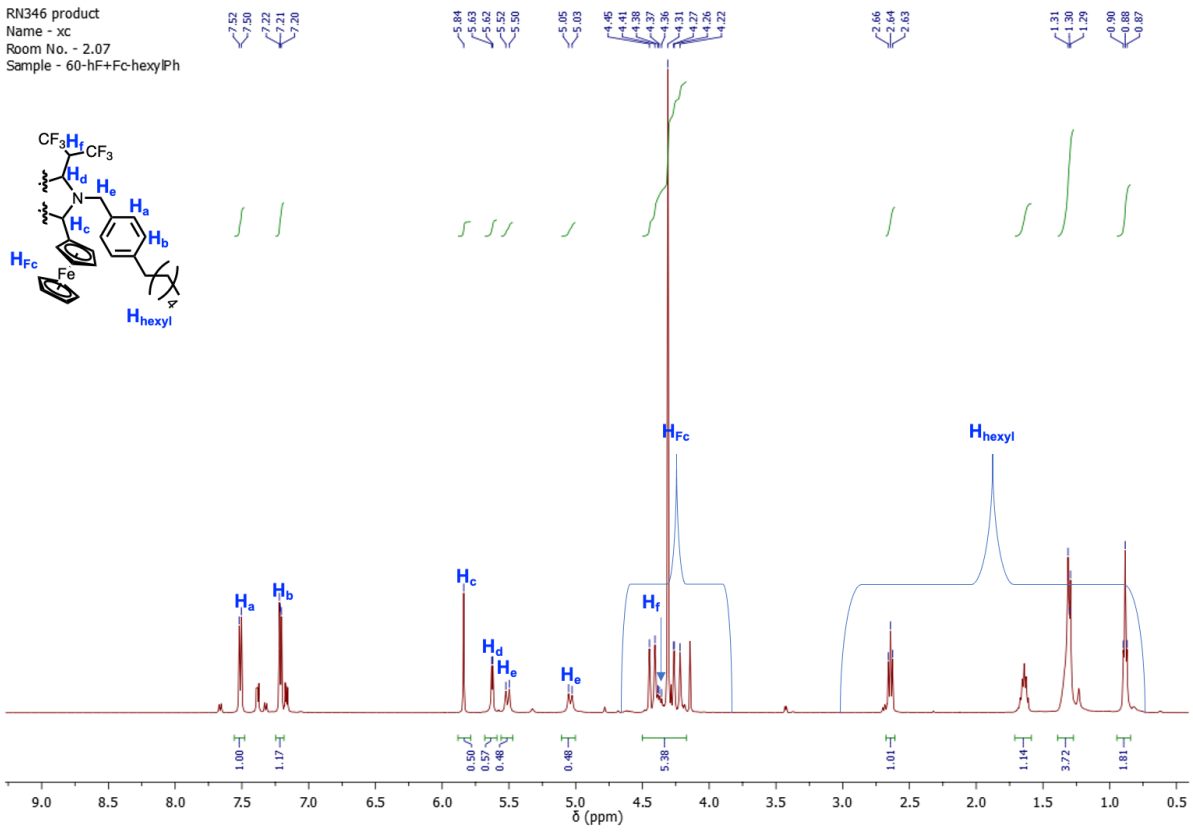

Figure 2.57 ^1H NMR (400 MHz, $CDCl_3$, δ, ppm) spectrum of **8c.**

2.3.4 Solubility Test of C60 derivatives in o-DCB

2.3.4.1 Experimental method

Thoroughly degassed, powdered sample of each fullerene species (~30 mg) was added to o-DCB (~0.05 mL) in a quartz NMR tube cut to 1 cm in length. The resulting mixture was sonicated for 1 hour and placed on a flat surface at room temperature for 24 hours to allow the undissolved solid to settle to the bottom of the tube. An aliquot (0.01 mL) was then carefully taken from the top, liquid layer, and diluted further to with *o*-DCB to a total volume of 5 mL. The solution was analysed by UV-Vis spectroscopy to determine the concentration of the solution using the corresponding calibration curves. The calibration curves were obtained by measuring the absorption of three solutions of known concentrations of the fullerene species in question at 446 nm and 560 nm. The solubilities were then obtained according to the equation below: [27]

$S_{(mg/m)} = (c*M*V)/V_{al}$

In the equation, c is the concentration of then unknown sample, M is the molecular weight of the corresponding compound, V is the volume of the dilution (5 mL); and V_{al} is the volume of the aliquot (0.01 mL). The calibration UV-Vis spectrum and corresponding calibration curve of **C_{60}Fc2** is shown below for illustrative purposes (see **Figure 2.58**).

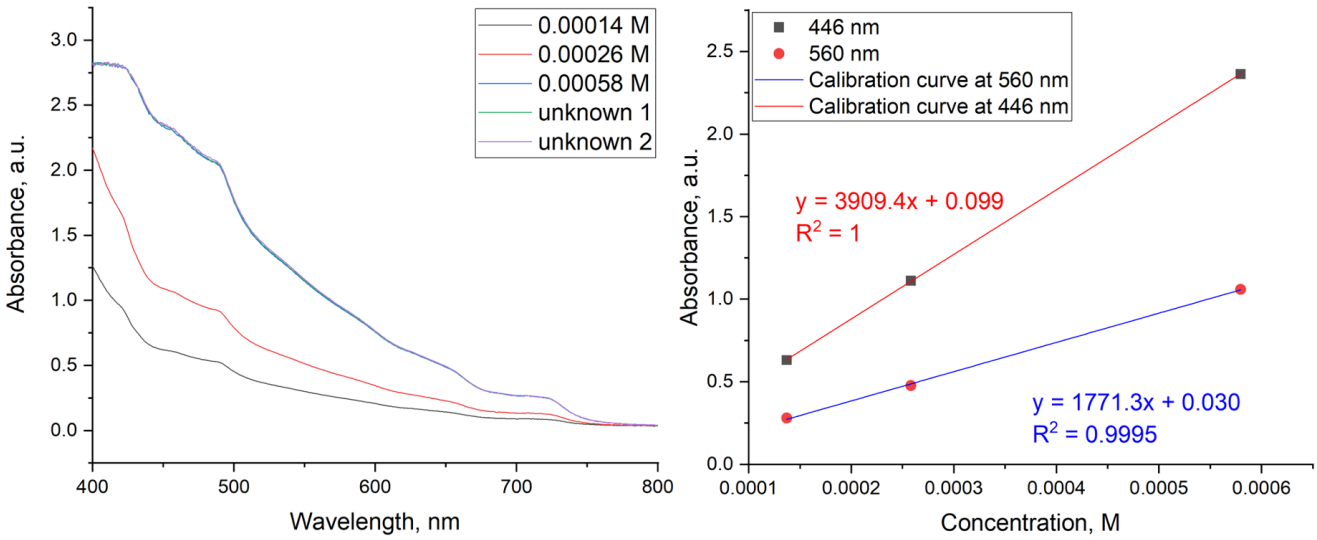

Figure 2.58 (left); UV-Vis absorption spectra of three solutions of known concentrations of **C60Fc2** and two repeat tests of the decanted saturated solution with an unknown concentration in *o*-DCB (right); and the corresponding calibration curve achieved at 446 nm (red line) and 560 nm (blue line).

2.3.4.2 Solubility test results

Table 2.5 Solubility test of fullerene derivatives, **1**-**8** and bis-adduct, **C60Fc1**-**3** in o-DCB and the solubility results from the literature for the tris- and tetrakis-adducts.

Compound	Solubility, mg/mL*	Solubility, mM
1a	--	--
1b	33 ± 1	41.2 ± 1.5
1c	75 ± 4	82.0 ± 4.0
2a	183 ± 17	192.3 ± 18.3
2b	327 ± 19	333.9 ± 19.5
2c	333 ± 0	302.2 ± 0.3
3a	8 ± 1	7.2 ± 0.7
3b	1 ± 1	1.4 ± 0.8
3c	2 ± 0	1.7 ± 0.1
4a	97 ± 11	85.8 ± 10.0
5a	168 ± 14	174.2 ± 14.8

5b	260 ± 15	261.5 ± 15.2
5c	14 ± 1	12.6 ± 1.2
6a	33 ± 2	28.4 ± 1.7
6b	33 ± 6	28.0± 4.9
6c	54 ± 2	41.8 ± 1.5
7a	242 ± 7	258.6 ± 7.2
7b	352 ± 6	364.4 ± 6.3
7c	291 ± 4	267.3 ± 3.4
8a	27 ± 2	23.8 ± 1.4
8b	25 ± 5	21.7 ± 4.8
8c	305 ± 1	239.8 ± 0.9
C_{60}Fc1 (6a$_{bis}$)	399 ± 11	252.4 ± 6.8
C_{60}Fc2 (8a$_{bis}$)	446 ± 3	292.5 ± 1.8
C_{60}Fc3 (8b$_{bis}$)	531 ± 17	335.9 ± 10.6
Ref1 (6a$_{tris}$)	214 ± 31	107.0 ± 15.0
Ref2 (6a$_{tetrakis}$)	300 ± 22	120.0 ± 10.0

* Average of two experiments. The error determined as (S_{max}-S_{min})/2. N. B. We define that the solubility of a species is undetectable when the ≤1 mg of material does not completely dissolve in 5 mL of *o*DCB.

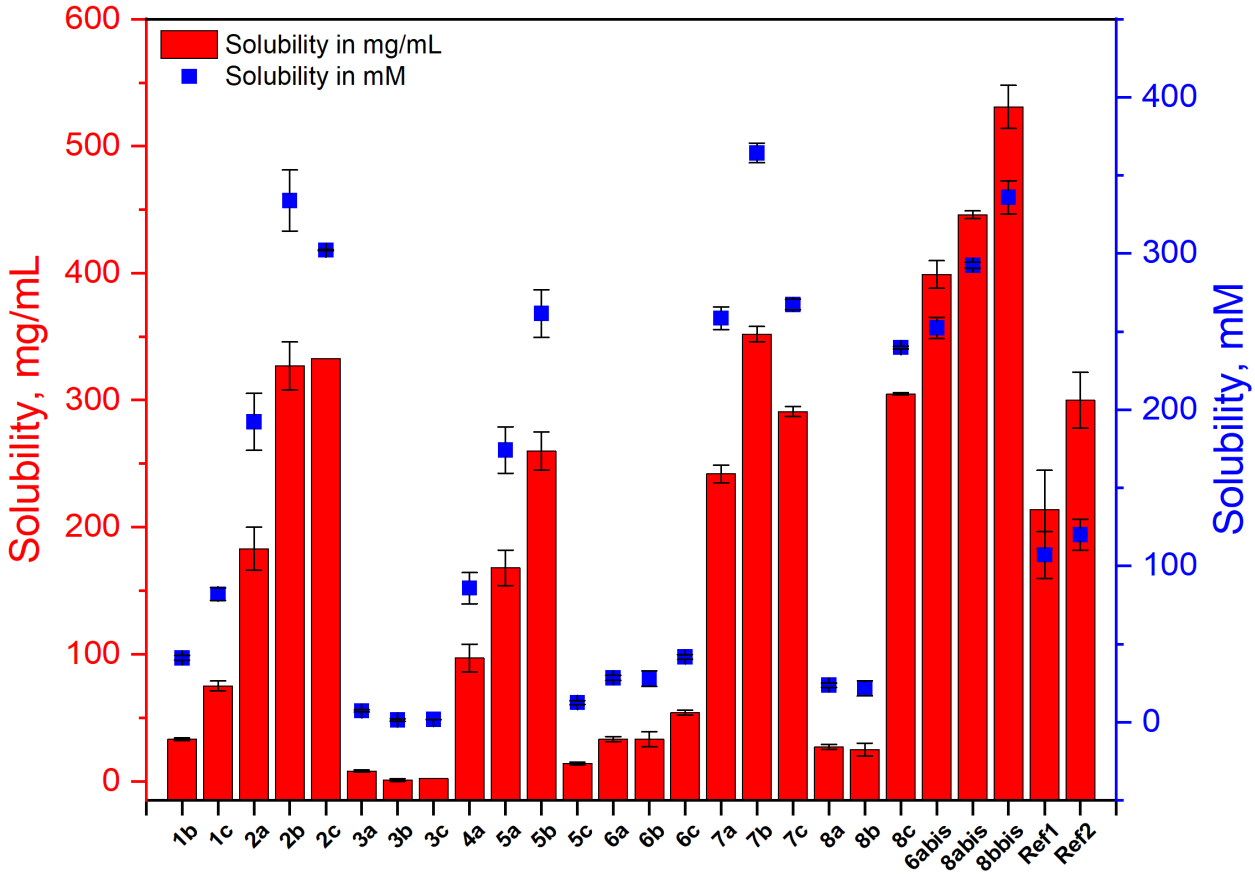

Figure 2.59 Solubility test results in *o*-DCB, red bars demonstrate the solubility in mg/mL, blue dots demonstrate the solubility in mM, in which molecules **3**, **4**, **6** and **8** are molecules with both solubilising groups, Ref 1 and 2 are $6a_{tris}$ and $6a_{tetrakis}$ respectively.

As seen in **Table 2.5**, all the molecules synthesised via route 1 and route 2 were tested the solubility in *o*-DCB. The solubility of **1a** in *o*-DCB was deemed to be not detectable as its solubility was lower than 1 mg/mL. All the solubility results were plotted in **Figure 2.59** to facilitate comparison of the data.

Comparison of the three analogues of **1** that only have different solubilising substituents on the pyrrolidine ring reveals that the addition of the dimethyl and hexafluoroisopropanyl groups increases the solubility of fulleropyrrolidine from undetectable for **1a** to 41 mM for **1b** and 82 mM for **1c**. The products from the

nucleophilic addition of the **1** species and 4-hexylbenzoyl chloride, i.e. the **2** analogues, were observed to have an increased the solubility in *o*DCB of 198 mM going from **1a** to **2a**, 292.7 mM going from **1b** to **2b** and 220 mM going from **1c** to **2c**. **2b** and **2c** achieved similar solubilities in terms of mass, i.e. 327 and 333 mg/mL respectively, whilst **2b** achieved higher solubility in terms of moles than **2c** due to its lower molecular weight. From the solubility results for **1** and **2**, it is concluded that, the addition of dimethyl and hexafluoroisopropanyl on fulleropyrrolidine ring and the addition of a long alkyl chain group to N atom can both increase the solubility significantly. In comparison, analysis of the difference in the solubility of **1** and **3** analogues, the ferrocene containing species, **3**, were observed to have reduced solubilities, with all values lower than 10 mM and 10 mg/mL. The only exception is the almost neglectable change nondetectable for **1a** to 7.24 mM for **3a** that was observed and it is hypothesised that this is due to the ferrocene group disturbing the tight packing of **1a**. **4a** was the only successfully synthesised analogue of **4** and achieved a solubility of 85.8 mM in *o*DCB, which represents an increased of 78.6 mM compared with **3a** and a decrease of 106.5 mM comparing with **2a** implying the presence of ferrocene group contributes negatively to the solubility of fullerene derivative in *o*-DCB. Comparison of the results for the **5** analogues reveals that **5a** and **5b** achieved good solubility, 174 and 261 mM respectively, whilst a relatively lower solubility was observed for **5c** of 12.6 mM. This is explained by considering the existence of the two bulky functionalities in **5c**, hexafluoroisopropanyl and diterbutylbenzyl inducing a tightly packed aggregate and thus the lowering the solubility. The better solubilising effects of hexylbenzoyl compared to ditertbutylbenzyl were concluded from the comparison of the **2** and **5** analogues. Analogues of **6** were observed to generally have significantly reduced solubility compared with **5**, with the value of 28.4, 28.0 and 41.8 mM for **6a**, **b** and **c**

respectively, however, **6c** was an exception with a 30 mM increase. For analogues of **7**, the highest solubility in mole was achieved for **7b** (364.4 mM). Comparison between **2** and **7** analogues shows an increased solubility as a result of replacing carbonyl linker between N and the aromatic group to methylene, this is not surprising as the increasing rotational flexibility of this group will enable for conformational degrees of freedom and the possibly a greater number of interactions with solvent molecules. Comparison between analogues of **5** and **7** reveals that the hexylbenzyl group has a better solubilising effect than ditertbutylbenzyl, essentially pushing adjacent molecules apart more effectively. Comparison between analogues of **7** and **8**, show a notable desolubilising effect due to the addition of the ferrocene group, which is in agreement with the that observed and discussed above for **4a**, **3** and **6** analogues. However, the drop from **7c** to **8c** was only 27 mM, resulting in **8c** being the most soluble ferrocene containing mono-adduct with a solubility of 240 mM.

From the solubility results for the mono-adducts, it is concluded that adding functionalities onto the fulleropyrrolidine C and N atoms can both increase the solubility significantly, however, the addition of the ferrocene moiety causes significant reduction in solubility in *o*DCB. The order of the solubility improving property of functionalities on the C atom of the pyrrolidine ring is hexafluoro > dimethyl > no substituted. The order of the solubility improving functionalities of the aromatic moieties on the N atom is hexylbenzyl > hexylbenzoyl > ditertbutylphenyl.

As a result of the enhanced solubility and high yields of these adducts, the best functional groups highlighted above were taken forward and the bis-adducts of **6a**, **8a** and **8b** synthesised (see above for details) and their solubility in *o*DCB evaluated. As seen in ***Figure 2.59***, all three fullerene bis-adducts achieved high solubility in *o*DCB. The addition of an extra functionality to mono-adduct introduces massive solubility

improvement, with bis-adducts, **C60Fc1**, **C60Fc2** and **C60Fc3**, 9, 12 and 10 times respectively more soluble than their mono-adducts respectively. This increase in solubility has been observed previously for higher adducts of fullerene and is explained by the formation of the mixture of bis-adduct isomers, which have very different shapes which pack irregularly and essentially require extremely high energies to aggregate, which increases the solubility.[49] Comparison bwtween **C60-Fc1** and **C60-Fc2** reveals that the later one to be 40 mM more soluble than the former one, which is in agreement with the previous observation that the hexylbenzyl group is a better solubilising group than the ditertbutyllbenzyl group. Meanwhile, the increased solubility obtained via appending extra dimethyl groups onto the pyrrolidine ring is concluded from the comparison of **C60-Fc2** and **3**.

Interesting results were found by correlation of the number of functionalities and solubility. Comparing the solubility of **C60-Fc1** with the fullerene redox charge carriers reported in the literature, in which tested the solubility of the tris- and tetrakis- adduct with the same functionalities of **C60-Fc1** was reported, it is observed that the solubility of bis-adduct (252 mM), **C60-Fc1**, is higher than both the **Ref1** (tris-adduct, 107 mM) and **Ref2** (tetrakis-adduct, 120 mM), which goes against the intuition and the behavior observed typically for fullerene derivatives in which there is a positive correlation of number of functionalities and solubility.[49] The reason for this negative correlation could be that the increased number of ferrocene and ditertbutylphenyl groups in tris- and tetrakis-adduct interact more readily with adjacent fullerene derivatives, forming a sort of matrix, resulting in a low energy, aggregated species and thus the higher adduct species have a lower solubility. Further works need to be carried out to thoroughly study this behavior, e.g. computational simulation, NMR or UV-Vis titration analysis, if full understanding of the structure/solubility relationship for fullerene adducts it to be

achieved. Clearly, if higher adducts reduce the solubility more generally, as observed here, there might have to be a trade of between adding electroactive moieties to carry charge if they reduce the overall concentration of charge carriers possible in the electrolyte solution.

2.3.5 Electrochemistry analysis of fullerene derivatives

2.3.5.1 Experimental method

All the fullerene derivatives synthesised from route 1 and 2 were analysed by cylic voltammetry to study the redox potential, stability and reversibility of each redox couple, potential windows between different redox couples, physical parameter of fullerene derivatives in electrolyte, which is important to direct the subsequent RFB cell performance tests. Cyclic voltammetry (CV) analysis of fullerene derivatives was carried out by Xiangyi Chen in University of Leeds and Catherine Peake in University of Nottingham. Xiangyi recorded the redox potential of all the fullerene derivatives synthesised and investigated the redox potential changes induced by different functionalities. Cath focused on C_{60}-Fc bis-adducts and thoroughly investigated their diffusion coefficient, D, heterogeneous electro transfer rate constant, k^0, and the cycling stability. Due to the different internal standard used in different departments, the data reported varies slightly, which will be clearly mentioned.

In the University of Leeds, the working electrode (WE) was a burnt platinum disk, the counter electrode (CE) was a platinum rod and the reference electrode (RE) was a Ag/Ag^+ electrode. The platinum working electrode is not the best choice typically due to its reactive nature, however, both fullerene and ferrocene moieties are very stable, which makes the platinum electrode viable for this study. The anhydrous *o*-DCB for electrochemistry analysis was ordered from Sigma and used directly without further purification. Tetrabutylamounium tetrafluoroborate (TBATFB, 0.4 M) was added to *o*-

DCB as supporting electrolyte for enhancing conductivity. The electrolyte was purged with Ar for 30 minutes prior to the CV analysis. Decamethyl ferrocene was used as an internal standard to report the standard potential. The potentiostat used for operating the potential-current and data collection was from brand Nanolab. The concentration of the all the fullerene derivatives in the CV experiments was 1 mM. The standard potential of redox processes was reported at a scan rate, v, 100 mV s^{-1}. The cyclic voltammogram of **7a**, **8a**, and **8a$_{bis}$** are shown below in **Figure 2.60a** as examples. C_{60}Fc mono-adduct, **8a**, and bis-adduct, **8a$_{bis}$** were observed with three reduction processes (labelled I′-III′ from positive to negative potentials) and their corresponding oxidation processes that are labelled as I-III. I/I' is associate with the reduction and oxidation of the ferrocene group, which is one-

electron redox couple in

mono-adduct but two-electron redox couple in bis-adduct due to the presence of extra ferrocene group. Processes II/II' and III/III' are one-electron redox couples centred at C_{60}. The redox processes of ferrocene containing fullerene derivatives were summarized as below:

C_{60}-Fc mono-adduct

I/I': $C_{60}Fc \rightleftharpoons C_{60}Fc^{1+} + e^-$

II/II': $C_{60}Fc + e^- \rightleftharpoons C_{60}Fc^-$

III/III': $C_{60}Fc^- + e^- \rightleftharpoons C_{60}Fc^{2-}$

C_{60}-Fc bis-adduct

I/I': $C_{60}Fc \rightleftharpoons C_{60}Fc^{2+} + 2e^-$

II/II': $C_{60}Fc + e^- \rightleftharpoons C_{60}Fc^-$

III/III': $C_{60}Fc^- + e^- \rightleftharpoons C_{60}Fc^{2-}$

Whereas, only two redox couples (labelled as I/I' and II/II') were found in the CV of fullerene derivatives without ferrocene groups, **7a**, which were summarised as below:

Non ferrocene C_{60} derivatives

I/I': $C_{60} + e^- \rightleftharpoons C_{60}^{1-}$

II/II': $C_{60}^{1-} + e^- \rightleftharpoons C_{60}^{2-}$

The redox potential of each redox couple, E^o, is determined from 0.5(Epa + Epc). Potential window, ΔU, is determined from the different between the E^o of different redox couples, in which ΔU^0 is the potential window between the E^o of C_{60}^{2-}/ C_{60}^{1-} and C_{60}^{1-}/ C_{60}, and ΔU^1 is the potential window between the E^o of Fc/Fc^+ and C_{60}^{1-}/ C_{60} and ΔU^2 is the potential window between the E^o of Fc/Fc^+ and C_{60}^{2-}/ C_{60}^{1-}. The cyclic voltammogram of the soluble C_{60}-ferrocene species that have the potential to act as charge carriers in RFBs are shown in **Figure 2.60b**, and all have acceptably wide potential windows. All the standard potentials acquired from CV are listed in the **Table 2.6**.

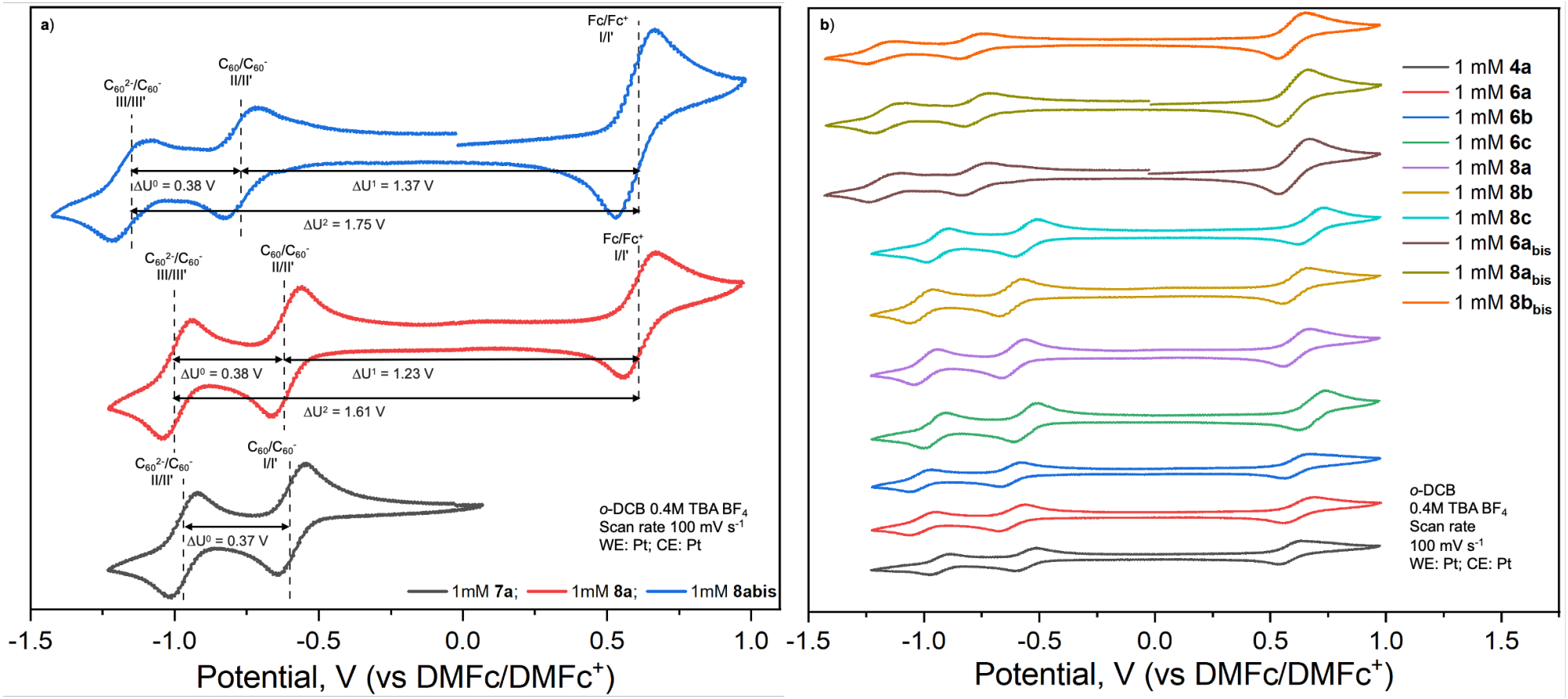

Figure 2.60 Cyclic voltammograms of a) **7a**, **8a** and **8abis** (**C_{60}Fc1**); and b) all soluble analogues of **4**, **6**, **8** and bis-adducts **C_{60}Fc1**, **2**, **3**, in *o*-DCB with 0.4 M TBATFB as supporting electrolyte.

Table 2.6 Standard redox potentials, E^o, of all fullerene derivatives analysed in this study obtained from CV in *o*-DCB with 0.4 M of NBu_4BF_4 as supporting electrolyte at 100 mV s^{-1}. $E^o = 0.5(E_{pa} + E_{pc})$, where *E*pa and *E*pc are anodic and cathodic peak potential.

Compound	$E^o(Fc^+/Fc)$, V	$E^o(C_{60}/C_{60}^{1-})$, V	$E^o(C_{60}^{1-}/C_{60}^{2-})$, V
1a	-	-	-
1b	N/A	-0.59	-0.97
1c	N/A	-0.54	-0.91
2a	N/A	-0.55	-0.93
2b	N/A	-0.56	-0.94
2c	N/A	-0.50	-0.89
3a	0.56	-0.61	-0.99
3b	0.55	-0.61	-0.99
3c	0.62	-0.55	-0.94
4a	0.58	-0.56	-0.93
5a	N/A	-0.60	-0.98
5b	N/A	-0.60	-0.98
5c	N/A	-0.54	-0.92
6a	0.63	-0.62	-1.01
6b	0.62	-0.62	-1.01
6c	0.68	-0.56	-0.95
7a	N/A	-0.60	-0.97
7b	N/A	-0.60	-0.98
7c	N/A	-0.53	-0.92
8a	0.61	-0.62	-1.00
8b	0.60	-0.62	-1.01
8c	0.68	-0.56	-0.94
C60Fc1 ($6a_{bis}$)	0.60	-0.77	-1.17
C60Fc2 ($8a_{bis}$)	0.60	-0.77	-1.15
C60Fc3 ($8b_{bis}$)	0.59	-0.79	-1.19

N.B. All potentials are reported versus the $DMFc/DMFc^+$ redox couple.

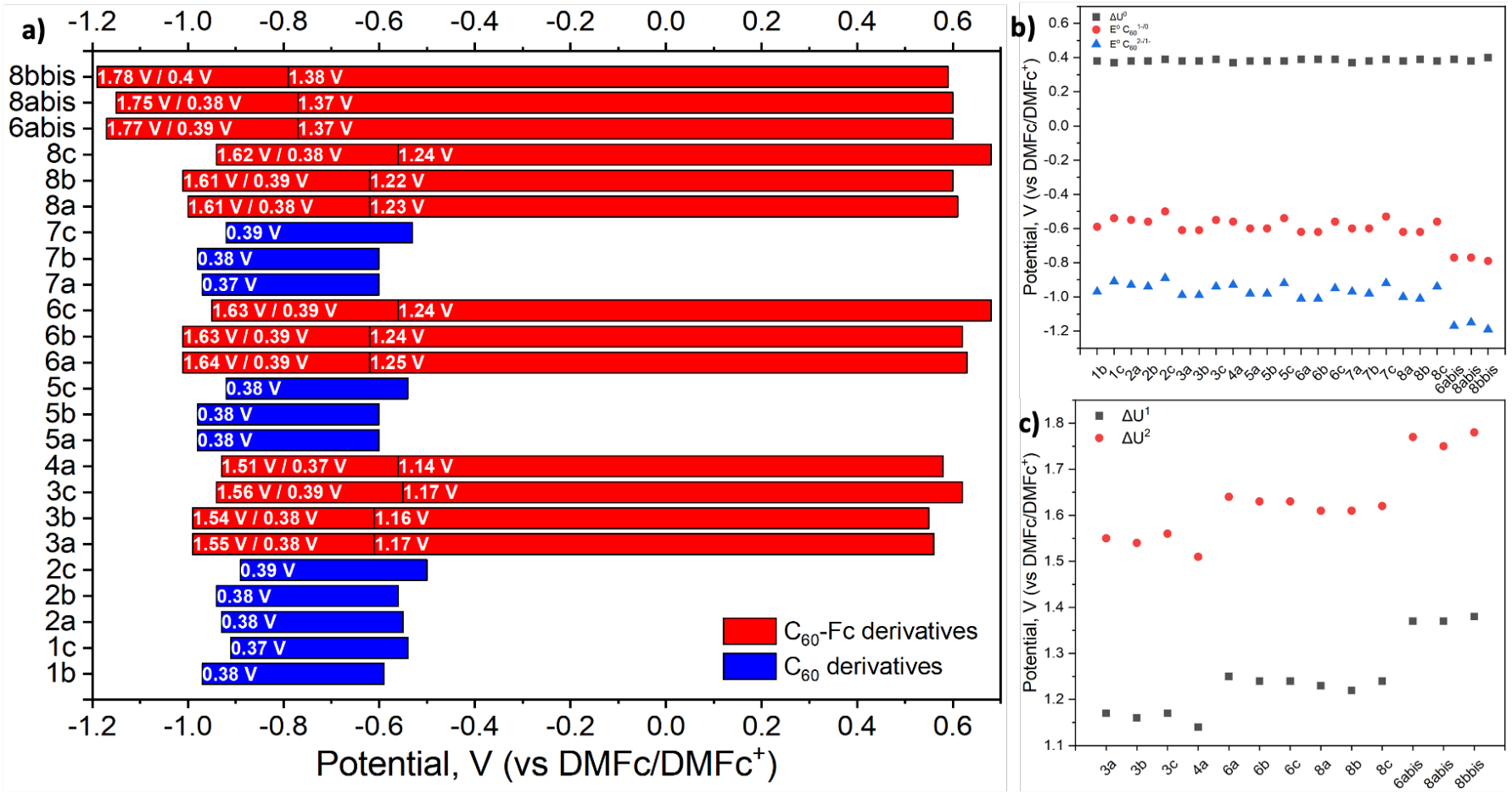

Figure 2.61 a) Potential window of all of the fullerene derivatives, in which the ferrocene containing species and non-ferrocene derivatives are shown as red and blue bar respectively; b) ΔU^0 of all the fullerene derivatives; c) ΔU^1 and ΔU^2 of ferrocene containing fullerene derivatives.

As seen in **Figure 2.61a and b**, the different nature and number of functionalities on the fullerene cage caused negligible changes in the potential window of the two fullerene electron redox process, ΔU^0, but shifted the absolute values of the redox potentials, E^o, of the fullerenes differently. In terms of functionalities on the pyrrolidine ring, the redox potentials of the unsubstituted and dimethyl substituted derivatives are close to each other, whereas a noticeable shift to more positive potentials was observed for the hexafluoroisopropanyl substituted derivatives, which is explained by the strong electron withdrawing nature of the hexafluoroisopropanyl group on the fulleropyrrolidine reducing the barrier to electrons being added to the cage, resulting in a lower potential being required. In the ferrocene containing fullerene derivatives, **3**, **6** and **8**, the same effect influences the redox potential of ferrocene group, with similar ferrocene E^o in unsubstituted and dimethyl substituted derivatives and a positive shift observed for the hexafluoroisopropanyl derivatives. Again, this is rationalized as a result of the strong electron withdrawing hexafluoroisopropanyl groups making the ferrocene groups harder to oxidase and easier to reduce, resulting in a more positive potential required to trigger the loss of an electron from ferrocene, i.e. the oxidation process. The E^o change of the fullerene cage related to the addition of ferrocene was not observed when comparing C60-Fc derivatives and their non-ferrocene analogues (**2a** vs **4a**, **5** vs **6**, and **7** vs **8**). For the molecules synthesised using route 1, a slight positive shift of E^o of both fullerene and ferrocene processes were observed when making comparisons between **1b,c** and **2b,c**, and **3a** and **4a** due to the addition of the hexylbenzoyl moiety. This is ascribed to the inductive effect caused by the electron withdrawing carbonyl linker. As can be seen in **Figure 2.61c**, the C_{60}Fc derivetives synthesised via route **1**, **3** and **4**, show lower values for ΔU^1 and ΔU^2 than those synthesised via route 2, **6** and **8**, which is attributed to the increased redox potential

of the ferrocene of ~0.1 V due to the addition of the methylene linker to the N atom. Whereas this benefit was eliminated in **4a** due to the presence of the carbonyl linker. **C_{60}Fc**, **6** and **8**, have very similar values for ΔU^1 and ΔU^2 meaning that the different substituents on the aromatic ring, i.e. ditertbutyl or hexyl, do not affect the redox potential of the ferrocene moiety. In contrast, comparison of the fullerene-ferrocene mono-adducts, **6a**, **8a** and **8b**, and bis-adducts, **$6a_{bis}$**, **$8a_{bis}$** and **$8b_{bis}$** (see **Figure 2.61c**), reveals a significant negative shift in the fullerene redox potential by 0.16 as a result of increasing number of functionalities, whilst the redox potential of the ferrocene couples remains the similar in the mono- and bis-adducts, resulting in an extended ΔU^1 and ΔU^2 for fullerene bis-adducts of ~ 0.15 V. Therefore, it is concluded that the size of the potential window of the fullerene-based charge carriers for RFB is only influenced by the N-substituent linker and the number of functionalities, with the nature of the other substituents on the pyrrolidine not important as they only affect the position rather than the size of the potential window. That said, as typically electron withdrawing groups will induce an overall positive shift in the potential of the system this might be a beneficial tool in the future when electing a charge carrier system to use in specific organic solvents with narrower potential windows themselves.

2.3.6 Extended Electrochemical analysis of C60Fc1, 2 and 3

Extended electrochemical analysis of **C60Fc1**, **2** and **3** was carried out prior to the cell performance tests to determine the diffusion coefficient, *D*, and heterogeneous electron transfer rate constant, k^0, by investigating the effect of the scan rate on the voltametric response. Both are important parameters as the fast mass transport and electron transfer of charge carriers is key to enabling high power density in RFBs. This works was carried out by Catherine Peake at the University of Nottingham.

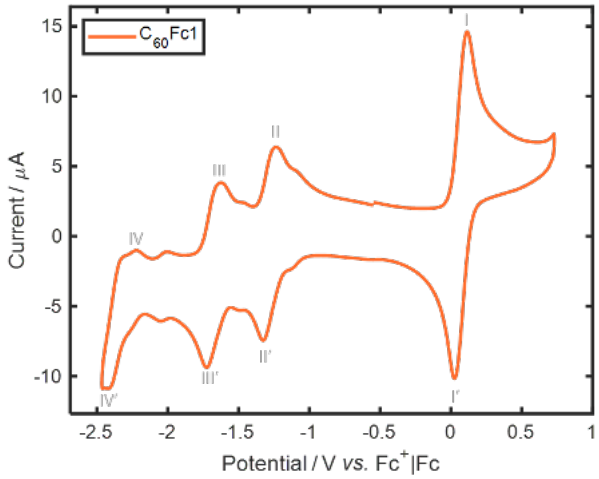

Figure 2.62 CV of 1 mM **C60Fc1** in 0.5 M TBATFB in oDCB at a glassy carbon WE (0.071 cm^2) with Pt wire CE and reference to Fc+/Fc at a scan rate of 100 mV s^{-1}.

The higher concentration of TBATFB, i.e. 0.5 M, was used in the CV test compared to the experiment carried out in Leeds to improve conductivity, and this concentrations was also used for the subsequent cell performance test. Meanwhile, the standard potential reported was different to the value in Leeds due to the different internal standard used, i.e. Fc/Fc^+. As seen in **Figure 2.62**, the CV of **C60Fc1** repeated in Nottingham revealed the third fullerene related redox couple (labelled as IV/IV'), however it is only partially accessed as it occurs at the boundary of the electrolyte window of electrochemical stability. As seen in Table 2.7, the standard potential, E^o, and the peak to peak separation, ΔE_p, of each redox process are listed, in which ΔE_p of each redox couple showed a greater value than 59 / 29 mV that is expected for electrochemically reversible one/two-electron transfer processes. Moreover, an increased ΔEp was observed with the increase of the voltametric scan rate (see **Figure 2.63**). The ratio of Ipc/Ipa for the redox process of I/I' was 0.93 and the equivalent values for the fullerene related redox couples are not given as due to the

difficulty of attaining an accurate baseline in this region. The electrochemically quasi-reversible features of each redox couple are proved by all of these results.

Table 2.7 E^o and ΔE_p determined from the CV of C_{60}Fc1 recorded at 100 mV s^{-1} with iR compensation applied. All potentials are reported versus that of an $Fc^+|Fc$ internal reference. $E^o = (E_{pc} + E_{pa})/2$, where E_c = cathodic peak potential and E_a = anodic peak potential.

Redox process	E^o / V	ΔE_p / mV
I/I'	0.06	108
II/II'	−1.30	104
III/III'	−1.69	111

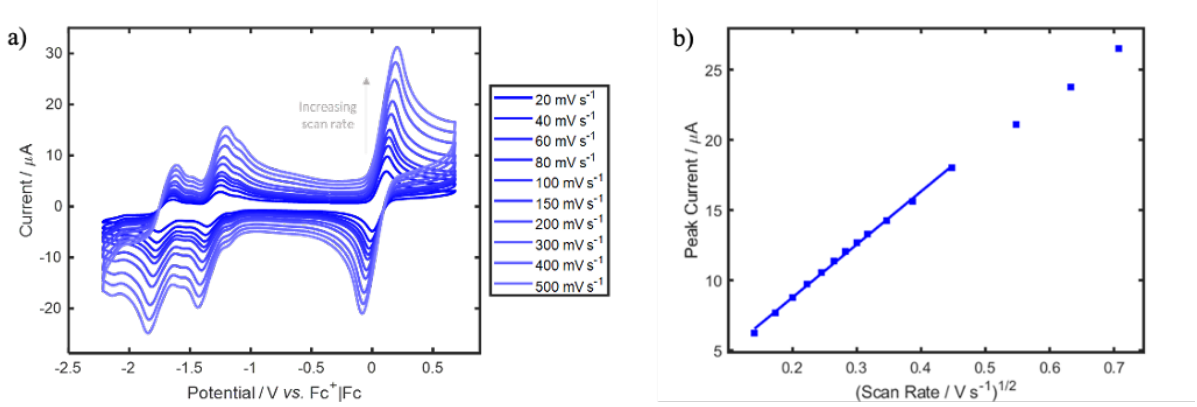

Figure 2.63 a) CV of 1 mM C_{60}Fc1 in 0.5 M TBATFB in *o*DCB at a glassy carbon WE (0.071 cm^2) with Pt wire CE, referenced to Fc^+/Fc at a scan rate of 20 - 500 mV s^{-1} and with iR compensation applied. b) Peak current versus square root of scan rate for the oxidation of C_{60}Fc1 (process I). Data was attained from the second voltammetry sweep of 1 mM C_{60}Fc1 in 0.5 M TBATFB in *o*DCB over the scan rate range of 10 - 500 mV s^{-1}.

At v > 200 mV s−1, the plot of I_{pa}, versus $v^{1/2}$ for the oxidation of **C_{60}Fc1** (process I) is out of the linear fitting region. Therefore, the gradient in the region 10 mV s^{-1} < v < 200 mV s^{-1} was used in conjunction with equation below to estimate *D*:

$$I_p = 2.99 \times 10^5 \alpha^{1/2}\ n^{3/2}\ D^{1/2}\ C\ A\ v^{1/2} \qquad (1)$$

In this equation, α is the transfer coefficient, 0.6, which was determined by Chamberlain and coworkers,[38] *n* is the number of the electron transferred, 2 for C_{60}Fc1, *C* is the bulk concentration of the charge carrier, 1 mM, and *A* is the surface area of the electrode, 0.071 cm^2. A value of *D* of C_{60}Fc1 of 0.86 × 10^{-7} cm^2 s^{-1} was obtained in our study, which is smaller than the the reported value of unfunctionalised C_{60} (3.9 × 10^{-6} cm^2 s^{-1} in 0.1 M TBATBF in *o*DCB[50] and 1.15 × 10^{-6} cm^2 s^{-1} in 0.5 M TBABr in *o*DCB). This could be explained by that the bulky ferrocene substituents hindering the diffusion of the molecules through the solvent.

The heterogeneous electron transfer coefficient, k^0, for redox processes I/I′ and II/II′[51] was determined by useing the Nicholson method. *D* and E_p were obtained from different scan rates, followed by using Equation 2 to obtain the corresponding dimensionless transfer parameter, Ψ. Equation 3 was then used to calculate k^0 using the gradient of the slope from the plot of Y versus $[\pi \mathrm{DnF/RT}]^{-1/2}\, v^{-1/2}$.

$$\Psi = \frac{(-0.6288 + 0.0021\ \Delta E_p n)}{(1 - 0.017\ \Delta E_p n)} \qquad (2)$$

$$\Psi = k^0 \left[\frac{\pi DnF}{RT}\right]^{-1/2} v^{-1/2} \qquad (3)$$

The k^0 for the first reduction process of **C_{60}Fc1**/ **C_{60}Fc1**$^{1-}$ was calculated to be 7.25 x 10^{-4} cm s^{-1}, whereas the k^0 for unfunctionalised C_{60} was calculated to be 0.46 cm s^{-1}.[7] The k^0 for the oxidation process of C_{60}Fc1/ C_{60}Fc1^{2+} was calculated to be 5.36 x

10^{-4} cm s^{-1}, whereas the the k^0 of the fullerene ferrocene mono-adduct was reported to be = 0.34 cm s^{-1} with 0.1 M TBATFBF in *o*DCB using sampled current voltammetry. For initially testing the cycling stability of the **C_{60}Fc1**, over 1000 CV cycles in the potential window of 0.7 V to -2.2 V were performed (see **Figure 2.64**), which indicated minimal change related to the fullerene redox processes (II/II′ and III/III′) and a distinct change of ferrocene redox process (I/I′) after 200 cycles with increased ΔE_p and reduced peak currents. It is concluded that the ferrocene redox couple becomes less electrochemically reversible with cycling.

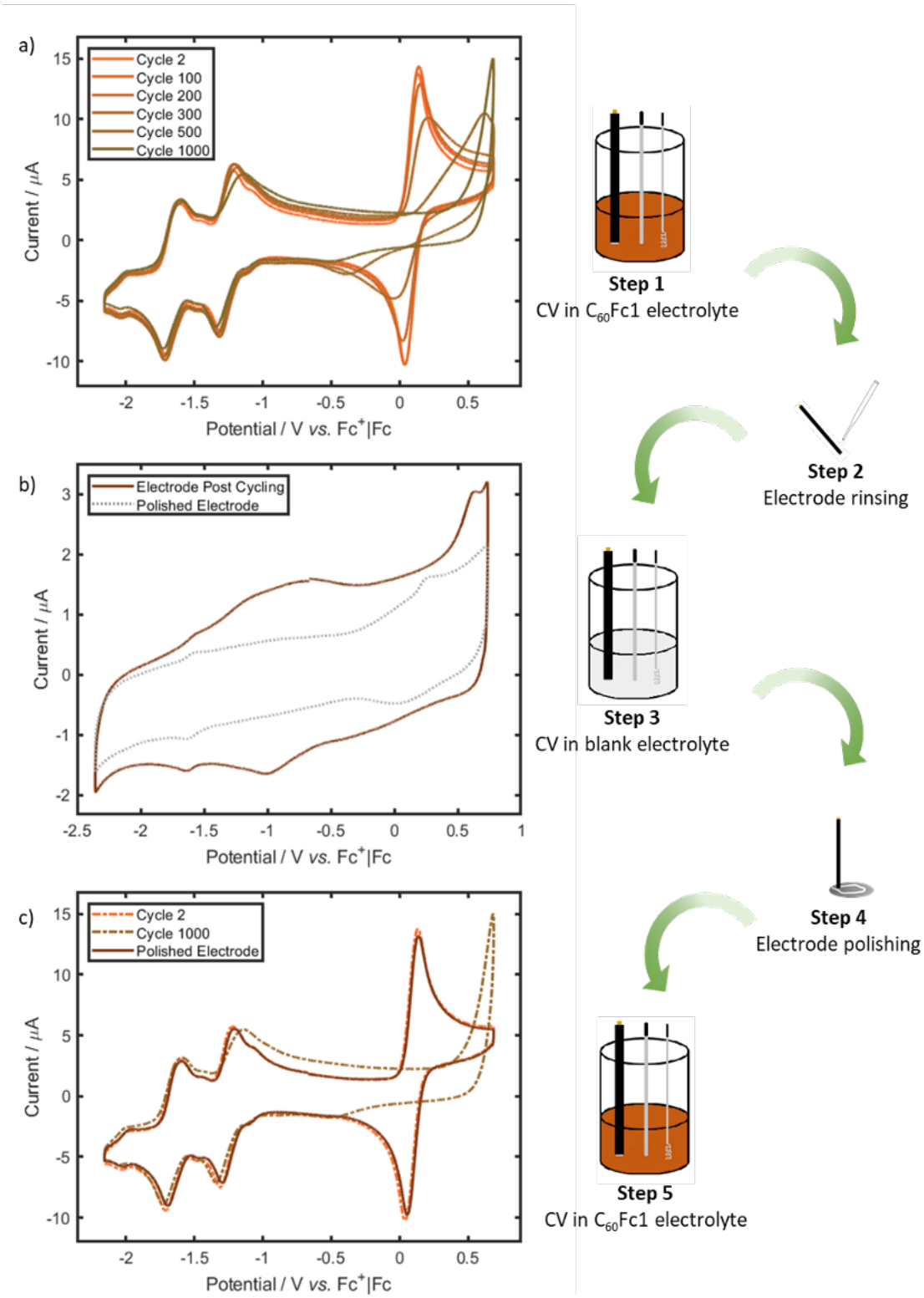

Figure 2.64 a) CV cycling of **C_{60}Fc1** electrolyte at a glassy carbon WE (0.071 cm^2) with Pt wire CE and referenced to Fc^+/Fc at a scan rate of 100 mV s^{-1} and (step 1). Cycle 2, 100, 200, 300, 500 and 1000 are overlaid b) CV of blank electrolyte at the

cycled and polished glassy carbon WE (step 3). c) CV of **C_{60}Fc1** electrolyte from step 1 at a polished glassy carbon WE (step 5).

After 1000 cycles in C_{60}Fc1 electrolyte, the glassy carbon WE was removed and rinsed with 0.5 M TBATFB in *o*DCB (termed blank electrolyte). As seen in **Figure 2.64b** – the brown trace, an increased capacitive current and an oxidation peak at 0.63 V were observed when compared with the CV that used the polished glassy carbon WE in the same electrolyte (**Figure 2.64b** - grey dashes), which indicated that the current response observed was due to fouling of the electrode surface during cycling.

The glassy carbon WE used for 1000 cycles was removed from the electrolyte, cleaned, thoroughly polished with 1 µm, 0.3 µm and 0.05 µm alumina slurry, rinsed and dried. Then the electrode was returned to the same C_{60}Fc1 electrolyte used in the CV cycling experiment. This results in the generation of the CV which overlays well with the CV of **C_{60}Fc1** electrolyte at the beginning of the cycling experiment, which indicates that there is no degradation of the charge carrier occurring after 1000 CV cycles.

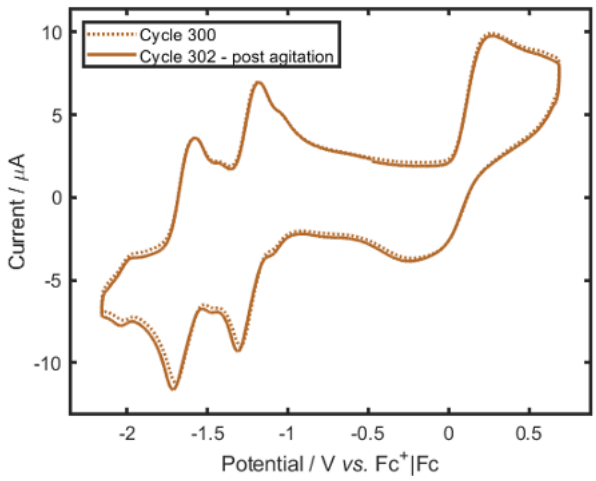

Figure 2.65 CV cycling study of **C_{60}Fc1** electrolyte at a glassy carbon WE (0.071 cm^2) with Pt wire CE and referenced to $Fc^+|Fc$ at a scan rate of 100 mV s^{-1} and iR compensation applied. After 300 cycles, the electrolyte was agitated to disperse the

diffusion layer at the electrode surface. Cycle 300 and 302 (post agitation) are overlayed.

In a separate experiment, the cycling was paused after 300 cycles and the solution was agitated to mix the electrolyte, after which the cycling was continued. As seen in **Figure 2.65**, the voltammogram is unchanged before and after agitation, which negates possibility that the change was caused by the charge carrier degradation occurring within the diffusion layer at the electrode surface.

It is interesting that the ferrocene redox process is affected by the electrode fouling while the C_{60} redox processes remain unimpacted. We hypothesise that the ferrocene-centred redox process has an inner-sphere electron transfer mechanism which is severely impacted by the change in electrode surface while the C_{60}-centred redox process occurs by an outer-sphere electron transfer mechanism.

Similar fouling could be expected in the RFB cell tests of **C_{60}Fc1** that uses a graphite felt electrode. The fouling in the cell could happen more quickly due to the fact that the electrode will be exposed to fully charged electrolyte for a longer time compared with the CV cycling, which could cause increased overpotentials and significant capacity fade at the positive electrode due to the ferrocene centred redox process becoming electrochemically irreversible and inhibited.

2.3.6.1 Comparison of C60Fc Electrochemical properties

Full electrochemical analysis of **C_{60}Fc2** and **C_{60}Fc3** were also performed, including CV, scan rate analysis and CV cycling studies. The key electrochemical properties of **C_{60}Fc1-3** are summarised and compared here.

Table 2.8 E^o of processes I/I′, II/II′ and III/III′ for **C_{60}Fc1-3** referenced to $Fc^+|Fc$.

Charge Carrier	E^o I/I′ / V	E^o II/II′ / V	E^o III/III′ / V
C_{60}Fc1	0.06	−1.30	−1.69
C_{60}Fc2	0.11	−1.23	−1.62
C_{60}Fc3	0.01	−1.36	−1.76

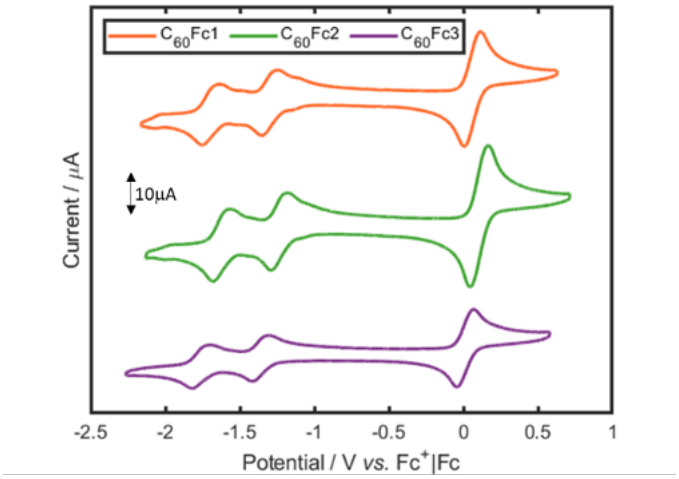

Figure 2.66 CVs of **C_{60}Fc1**, **C_{60}Fc2** and **C_{60}Fc3** in 0.5 M [TBA][BF_4] in *o*DCB at a glassy carbon WE (0.071 cm^2) with Pt wire CE and referenced to Fc^+/Fc at a scan rate of 100 mV s^{-1}.

As seen in **Figure 2.66**, the voltammetry **of C_{60}Fc1**, **C_{60}Fc2** and **C_{60}Fc3** are very similar, which agrees with the CV data collected in Leeds. After calculation, *D* and k^0 for process I/I′ and II/II′ are very similar for each charge carrier as seen in **Table 2.9**. The difference in the value of *D* is partly caused by the inaccuracy in the preparing a 1 mM fullerene charge carrier solution. These reveal that the different functionalities of **C_{60}Fc1-3** change the solubility of the species but not the electrochemical properties, which agrees with the CV study in Leeds, which also revealed that all three fullerene charge carriers have very similar electrochemical properties. As a result, they are expected to have comparable performance in the RFB tests.

Table 2.9 Diffusion coefficients, *D* and heterogeneous electron transfer coefficients, k^0 for processes I/I′ and II/II′ for C_{60}Fc1-3. For each charge carrier, the gradient in the region 10 mV s^{-1} < ν < 200 mV s^{-1} was used in conjunction with equation 5 to estimate *D*. k^0 was calculated using the Nicholson method.

Charge Carrier	D / cm^2 s^{-1}	k^0 I/I′ / cm s^{-1}	k^0 II/II′ / cm s^{-1}
C_{60}Fc1	6.86×10^{-7}	4.17×10^{-4}	9.28×10^{-4}
C_{60}Fc2	1.24×10^{-6}	4.39×10^{-4}	1.03×10^{-3}
C_{60}Fc3	3.94×10^{-7}	2.49×10^{-4}	5.14×10^{-4}

2.3.7 Flow battery performance

A symmetric RFB was assembled in a N_2-filled glove box. Both the positive and negative electrolyte consisted of 10 mL of 1 mM C_{60}Fc1 in 0.5 M TBATFB in *o*DCB. Two sheets of polypropylene porous separator (Celgard) were used to separate the half-cells and electrolytes were pumped through the cell at a flow rate of 20 mL min^{-1}. **Table 2.10** summarises the redox reactions expected to occur in the positive and negative electrolyte and the expected potential of charge/discharge plateaus upon cycling. **Figure 3.67** provides a visual representation of the redox reactions occurring in the battery and origin of the charge/discharge plateaus.

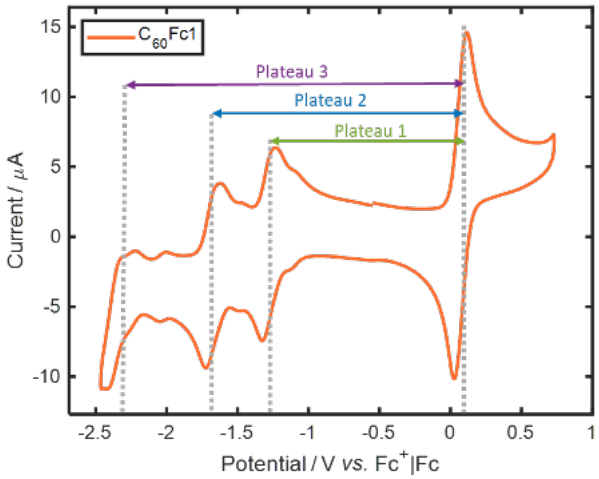

Figure 2.67 CV of 1 mM **C60Fc1** in 0.5 M TBATFB in *o*DCB at a glassy carbon WE (0.071 cm^2) with Pt wire CE referenced to Fc^+/Fc at a scan rate of 100 mV s^{-1} and with iR compensation applied. Dashed lines indicate E^o of each redox couple and arrows indicate the expected potential of charge/discharge plateaus in a symmetric **C60Fc1** RFB.

Table 2.10 Expected charge/discharge reactions of the positive and negative electrolytes in a symmetric $C_{60}Fc1$ RFB. The expected potential of plateaus have been calculated based on the E^o values from the CV of $_{60}Fc1$.

Plateau	**Positive electrolyte rxn. (E^o *vs.* Fc^+/Fc / V)**	**Negative electrolyte rxn. (E^o *vs.* Fc^+/Fc / V)**	**Plateau potential / V**
1	$C_{60}Fc1 \rightleftharpoons C_{60}Fc1^{2+} + 2e^-$ (0. 06)	$C_{60}Fc1 + e^- \rightleftharpoons C_{60}Fc1^-$ (−1.30)	1.36
2	$C_{60}Fc1 \rightleftharpoons C_{60}Fc1^{2+} + 2e^-$ (0. 06)	$C_{60}Fc1^- + e^- \rightleftharpoons C_{60}Fc1^{2-}$ (−1.69)	1.75
3	$C_{60}Fc1 \rightleftharpoons C_{60}Fc1^{2+} + 2e^-$ (0. 06)	$C_{60}Fc1^{2-} + e^- \rightleftharpoons C_{60}Fc1^{3-}$ (approx. −2.30)	2.36

Before the addition of fullerene-Fc charge carriers, an electrolyte comprsing 0.5M TBATFB in *o*DCB was loaded into the cell inorder to soak the separator and the electrodes. The resistance across the flow cell was determined by potentiostatic electrochemical impedance spectroscopy (EIS) after 30 minutes. Measurements were recorded within the frequency range of 100 kHz to 100 mHz. R_{ohm} is the sum of ohmic resistance across the whole cell, which includes contributions from the electrolyte, porous separators, graphite felt electrodes, and electrical leads between the cell and the potentiostat. A 21 Ω of R_{ohm} for cell was obtained, which corresponded to an area specific resistance (ASR) of 4.2 Ω cm^{-2}, whereas Chamberlain et al. reported a resistance of 42 Ω across the coin cell set up they used previously with 1 M TBATFB in *o*DCB as electrolyte. The ASR of the coin cell could be up to 10 times of the value of our flow cell setup, 42 Ω cm^{-2}, whilst the active area for the coin cell is 1 cm^2. The reduced R_{ohm} of our flow cell is explained by the geometry of the cell assembly which has less distance between electrodes and a thinner separator than the coin cell.

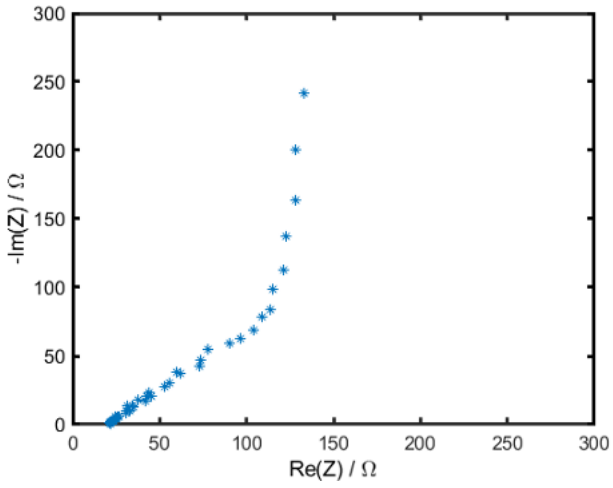

Figure 2.68 Nyquist plot of the EIS measurement of full RFB assembly with a 0.5 M TBATFB in *o*DCB electrolyte solution flowing through cell at 20 mL min^{-1}.

Initially, the conditions that used in the literature, which cycled within the voltage window of 0 to 2.5 V, was replicated. Galvanostatic cycling was conducted at a current

density of 0.1 mA cm^{-2} (±0.5 mA). Three charge plateaus were observed and are labelled charge 1-3 in **Figure 2.69**. Charge 1-3 occur at potentials of 1.35 V, 1.80 V and 2.25 V respectively and correspond well to the reactions outlined in **Table 2.10**.

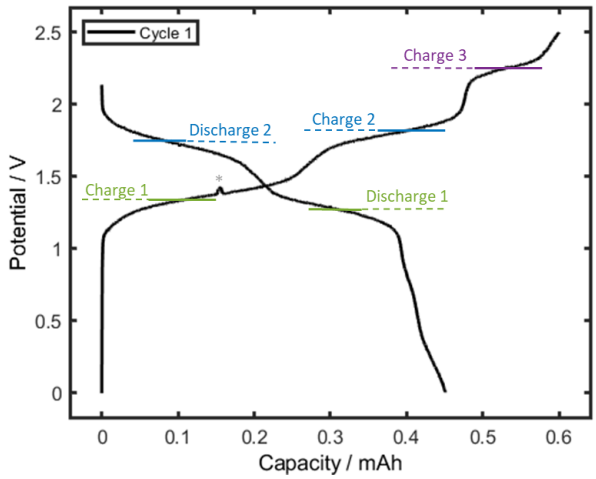

Figure 2.69 Charge-discharge profiles from cycle 1 of **C_{60}Fc1** RFB. Voltage window of 0 to 2.5 V.* the minor variation in potential is due to the electrolyte pump briefly stopping.

Charge plateau 3 is thought to occur due to the fullerene-centred reduction of $C_{60}Fc1^{2-}$ to $C_{60}Fc1^{3-}$ at the negative electrode and simultaneous ferrocene-centred oxidation of **C_{60}Fc1** at the positive electrode. In an ideal system, the positive electrolyte would be fully oxidised to **$C_{60}Fc1^{2+}$** once charge plateau 2 was complete. The presence of the third plateau indicates that **C_{60}Fc1** and/or **$C_{60}Fc1^{1+}$** was present in the positive electrolyte after charge plateau 2 was complete. This may be due to inaccuracy in distribution of electrolyte between reservoirs, the presence of impurities or due to crossover of charge carrier to the negative reservoir where it can be reduced and return to the positive reservoir. While the third charge plateau is not explored further in this study, it demonstrates that there is promise in exploring the C_{60}Fc tris-adduct i.e. three ferrocene groups covalently bound to a fullerene centre. The tris-adduct

would enable enhanced energy density by enabling a three-electron charge/discharge redox reaction per molecule.

The working conditions were adjusted to a voltage window of 0 to 2.1 V and the galvanostatic cycling was performed for 100 cycles over the period of 150 hours. An electrochemical yield (percentage of the theoretical capacity achieved upon charge) of 89% was obtained from the initial cycle. The RFB showed an average coulombic efficiency (CE), voltage efficiency (VE) and energy efficiency (EE) of 96 %, 77 % and 74 % respectively over the 100 cycles. The high CE is achieved due to the reversible electron transfer to and from **C_{60}Fc1**. In comparison with the coin cell, the VE is significantly improved at the same current density, which is attributed to the reduced ohmic resistance of the flow cell.

The charge and discharge profiles are shown in **Figure 2.70**, which indicated that the shape of the profiles changes over the cycling experiment. Most notably, an extra discharge plateau at 0.8 V was observed after 20 cycles. A consistent capacity fade of 0.3% per cycle was also observed over the course of 100 cycles (based on discharge capacities), which is smaller than the equivalent system in the coin cell, 0.4%. The authors explained that the capacity fade was caused by the loss of the charge carrier due to the glass-fibre separator absorbing the electrolyte. In our case, the fade was reduced, which was attributed to the thinner polypropylene separator used and the large volume of the electrolyte (20 mL for the flow cell verses 400 μL for the coin cell).

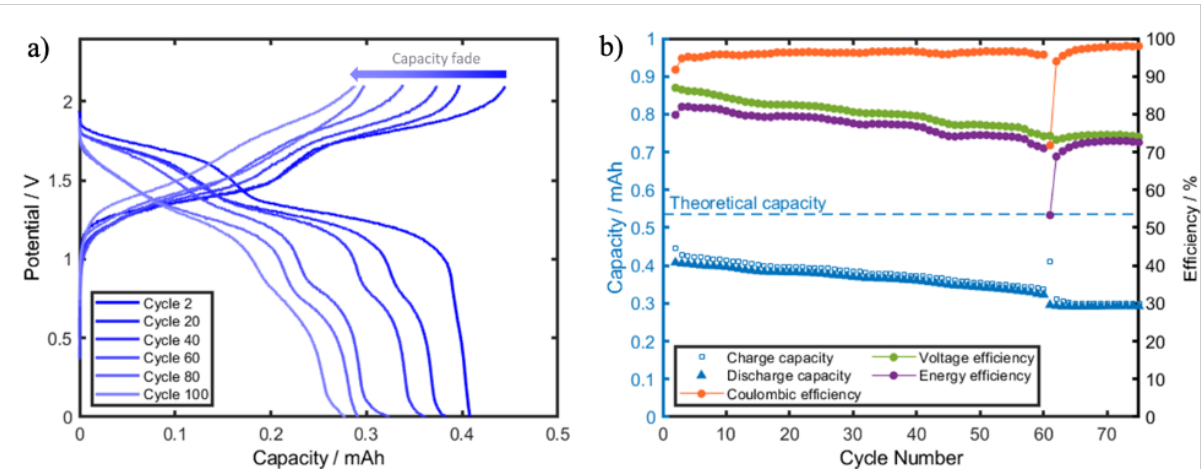

Figure 2.70 Symmetric **C_{60}Fc1** RFB cycling within the voltage threshold of 0 to 2.1 V. Half-cells were separated by a Celgard separator with a current density of 0.1 mA cm^{-2} (C-rate of approximately 1C) and flow rate of 20 mL min^{-1}. a) Charge/discharge profiles of cycle 2-100, b) capacity and efficiency values per cycle.

After 60 cycles, the positive and negative electrolytes were mixed together and redistributed evenly between the electrolyte reservoirs (10 mL each). The electrolyte redistribution did not regain the lost capacity as seen by the charge and discharge capacity shown in **Figure 2.70**, which indicated that asymmetric membrane crossover (net migration of charge carrier to a single half-cell) was not the significant cause of capacity fade in the battery.

2.3.8 Post cycling analysis

To understand the reason of the capacity fade during the cell cycling, the positive and negative electrolytes were removed from the cell, collected and analysed separately by CV, TLC, MALDI ToF ms and NMR spectroscopy. Scanning electron microscopy (SEM) was used to image the graphite felt electrodes following 100 cycles. The electrodes were rinsed with *o*DCB and dried in a vacuum oven at 40°C for a minimum of 72 hours before analysis.

Figure 2.71 shows the CV of electrolytes pre cycling and following 100 charge-discharge cycles. Given the high boiling point of *o*DCB (178 °C), it can be assumed that minimal evaporation of solvent occurred during the flow battery cycling. Redox processes I/I′ - III/III′ are all observed in the CV of the electrolyte from each side of the cell after 100 cycles with a reduced current magnitude of the peaks indicative of a reduction in the concentration of **C_{60}Fc1** in the electrolyte and is likely the primary cause of capacity fade in the battery. New redox couples are observed at ~0.2 V and ~0.5 V verses Fc^+/Fc for both electrolytes post cycling. The additional redox couples observed at positive potentials are proposed to be indicative of new ferrocene environments. It can be speculated that they are a result of the mono-adduct of **C_{60}Fc1**, **6a**, and free ferrocene, see below. In addition, a loss of definition and introduction of new redox couples are observed in the fullerene-centred redox region. The presence of the mono-adduct, **6a**, and the ferrocene detached mono- or bis-adducts are hypothesised. These results all indicate the degradation of C_{60}Fc1 during cycling.

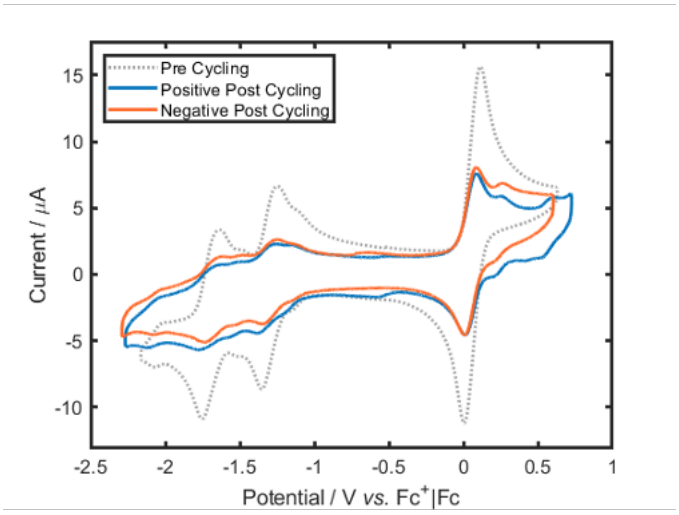

Figure 2.71 CV of positive and negative electrolyte pre cycling and after 100 charge-discharge cycles in a RFB. CV was recorded at glassy carbon WE (0.071 cm^2) with Pt wire CE at a scan rate of 100 mV s^{-1} and the iR compensation applied.

Ag wire QRE was used and voltammograms were referenced to the internal ferrocene/ferrocenium redox couple of the charge carriers.

The solvent of the electrolyte was removed under the reduced pressure. To remove the excess of tetrabutylammonium tetrafluoroborate (TBATFB), the residue was treated with methanol (100 mL), the resulting mixture was sonicated for 15 min, followed by filtration using a PTFE membrane filter (pore size 0.4 μm). The solid was dried and analysed by TLC.

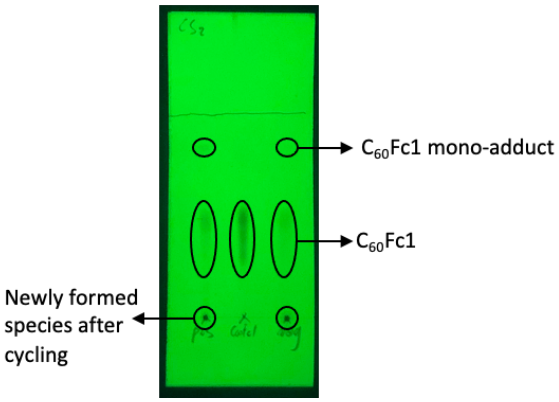

Figure 2.72 TLC results of the (left) catholyte solid, (right) anolyte solid and (middle) pure **C_{60}Fc1** sample. CS_2 was used as the mobile phase.

As seen in **Figure 2.72**, some polar species were formed in both the catholyte and anolyte during the cell cycling, which were stuck on the baseline of the TLC plate. This was also mentioned in the post cycling analysis of the literature.[38] At the same time, spots with R_f = 0.85 were observed in both catholyte and anolyte samples, which could be the corresponded to the mono-adduct, **6a**, formed via by the degradation of **C_{60}Fc1** during the cell studies.

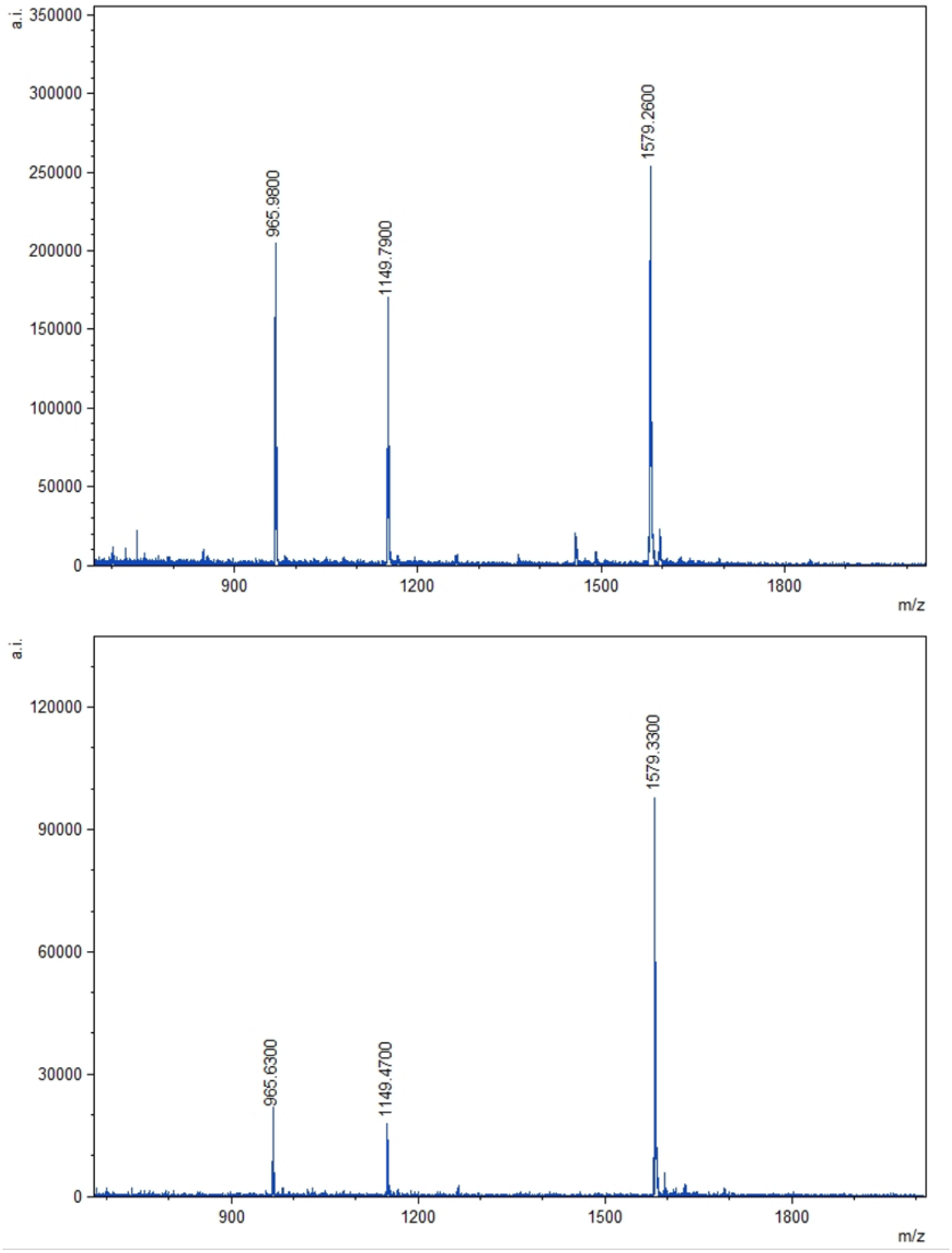

Figure 2.73 MALDI ToF ms data of the catholyte (top) and anolyte (bottom) samples in o-DCB from the C60Fc1 cell, washed with methanol, then redissolved the solid in CS2 indicating the existence of **C_{60}Fc1** (m/z = 1579), the corresponding mono-adduct, **6a** (m/z = 1149) and the mono-adduct without a ferrocene moiety, **5a** (m/z = 965).

As seen in **Figure 2.73**, **C_{60}Fc1** (m/z = 1579) was the peak with the highest intensity in both catholyte and anolyte spectra, which meant most of the **C_{60}Fc1** remained intact after the cycling. At the same time, the ferrocene monoadduct, **6a** (m/z = 1149) and the mono-adduct without ferrocene, **5a** (m/z = 965) were detected in both samples, which indicated that there was some degradation **C_{60}Fc1** during the cell cycling test. Comparison of the peak intensities of catholyte and anolyte samples revealed that the relative ratio of degradation product to **C_{60}Fc1** in catholyte (1.46 / 1) was higher than in anolyte (1 / 2.54). From this, it is possible to conclude that the degradation process in the catholyte was severer than in anolyte, which could be a result of the observed asymmetrical membrane crossover that occurred during the cell cycling. It could also be that the degraded products passed more easily through the membrane than **C_{60}Fc1**, resulting in inhomogeneity in the distribution of products in the two sides of the cell and thus the different impurity to **C_{60}Fc1** ratios in MALDI spectra of the solutions from two sides.

The NMR spectroscopy was used to further understand the degradation of the post cycling electrolyte *(***Figure 2.74**). Comparison of the spectra of post cycled electrolytes with the spectra of fresh **C_{60}Fc1**, it was obvious that the peak patterns have changed. The ratio of respective integrations of the aromatic protons, the pyrrolidine with linked ferrocene protons, and the ditertbutyl protons was [1 / 4.67 / 6] in the original spectrum, and [1 / 3.5 / 9.95] and [1 / 2.72 / 9.28] in the catholyte and anolyte respectively. The aromatic proton peaks in the **C_{60}Fc1** spectrum were within the region from δ = 7.31 ppm to 7.89 ppm, whereas the region of the aromatic proton peaks extended to between δ = 7.05 ppm - 7.89 ppm in the spectra of catholyte and anolyte samples. The peaks pattern of the ditertbutyl peaks changed from multiplets with sharp definition in **C_{60}Fc1** to multiplets with a broad bottom in post cycled catholyte and anolyte.

However, it was impossible to assign the new peaks fully and study the composition via the NMR spectra due to the complexity of the fullerene poly-adduct and mono-adduct mixtures.

In conclusion, the degradation of the **C_{60}Fc1** sample during the cell cycling process was directly proved by results of TLC, MALDI ToF MS and NMR spectroscopy, which rationalised observed capacity fade during the cell study. From the MALDI spectra, the detected degradation products are **5a** and **6a**. The newly formed polar species observed on the TLC plate are still unknown. More techniques, e.g. HPLC (with a Buckyprep column), could be utilized in order to conduct a more thorough degradation study in the future

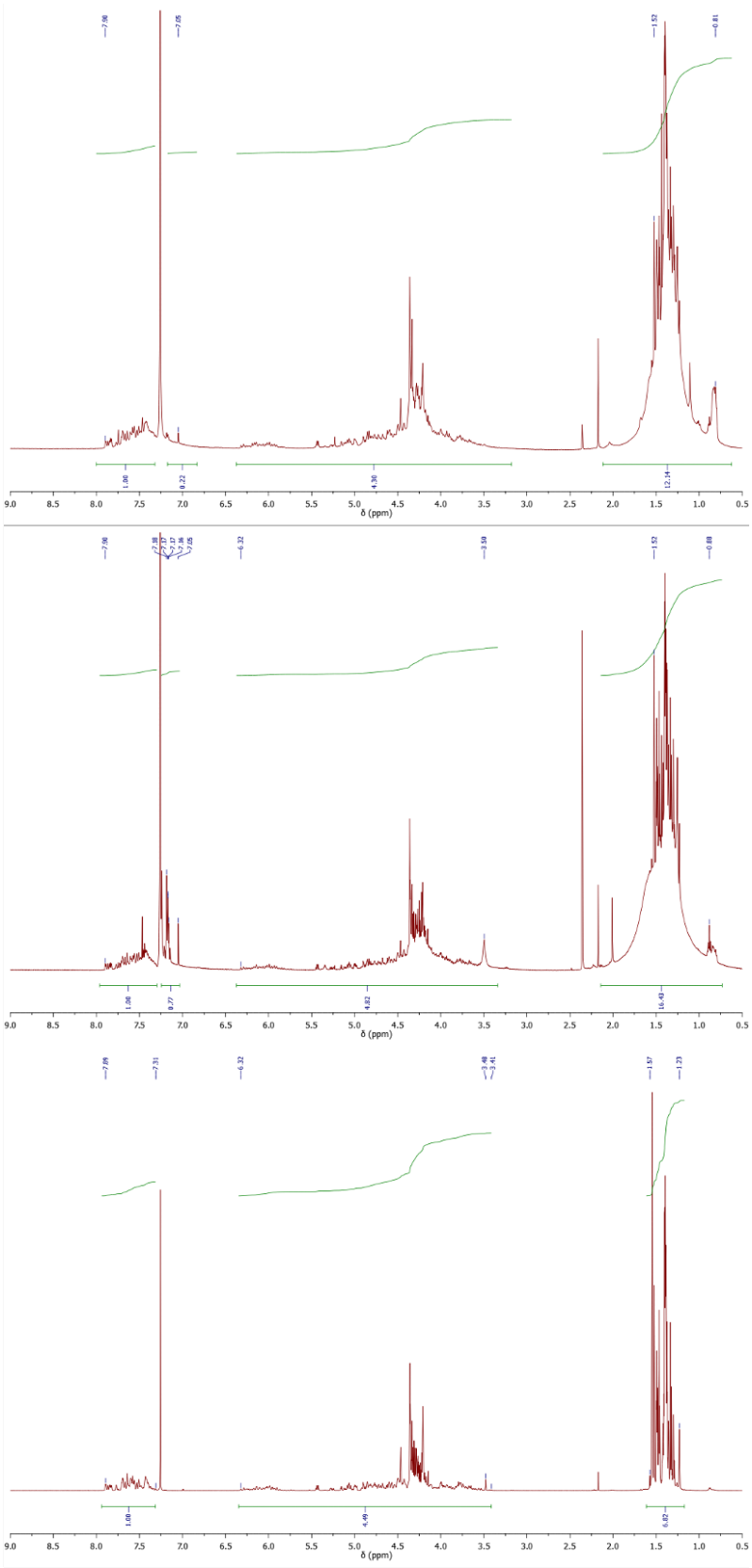

Figure 2.74 ^{1}H NMR spectra of (top) the catholyte sample and (middle) the anolyte sample isolated from the **C_{60}Fc1** cell, after removing the *o*-DCB, washing with

methanol and redissolving the remaining solid in $CDCl_3$. (bottom) ^1H NMR spectrum of **C_{60}Fc1** in $CDCl_3$ for comparison.

As mentioned above, different pyrrolidine ring substituents and the solubilising groups attached to N of **C_{60}Fc1-3** are only considered to impact the solubility but not to change the electrochemical properties or stability of the charge carrier. An equivalent RFB was assembled using **C_{60}Fc2** charge carriers. Extended charge-discharge cycling was compromised by engineering failures. However, **Figure 2.75** compares the charge-discharge profiles from cycle 2 of **C_{60}Fc1** and **C_{60}Fc2** RFBs. The potential plateaus and achieved capacities are remarkably similar and therefore cycling performance **of C_{60}Fc2** can be assumed.

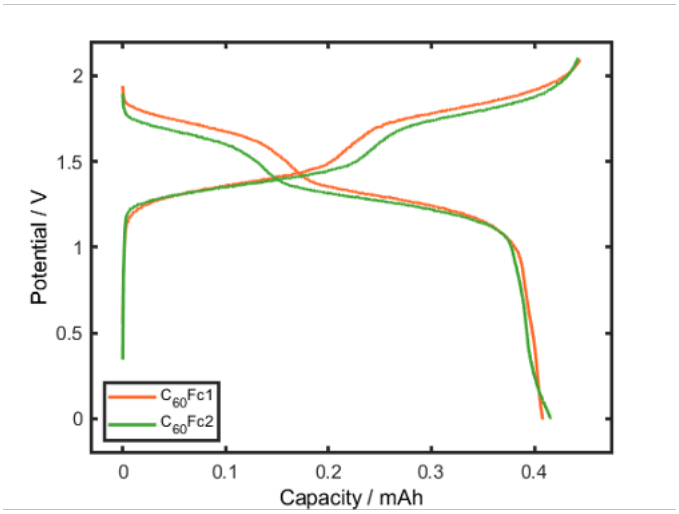

Figure 2.75 Comparison of C_{60}Fc1 and C_{60}Fc2 RFBs. Overlay of cycle 2 charge and discharge profiles (voltage window of 0 to 2.1 V).

2.4 Conclusion

Overall, 25 fullerene derivatives were synthesied including 21 novel molecules. Their solubility in *o*DCB and electrochemical properties were thoroughly studied. Of the 11 novel ferrocene-containing molecules synthesised, bis-adducts **C_{60}Fc2-3** revealed the

highest solubility of 290 mM and 336 mM *o*DCB, which is approximately three times more soluble than similar species reported in the literature.[38] Interestingly, we also found that the bis-adduct could be more soluble than the tris- and tetrakis- adducts from the comparison between **C_{60}Fc1** and the literature. Molecule, **8c**, is the most soluble fullerene-Fc mono-adduct in in this library. In the future, the synthesis of the bis- or higher adducts version of 8c could lead to impressive solubility in *o*DCB or other solvents with wider potential windows, attaining fullerene based RFB system with greater energy densities. For the non-ferrocene fullerene derivatives, **2**, **5** and **7** analogues all achieved good solubility in *o*DCB, especially, **7b** which showed the highest solubility, 364 mM, and thus could be utilised as a promising anolyte charge carrier for building the asymmetric systems. The order of the solubility improving properties of the different functionalities explored in this study at the C atom of the pyrrolidine ring is hexafluoro > dimethyl > no substituted. The order of the solubility improving functionalities of the aromatic moieties explored at the N atom is hexylbenzyl > hexylbenzoyl > ditertbutylphenyl. To further improve the solubility of the fullerene charge carriers in *o*DCB, longer alkyl substituents on the pyrrolidine, e.g. diethyl, and increase both the numbers of and length of the alkyl chains on the benzene ring. The preparation of poly-adducts could also improve the solubility significantly.

Three fullerene-Fc bis-adduct, **C_{60}Fc1**-**3**, obtained wide potential windows in CV experiments. The **C_{60}Fc2** achieved the widest potential window, 1.78 V, whereas **C_{60}Fc1** the same molecule tested in literature achieved 1.77 V under our testing conditions. Increasing the number of functionalities on the same cage can effectively increase the potential window with ~0.15 V increase from mono-to bis- adducts. Meanwhile, changing the linker between phenyl group and N of the pyrrolidine ring

from carbonyl to methylene can also increase the potential window by ~0.06 V. The strong electron withdrawing group will induce a positive shift, which might be a beneficial tool in the future when electing a charge carrier system to use in specific organic solvents with narrower potential windows themselves.

Three fullerene bis-adducts, **C_{60}Fc1**-**3** were tested in the flow cells with a current density of 0.1 mA cm^{-2}. In comparison with previously reported coin cell, the flow cell using **C_{60}Fc1** as the charge carrier achieved a greater VE, 77%, than the corresponding test in coin cell, which is attributed to the reduced R_{ohm} of the flow cell. Due to the thin separator and large volume of the electrolyte used, the loss of the fullerene charge carrier is reduced, resulting in slower capacity fad 0.37% per cycle (0.4% per cycle in coin cell). The flow cell tests of **C_{60}Fc2** and **3** are still under investigation. They are expected to have the comparable performance to **C_{60}Fc1** due to their similarities of potential window and chemical stability. However, their theoretical energy densities are expected to be greater due to their higher solubility in *o*DCB.

Further development of the fullerene based redox flow batteries can be summarised as: 1) make more *o*DCB soluble fullerene derivatives following the suggestions made above; 2) prepare the fullerene tris-adduct and test the cell performance in the solvent with a wider potential window; 3) further expand the potential window by combining fullerene with other redox couples; 4) expand the energy density of the system by combining fullerene molecule with other redox couples that have multi-electron redox processes.

2.5 Experimental

C_{60} (99.5%) was purchased from SES Research Corporation. All other reagents and solvents were purchased from Aldrich and were used without further purification. Infrared spectra were measured using Bruker ALPHA FT-IR spectrometer over the range 400-4000 cm^{-1}. ^{1}H and $^{13}C\{^{1}H\}$ NMR were obtained using Bruker AV(III) 400 or Bruker AV(III) 500 spectrometers. Mass spectrometry was carried out using a MALDI ToF spectrometer (Shimadzu AXIMA performance). UV-Vis spectra were measured using an Agilent Technologies Cary Series Spectrometer.

2.5.2 Compounds preparation and characterisation

2.5.2.1 Synthesis of N-tritylfulleropyrrolidine

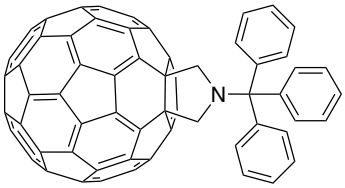

C_{60} (100 mg, 0.139 mmol), paraformaldehyde (20.8 mg, 0.695 mmol) and N-trityl glycine (44 mg, 0.69 mmol) were added to anhydrous oDCB (100 ml), degassed with N_2 and heated to reflux temperature for 3.5 h. The solvent was removed under reduced pressure, the residue was redissolved with 5 mL of CS_2, and purified by column chromatography (silica gel, CS_2). And further purification was carried out by washing with 50 mL of methanol to yield the product (56 mg, 40%) as a brown solid.

^{1}H NMR (400 MHz, $CS_2/CDCl_3$ 7:1 v/v, *δ*, ppm): 7.90 (d, 6H, *J*= 7.7 Hz, ArH), 7.43 (t, 6H, *J*= 7.7 Hz, ArH), 7.30 (t, 3H, *J*= 7.4 Hz, ArH), 4.19 (s, 4H, CH2).

$^{13}C\{^{1}H\}$ NMR (400 MHz, $CS_2/CDCl_3$ 7:1 v/v, *δ*, ppm): 154.56,147.19, 146.19, 146.05, 146.02, 145.55, 145.43, 145.22, 144.50, 143.01,142.61, 142.29, 142.00, 141.85, 140.21, 136.47, 130.45, 129.19 (fullerene C), 128.28, 128.21, 127.49,126.95 (Ar C), 73.97, 69.36 (pyrrolidine ring C), 60.71.

MALDI-ToF MS (DCTB/CS_2, m/z): 1005 $[M]^-$.

2.5.2.2 Synthesis of Fulleropyrrolidine, 1a

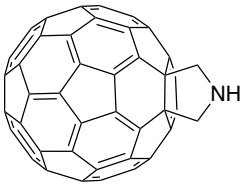

N-trityl fulleropyrrolidine (50 mg, 0.05 mmol) was suspended in anhydrous DCM (25 ml) and sonicated for 15 min. Then trifluoromethane fulfonic acid was added stirring for 1 hour. The reaction mixture was dried under reduced pressure. The residue was purified by centrifugation (diethyl ether, 10 mL x 3) to yield the product (38 mg, 100 %).

MALDI-TOF MS (DCTB/MeCN, m/z): 763.0 $[M]^-$.

IR (*v*, cm^{-1}): 3446 (s, NH), 2360 (w), 1385, 1274, 1171, 1026, 636.

2.5.2.3 Synthesis of 2,2-dimethyl fulleropyrrolidine, 1b

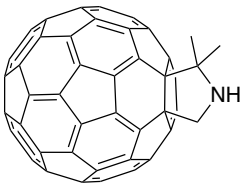

C_{60} (100 mg, 0.139 mmol), paraformaldehyde (20.8 mg, 0.695 mmol) and 2-aminoisobutyric acid (41.4 mg, 0.139 mmol) were added to anhydrous oDCB (20 ml), degassed with N_2 and heated to reflux temperature for 3.5 h. The solvent was removed under reduced pressure, the residue was redissolved with 5 ml of CS_2, and purified by column chromatography (silica gel, toluene/EtOAc 91/3). And further purification was carried out by washing with 50 ml of diethyl ether and 50 ml of methanol to yield the product (23 mg, 21%) as a brown solid.

^{1}H NMR (500 MHz, CS_2/$CDCl_3$ 7:1 v/v, *δ*, ppm): 4.88 (s, 2H, CH_2), 2.14 (s, 6H, CH_3).

^{13}C{^{1}H} NMR (500 MHz, CS_2/$CDCl_3$ 7:1 v/v, δ, ppm): 155.85, 154.50, 153.62, 147.10, 146.29, 146.11, 146.03, 145.79, 145.56, 145.35, 144.45, 143.28, 142.74, 142.25, 141.96, 140.31, 140.01, 135.61, 71.60, 61.26, 29.58, 38.15, 31.30, 30.12, 28.59.

MALDI-ToF MS (DCTB/CS_2, m/z): 791.1 $[M]^-$.

UV–Vis (ODCB): λ_{max}: 432, 706.

2.5.2.4 Synthesis of 2-(2,2,2,2',2',2'-hexafluoroisopropanyl) fulleropyrrolidine, 1c

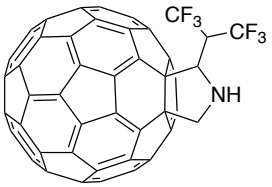

C_{60} (100 mg, 0.139 mmol), paraformaldehyde (20.8 mg, 0.695 mmol) and 4,4,4,4',4',4'-hexafluoro-DL-valine (31 mg, 0.139 mmol) were added to anhydrous oDCB (100 mL), degassed with N_2 and heated to reflux temperature for 1 h. The solvent was removed under reduced pressure, the residue was redissolved with 5 ml of CS_2, and purified by column chromatography (silica gel, toluene). And further purification was carried out by washing with 50 ml of methanol to yield the product (36 mg, 30%) as a brown solid.

^{1}H NMR (500 MHz, 297 K, CS_2/$CDCl_3$ 7:1 v/v, *δ*, ppm): 5.08 (s, 2H, CH_2), 4.72 (m, H, CH) 4.42 (m, H, CH).

^{13}C{^{1}H} NMR (500 MHz, CS_2/$CDCl_3$ 7:1 v/v, δ, ppm): 155.85, 154.50, 147.09, 146.29, 146.24, 146.11, 146.04, 145.79, 145.56, 145.40, 145.34, 145.29, 145.27, 144.48, 144.46, 143.29, 142.78, 142.76, 142.31, 142.25, 141.98, 141.86, 140.34, 140.08, 135.81, 135.63, 128.45, 126.41, 124.52 (fullerene cage sp2 carbons, 29 environments), 76.08, 71.63, 61.46 (pyrrolidine ring C), 28.62 (CH3).

MALDI-TOF MS (DCTB/CS_2, m/z): 913 $[M]^-$.

UV–Vis (ODCB): λ_{max}: 431, 700.

2.5.2.5 Synthesis of N-(4-hexylphenylcarbonyl)fulleropyrrolidine analogues, 2

Compound **1** (50 mg of **1a**; 52 mg of **1b**; 60 mg of **1c**, 0.065 mmol, 1 *equiv.*) was suspended in anhydrous DCM (50 mL) by sonicating for 15 min, and thoroughly degassed with N_2. DMAP (25 mg, 0.25 mmol, 3.8 *equiv.*) and pyridine (0.75 mL, 9.30 mmol, 143 *equiv.*) were added, and the resulting mixture was stirred for 10 min at room temperature. Then, 4-hexyl benzoyl chloride (0.17 mL, 0.75 mmol, 2.6 *equiv.*) was added and stirred for 17 hours at room temperature. The solvent was removed under the reduced pressure, the residue was redissolved in minimum amount of CS_2 and purified by column chromatography (silica gel, toluene). Further purification was carried out by washing with methanol (50 mL) to yield a brown solid as product.

***N*-(4-hexylphenylcarbonyl)fulleropyrrolidine**, **2a** (yield: 14 mg, 0.015 mmol, 23%).

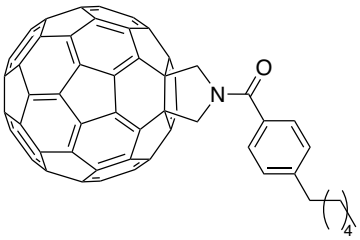

^{1}H NMR (400 MHz, $CDCl_3/CS_2$, *δ*, ppm): 7.81 (d, 2H, Ar H, *J*=8.3 Hz), 7.38 (d, 2H, Ar H, *J*=8.3 Hz), 5.55 (s, 4H, CH_2), 2.71 (t, 2H, CH_2, *J*=8.0 Hz), 1.73-1.64 (m, 2H, CH_2), 1.44 - 1.28 (m, 6H, $(CH_2)_3$), 0.86 - 0.93 (m, 3H, CH_3).

^{13}C{^{1}H} NMR (500 MHz, $CDCl_3/CS_2$, *δ*, ppm): 170.41, 153.30, 147.31, 146.46, 146.30, 146.10, 145.55, 145.49, 145.46, 145.31, 144.44, 143.07, 142.65, 142.21, 142.05, 141.89, 140.18, 135.90, 132.13, 128.79, 128.38, 70.78, 50.84, 36.07, 31.80, 31.30, 29.13, 22.75, 14.19.

MALDI-ToF MS (DCTB/CS_2, m/z): 950.73 $[M]^-$.

IR (*v*, cm^{-1}): 2915 (s), 2284 (s), 1639 (s, CON), 1394, 1074, 831, 736, 524.

UV–Vis (*o*DCB): λ_{max}: 701, 431.

***N*-(4-hexylphenylcarbonyl)-2,2-dimethyl fulleropyrrolidine**, **2b** (yield: 16 mg, 0.016 mmol, 25%).

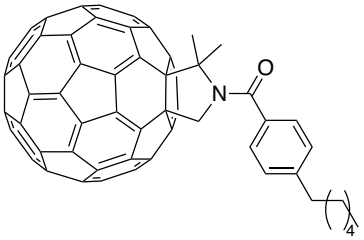

^{1}H NMR (400 MHz, $CDCl_3$, *δ*, ppm): 7.80 (d, 2H, Ar H, *J*=8.0 Hz), 7.35 (d, 2H, Ar H, *J*=8.0 Hz), 5.39 (s, 1H, CH_2), 2.69 (t, 2H, CH_2, *J*= 7.6 Hz), 2.49 (s, 6H, $(CH_3)_2$), 1.77-1.61 (m, 2H, CH_2), 1.46 - 1.27 (m, 6H, $(CH_2)_3$), 1.01 - 0.79 (m, 3H, CH_3).

^{13}C{^{1}H} NMR (400 MHz, $CDCl_3$, *δ*, ppm): 172.49, 154.55, 153.17, 147.47, 146.45, 146.35, 146.27, 146.23, 146.17, 145.58, 145.47, 145.40, 145.30, 144.58, 144.54, 143.24, 142.78, 142.74, 142.33, 142.10, 141.97, 141.90, 141.79, 140.24, 139.78, 136.25, 136.12, 134.67, 128.93, 127.98, 79.95, 70.29, 68.08, 60.80, 35.97, 31.71, 31.24, 28.99, 26.68, 22.61, 14.12.

MALDI-ToF MS (DCTB/CS_2, m/z): 978.62 $[M]^-$.

IR (*v*, cm^{-1}): 2916 (s), 2849 (s), 1778, 1649 (s, CON), 1352, 993, 746, 523.

UV–Vis (*o*DCB): λ_{max}: 701, 432.

***N*-(4-hexylphenylcarbonyl)-2-(3,3,3,3',3',3'-hexafluoroisopropanyl)fulleropyrrolidine**, **2c** (yield: 13mg, 0.012 mmol, 19%).

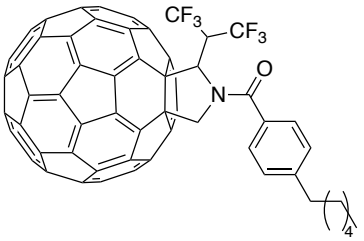

^{1}H NMR (400 MHz, $CDCl_3/CS_2$, *δ*, ppm): 7.82 (d, 2H, Ar H, *J*=8.1 Hz), 7.44 (s, 1H, CH), 7.39 (d, 2H, Ar H, *J*=8.1 Hz), 5.58 (d, 1H, CH_2, *J*= 12.3 Hz), 5.52 (d, 1H, CH_2, *J*=

12.3 Hz), 4.61 - 4.44 (m, 1H, CH), 2.72 (t, 2H, CH_2, *J*= 7.6 Hz), 1.75 - 1.62 (m, 2H, CH_2), 1.46 – 1.23 (m, 6H, $(CH_2)_3$), 0.89 (t, 3H, CH_3, *J*= 6.9 Hz).

$^{13}C\{^1H\}$ NMR (400 MHz, $CDCl_3/CS_2$, *δ*, ppm): 171.50, 154.54, 153.32, 152.09, 148.07, 147.57, 147.44, 146.60, 146.43, 146.32, 146.24, 146.18, 146.09, 145.65, 145.59, 145.53, 145.48, 145.34, 144.77, 144.50, 144.18, 143.64, 143.29, 143.13, 142.86, 142.81, 142.48, 142.34, 142.25, 142.17, 142.09, 142.01, 141.90, 141.65, 141.53, 140.40, 140.25, 140.21, 139.58, 139.35, 136.38, 134.97, 133.97, 131.29, 128.98, 128.88, 74.24, 71.30, 62.72, 61.20, 52.01, 51.74, 51.47, 36.11, 31.77, 31.27, 29.08, 22.70, 14.18.

^{19}F NMR (400 MHz, $CDCl_3/CS_2$, *δ*, ppm): -59.93, -63.76.

MALDI-ToF MS (DCTB/CS_2, m/z): 1100.47 $[M]^-$.

IR (*v*, cm^{-1}): 2918 (s), 2848 (s), 1655 (s, CON), 1286, 1160, 1084, 705, 526.

UV–Vis (*o*DCB): λ_{max}: 694, 430.

2.5.2.6 Synthesis of 2-ferrocenyl fulleropyrrolidine analogues, 3

Fullerene (50 mg, 0.069 mmol, 1 *equiv.*), ferrocene carboxaldehyde (17.8 mg, 0.083 mmol, 1.2 *equiv.*) and glycine (26 mg of N-trityl glycine for **3a**; 9 mg of 2-aminoisobutyric acid for **3b;** 19 mg of 4,4,4,4’,4’,4’-hexafluoro-DL-valine for **3c**, 0.083 mmol, 1.2 *equiv.*) were dissolved in anhydrous *o*DCB (50 mL) by sonicating for 15 min and thoroughly degassed with N_2, the resulting mixture was heated to reflux for 4 hours. The solvent was removed under reduced pressure, then re-dissolved in minimum amount of CS_2 and purified by column chromatography, further purification was carried out by washing with methanol (50 mL), giving black solid as product.

2-Ferrocenyl fulleropyrrolidine, **3a** (yield: 31 mg, 0.034 mmol, 49%). Column chromatography was eluted with toluene.

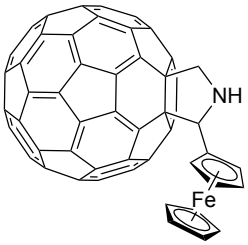

^{1}H NMR (500 MHz, $CDCl_3/CS_2$, δ, ppm): 5.53 (s, 1H, CH), 4.99 (d, 1H, CH_2, J=10.8 Hz), 4.84 (d, 1H, CH_2, J=10.8 Hz), 4.49 (d, 1H, Fc H, J= 1.2 Hz), 4.42 (d, 1H, Fc H, J= 1.2 Hz), 4.29 (s, 5H, Fc H), 4.15 (t, 2H, Fc H, J=1.8 Hz).

^{13}C{^{1}H} NMR (500 MHz, $CDCl_3/CS_2$, δ, ppm): 155.98, 153.86, 153.84, 153.79, 147.17, 147.11, 147.01, 146.69, 146.52, 146.35, 146.26, 146.23, 146.15, 146.08, 145.98, 145.94, 145.75, 145.56, 145.45, 145.42, 145.40, 145.32, 145.29, 145.25, 145.22, 145.21, 144.64, 144.43, 144.31, 143.24, 143.08, 142.76, 142.70, 142.68, 142.62, 142.50, 142.41, 142.26, 142.22, 142.22, 142.16, 142.11, 142.09, 141.95, 141.75, 141.64, 140.29, 140.25, 140.10, 139.73, 136.10, 135.95, 135.92, 135.67, 85.50, 78.56, 74.40, 74.32, 69.60, 69.18, 68.91, 68.89, 66.44, 62.37.

MALDI-ToF MS ($DCTB/CS_2$, m/z): 946.44 $[M]^-$.

IR (ν, cm^{-1}): 3083, 2916, 2326, 1423, 997, 815, 762, 524.

UV–Vis (*o*DCB): λ_{max}: 705, 432.

2-Ferrocenyl-5,5-dimethyl fulleropyrrolidine, **3b** (yield: 22 mg, 0.022 mmol, 32%). Column chromatography was eluted with toluene.

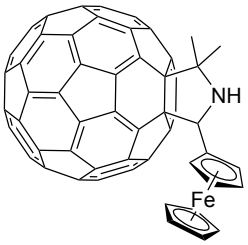

^{1}H NMR (500 MHz, $CDCl_3/CS_2$, δ, ppm): 5.85 (s, 1H, CH), 4.45 (t, 2H, Fc H, J=1.8 Hz), 4.30 (s, 5H, Fc H), 4.15 (t, 2H, Fc H, J=1.8 Hz), 2.28 (s, 3H, CH_3), 2.15 (s, 3H, CH_3).

^{13}C{^{1}H} NMR (500 MHz, $CDCl_3/CS_2$, δ, ppm): 155.26, 154.88, 154.51, 153.64, 146.92, 146.89, 146.15, 146.09, 146.03, 145.98, 145.93, 145.82, 145.75, 145.70, 145.66, 145.55, 145.20, 145.12, 145.08, 144.99, 144.95, 144.89, 144.43, 144.34, 144.17, 144.12, 143.09, 142.93, 142.57, 142.45, 142.13, 142.09, 142.03, 141.98, 141.92, 141.90, 141.82, 141.73, 141.38, 141.36, 139.88, 139.78, 139.45, 139.31, 135.87, 135.84, 135.43, 134.88, 128.23, 127.53, 85.15, 81.19, 79.79, 70.14, 69.30, 68.75, 68.49, 68.38, 65.98, 58.48, 29.88, 29.57.

MALDI-ToF MS (DCTB/CS_2, m/z): 974.78 $[M]^-$.

IR (v, cm^{-1}): 3091, 2922, 2324, 1423, 999, 809, 524.

UV–Vis (*o*DCB): λ_{max}: 707, 432.

2-Ferrocenyl-5-(3,3,3,3',3',3'-hexafluoroisopropanyl)fulleropyrrolidine, **3c,** mixture of isomers (yield: 30 mg, 0.027 mmol, 39%). Column chromatography was eluted with CS_2.

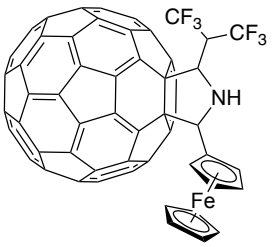

^{1}H NMR (500 MHz, $CDCl_3/CS_2$, δ, ppm): 5.58 (s, 0.5H, CH), 5.57 (s, 0.5H, CH), 5.34 – 5.32 (m, 0.5H, CH), 5.32 – 5.31 (m, 0.5H, CH), 4.68 (dd, 1H, Fc H, J= 3.3, 1.8 Hz), 4.45 (dd, 1H, Fc H, J= 3.3, 1.8 Hz), 4.28 (s, 5H, Fc H), 4.20 (t, 2H, Fc H, J= 1.9 Hz).

^{13}C{^{1}H} NMR (500 MHz, $CDCl_3/CS_2$, δ, ppm): 153.15, 152.86, 151.24, 149.56, 147.09, 146.99, 146.19, 146.07, 145.99, 145.94, 145.87, 145.84, 145.76, 145.74, 145.69, 145.60, 145.42, 145.34, 145.20, 145.14, 145.10, 145.04, 145.00, 144.95,

144.93, 144.55, 144.21, 144.17, 143.89, 143.02, 142.84, 142.49, 142.48, 142.45, 142.43, 142.06, 142.00, 141.95, 141.89, 141.86, 141.77, 141.75, 141.73, 141.53, 141.44, 141.32, 140.03, 139.91, 139.54, 138.31, 135.88, 135.86, 134.71, 128.83, 128.08, 125.19, 84.41, 75.70, 75.10, 71.61, 69.02, 68.98, 68.93, 68.81, 67.12, 65.30, 48.50, 48.29, 48.07, 47.86, 47.65.

^{19}F NMR (400 MHz, $CDCl_3/CS_2$, δ, ppm): -58.44, -66.19.

MALDI-ToF MS (DCTB/CS_2, m/z): 1097.72 $[M]^-$.

IR (ν, cm^{-1}): 1088, 1268, 1178, 562.

UV–Vis (*o*DCB): λ_{max}: 702, 431.

2.5.2.7 Synthesis of hexylbenzene, 4-(2-ferrocenyl fulleropyrrolidinyl carbonyl), 4a

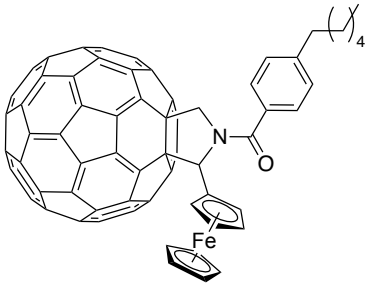

Fulleropyrrolidine, **3a** (10 mg, 0.011 mmols) and DMAP (4.1 mg, 0.033 mmols) were dissolved together in dry toluene (~ 10 mL) and degassed under inert conditions. Pyridine (0.1 mL, 1.51 mmols) was added to the reaction mixture and left to stir for 10 minutes before 4-hexylbenzoyl chloride (26 mL, 0.127 mmol) was added. The reaction mixture was left to stir overnight at room temperature under an inert atmosphere. The solvent was removed under reduced pressure, then redissolved in CS_2 and the product isolated via column chromatography (silica gel, toluene). The product was subsequently washed with methanol and isopropanol to yield a dark brown powder (6.8 mg, 56.8%).

^{1}H NMR (500 MHz, $CDCl_3/CS_2$, *δ*, ppm): 7.88 (d, 2H, Ar H, *J*=7.9 Hz), 7.63 (s,1H, CH), 7.41 (d, 2H, Ar H, *J*=7.9 Hz), 5.73 (d, 1H, CH_2, *J*= 12.0 Hz), 5.56 (d, 1H, CH_2, *J*= 12.0 Hz), 4.80 (s, 1H, Fc H), 4.61 – 4.56 (m, 1H, Fc H), 4.41 (s, 1H, Fc H), 4.36 (s, 5H, Fc H), 4.30 (s, 1H, Fc H), 2.73 (t, 2H, CH_2, *J*=7.7 Hz), 1.75 – 1.64 (m, 2H, CH_2), 1.46 – 1.20 (m, 6H, $(CH_2)_3$), 0.95 – 0.85 (m, 3H, CH_3).

^{13}C{^{1}H} NMR (500 MHz, $CDCl_3/CS_2$, *δ*, ppm): 170.24, 155.51, 153.77, 152.66, 152.29, 147.32, 147.25, 146.68, 146.30, 146.26, 146.16, 146.13, 146.05, 146.04, 145.98, 145.86, 145.60, 145.54, 145.37, 145.31, 145.29, 145.23, 145.12, 144.75, 144.66, 144.39, 144.32, 144.21, 143.08, 142.99, 142.69, 142.60, 142.55, 142.53, 142.38, 142.36, 142.23, 142.11, 142.04, 142.03, 141.96, 141.86, 141.81, 141.66, 141.57, 140.29, 140.01, 139.84, 139.78, 137.03, 136.50, 135.51, 134.34, 132.52, 128.99, 128.93, 128.57, 128.20, 125.27, 89.59, 76.19, 71.25, 70.08, 69.52, 68.62, 68.38, 66.24, 65.43, 62.16, 36.11, 31.81, 31.34, 29.15, 22.76, 14.21.

MALDI-ToF MS ($DCTB/CS_2$, m/z): 1135.80 $[M]^-$.

IR (*v*, cm^{-1}): 2916 (m), 2846, 1639 (s, CON), 1386, 1215, 997, 768, 524.

UV–Vis (*o*DCB): λ_{max}: 704, 432.

2.5.2.8 Synthesis of 2,2-dimethyl glycine methyl ester hydrochloride

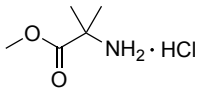

2,2-Dimethylisobutyric acid (4.12 g, 40 mmol, 1 *equiv*.) was added to 100 mL of methanol, the mixture was cooled down to 0 °C followed by adding thionyl chloride (14.5 mL, 200 mmol, 5 *equiv*.). The mixture was allowed to warm up to room temperature and stirred for 24 hours. The reaction was dried out using schlenk line with two liquid N_2 traps. The residue was added with 50 mL of DCM, filtered, giving white solid as product (4.1 g, 67%).

^{1}H NMR (400 MHz, $CDCl_3$, *δ*, ppm): 8.95 (s, 3H, NH_2•HCl), 3.81 (s, 3H, OCH_3), 1.72, (s, 6H, $C(CH_3)_2$).

^{13}C{^{1}H} NMR (400 MHz, $CDCl_3$, *δ*, ppm): 171.69 (C=O), 57.51, 53.39, 23.96.

2.5.2.9 Synthesis of 4-hexylbenzaldehyde

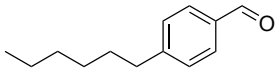

Hexylbenzene (1.82 g, 11 mmol, 1 *equiv*.) and hexamethylenetetramine (1.65 mg, 12 mmol, 1.1 *equiv*.) were added to trifluoro acetic acid (10 mL), the resulting mixture was heated at 80 °C overnight. The reaction mixture was allowed to cool down to room temperature, concentrated under reduced pressure using Schlenk line technique. The mixture was diluted with diethyl ether (50 mL), washed with aq $NaHCO_3$ (1 M) and dried over $MgSO_4$. The organic layer was concentrated, the residue was passed through column chromatography (SiO_2, DCM/hexane v/v 1/1), giving colourless oil (470 mg, 22%) as product.

^{1}H NMR (400 MHz, $CDCl_3$, *δ*, ppm): 9.91 (s, 1H, CHO), 7.75 (d, 2H, Ar H, *J*=8 Hz), 7.28 (d, 2H, Ar H, *J*=8 Hz), 2.63 (t, 2H, CH_2), 1.60 (m, 2H, CH_2), 1.29 (m, 6H, $(CH_2)_3$), 0.87 (m, 2H, CH_3).

^{13}C{^{1}H} NMR (400 MHz, $CDCl_3$, *δ*, ppm): 191.70 (CHO), 150.30, 134.42, 129.78, 128.97 (Ar C), 36.13, 31.63, 31.00, 28.92, 22.55, 14.01.

LC-MS (m/z): 191.14 $[M+H]^+$.

2.5.2.10 Synthesise N-substituted glycine methyl esters, ME1-4

Methyl ester hydrochloride (372 mg of glycine methyl ester hydrochloride for **ME1** and **ME2**; 455 mg of 2,2-dimethyl glycine methyl ester hydrochloride for **ME3** and **ME4**, 2.96 mmol, 1 *equiv.*) and benzaldehyde (500 mg of 3,5-ditert-butylbenzaldehyde for **ME1** and **ME2**; 435 mg of 4-hexylbenzaldehyde for **ME3** and **ME4**, 2.29 mmol, 0.77 *equiv.*) were degassed with N_2, added with DCM (15 mL) and Et_3N (0.41 mL, 2.97

mmol, 1 *equiv.*), the resulting mixture was stirred at room temperature for 17 hours with the presence of 4 Å molecular sieves. The reaction mixture was filtered, the filtrate was added with $NaBH(OAc)_3$ (0.63 g, 2.97 mmol, 1 *equiv.*) and AcOH (2 mL), and the resulting mixture was stirred at room temperature for 17 hours under N_2. The solvent was removed, methanol (5 mL) was readded to the residue, cooled to 0 °C, $NaHCO_3$ (1 M) was used to adjust the pH to 7. The resulting mixture was extracted in DCM (4 X 15 mL), the organic layer was combined, washed with water, and dried over $MgSO_4$. Further purification was carried out by column chromatography to give the product.

***N*-((3,5-di-tert-butylphenyl)methyl)glycine methyl ester**, **ME1**, was purified by column chromatography (silica gel, petroleum ether/ethyl acetate v/v 10/1->10/2), giving colourless oil as product (249 mg, 0.86 mmol, 37%).

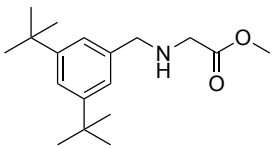

^{1}H NMR (400 MHz, $CDCl_3$, *δ*, ppm): 7.33 (s, 1H, Ar H), 7.17 (s, 2H, Ar H), 3.79 (s, 2H, CH_2), 3.70 (s, 3H, OCH_3), 3.45 (s, 2H, CH_2), 1.33 (s, 18H, $C(CH_3)_3$).

^{13}C{^{1}H} NMR (400 MHz, $CDCl_3$, *δ*, ppm): 172.91 (C=O), 150.87, 138.45, 122.52, 121.25 (Ar C), 54.00, 51.69, 50.06, 34.83, 31.55.

LC-MS (m/z): 292.23 $[M+H]^+$.

***N*-((3,5-di-tert-butylphenyl)methyl)-2,2-dimethyl glycine methyl ester**, **ME2**, was purified by column chromatography (silica gel, DCM), giving white solid as product (570 mg, 1.78 mmol, 80%).

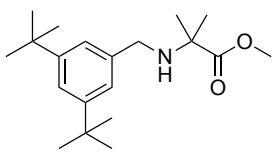

^{1}H NMR (400 MHz, $CDCl_3$, *δ*, ppm): 7.24 (s, 1H, Ar H), 7.09 (s, 2H, Ar H), 3.65 (s, 3H, OCH_3), 3.53 (s, 2H, CH_2), 1.30 (s, 6H, $(CH_3)_2$), 1.25 (s, 18H, $C(CH_3)_3$).

^{13}C NMR (400 MHz, $CDCl_3$, *δ*, ppm): 176.53 (C=O), 149.77, 138.20, 121.48, 120.15 (Ar C), 58.42, 50.84, 48.73, 33.77, 30.47, 24.35.

LC-MS (m/z): 320.26 $[M+H]^+$.

***N*-((4-hexylphenyl)methyl)glycine methyl ester**, **ME3**, was purified by column chrogatography (silica gel, DCM -> DCM/methanol v/v 99/1), giving colourless oil (277 mg, 1.05 mmol, 46%) as product.

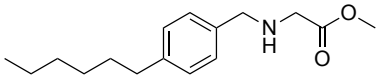

^{1}H NMR (400 MHz, $CDCl_3$, *δ*, ppm): 7.22 (d, 2H, ArH, *J*=8 Hz), 7.12 (d, 2H, ArH, *J*=8 Hz), 3.75 (s, 2H, CH_2), 3.70 (s, 3H, OCH_3), 3.40 (s, 2H, CH_2), 2.57 (t, 2H, CH_2, *J*=8 Hz), 1.59 (m, 2H, CH_2), 1.30 (m, 6H, $(CH_2)_3$)), 0.88 (m, 3H, CH_3).

^{13}C{^{1}H} NMR (400 MHz, $CDCl_3$, *δ*, ppm): 172.89 (C=O), 141.85, 136.65, 128.48, 128.20 (ArC), 53.05, 51.69, 49.89, 35.64, 31.75, 31.52, 29.00, 22.62, 14.10.

LC-MS (m/z): 264.20 $[M+H]^+$.

***N*-((4-hexylphenyl)methyl)-2,2-dimethyl glycine methyl ester**, **ME4**, was purified by column chrogatography (silica gel, DCM->2%methanol/DCM), giving colourless oil (286 mg, 0.98 mmol, 43%) as product.

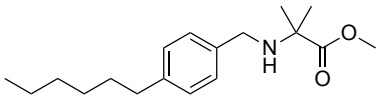

^{1}H NMR (400 MHz, $CDCl_3$, *δ*, ppm): 7.15 (d, 2H, ArH, *J*=8 Hz), 7.03 (d, 2H, ArH, *J*=8 Hz), 3.62 (s, 3H, OCH_3), 3.49 (s, 2H, CH_2), 2.48 (t, 2H, CH_2, *J*=8 Hz), 1.50 (m, 2H, CH_2), 1.27 (s, 6H, $(CH_3)_2$), 1.21 (m, 6H, $(CH_2)_3$), 0.79 (m, 3H, CH_3).

^{13}C{^{1}H} NMR (400 MHz, $CDCl_3$, *δ*, ppm): 141.70 (C=O),141.70, 137.47, 128.50, 128.27 (ArC), 59.32, 51.86, 48.84, 35.65, 31.77, 31.55, 28.99, 25.42, 22.64, 14.12.

LC-MS (m/z): 292.23 $[M+H]^-$.

2.5.2.11 Synthesis of amino acid AA1,2 and AA4,5

ME (1.68 mmol, 1 *equiv.*) was dissolved in methanol (10 mL), NaOH (150 mg, 3.75 mmol, 2.23 *equiv.*) was added, the resulting mixture was stirred at room temperature for 72 hours. Th solvent was removed, the residue was added with water (2 mL), which was adjusted to pH to 6.7 by adding HCl (1 M) slowly. The resulting white precipitate was centrifuged with water (11000 rpm x 5 min x 3) to give the crude product. The precipitate was washed in $CHCl_3$ (5 mL) giving product as white solid.

***N*-((3,5-di-tert-butylphenyl)methyl)glycine**, **AA1** (yield: 306 mg, 1.10 mmol, 66%).

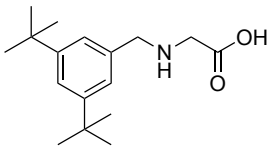

^{1}H NMR (400 MHz, D4-methanol, *δ*, ppm): 7.41 (s, 1H, ArH), 7.26 (s, 1H, ArH), 4.08 (s, 2H, CH_2), 3.38 (s, 2H, CH_2), 1.24 (s, 18H, $C(CH_3)_3$).

^{13}C{^{1}H} NMR (400 MHz, D4-methanol, *δ*, ppm): 169.35 (C=O), 151.72, 130.72, 123.72, 123.09 (ArC), 51.05, 48.40, 34.43, 30.39.

LC-MS (m/z): 276.20 $[M-H]^-$.

***N*-((3,5-di-tert-butylphenyl)methyl)-2,2-dimethyl glycine**, **AA2** (yield: 370 mg, 1.21 mmol, 80%).

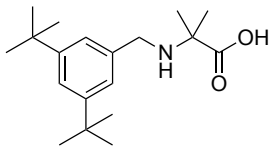

^{1}H NMR (400 MHz, D4-methanol, *δ*, ppm): 7.40 (s, 1H, ArH), 7.30 (s, 2H, ArH), 4.01 (s, 2H, CH_2), 1.45 (s, 6H, $(CH_3)_2$), 1.25 (s, 18H, $C(CH_3)_3$).

^{13}C{^{1}H} NMR (400 MHz, D4-methanol, *δ*, ppm): 174.81 (C=O), 151.54, 131.51, 123.88, 122.93 (ArC), 63.91, 47.75, 34.43, 30.41, 21.78.

LC-MS (m/z): 304.23 $[M-H]^-$.

***N*-((4-hexylphenyl)methyl)glycine**, **AA4** (yield: 250 mg, 1 mmol, 60%).

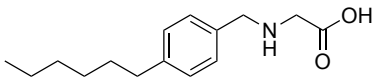

^{1}H NMR (400 MHz, D4-methanol, *δ*, ppm): 7.28 (d, 2H, ArH, *J*=8 Hz), 7.17 (d, 2H, ArH, *J*=8 Hz), 4.06 (s, 2H, CH_2), 3.37 (s, 2H, CH_2), 2.54 (t, 2H, CH_2, *J*=8 Hz), 1.52 (m, 2H, CH_2), 1.22 (m, 6H, $(CH_2)_3$), 0.79 (m, 3H, CH_3).

^{13}C{^{1}H} NMR (400 MHz, D4-methanol, *δ*, ppm): 169.25 (C=O), 144.37, 129.52, 128.88, 128.63 (ArC), 50.28, 48.33, 35.18, 31.44, 31.13, 28.54, 22.26, 12.98.

LC-MS (m/z): 248.17 $[M-H]^-$.

***N*-((4-hexylphenyl)methyl)-2,2-dimethyl glycine**, **AA5** (yield: 287 mg, 1.04 mmol, 62%).

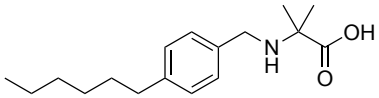

^{1}H NMR (400 MHz, D4-methanol, *δ*, ppm): 7.33 (d, 2H, ArH, *J*=8 Hz), 7.16 (d, 2H, ArH, *J*=8 Hz), 3.99 (s, 2H, CH_2), 2.54 (t, 2H, CH_2, *J*=8 Hz), 1.51 (m, 2H, CH_2), 1.44 (s, 6H, $(CH_3)_2$), 1.21 (m, 6H, $(CH_2)_3$), 0.79 (m, 3H, CH_3).

^{13}C{^{1}H} NMR (400 MHz, D4-methanol, *δ*, ppm): 174.73 (C=O), 144.12, 129.62, 129.50, 128.77 (ArC), 63.85, 46.96, 35.17, 31.44, 31.18, 28.49, 22.27, 21.75, 12.97.

LC-MS (m/z): 276.20 $[M-H]^-$.

2.5.2.12 Synthesise of N-substituted-4,4,4,4',4',4'-DL-valine, AA3 and AA6

4,4,4,4',4',4'-Hexafluoro-DL-valine (250 mg, 1.11 mmol, 1 *equiv.*) and substituted benzaldehyde (187 mg of 3,5-ditert-butylbenzaldehyde for **AA3**; 164 mg of 4-hexylbenzaldehyde for **AA6**, 0.86 mmol, 0.77 *equiv.*) were added to degassed round bottom flask with 4 Å molecular sieves inside, followed by adding with anhydrous methanol (6 mL). The resulting mixture was stirred at room temperature under N_2 for

overnight. The mixture was filtered, the filtrate was dried up, then, added with anhydrous DCM (8mL), $NaBH(OAc)_3$ (236 mg, 1.11 mmol, 1 *equiv.*) and AcOH (0.75 mL), the resulting mixture was concentrated to 4 mL using Schlenk line technique, stirred at room temperature under N_2 for 3 days. The solvent was removed, the residue was added with 2 mL of water and cooled down to 0 °C, $NaHCO_3$ (1 M) was used to adjust the pH to 6.7. The mixture was centrifuged with water (11000 rpm x 5 min x 3) to give the crude product. the precipitate was then washed with DCM (5 mL) giving product (215 mg, 45%) as white solid.

***N*-((3,5-di-tertbutylphenyl)methyl)-4,4,4,4',4',4'-DL-valine**, **AA3**. The crude product was washed with DCM (5 mL), giving white solid (215 mg, 0.53 mmol, 45%) as product.

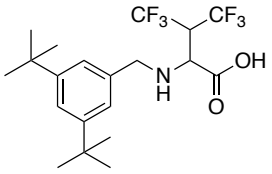

^{1}H NMR (400 MHz, D4-methanol, *δ*, ppm): 7.30 (s, 1H, Ar H), 7.15 (s, 2H, Ar H), 4.01 (septuple d, 1H, CH, *J*=8 Hz, 4 Hz), 4.01 (d, 1H, CH_2, *J*=12 Hz), 3.85 (d, 1H, CH_2, *J*=12 Hz), 3,76 (d, 1H, CH, *J*=4 Hz).

^{13}C{^{1}H} NMR (500 MHz, D4-methanol, *δ*, ppm): 170.17 (COOH), 150.94, 135.14, 123.34, 123.23 (CF_3C), 123.12, 121.66, 55.06, 52.92, 49.65, 34.28, 30.42.

^{19}F NMR (400 MHz, D4-methanol, *δ*, ppm): -63.22, -66.11.

LC-MS (m/z): 426 $[M-H]^-$.

***N*-((4-hexylphenyl)methyl)-4,4,4,4',4',4'-DL-valine**, **AA6**. The crude was washed with chloroform (5 mL), giving product (156 mg, 0.39 mmol, 35%) as white solid.

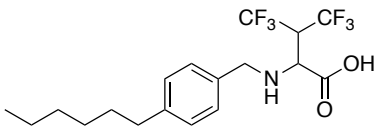

^{1}H NMR (400 MHz, D4-methanol, *δ*, ppm): 7.17 (d, 2H, Ar H, *J*=8 Hz), 7.06 (d, 2H, Ar H, *J*=8 Hz), 3.99 (septuple d, 1H, CH, *J*=8 Hz, 4 Hz), 3.94 (d, 1H, CH_2, *J*=12 Hz), 3.76 (d, 1H, CH_2, *J*=12 Hz), 3.69 (d, 1H, CH, *J*= 4 Hz), 2.50 (t, 2H, CH_2, *J*=8 Hz), 1.50 (m, 2H, CH_2), 1.22 (m, 6H, CH_2), 0.79 (m, 3H, CH_3).

^{13}C{^{1}H} NMR (500 MHz, D4-methanol, *δ*, ppm): 170.28 (COOH), 142.59, 133.78, 128.73, 128.26 (Ar C), 123.26, 123.22 (CF_3 C), 55.25, 52.36, 49.72. 35.19, 31.47, 31.25, 28.55, 22.27, 12.99.

^{19}F NMR (400 MHz, D4-methanol, *δ*, ppm): -63.29, -66.13.

LC-MS (m/z): 398.16 $[M-H]^-$.

2.5.2.13 Synthesis of N-(3,5-di-tert-butylphenylmethyl)fulleropyrrolidine analogues, 5

C_{60} (50 mg, 0.070 mmol, 1 *equiv.*), paraformaldehyde (11 mg, 0.35 mmol, 5 *equiv*.) and corresponding amino acid (23 mg of **AA1**; 26 mg of **AA2**; 36 mg of **AA3**, 0.084 mmol,1.2 *equiv.*) were dissolved in toluene (50 mL) by sonicating for 15 minutes, and thoroughly degassed with N_2. The resulting mixture was heated to reflux for 4 hours. The solvent was removed under reduced pressure, the residue was re-dissolved with minimum amount of CS_2, and purified by column chromatography (silica gel, CS_2). Further purification was carried out my washing with methanol (50 mL) giving black solid as product.

***N*-(3,5-di-tert-butylphenylmethyl)fulleropyrrolidine**, **5a** (yield: 44 mg, 0.046 mmol, 65%).

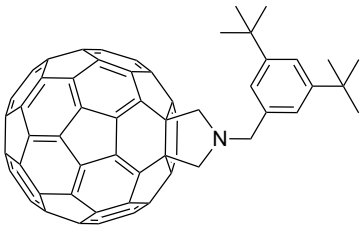

^{1}H NMR (400 MHz, $CDCl_3$, *δ*, ppm): 7.58 (d, 2H, Ar H, *J*= 1.7 Hz), 7.43 (t, 1H, Ar H, *J*= 1.7 Hz, 1H), 4.46 (s, 4H, pyridine H), 4.33 (s, 2H, CH_2), 1.40 (s, 18H, $(CH_3)_3C$).

^{13}C{^{1}H} NMR (400 MHz, $CDCl_3$, *δ*, ppm): 155.21, 151.09, 147.33, 146.28, 146.19, 146.09, 145.77, 145.43, 145.32, 144.61, 143.12, 142.65, 142.31, 142.11, 141.89, 140.16, 137.19, 136.31, 122.96, 121.37, 70.96, 67.30, 58.71, 34.98, 31.64.

MALDI-ToF MS (DCTB/CS_2, m/z): 965.39 $[M]^-$.

IR (*v*, cm^{-1}): 2946 (m), 2771 (m), 1595, 709, 524.

UV–Vis (*o*DCB): λ_{max}: 706, 432.

***N*-(3,5-di-tert-butylphenylmethyl)-2,2-dimethyl fulleropyrrolidine, 5b** (yield: 20 mg, 0.020 mmol, 29%).

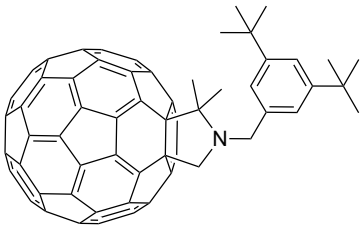

^{1}H NMR (400 MHz, $CDCl_3$, *δ*, ppm): 7.68 (s, 2H, Ar H), 7.39 (s, 1H, Ar H), 4.53 (s, 2H, CH_2), 4.26 (s, 2H, CH_2), 2.08 (s, 6H, $(CH_3)_2$), 1.41 (s, 18 H, $(CH_3)_3C$).

^{13}C{^{1}H} NMR (500 MHz, $CDCl_3$, *δ*, ppm): 156.52, 154.71, 151.02, 147.33, 146.75, 146.27, 146.24, 146.15, 146.03, 145.73, 145.32, 145.27, 145.26, 145.22, 144.62, 144.56, 143.15, 142.64, 142.61, 142.42, 142.18, 142.08, 141.77, 141.67, 140.12, 139.73, 138.80, 136.58, 136.08, 132.56, 130.54, 127.71, 122.04, 120.97, 79.60, 69.42, 68.87, 61.79, 50.92, 50.63, 34.99, 31.59, 23.74.

MALDI-ToF MS (DCTB/CS_2, m/z): 993.34 $[M]^-$.

IR (*v*, cm^{-1}): 2914 (m), 1360, 1184, 709, 524.

UV–Vis (*o*DCB): λ_{max}: 707, 433.

***N*-(3,5-di-tert-butylphenylmethyl)-2-(3,3,3,3',3',3'-hexafluoroisopropyl)fulleropyrrolidine, 5c** (yield: 37 mg, 0.033 mmol, 47%).

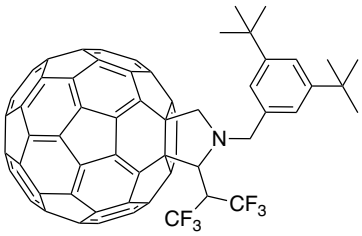

^{1}H NMR (400 MHz, $CDCl_3$, *δ*, ppm): 7.52 (s, 2H, Ar H), 7.45 (s, 1H, Ar H), 5.47(s, 1H, CH), 4.96 (d, 1H, CH_2, *J*=12.1 Hz), 4.86 (d, 1H, CH_2, *J*=13.2 Hz), 4.61 (d, 1H, CH_2, *J*=13.2 Hz), 4.56 (d, 1H, CH_2, *J*=12.1 Hz), 4.56 (m, 1H, CH), 1.39 (s, 18H, $(CH_3)_3C$).

^{13}C{^{1}H} NMR (500 MHz, $CDCl_3$, *δ*, ppm): 155.23, 155.08, 154.76, 151.23, 149.69, 147.36, 147.18, 146.46, 146.31, 146.25, 146.12, 146.07, 146.01, 145.88, 145.69, 145.59, 145.51, 145.43, 145.42, 145.32, 145.31, 145.27, 144.70, 144.54, 144.47, 144.39, 144.18, 143.27, 143.21, 143.10, 142.74, 142.71, 142.69, 142.32, 142.30, 142.20, 142.17, 142.13, 141.95, 141.93, 141.86, 141.78, 140.35, 140.33, 140.23, 139.53, 138.69, 137.54, 135.65, 134.57, 134.43, 132.57, 130.54, 127.71, 122.90, 121.61, 74.03, 71.94, 67.34, 61.06, 51.66, 34.93, 31.53.

^{19}F NMR (400 MHz, $CDCl_3$, *δ*, ppm): -58.05, -66.33.

MALDI-ToF MS (DCTB/CS_2, m/z): 1115.09 $[M]^-$.

IR (*v*, cm^{-1}): 2948 (m), 1272, 1170, 1086, 709, 526.

UV–Vis (*o*DCB): λ_{max}: 700, 431.

2.5.2.14 Synthesis of N-(3,5-di-tert-butylphenylmethyl)-2-ferrocenyl fulleropyrrolidine analogues, 6

C_{60} (50 mg, 0.070 mmol, 1 *equiv.*), ferrocene carboxaldehyde (18 mg, 0.084 mmol, 1.2 *equiv*.) and corresponding amino acid (23 mg of **AA1**; 26 mg of **AA2**; 36 mg of **AA3**, 0.084 mmol, 1.2 *equiv.*) were dissolved in toluene (50 mL) by sonicating for 15

minutes, and thoroughly degassed with N_2. The resulting mixture was heated to reflux condition (4 hours for **6a**; 17 hours for **6b**; 24 hours for **6c**). Upon completion the solvent was removed under reduced pressure, the residue was re-dissolved with minimum amount of CS_2, and purified by column chromatography (silica gel, CS_2). Further purification was carried out my washing with methanol (50 mL) giving black solid as product.

***N*-(3,5-di-tert-butylphenylmethyl)-2-ferrocenyl fulleropyrrolidine**, **6a** (yield: 25 mg, 0.022 mmol, 31%).

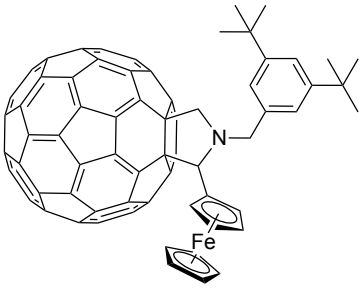

^{1}H NMR (400 MHz, $CDCl_3$, δ, ppm): 7.74 (s, 2H, Ar H), 7.46 (s, 1H, Ar H), 6.17 (d, 1H, CH_2, J=13.7 Hz), 5.23 (s, 1H, CH), 4.84 (d, 1H, CH_2, J=9.5 Hz), 4.60 (m, 2H, Fc H), 4.33 (s, 5H, FcH), 4.25 (m, 2H, Fc H), 4.13 (d, 1H, CH_2, J=9.5 Hz), 3.91 (d, 1H, CH_2, J=13.7 Hz), 1.43 (s, 18H, $(CH_3)_3C$).

^{13}C{^{1}H} NMR (400 MHz, $CDCl_3$, δ, ppm): 156.55, 154.39, 154.14, 153.38, 151.28, 147.73, 147.26, 146.60, 146.34, 146.24, 146.14, 146.06, 145.94, 145.87, 145.61, 145.51, 145.45, 145.23, 144.75, 144.69, 144.46, 143.10, 143.00, 142.69, 142.60, 142.25, 142.05, 141.80, 141.60, 141.46, 140.18, 140.02, 139.48, 138.86, 138.75, 136.38, 136.27, 136.14, 135.88, 122.22, 121.15, 86.67, 78.25, 75.40, 69.41, 68.58, 68.33, 67.69, 67.49, 67.38, 67.20, 57.36, 35.07, 31.69.

MALDI-ToF MS (DCTB/CS_2, m/z): 1149.12 $[M]^-$.

IR (ν, cm^{-1}): 2918 (s), 1594, 815, 524.

UV–Vis (*o*DCB): λ_{max}: 704, 432.

***N*-(3,5-di-tert-butylphenylmethyl)-2,2-dimethyl-5-ferrocenyl fulleropyrrolidine**, **6b** (yield: 24 mg, 0.020 mmol, 29%).

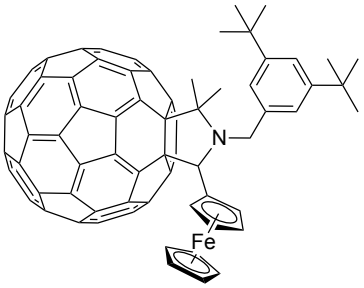

^{1}H NMR (400 MHz, $CDCl_3$, *δ*, ppm): 7.78 (s, 2H, Ar H), 7.24 (s, 1H, Ar H), 6.25 (d, 1H, CH_2, *J*= 17.1 Hz), 5.72 (s, 1H, CH), 4.45 (s, 1H, Fc H), 4.32 (d, 1H, CH_2, J = 17.1 Hz), 4.28 (s, 1H, Fc H), 4.12 (s, 5H, Fc H), 4.09 (s, 1H, Fc H), 4.02 (s, 1H, Fc H), 2.16 (s, 3H, CH_3), 1.75 (s, 3H, CH_3), 1.39 (s, 18H, $(CH_3)_3C$).

^{13}C{^{1}H} NMR (400 MHz, $CDCl_3$, *δ*, ppm): 156.19, 156.13, 153.92, 153.75, 150.59, 148.12, 147.35, 146.83, 146.60, 146.45, 146.36, 146.16, 145.94, 145.61, 145.54, 145.39, 145.27, 145.17, 144.90, 144.71, 144.52, 144.40, 143.27, 143.20, 143.11, 142.82, 142.68, 142.32, 142.23, 142.06, 141.97, 141.88, 141.75, 141.48, 141.42, 140.01, 139.50, 138.84, 136.92, 136.77, 136.23, 135.44, 121.36, 120.25, 88.05, 70.99, 70.50, 69.82, 69.02, 68.70, 67.90, 67.42, 47.61, 34.95, 31.88, 28.62, 19.77.

MALDI-ToF MS (DCTB/CS_2, m/z): 1177.05 $[M]^-$.

IR (*v*, cm^{-1}): 2946, 1594, 1360, 1178, 813, 524.

UV–Vis (*o*DCB): λ_{max}: 706, 433.

***N*-(3,5-di-tert-butylphenylmethyl)-2-DL-(2,2,2,2',2',2'-hexafluoroisopropyl)-5-DL-ferrocenyl fulleropyrrolidine**, **6c** (yield: 8 mg, 0.006 mmol, 9%).

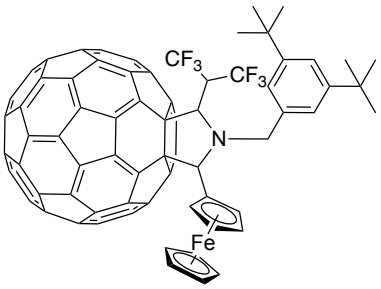

^{1}H NMR (500 MHz, $CDCl_3/CS_2$ v/v 7/1, *δ*, ppm): 7.45 (d, 2H, Ar H, *J*= 1.6 Hz, 1H), 7.36 (t, 1H, Ar H, *J*= 1.8 Hz), 5.77 (s, 1H, CH), 5.66 (d, 1H, CH, *J*= 6.0 Hz), 5.48 (d, 1H, CH_2, *J*= 12.0 Hz), 5.23 (d, 1H, CH_2, *J*= 12.0 Hz), 4.44 – 4.40 (m, 2H, Fc H), 4.46 – 4.32 (m, 1H, CH), 4.39 (s, 5H, Fc H), 4.30 – 4.26 (m, 1H, Fc H), 4.25 – 4.21 (m, 1H, Fc H), 1.32 (s, 18H, $(CH_3)_3C$).

^{13}C{^{1}H} NMR (500 MHz, $CDCl_3/CS_2$ v/v 7/1, *δ*, ppm): 155.83, 154.53, 154.02, 150.86, 149.59, 146.88, 146.61, 146.53, 146.22, 146.04, 145.98, 145.88, 145.86, 145.81, 145.76, 145.70, 145.65, 145.43, 145.26, 145.12, 145.08, 145.05, 145.02, 144.99, 144.86, 144.33, 144.26, 144.22, 143.69, 142.98, 142.79, 142.55, 142.52, 142.51, 142.43, 142.13, 142.02, 141.94, 141.91, 141.76, 141.75, 141.71, 141.65, 141.63, 141.36, 141.23, 139.89, 139.66, 139.53, 138.62, 137.63, 135.41, 134.91, 134.34, 134.02, 124.97, 121.60, 88.21, 81.92, 80.80, 78.68, 72.18, 70.13, 69.97, 69.56, 69.41, 68.97, 68.00, 67.58, 53.80, 52.43, 52.23, 52.02, 51.81, 51.61, 34.47, 31.34, 31.21, 29.90.

MALDI-ToF MS (DCTB/CS_2, m/z): 1298.73 $[M]^-$.

IR (*v*, cm^{-1}): 2948 (m), 1598, 1168, 815, 711, 524.

UV–Vis (*o*DCB): λ_{max}: 696, 431.

2.5.2.15 Synthesis of N-(4-hexylphenylmethyl)fulleropyrrolidine analogues, 7

C_{60} (50 mg, 0.070 mmol, 1 *equiv.*), paraformaldehyde (11 mg, 0.35 mmol, 5 *equiv*.) and corresponding amino acid (21 mg of **AA4**; 23 mg of **AA5**; 34 mg of **AA6**, 0.084 mmol,1.2 *equiv.*) were dissolved in toluene (50 mL) by sonicating for 15 minutes, and thoroughly degassed with N_2. The resulting mixture was heated to reflux for 4 hours. The solvent was removed under reduced pressure, the residue was re-dissolved with minimum amount of CS_2, and purified by column chromatography (silica gel, CS_2).

Further purification was carried out my washing with methanol (50 mL) giving black solid as product.

***N*-(4-hexylphenylmethyl)fulleropyrrolidine**, **7a** (37 mg, 0.040 mmol, 57%).

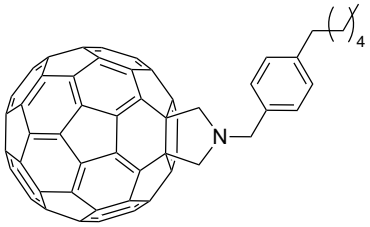

^{1}H NMR{^{1}H} (400 MHz, $CDCl_3$, *δ*, ppm): 7.61 (d, 2H, Ar H, *J*=8.0 Hz), 7.30 (d, 2H, Ar H, *J*=8.0 Hz), 4.43 (s, 4H, CH_2), 4.28 (s, 2H, CH_2), 2.68 (t, 2H, CH_2, *J*=7.6 Hz), 1.68 (m, 2H, CH_2), 1.34 (m, 6H, CH_2), 0.90 (m, 3H, CH_3).

^{13}C{^{1}H} NMR (500 MHz, $CDCl_3$, *δ*, ppm): 155.14, 147.31, 146.25, 146.13, 146.07, 145.72, 145.40, 145.30, 144.58, 143.10, 142.63, 142.38, 142.28, 142.08, 141.88, 140.13, 136.27, 135.05, 128.85, 128.71, 70.78, 67.50, 58.59, 35.78, 31.76, 31.54, 29.13, 22.63, 14.13.

MALDI-ToF MS (DCTB/CS_2, m/z): 936.76 $[M]^-$.

IR (*v*, cm^{-1}): 2912 (m), 1421, 1086, 764, 524.

UV–Vis (*o*DCB): λ_{max}: 706, 432.

***N*-(4-hexylphenylmethyl)-2,2-dimethyl fulleropyrrolidine**, **7b** (39 mg,0.040 mmol, 57%).

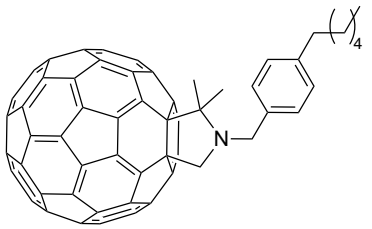

^{1}H NMR (400 MHz, $CDCl_3$, *δ*, ppm): 7.65 (d, 2H, Ar H, *J*=8.0 Hz), 7.28 (d, 2H, Ar H, *J*=8.0 Hz), 4.47 (s, 2H, CH_2), 4.19 (s, 2H, CH_2), 2.68 (t, 2H, CH_2, *J*=7.6 Hz), 2.70 (s, 6H, $(CH_3)_2$), 1.67 (m, 2H, CH_2), 1.33 (m, 6H, CH_2), 0.89 (m, 3H, CH_3).

$^{13}C\{^1H\}$ NMR (400 MHz, $CDCl_3$, *δ*, ppm): 156.52, 154.68, 147.35, 146.67, 146.26, 146.24, 146.18, 146.04, 145.70, 145.29, 145.23, 144.63, 144.58, 143.18, 142.65, 142.63, 142.51, 142.21, 142.10, 142.03, 141.98, 141.80, 141.70, 140.11, 139.73, 136.71, 136.62, 136.07, 128.71, 128.15, 79.50, 69.69, 68.78, 62.32, 50.99, 35.78, 31.79, 31.58, 29.16, 23.79, 22.66, 14.16.

MALDI-ToF MS (DCTB/CS_2, m/z): 965.09 $[M]^-$.

IR (*v*, cm^{-1}): 2912 (m), 1421, 1182, 762, 524.

UV–Vis (*o*DCB): λ_{max}: 708, 433.

***N*-(4-hexylphenylmethyl)-2-(2,2,2,2',2',2'-hexafluoroisopropyl)fulleropyrrolidine, 7c** (18 mg, 0.017 mmol, 24%).

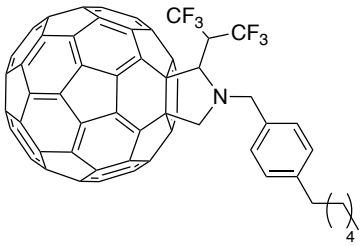

^1H NMR (400 MHz, $CDCl_3$, *δ*, ppm): 7.56 (d, 2H, Ar H, *J*=7.9 Hz), 7.29 (d, 2H, Ar H, *J*=7.9 Hz), 5.30 (s, 1H, CH), 4.19 (s, 2H, CH_2), 4.88 (d, 1H, CH_2, *J*=11.8 Hz), 4.87 (d, 1H, CH_2, *J*=12.9 Hz), 4.62 (m, 1H, CH), 4.42 (d, 1H, CH_2, *J*=11.8 Hz), 4.37 (d, 1H, CH_2, *J*=12.9 Hz), 2.67 (t, 2H, CH_2, *J*=7.7 Hz), 1.67 (m, 2H, CH_2), 1.33 (m, 6H, CH_2), 0.90 (m, 3H, CH_3).

$^{13}C\{^1H\}$ NMR (500 MHz, $CDCl_3$, *δ*, ppm): 155.11, 154.94, 154.19, 149.69, 147.40, 147.23, 146.48, 146.32, 146.27, 146.14, 146.10, 146.08, 146.06, 146.04, 145.72, 145.69, 145.66, 145.55, 145.51, 145.44, 145.37, 145.32, 145.30, 145.27, 144.75, 144.54, 144.43, 144.41, 144.24, 143.24, 142.75, 142.74, 142.69, 142.63, 142.29, 142.19, 142.14, 142.12, 141.98, 141.93, 141.90, 141.86, 141.83, 141.73, 140.34, 140.30, 140.27, 139.58, 138.75, 135.85, 135.59, 134.82, 134.45, 128.83, 128.69, 73.96, 71.06, 67.50, 60.37, 51.19, 50.93, 35.77, 31.76, 31.55, 29.10, 22.63, 14.13.

MALDI-ToF MS (DCTB/CS_2, m/z): 1087.31 $[M]^-$.

IR (ν, cm^{-1}): 2916 (m), 1511, 1329, 1272, 1084, 1170, 709, 524.

UV–Vis (*o*DCB): λ_{max}: 700, 431.

2.5.2.16 Synthesis of N-(4-hexylphenylmethyl)-2-ferrocenyl fulleropyrrolidine analogues, 8

C_{60} (50 mg, 0.070 mmol, 1 *equiv.*), ferrocene carboxaldehyde (18 mg, 0.084 mmol, 1.2 *equiv*.) and corresponding amino acid (21 mg of **AA4**; 23 mg of **AA5**; 34 mg of **AA6**, 0.084 mmol, 0.084 mmol, 1.2 *equiv.*) were dissolved in toluene (50 mL) by sonicating for 15 minutes, and thoroughly degassed with N_2. The resulting mixture was heated to reflux condition (4 hours for **8a**; 17 hours for **8b**; 24 hours for **8c**). Upon completion the solvent was removed under reduced pressure, the residue was re-dissolved with minimum amount of CS_2, and purified by column chromatography (silica gel, CS_2). Further purification was carried out my washing with methanol (50 mL) giving black solid as product.

***N*-(4-hexylphenylmethyl)-2-ferrocenyl fulleropyrrolidine analogues**, **8a** (30 mg, 0.027 mmol, 38%).

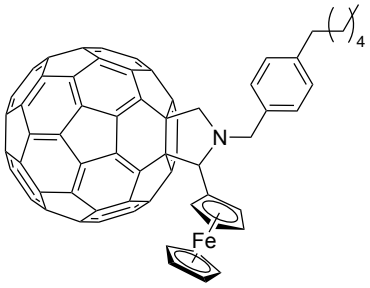

^{1}H NMR (400 MHz, $CDCl_3/CS_2$ v/v 7/1, δ, ppm): 7.63 (d, 2H, Ar H, *J*=7.7 Hz), 7.23 (d, 2H, Ar H, *J*=7.7 Hz), 6.13 (d, 1H, CH_2, *J*=13.2 Hz), 5.07 (s, 1H, CH), 4.74 (d, 1H, CH_2, *J*=9.5 Hz), 4.65 – 4.45 (m, 2H, Fc H), 4.21 (s, 5H, Fc H), 4.19 (m, 2H, Fc H), 4.04 (d, 1H, CH_2, *J*=9.5 Hz), 3.70 (d, 1H, CH_2, *J*=13.2 Hz), 2.65 (t, 2H, CH_2, *J*=7.7 Hz), 1.66 (m, 2H, CH_2), 1.32 (m, 6H, CH_2), 0.90 (m, 3H, CH_3).

$^{13}C\{^1H\}$ NMR (500 MHz, $CDCl_3/CS_2$ v/v 7/1, *δ*, ppm): 156.22, 154.20, 153.75, 153.32, 147.55, 147.31, 147.28, 147.16, 146.52, 146.38, 146.31, 146.28, 146.19, 146.11, 145.98, 145.87, 145.62, 145.59, 145.57, 145.38, 145.31, 145.27, 145.25, 145.21, 144.78, 144.76, 144.49, 144.44, 143.18, 143.08, 142.76, 142.68, 142.66, 142.35, 142.24, 142.23, 142.22, 142.19, 142.16, 142.12, 141.98, 141.95, 141.86, 141.67, 141.52, 140.30, 140.24, 139.63, 139.07, 136.56, 136.50, 136.01, 135.79, 129.17, 128.38, 86.74, 78.01, 76.02, 69.85, 68.84, 68.27, 68.09, 67.91, 67.60, 67.44, 58.28, 36.34, 32.40, 32.15, 29.76, 23.46, 14.80.

MALDI-ToF MS (DCTB/CS_2, m/z): 1121.41 $[M]^-$.

IR (*v*, cm^{-1}): 2914 (m), 1509, 1423, 1105, 997, 813, 524.

UV–Vis (*o*DCB): λ_{max}: 705, 432.

***N*-(4-hexylphenylmethyl)-2,2-dimethyl-5-ferrocenyl fulleropyrrolidine, 8b** (22 mg, 0.019 mmol, 27%).

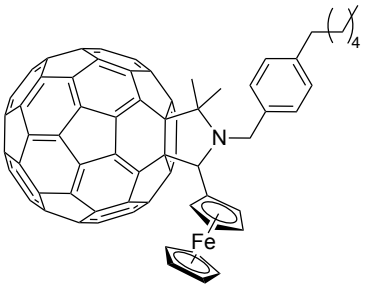

^1H NMR (400 MHz, $CDCl_3$, *δ*, ppm): 7.86 (d, 2H, Ar H, *J*=7.9 Hz), 7.33 (d, 2H, Ar H, *J*=7.9 Hz), 6.44 (d, 1H, CH_2, *J*=16.5 Hz), 5.68 (s, 1H, CH), 4.55 (m, 2H, Fc H), 4.32 (d, 1H, CH_2, *J*=16.5 Hz), 4.21 (s, 5H, Fc H), 4.20 – 4.14 (m, 2H, Fc H), 2.70(t, 2H CH_2, *J*=7.7 Hz), 2.17 (s, 6H, $(CH_3)_2$), 1.77 – 1.65 (m, 3H), 1.47 – 1.24 (m, 3H), 0.91 (t, 3H, CH_3, *J*=7.0 Hz).

$^{13}C\{^1H\}$ NMR (400 MHz, $CDCl_3$, *δ*, ppm): 156.15, 155.76, 154.04, 153.81, 148.03, 147.36, 146.79, 146.44, 146.34, 146.21, 146.13, 145.94, 145.86, 145.63, 145.54, 145.35, 145.29, 145.21, 145.11, 144.93, 144.70, 144.56, 144.38, 143.26, 143.13,

142.82, 142.71, 142.66, 142.32, 142.17, 142.00, 141.86, 141.76, 141.44, 141.40, 141.01, 139.98, 139.80, 139.50, 139.46, 138.71, 136.86, 136.52, 136.45, 135.58, 128.93, 127.04, 88.19, 77.60, 76.77, 71.21, 70.75, 69.81, 68.97, 68.73, 67.86, 67.39, 48.27, 36.26, 32.37, 32.08, 30.27, 29.78, 29.24, 23.40, 19.52, 14.75.

MALDI-ToF MS (DCTB/CS_2, m/z): 1149.60 $[M]^-$.

IR (ν, cm^{-1}): 2916 (m), 2840, 1509, 1174, 813, 524.

UV–Vis (*o*DCB): λ_{max}: 707, 433.

***N*-(4-hexylphenylmethyl)-2-(2,2,2,2',2',2'-hexafluoroisopropyl)-5-ferrocenyl fulleropyrrolidine**, **8c** (4 mg, 0.003 mmol, 5%).

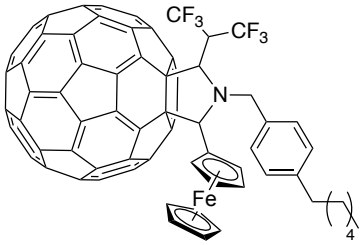

^{1}H NMR (500 MHz, CS_2/$CDCl_3$ v/v 7/1, δ, ppm): 7.51 (d, J = 7.8 Hz, 2H, Ar H), 7.24 – 7.19 (d, J = 7.8 Hz, 2H, Ar H), 5.84 (s, 1H, CH), 5.63 (d, J = 5.3 Hz, 1H, CH), 5.51 (d, J = 12.8 Hz, 1H, CH_2), 5.04 (d, J = 12.7 Hz, 1H, CH_2), 4.46 – 4.40 (m, 2H, Fc H), 4.50 – 4.33 (m, 1H, CH), 4.31 (s, 5H, Fc H), 4.27 – 4.20 (m, 2H, Fc H), 2.64 (t, J = 7.6 Hz, 2H, CH_2), 1.71 – 1.58 (m, 2H, CH_2), 1.41 – 1.18 (m, 6H, CH_2), 0.95 – 0.84 (m, 3H, CH_3).

^{13}C{^{1}H} NMR (500 MHz, CS_2/$CDCl_3$ v/v 7/1, δ, ppm): 156.28, 154.77, 154.06, 149.86, 147.23, 147.00, 146.86, 146.56, 146.36, 146.26, 146.24, 146.20, 146.13, 146.11, 146.01, 146.00, 145.79, 145.56, 145.45, 145.38, 145.36, 145.35, 145.34, 145.32, 145.25, 145.18, 144.63, 144.59, 144.55, 144.04, 143.26, 143.19, 143.12, 142.88, 142.86, 142.85, 142.76, 142.62, 142.43, 142.34, 142.31, 142.29, 142.21, 142.08, 142.02, 142.00, 141.88, 141.77, 141.65, 140.26, 139.87, 139.66, 139.01, 138.10, 135.35, 134.49, 134.24, 133.03, 130.62, 130.11, 129.40, 129.07, 128.95,

127.68, 82.70, 80.44, 78.52, 76.46, 75.67, 71.91, 70.23, 69.99, 69.84, 69.71, 68.71, 68.04, 52.82, 52.50, 52.29, 52.09, 51.88, 36.16, 32.25, 31.87, 29.38, 23.27, 14.61.

MALDI-ToF MS (DCTB/CS_2, m/z): 1271.26 $[M]^-$.

IR (ν, cm^{-1}): 2916 (m), 1272, 1207, 1164, 1084, 815, 713, 524.

UV–Vis (*o*DCB): λ_{max}: 695, 431.

2.5.2.17 Synthesis of fullerene charge carriers, C60Fc

C_{60} (50 mg, 0.070 mmol, 1 *equiv.*), ferrocene carboxaldehyde (18 mg, 0.084 mmol, 1.2 *equiv*.) and corresponding amino acid (38 mg of **AA1**; 35 mg of **AA4**; 38 mg of **AA5**, 0.084 mmol, 0.14 mmol, 2 *equiv.*) were dissolved in toluene (50 mL) by sonicating for 15 minutes, and thoroughly degassed with N_2. The resulting mixture was heated to reflux condition (4 hours for **C_{60}Fc1** and **C_{60}Fc2**, 17 hours for **C_{60}Fc3**). Upon completion the solvent was removed under reduced pressure, the residue was re-dissolved with minimum amount of CS_2, and purified by column chromatography (silica gel, CS_2). Further purification was carried out my washing with methanol (50 mL) giving black solid as product.

Bis-*N*-(3,5-di-tert-butylphenylmethyl)-2-ferrocenyl fulleropyrrolidine, **C_{60}Fc1** (yield: 23 mg, 0.015 mmol, 21%).

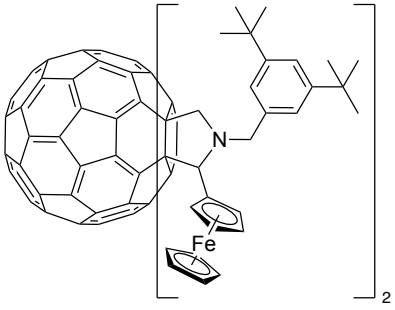

^{1}H NMR (400 MHz, $CDCl_3$, δ, ppm): 7.31-7.90 (m, 3H, ArH), 3.41-6.32 (m, 14H, FcH, CH_2 and pyrrolidineH), 1.29-1.52 (m, 18H, $(CH_3)C$).

MALDI ToF MS (DCTB/MeCN, m/z): 1577.84 $[M]^-$.

Bis-*N*-(4-hexylphenylmethyl)-2-ferrocenyl fulleropyrrolidine, **C_{60}Fc2** (yield: 50 mg, 0.033 mmol, 47%).

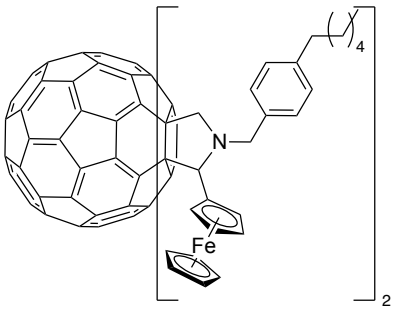

^{1}H NMR (400 MHz, $CDCl_3$, *δ*, ppm): 7.22-7.88 (m, 4H, ArH), 3.32-6.34 (m, 14H, FcH, CH_2 and pyrrolidineH), 0.85-2.87 (m, 13H, hexyl)

MALDI ToF MS (DCTB/MeCN, m/z): 1522.29 $[M]^-$.

Bis-*N*-(4-hexylphenylmethyl)-2,2-dimethyl-5-ferrocenyl fulleropyrrolidine, **C_{60}Fc3** (yield: 10 mg, 0.006 mmol, 9%).

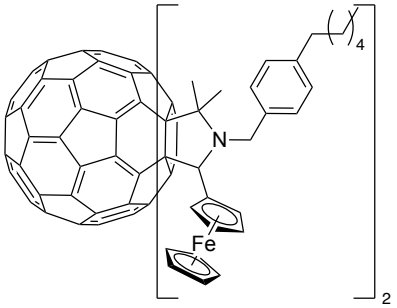

^{1}H NMR (400 MHz, $CDCl_3$, *δ*, ppm): 7.09-8.03 (m, 4H, Ar H), 3.78-6.60 (m, 12H, Fc H, CH_2 and pyrrolidine H), 0.88-2.78 (m, 19H, hexyl and $(CH_3)_2$).

MALDI ToF MS (DCTB/MeCN, m/z): 1578.14 $[M]^-$.

2.6 References

1. Arenas, L. F., Ponce de León, C. & Walsh, F. C. Engineering aspects of the design, construction and performance of modular redox flow batteries for energy storage. *Journal of Energy Storage* **11**, 119–153 (2017).
2. Arenas, L. F., Ponce de León, C. & Walsh, F. C. Engineering aspects of the design, construction and performance of modular redox flow batteries for energy storage. *Journal of Energy Storage* **11**, 119–153 (2017).
3. Huskinson, B. *et al.* A metal-free organic–inorganic aqueous flow battery. *Nature 2014 505:7482* **505**, 195–198 (2014).
4. Aaron, D. *et al.* In Situ Kinetics Studies in All-Vanadium Redox Flow Batteries. *ECS Electrochemistry Letters* **2**, A29 (2013).
5. Thaller, L. Recent advances in redox flow cell storage systems. (1979).
6. Yang, Z. *et al.* Electrochemical Energy Storage for Green Grid. *Chemical Reviews* **111**, 3577–3613 (2011).
7. Skyllas-Kazacos, M. & Grossmith, F. Efficient Vanadium Redox Flow Cell. *Journal of The Electrochemical Society* **134**, 2950 (1987).
8. Skyllas-Kazacos, M., Rychcik, M., Robins, R. G., Fane, A. G. & Green, M. A. New All-Vanadium Redox Flow Cell. *Journal of The Electrochemical Society* **133**, 1057 (1986).
9. Rahman, F. & Skyllas-Kazacos, M. Vanadium redox battery: Positive half-cell electrolyte studies. *Journal of Power Sources* **189**, 1212–1219 (2009).
10. Lin, K. *et al.* Alkaline quinone flow battery. *Science* **349**, 1529–1532 (2015).
11. Soloveichik, G. L. Flow Batteries: Current Status and Trends. *Chemical Reviews* **115**, 11533–11558 (2015).

12. Beh, E. S. *et al.* A Neutral pH Aqueous Organic–Organometallic Redox Flow Battery with Extremely High Capacity Retention. *ACS Energy Letters* **2**, 639–644 (2017).

13. Janoschka, T. *et al.* An aqueous, polymer-based redox-flow battery using non-corrosive, safe, and low-cost materials. *Nature 2015 527:7576* **527**, 78–81 (2015).

14. Wang, W. *et al.* Recent Progress in Redox Flow Battery Research and Development. *Advanced Functional Materials* **23**, 970–986 (2013).

15. Cathro, K. J., Cedzynska, K. & Constable, D. C. Preparation and performance of plastic-bonded-carbon bromine electrodes. *Journal of Power Sources* **19**, 337–356 (1987).

16. Reddy, T. B. Linden's Handbook of Batteries, Fourth Edition. *Amazon* 1200 (2011).

17. Hruska, L. W. & Savinell, R. F. Investigation of Factors Affecting Performance of the Iron-Redox Battery. *Journal of The Electrochemical Society* **128**, 18 (1981).

18. Puiki Leung *et al.* Progress in redox flow batteries, remaining challenges and their applications in energy storage. *RSC Advances* **2**, 10125–10156 (2012).

19. Skyllas-Kazacos, M., Chakrabarti, M. H., Hajimolana, S. A., Mjalli, F. S. & Saleem, M. Progress in Flow Battery Research and Development. *Journal of The Electrochemical Society* **158**, R55 (2011).

20. Mun, J. *et al.* Non-Aqueous Redox Flow Batteries with Nickel and Iron Tris(2,2'-bipyridine) Complex Electrolyte. *Electrochemical and Solid-State Letters* **15**, A80 (2012).

21. Duan, W. *et al.* "Wine-Dark Sea" in an Organic Flow Battery: Storing Negative Charge in 2,1,3-Benzothiadiazole Radicals Leads to Improved Cyclability. *ACS Energy Letters* **2**, 1156–1161 (2017).

22. Park, M., Ryu, J., Wang, W. & Cho, J. Material design and engineering of next-generation flow-battery technologies. *Nature Reviews Materials 2016 2:1* **2**, 1–18 (2016).

23. Zhu, Y. *et al.* Enhanced cyclability of organic redox flow batteries enabled by an artificial bipolar molecule in neutral aqueous electrolyte. *Journal of Power Sources* **417**, 83–89 (2019).

24. Sevov, C. S., Fisher, S. L., Thompson, L. T. & Sanford, M. S. Mechanism-Based Development of a Low-Potential, Soluble, and Cyclable Multielectron Anolyte for Nonaqueous Redox Flow Batteries. *Journal of the American Chemical Society* **138**, 15378–15384 (2016).

25. Winsberg, J. *et al.* TEMPO/Phenazine Combi-Molecule: A Redox-Active Material for Symmetric Aqueous Redox-Flow Batteries. **1**, 23 (2016).

26. Li, L. *et al.* A stable vanadium redox-flow battery with high energy density for large-scale energy storage. *Advanced Energy Materials* **1**, 394–400 (2011).

27. Gong, K. *et al.* All-Soluble All-Iron Aqueous Redox-Flow Battery. *ACS Energy Letters* **1**, 89–93 (2016).

28. Nambafu, G. S. *et al.* An organic bifunctional redox active material for symmetric aqueous redox flow battery. *Nano Energy* **89**, 106422 (2021).

29. Janoschka, T., Martin, N., Hager, M. D. & Schubert, U. S. An Aqueous Redox-Flow Battery with High Capacity and Power: The TEMPTMA/MV System. *Angewandte Chemie - International Edition* **55**, 14427–14430 (2016).

30. High-Performance Aqueous Organic Flow Battery with Quinone-Based Redox Couples at Both Electrodes. doi:10.1149/2.1371607jes.

31. Yang, Z. *et al.* Alkaline Benzoquinone Aqueous Flow Battery for Large-Scale Storage of Electrical Energy. *Advanced Energy Materials* **8**, 1702056 (2018).

32. Wang, C. *et al.* Molecular Design of Fused-Ring Phenazine Derivatives for Long-Cycling Alkaline Redox Flow Batteries. **8**, 15 (2021).

33. Hollas, A. *et al.* A biomimetic high-capacity phenazine-based anolyte for aqueous organic redox flow batteries. (2018) doi:10.1038/s41560-018-0167-3.

34. Pratt, H. D., Hudak, N. S., Fang, X. & Anderson, T. M. A polyoxometalate flow battery. *Journal of Power Sources* **236**, 259–264 (2013).

35. Nagarjuna, G. *et al.* Impact of Redox-Active Polymer Molecular Weight on the Electrochemical Properties and Transport Across Porous Separators in Nonaqueous Solvents. *Journal of the American Chemical Society* **136**, 16309–16316 (2014).

36. Winsberg, J., Hagemann, T., Janoschka, T., Hager, M. D. & Schubert, U. S. Redox-Flow Batteries: From Metals to Organic Redox-Active Materials. *Angewandte Chemie International Edition* **56**, 686–711 (2017).

37. D. Milshtein, J. *et al.* High current density, long duration cycling of soluble organic active species for non-aqueous redox flow batteries. *Energy & Environmental Science* **9**, 3531–3543 (2016).

38. Friedl, J., Lebedeva, M. A., Porfyrakis, K., Stimming, U. & Chamberlain, T. W. All-Fullerene-Based Cells for Nonaqueous Redox Flow Batteries. *Journal of the American Chemical Society* **140**, 401–405 (2018).

39. Non-aqueous vanadium acetylacetonate electrolyte for redox flow batteries | Elsevier Enhanced Reader. https://reader.elsevier.com/reader/sd/pii/S1388248109004925?token=FEAB4F43A0982EFA6C50263E0467CC40CE8CA34F60BF9B3F0AB515B805136D6CB480799CCDAC0195A51B0FA13585757D&originRegion=eu-west-1&originCreation=20211208110704.

40. Chakrabarti, M. H., Dryfe, R. A. W. & Roberts, E. P. L. Evaluation of electrolytes for redox flow battery applications. *Electrochimica Acta* **52**, 2189–2195 (2007).

41. Matsuda, Y. *et al.* A rechargeable redox battery utilizing ruthenium complexes with non-aqueous organic electrolyte. *Journal of Applied Electrochemistry 1988 18:6* **18**, 909–914 (1988).

42. Li, Z. *et al.* Electrochemical Properties of an All-Organic Redox Flow Battery Using 2,2,6,6-Tetramethyl-1-Piperidinyloxy and N-Methylphthalimide. *Electrochemical and Solid-State Letters* **14**, A171 (2011).

43. Wei, X. *et al.* TEMPO-Based Catholyte for High-Energy Density Nonaqueous Redox Flow Batteries. *Advanced Materials* **26**, 7649–7653 (2014).

44. Kaur, A. P., Holubowitch, N. E., Ergun, S., Elliott, C. F. & Odom, S. A. A Highly Soluble Organic Catholyte for Non-Aqueous Redox Flow Batteries. *Energy Technology* **3**, 476–480 (2015).

45. Redox Active Polymers for Non-Aqueous Redox Flow Batteries: Validation of the Size-Exclusion Approach. doi:10.1149/2.1511707jes.

46. Attanayake, N. H. *et al.* Tailoring Two-Electron-Donating Phenothiazines To Enable High-Concentration Redox Electrolytes for Use in Nonaqueous Redox Flow Batteries. *Chem. Mater* **31**, 5 (2019).

47. Lebedeva, M. A., Chamberlain, T. W., Schröder, M. & Khlobystov, A. N. An efficient route to the synthesis of symmetric and asymmetric diastereomerically pure fullerene triads. *Tetrahedron* **68**, 4976–4985 (2012).

48. Lebedeva, M. A. *et al. Supporting information for Stabilising the Lowest Energy Charge-Separated State in a {Metal Chromophore-Fullerene} Assembly: A Tuneable Panchromatic Absorbing Donor-Acceptor Triad*. (2016).

49. Alejandro Montellano, Ros, T. D., Alberto Bianco & Maurizio Prato. Fullerene C 60 as a multifunctional system for drug and gene delivery. *Nanoscale* **3**, 4035–4041 (2011).

50. Mirkin, M. v., Bard, A. J. & Bulhões, L. O. S. Determination of the Kinetic Parameters for the Electroreduction of C60 by Scanning Electrochemical Microscopy and Fast Scan Cyclic Voltammetry. *Journal of the American Chemical Society* **115**, 201–204 (1993).

51. Nicholson, R. S. Theory and Application of Cyclic Voltammetry for Measurement of Electrode Reaction Kinetics. *Analytical Chemistry* **37**, 1351–1355 (1965).

Chapter 3 Synthesis of C60-CTG complexes

3.1 Introduction

Fullerene has unique chemical and physical properties, such as efficient multi-electron absorption, strong UV-Vis response, singlet oxygen sensitivity, and solid state magnetic and superconducting behavior. To make the fullerene related materials useful for practical applications, fullerene based supramolecular chemistry acts as an efficient way to organise the distribution of fullerene cages through a solid and has been a hot research area for decades.[1–6] Direction of the carbon cages into regulated supramolecular arrays on the surface or through a material are widely reported using approaches such as; C_{60} related host-guest assembly, and synthesising fullerene ligand metal complexes, fullerene donor-acceptor diads and etc.[7] Of these approaches, supramolecular assembly driven by host-guest interactions is the most pertinent to this chapter and exciting more generally as it has been exploited to form molecular machines, which were recently the recipient of a Nobel prize in Chemistry.[8] After careful selection of the host molecule and the proper functionalisation of the fullerene cage, a wide variers of fullerene containing supramolecular arrays have been achieved, a number of the most interesting examples are summarised below.

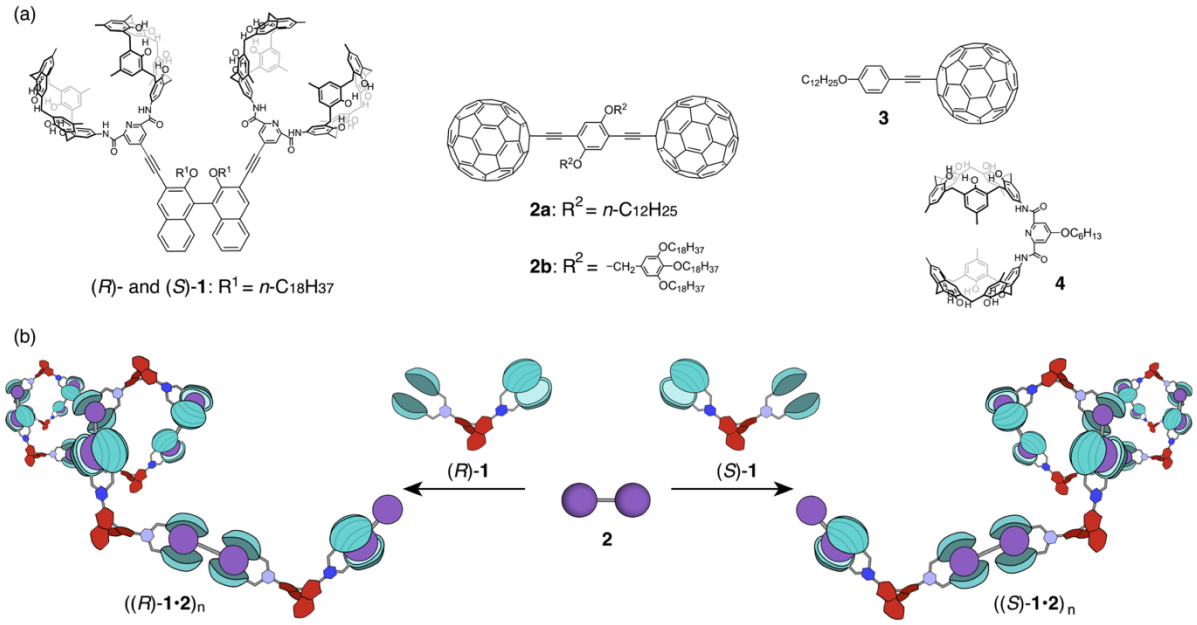

Figure 3.1 a) Molecular structure of tetrakis-calix[5]arene-(R) and (S) fullerene receptor and fullerene dimer. b) Diagram of the host-guest directed fullerene-supramolecular polymer with nonracemic helicity.

Takehiro Hirao recently reported a unique helically organized fullerene-based supramolecular polymers that were composed of the dumbbell shaped fullerene dimers and a fullerene receptor, nonracemic tetrakiscalix[5]arene-(*R*) and (*S*) (see **Figure 3.1**).[9] Calix[5]arene derivatives are well known fullerene host molecule and its ditopic tetrakis form was adopted due to its increased ability to bind fullerene. The receptor can bind the fullerene dimer in a 1 to 1 ratio resulting in a step-growth manner. Importantly, the chiral binaphthyl moiety-*R* and *S* was introduced as the linker of the two binding sites, resulting in the nonracemic helicity.

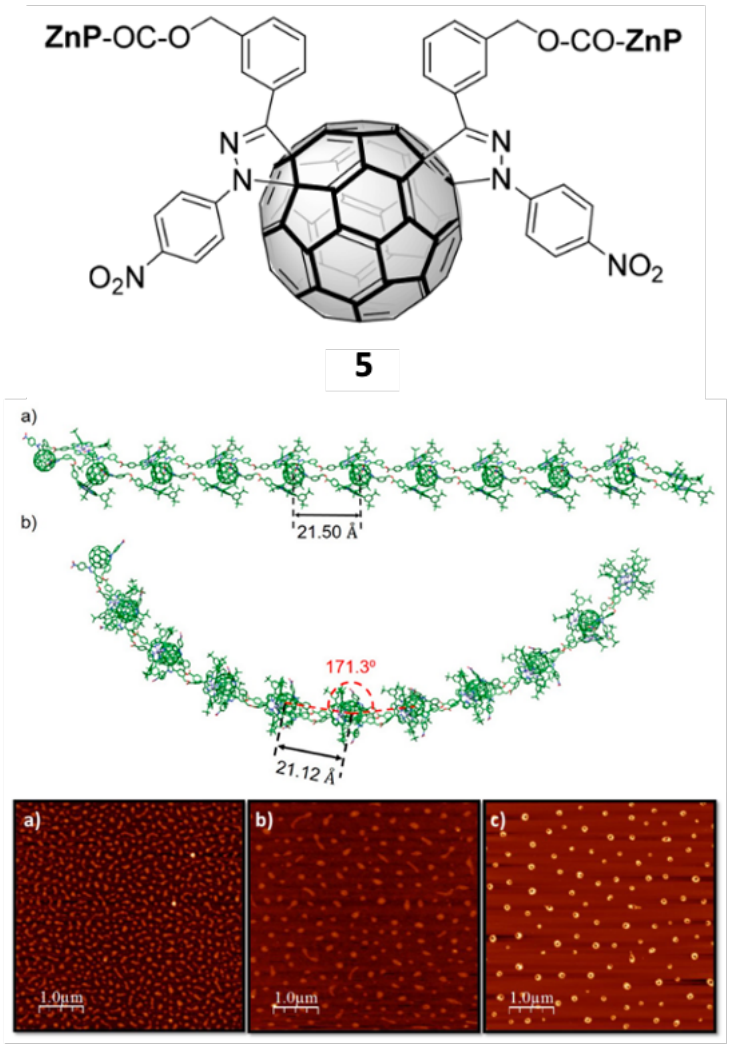

Figure 3.2 top) Chemical structure of the fullerene-bis-Zn-porphyrin moelcules, b) diagram of the supramolecular aggregate of fullerene bis-adduct, **5**; c) AFM images showing the formation of the donut shaped aggregate over time.

Fullerene molecules can also be functionalised with groups that can serve as the host moiety. Langa and coworker[10] recently reported the synthesis of fullerene-bis-Zn-porphyrin, in which the fullerene was appended with two electron donor arms, i.e. Zn porphyrin, that can bind the vicinal fullerene cage (see **Figure 3.2**). This molecule was proved to form the supramolecular oligomers that have the repeat unit of donor-acceptor and subsequently generate the aggregates with a donut shape that was shown using AFM. Spectroscopy and electrochemical studies revealed a charge

separated state with a 40 μs lifetime was found, making the material suitable for light energy harvesting applications.

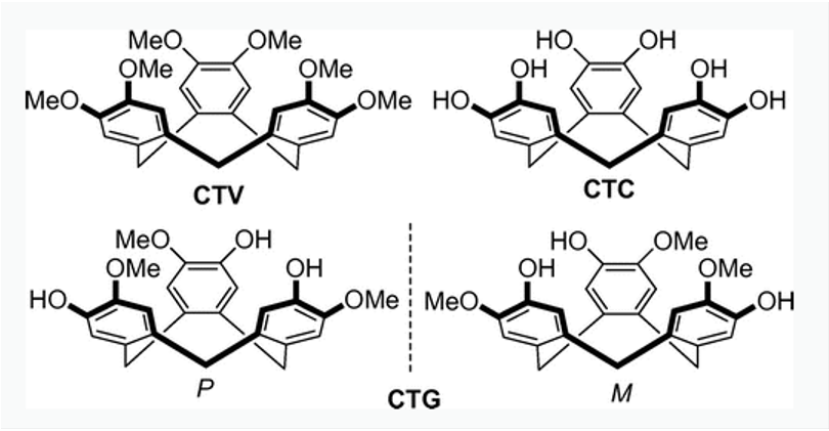

Figure 3.3 Chemical structure of cyclotriguaiacylene (CTG), cyclotricatechylene (CTC) and cyclotriveratrylene (CTV).

CTV molecules are a cyclic trimer of veratrole with a tribenzo[a,d,g] cyclononatriene core, which has two analogues, CTG with one hydroxy group and one methoxy group on each benzene ring, and CTC with two hydroxy groups on each benzene ring (**Figure 3.3**).[11] Due to their pyramidal conformation and inherent hydrophobic molecular cavity, they are recognised as good host molecules for binding fullerenes. In comparison with CTC and CTV, CTG has two different substituents, resulting in the CTG exhibiting chirality, i.e. *P* and *M* enantiomers.[11] Meanwhile, the free hydroxyl groups of the CTG enables further functionalization of the molecule, which can be used to add functionality and form via tris-extended-arm derivatives. Huerta and co-workers[12] reported the synthesis of a CTG derivatives that contained three 4-ureidopyrimidinone groups that can form quadruple hydrogen bonds with itself (see **Figure 3.4**). These molecules can self-assembly into a hydrogen driven cage that shows the ability to bind the fullerene molecule in its central cavity. Interestingly, this supramolecular cage indicates higher binding affinity to a higher fullerene, C_{84}, than

the more abundant C_{60} due to the better shape complements between the cavity and the larger sized C_{84}.

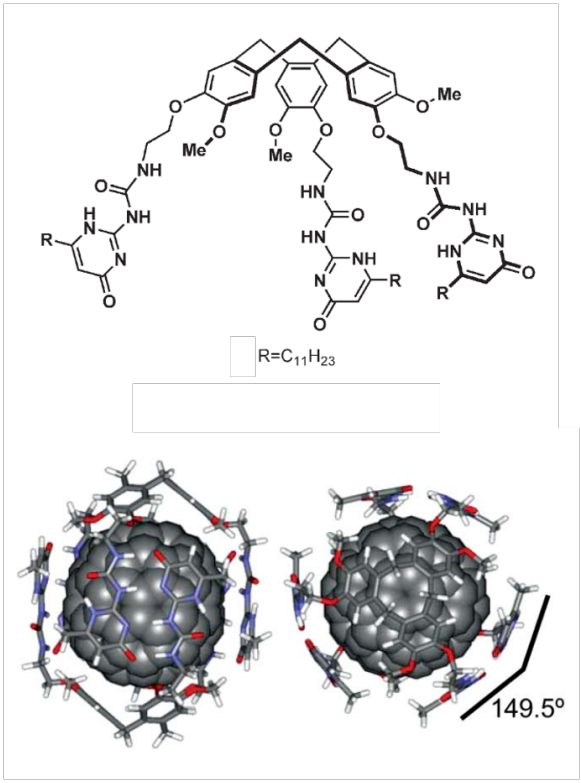

Figure 3.4 top) Chemical structure of the tris-4-ureidopyrimidinone CTG derivatives, bottom) optimised model for guest molecule, C_{84}.

Considering the possibility of adding functionality to both fullerene and CTG, and the specific recognition of the inherent cavity of CTG to fullerene, CTG functionalised with three fullerene arms could act as a building blocks, in which the fullerene arms can subsequently bind other CTG or host molecules, with the potential to generate novel supramolecular assemblies, i.e. supramolecular polymers, dendrimers, quasi 3D arrays etc. However, this kind of work is yet to be reported.

3.2 Aims and objectives

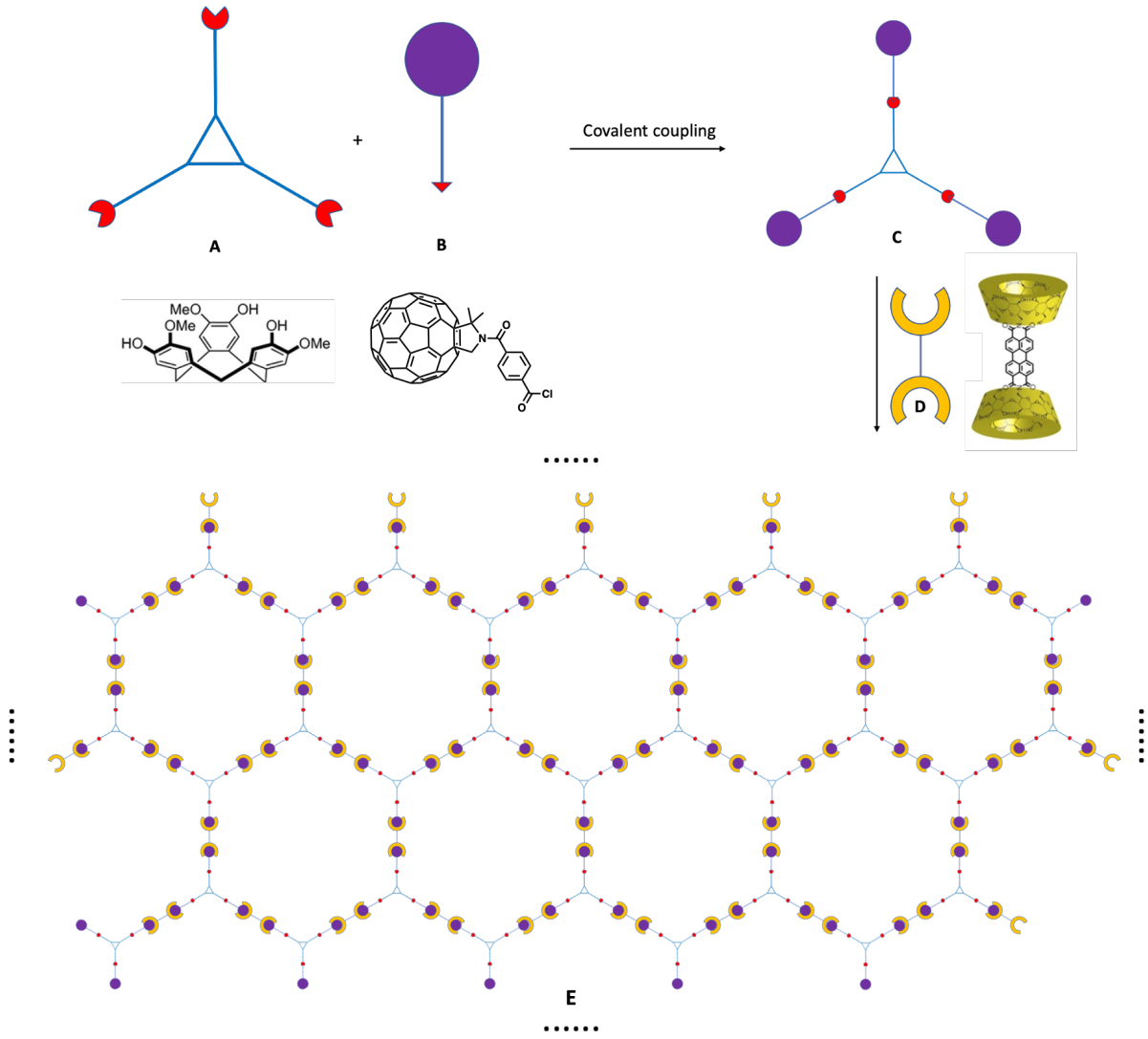

Figure 3.5 Schematic of building up the 2D supramolecular arrays (E) based on host-guest interaction between tris-fullerene-CTG derivatives (C) and host dimer molecules (D). C is formed from the coupling reaction between CTG (A) and the fullerene derivatives (B). Red sign: reactive groups, purple sign: fullerene, triangle: CTG scaffold, yellow sign: host dimer.

The aim of this study is to synthesise and characterise the multi-fullerene derivatives that shows the potential to develop the supramolecular arrays based on host-guest interaction between fullerene and its host species, e.g. CTG, calixarenes and

cyclodextrin. CTG is selected as the building block to conduct the research (**A** in **Figure 3.5**), which has three hydroxyl groups that can couple with other groups to form covalent bond, e.g. ester, ether. Functionalised fullerene derivatives with reactive ends (**B** in **Figure 3.5**), e.g. acyl chloride, can react with CTG to form the tris-fullerene armed CTG derivatives (**C** in **Figure 3.5**). The fullerene moiety can bind the other macrocycle host molecule in supramolecular fashion, host-guest interaction. When host dimer molecules (**D** in **Figure 3.5**) are mixed together with **C**, a 2D supramolecular arrays can be formed. This will be achieved by via completion of the following objectives:

1. Find out a workable synthetic routes and conditions, which can yield the tris-fullerene-CTG molecules in a viable, reproducible yield.
2. Purify and fully characterise the target molecules
3. Scale up or repeat the reaction in parallel to yield enough material to explore supramolecular assembly in isolation and with other host species including CTG.

3.2.1 Synthetic strategy

Two synthetic strategies were proposed for this study via, 1) a nucleophilic coupling reaction between a CTG molecule and the derivatised bridge molecule that has been reported by the group previoursly,[13] and 2) a one-pot Prato reaction of the fullerene with functionalised tris-aldehyde CTG or tris-amino acid derivatized CTG.

3.2.1.1 Route to synthesise CTG

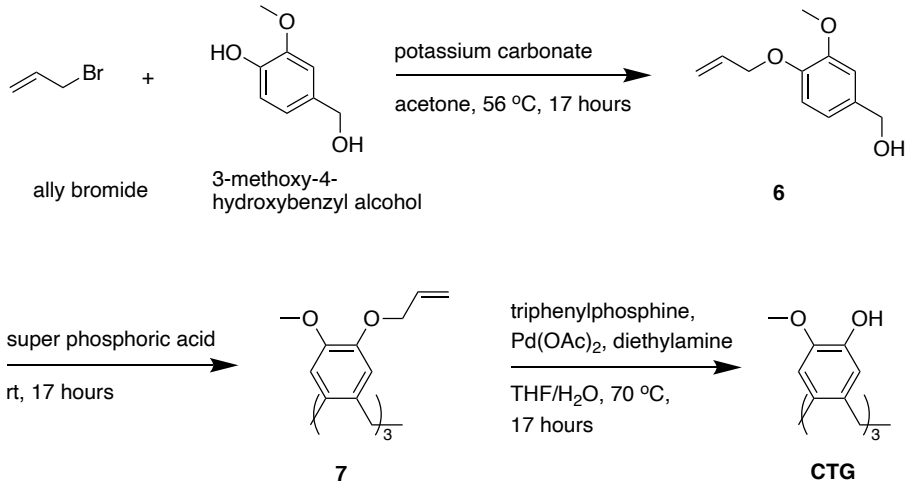

Scheme 3.1 Route to synthesise cyclotriguaiacylene CTG.

The preparation of the CTG is well established in the literature[11] and within the Hardie group. To synthesise the CTG, the hydroxyl group that attached directedly to the benzene ring of the monomer, 3-methoxyl-4-hydroxybenzyl alcohol, is required to be protected with an allyl group, giving molecule **6**, which is for avoiding the uncontrolled, next step polymerization. In the presence of the super phosphoric acid, the monomer starts to polymerise, forming the closed ring trimer, **7**. The reaction mechanism was shown in the **Scheme 3.2**. Three allyl groups on compound **7** was subsequently deprotected to expose the hydroxyl groups, giving the target molecule, CTG.

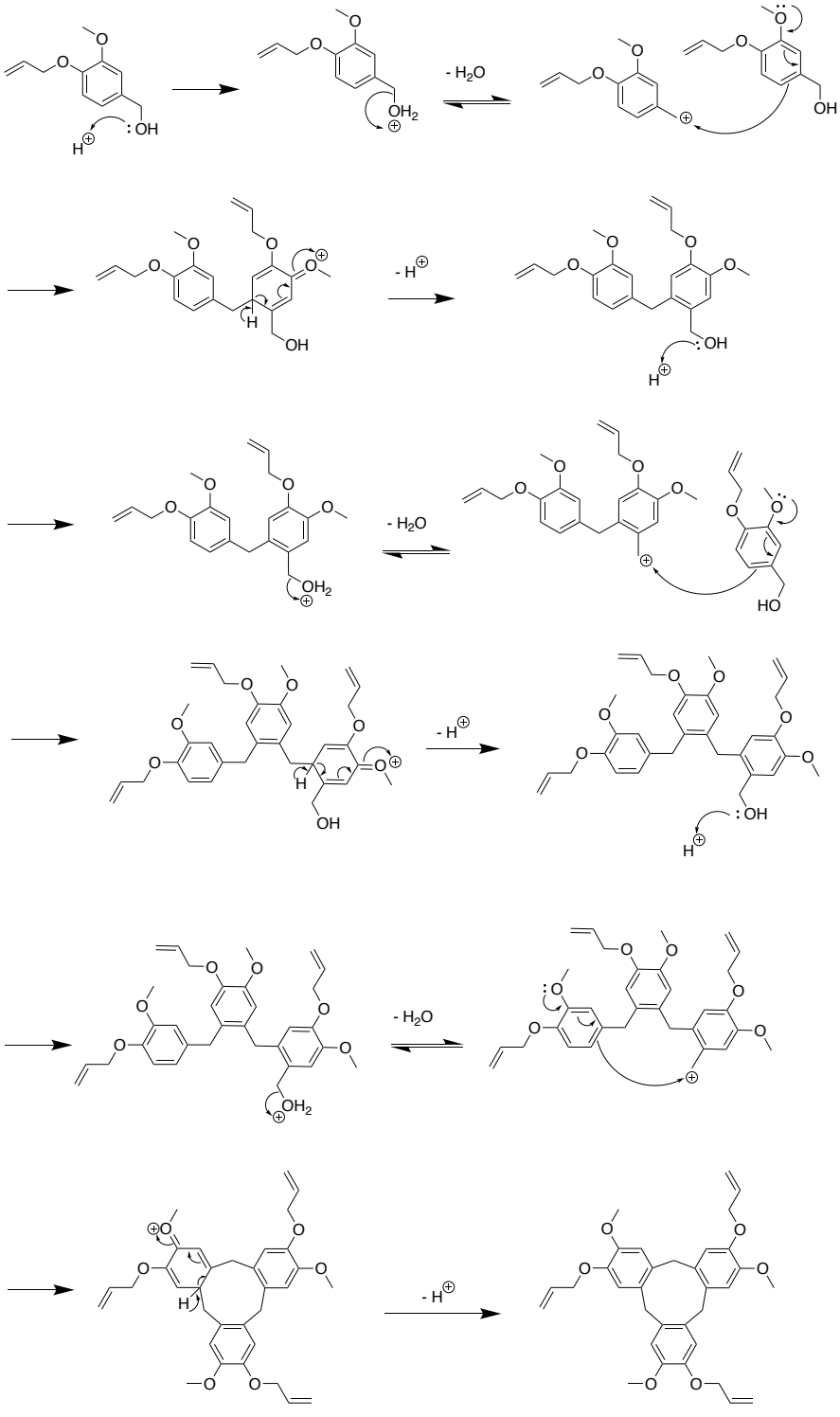

Scheme 3.2 Mechanism of the polymerization, from monomer, **6**, to trimer, **7**.

3.2.1.2 Route 1: Nucleophilic coupling reaction between fullerene bridge molecule and the CTG molecule

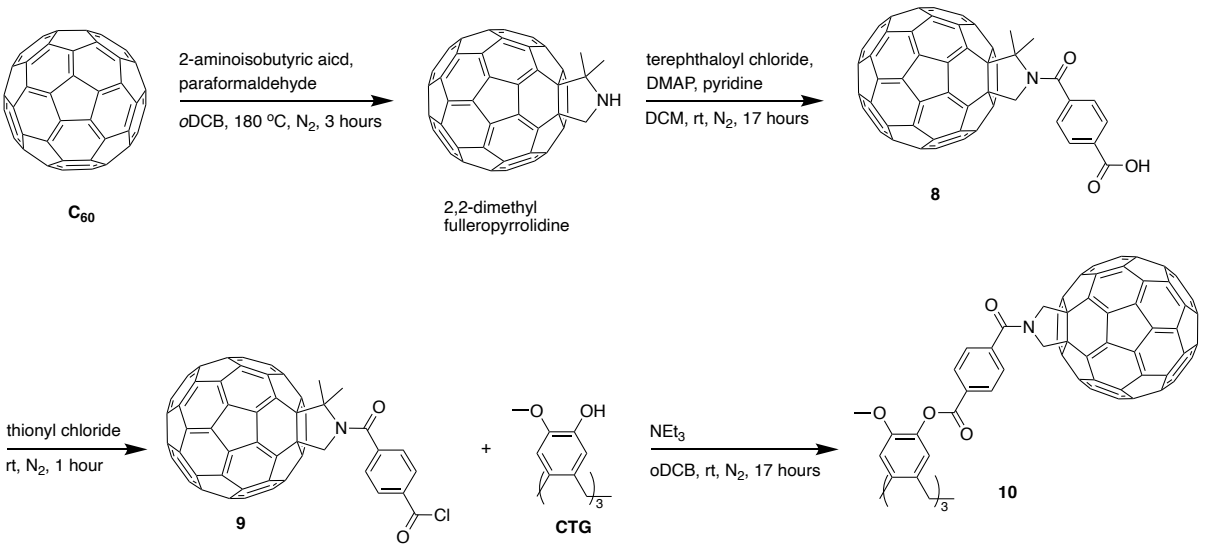

Scheme 3.3 Route to synthesise tris-fullerene CTG molecule via Nucleophilic coupling reaction.

As seen in **Scheme 3.3**, this route adopted the fullerene derivatives, **8**, with the carboxylic acid end that was reported in the group's previous work,[13] which can be transformed into the acyl chloride, **9**, by reacting with thionyl chloride. The acyl chloride group within **9** can subsequently react with the CTG molecule in the presence of excess triethylamine via Nucleophilic substitution, in which the functions of the triethylamine are for deprotonating the CTG molecule and sweeping off the hydrochloride by product, giving final target molecule, **10**. This route is easy to follow as this type of reaction have been done in the Hardie group. The challenges of performing this route are, 1) in the previous reactions, the solvent used was THF which is not going to dissolve the fullerene and 2) the yield of the fullerene bridge molecule is low, ~9% to C_{60}. As the result, several test reactions are required to find out the reaction condition before using the precious fullerene derivatives, and thus the

reaction to synthesise CTG-pyridine was selected (see **Figure 3.6**), which will be repeated in the THF followed by finding the correct reaction in *o*DCB that is generally considered as the best solvent for fullerene derivatives.

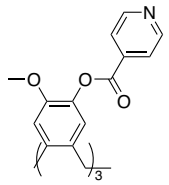

Figure 3.6 The CTG-pyridine molecule that is proposed to investigate the reaction condition for the coupling reaction of fullerene bridge molecule and CTG.

3.2.1.3 Route 2: One-pot Prato reaction to synthesise tris-fullerene-CTG molecule

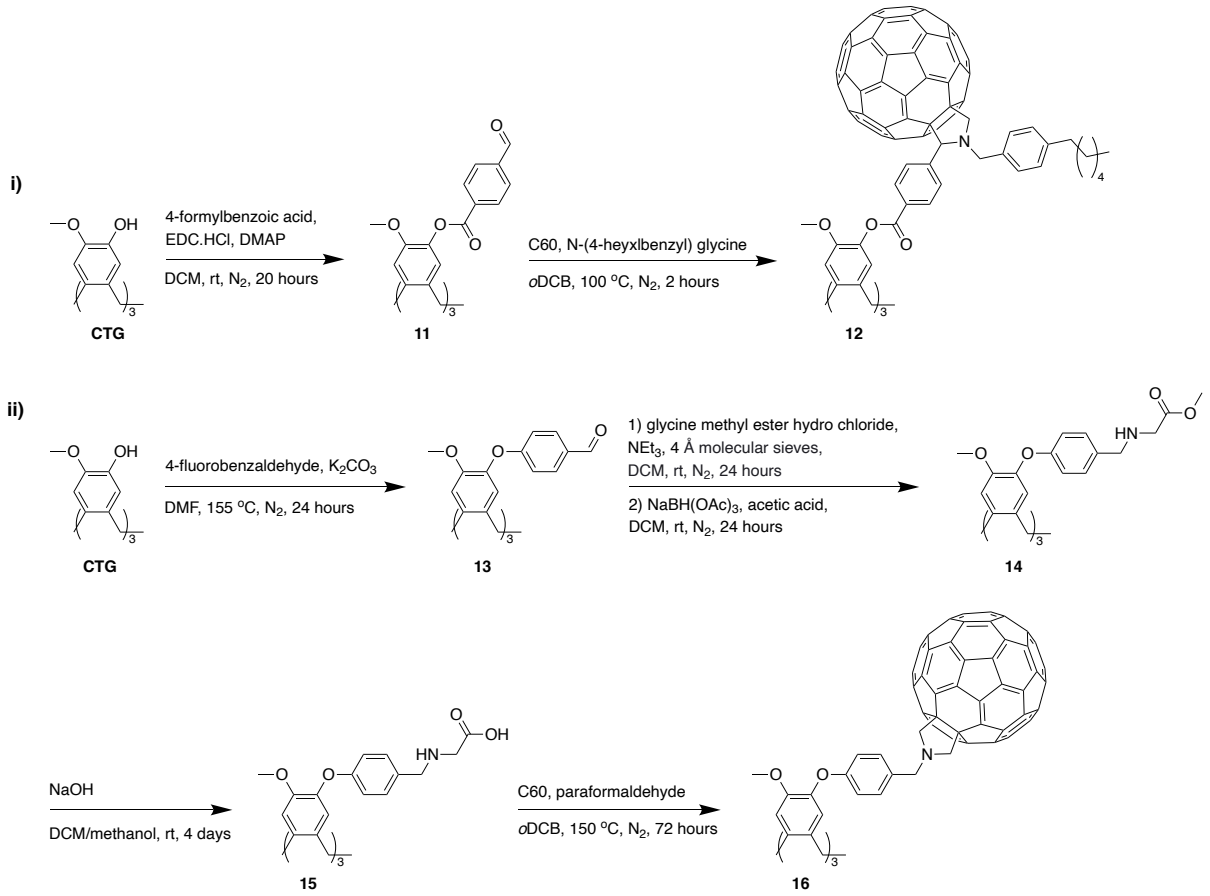

Scheme 3.4 Route to synthesise tris-fullerene-CTG via one-pot Prato reaction, i) synthesis of the tris-aldehyde CTG as the starting material for Prato reaction, ii) synthesis of the tris-amino acid as the Prato reaction starting material.

Beside the above-mentioned coupling reaction, routes of one-pot Prato reaction were also proposed. The Prato reaction used the C_{60}, aldehyde and aminoacidic starting materials to form the five membered pyrrolidine ring. So, we decided to functionalised the CTG molecule with three aldehyde and amino acid ends, followed by reacting with fullerene respectively. These routes negate the early stage step-wise fullerene derivative synthesis, which shows the potential to synthesise the targe molecule with good yield. In the **Scheme 3.4i**, the carboxylic acid activating agent, EDC.HCl, was

used to work on the carboxylic group of the 4-formylbenzoic acid, then subsequently react with the hydroxyl group of the CTG molecule, giving the tris-aldehydes CTG, **11**. C_{60}, compound **11**, and the previously synthesised amino acid, N-(4-hexylbenzyl) glycine were used to perform the Prato reaction, giving the tris-fullerene-CTG molecule, **12**, with three alkyl chains.

For preparing the tris-aminoacid CTG molecules, the reductive amination was adopted to synthesise the methyl ester initially, then deprotect the methyl group under basic condition, giving the amino acid. Therefore, molecule **11** cannot be used directed to perform the reductive amination due to its ester linker between the CTG and benzene is going to break together with the methyl ester bond under the basic condition. So, a linker between the aldehyde group and the CTG is required to be pH stable. Ether linker is found to be suitable, and thus the molecule **13** was proposed and synthesised via the aromatic substitution between the CTG and 4-fluorobenzaldehyde. After the reductive amination step, the tris-methyl ester CTG, **14**, was synthesised, followed by the deprotection of methyl giving the tris-aminoacid CTG, **15**. Compound **15** was used to perform the Prato reaction with C_{60} and paraformaldehyde to give the target molecule **16**.

3.3 Results and discussion

3.3.1 The preparation of CTG

3.3.1.1 Synthesis of 3-methoxy-4-propenyloxybenzyl alcohol, 6

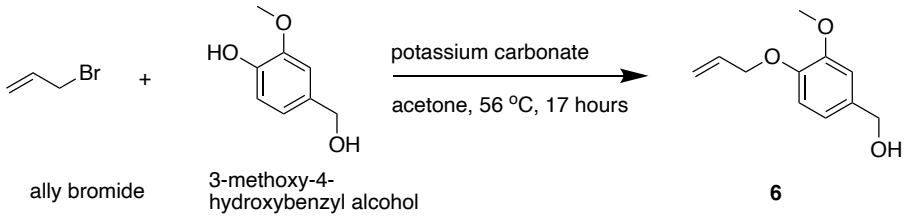

Scheme 3.5 Route to synthesise compound **6**.

The reaction to synthesise molecule **6** was successfully performed by followed the reported procedures.[11] The reaction mixture was extracted with DCM, and washed with water, followed by drying with $MgSO_4$, giving cream yellow solid as product on 78% yield. The formation of the molecule **6** was proved by ^{1}H NMR spectrometry, in which characteristic multiplets, δ = 6.02-6.15 ppm, and two aromatic proton environments, δ = 6.94 ppm and 6.86 ppm, were found and corresponded to the ally methine proton (labelled as H_d in **Figure 3.7**) and the three aromatic protons (labelled as H_a and $H_{b/c}$ in **Figure 3.7**).

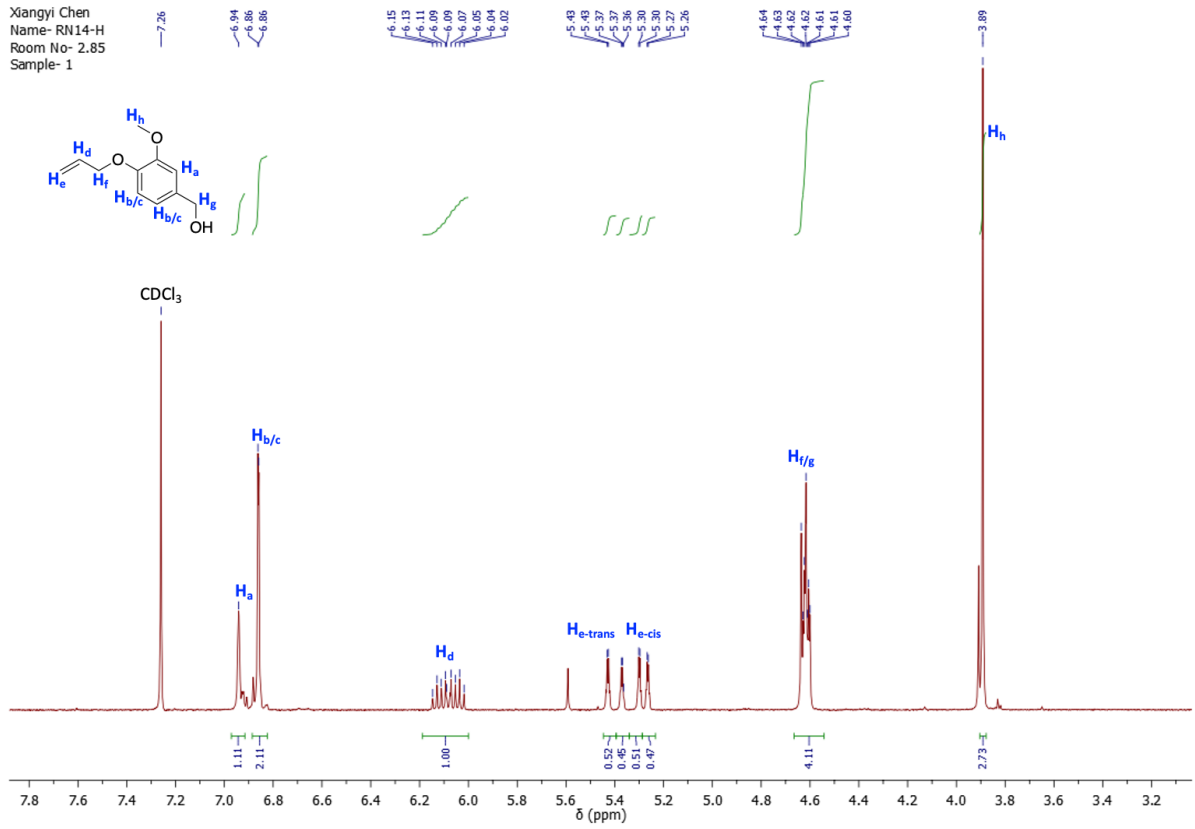

Figure 3.7 ^{1}H NMR spectrum (400 MHz, $CDCl_3$, δ, ppm) of compound **6**.

3.3.1.2 Synthesis of (±)-2,7,12-trimethoxy-3,8,13-tris(propenyloxy)-10,15-dihydro-5H-tribenzo[a,d,g] cyclononatriene, 7

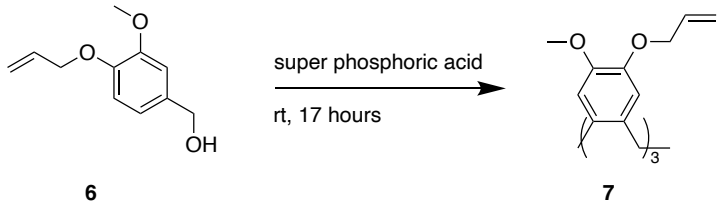

6 7

Scheme 3.6 Route to synthesise coumpound **7**.

The reaction to synthesise molecule **7** was shown in **Scheme 3.6**. Compound **1** in the round bottom flask is heated to the melting state (100 °C) with the heat gun. One spatula tip of super phosphoric acid was measured and added to the melting **6** followed by stirring overnight at room temperature. According to the mechanism showed above, the trimer, **7**, is formed from a reversible reaction. In order to achieve high yield, water need to be removed to get high yield. So at the beginning of the reaction, the heat gun was used to heat the neck of the round bottom flask to avoid the water condensing back to the reaction mixture. After overnight reaction, a brown solid formed, which was triturated in large amount of methanol, sonicated and then filtered to obtain a fine white powder. The white powder was further purified by washing with methanol followed by diethyl ether and then dried under reduced pressure to yield the product **7** on 9.3% yield. NMR spectrometry was used to characterise the product. In ^{1}H NMR spectrum (see **Figure 3.8**), two characteristic doublets at chemical shift of 4.74 and 3.52 ppm were detected and corresponded to the methylene linker of the benzene rings. As the results of the closed ring and the inherent concave conformation of the molecule **7**, the two protons on the linker became chemically and magnetically unequal, the one pointed inward the ring (labelled as $H_{e\text{-}exo}$) is located in a more electron rich environment causing the shielding effect, and thus it has the lower

chemical shift. Another one that pointed outward of the ring is located in a relatively electron poor environment, which induces the de-shielding effect exhibiting the higher chemical shift. All these reasons proved the success of the synthesis of molecule **7**.

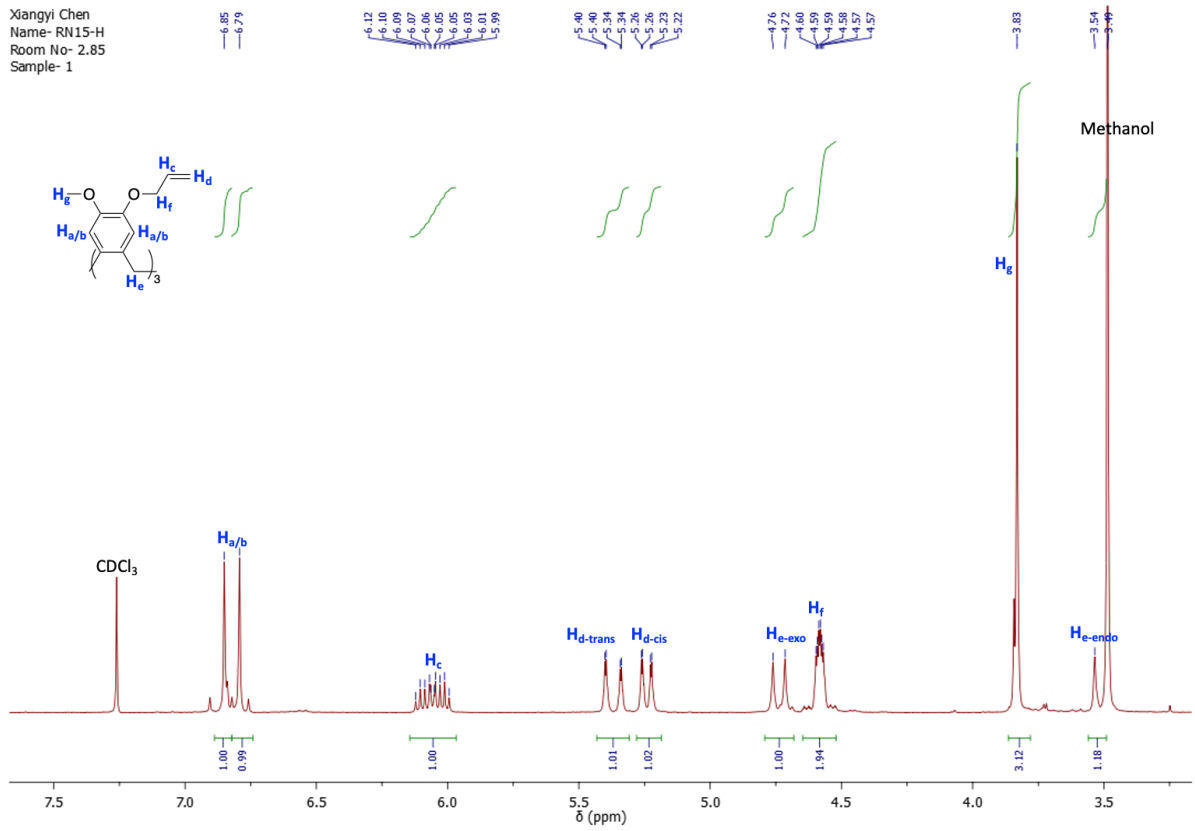

Figure 3.8 ^{1}H NMR (400 MHz, $CDCl_3$, δ, ppm) spectrum of molecule **7**.

3.3.1.3 Synthesis of CTG

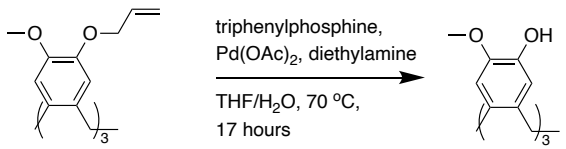

Scheme 3.7 Route to synthesise **CTG**.

The reaction to synthesise CTG has been shown in the **Scheme 3.7**. The reaction mixture was heated up to 70 °C for 17 hours, followed by filtration through celite. The filtrate was collected and concentrated under the reduced pressure to give a brown

residue as the crude product. Further purification was carried out by washing with methanol, the resulting suspension was filtered to give the greyish white power as product on 65.45% yield. The formation of the CTG was proved by the ^{1}H NMR spectroscopy, in which the peaks related to the ally protons disappeared, instead a peak at δ = 8.59 ppm was detected corresponding to the hydroxy protons (see **Figure 3.9**).

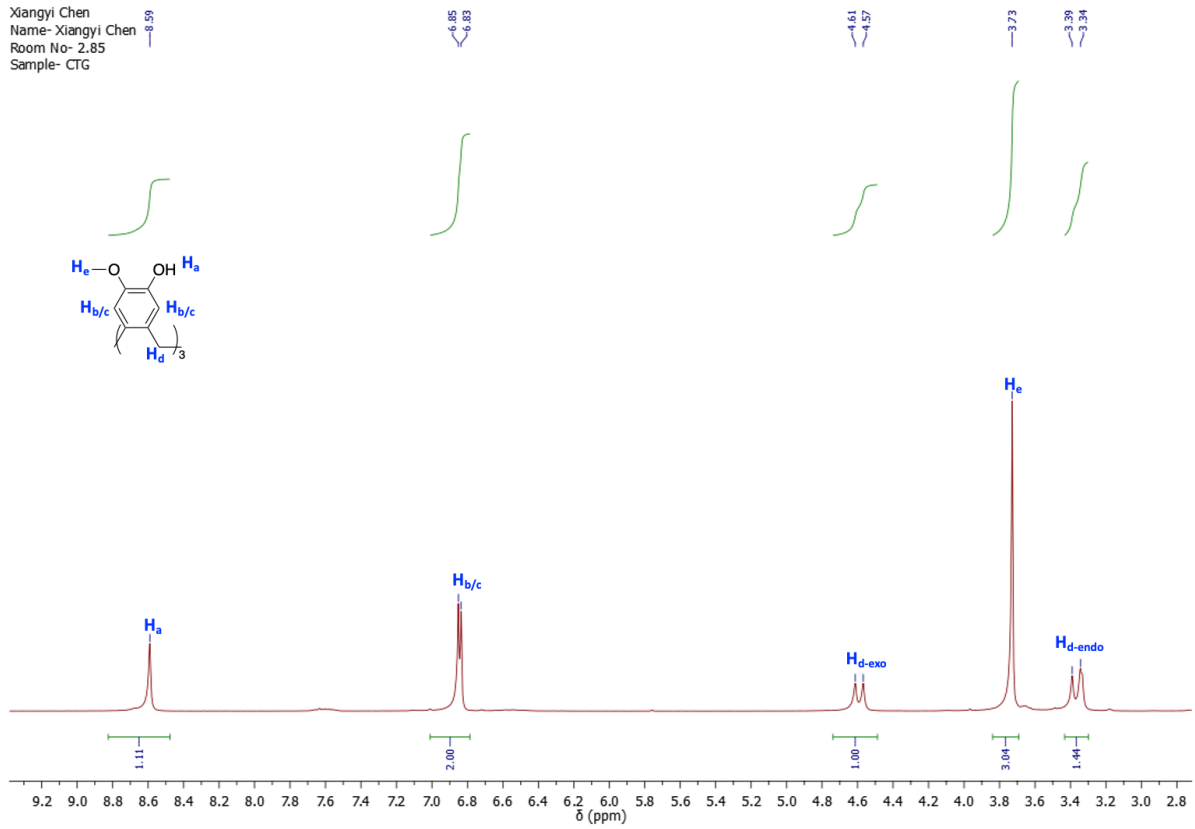

Figure 3.9 ^{1}H NMR (400 MHz, DMSO, δ, ppm) spectrum of molecule **CTG**.

3.3.2 Molecules synthesised from route 1

3.3.2.1 Synthesis of 4-(2,2-dimethyl [60]fulleropyrrolidinyl carbonyl) benzoic acid, 8

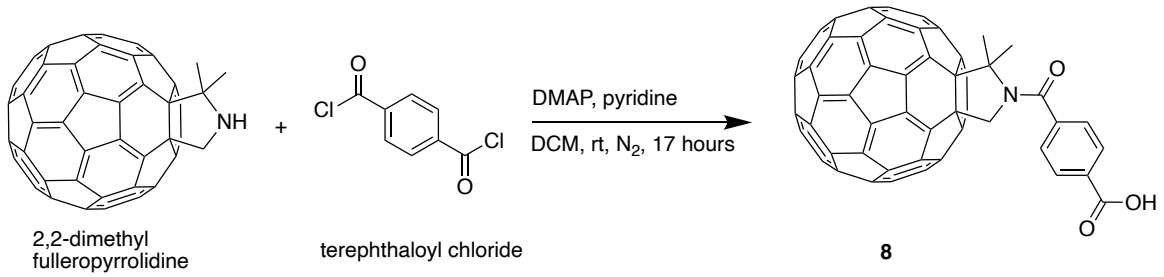

Scheme 3.8 Route to synthesise molecule **8**.

2,2-Dimethyl fulleropyrrolidine used was taken from the project of fullerene redox flow batteries. DMAP as a based was used to deprotonate the amine group of the 2,2-dimethyl fulleropyrrolidine forming the nucleophile that subsequently attack the carbonyl of the terephthaloyl chloride then kick the chlorine away as the leaving group. The starting material terephthaloyl chloride has two reactive acyl chloride group, which has the potential to bind two **8** molecules, so excess terephthaloyl chloride is required (11.53 equivalent) to avoid the formation of fullerene dimer (**Figure 3.10**). The reaction mixture was monitored by TLC (*o*DCB/IPA 9:1 v/v), where the spot of the product appeared at the position of R_f = 0.01. The purification process was carried out by passing the reaction mixture through the silica gel pad (toluene/methanol 4/1 v/v) to remove the insoluble by products. Then all the fractions were washed with water to remove the acid that was generated from the hydrolysis of terephthaloyl chloride, the organic layer was collected, and the water layer was extracted with CS_2. All the organic fractions were collected and purified by column chromatography (SiO_2, *o*DCB/IPA v/v 99.5/0.5->97/3). The formation of 22 was proved by ^{1}H NMR spectrometry and MALDI-ToF mass spectrometry (see **Figure 3.11**). In ^{1}H NMR spectrum (see **Figure 3.11a**),

two characteristic doublets with δ = 7.92 ppm and 8.25 ppm and the pyrrolidine singlet at δ = 5.31 ppm were detected as the evidence of that the aromatic group have been successfully attached to the N atom. In the MALDI-ToF ms result (see **Figure 3.11b**), the ion peak at m/z = 938.9 was detected to match the $[M]^-$ ion of molecule **3**. Other characterization data can be found in the appendix, which agreed with the literature.[13]

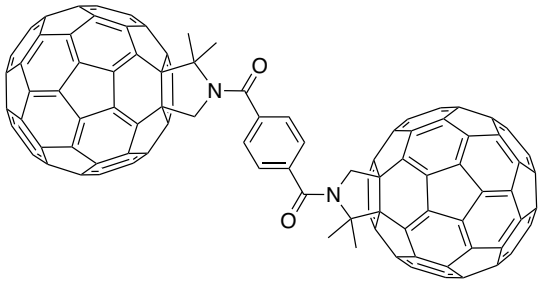

Figure 3.10 The schematic of the fullerene dimer that could form when the terephthaloyl chloride used is insufficient.

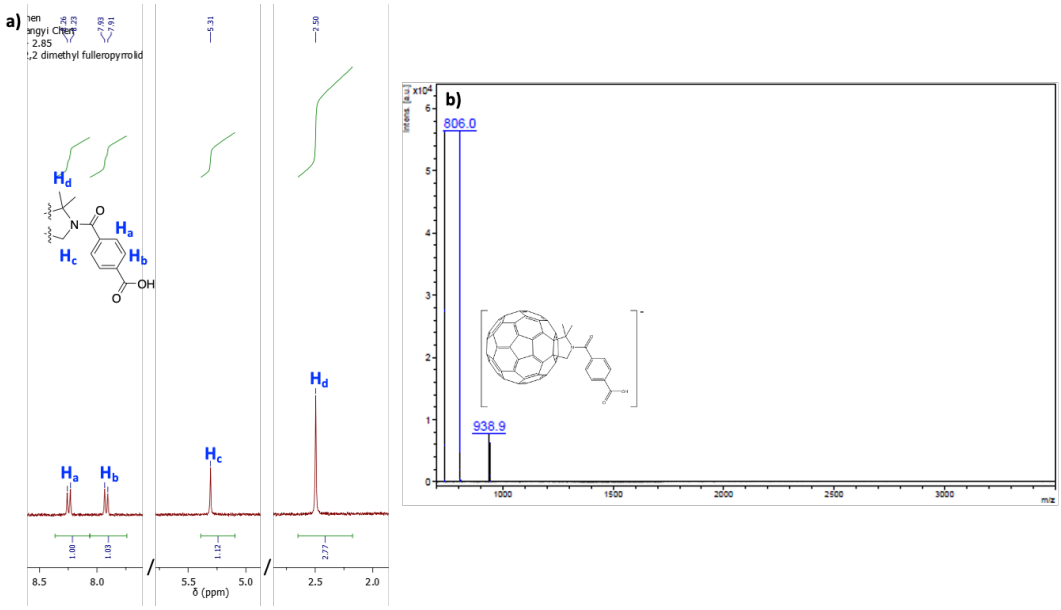

Figure 3.11 a) ^{1}H NMR spectrum (400 MHz, $CDCl_3/CS_2$ 1/7 v/v, δ, ppm) of compound **8**; b) MALDI ToF mass spectrum (negative mode, MeCN/DCTB) of molecule **8**, with a $[M]^-$ ion peak m/z = 938.9.

3.3.2.2 Synthesis of 4-(2,2-dimethyl [60]fulleropyrrolidinyl carbonyl) benzoyl chloride, 9

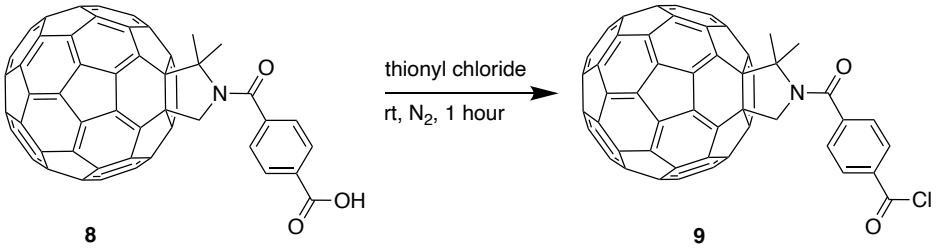

Scheme 3.9 Route to synthesise fullerene acyl chloride, **9**.

Using the thionyl chloride, the carboxylic group of **8** was converted to acyl chloride group to yield **9**. The reaction was completed by diagnostic TLC (*o*DCB/IPA 8/2 v/v), the formation of the **8** was indicated by that the spot of **3** disappeared and a trace from baseline to R_f = 0.4 formed, which is due to the acyl chloride group is reactive to silica gel. The formation of **9** was also observed as the reaction mixture changed from suspension to clear solution, which is caused by the higher solubility of **9** than **8**. After the reaction, the toxic thionyl chloride was removed by Schenk line technique, leaved brown residue as the product on 100% yield. With the consideration of the moisture sensitivity of **9**, it was not analysed by NMR or mass spectroscopy, but used directly for CTG coupling reaction.

3.3.2.3 Test reaction to synthesise of (±)-2,7,12-trimethoxy-3,8,13-tris(isonicotinoyl)-10,15-dihydro-5H-tribenzo[a,d,g] cyclononatriene in THF and *o*DCB

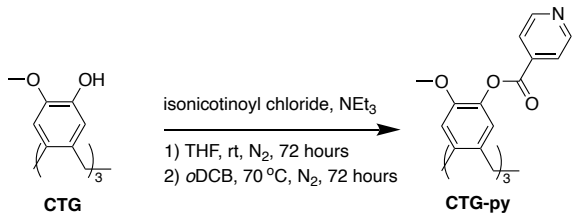

Scheme 3.10 Route to synthesise the **CTG-py**.

Before performing the reaction between CTG and fullerene derivative **9**, test reactions were performed to figure the reaction condition, including the, solvent, temperature, and reaction time. The synthesis of CTG-py is based on the same type of reaction that is between hydroxy group and acyl chloride, which has been reported in the previous literature.[11]

First, we want to transfer the solvent from THF, a good solvent for **CTG**, to *o*DCB that is the good solvent for fullerene. In comparison with THF, the solubility of **CTG** in *o*DCB is not very promising, which requires heating to help the **CTG** to be dissolved in. Stirring at the temperature of 70 ^{o}C can maintain the solution state. The same reaction time of the reaction in THF was adopted in *o*DCB, 72 hours. **CTG** (0.2 g, 0.48 mmol, 1 *equiv*) was added to a well degassed round bottom flask, anhydrous *o*DCB (40 mL) was added, followed by adding with isonicotinoyl chloride hydrochloride (0.46 mg, 2.54 mmol, 5.3 *equiv*) and anhydrous triethylamine (1.06 mL, 6 mmol, 12.5 *equiv*), the resulting mixture was stirred at 40 ^{o}C under a N_2 atmosphere for 72 hours. The reaction mixture was monitored by LC-MS (see **Figure 3.12a**), in which an ion peak with m/z = 724 was found corresponding to $[M+H]^+$ of CTG-py. The solvent was removed to give the yellow residue, followed by washing with ethanol (100 mL) and diethyl ether (20 mL), resulting a white solid (0.228 g, 0.32 mmol, 67.1%) as the product CTG-py. The product was characterised by ^{1}H NMR spectrometry (see **Figure 3.12b**), in which the hydroxy peak disappeared, and two newly formed doublets were detected in the aromatic region with δ = 8.87 ppm and 8.07 ppm corresponding to the pyridine ring. So, the condition in *o*DCB to perform the coupling reaction between CTG and fullerene bridge molecule that heating up to 70 ^{o}C under a N_2 atmosphere for 72 hours.

Then the reaction in *o*DCB was performed on small scale, 5 mg of **CTG** used. This is meaningful as the small scale and the low yield of reaction to synthesise fullerene

bridge molecule. With the same ratio of the CTG : acychloride 1: 5, the conversion become low on small scale. In the LC-MS data of the reaction mixture, mono-adduct, bis-adduct and the tris-adduct were detected at the same time. Keep adding more acyl chloride and the triethylamine into the reaction mixture failed to push the reaction to completion. In order to solely synthesise CTG tris-adduct directly, excess acyl chloride is required. This reaction was repeated and increased the equivalent of the acyl chloride gradually. Eventually, the reaction went to completion when 9 equivalents of the acyl chloride was added. This means for 5 mg (0.012 mmol) of the CTG molecule, 108 mg (0.108 mmol) of the molecule **8** is required, which really challenges the preparation of the fullerene derivatives.

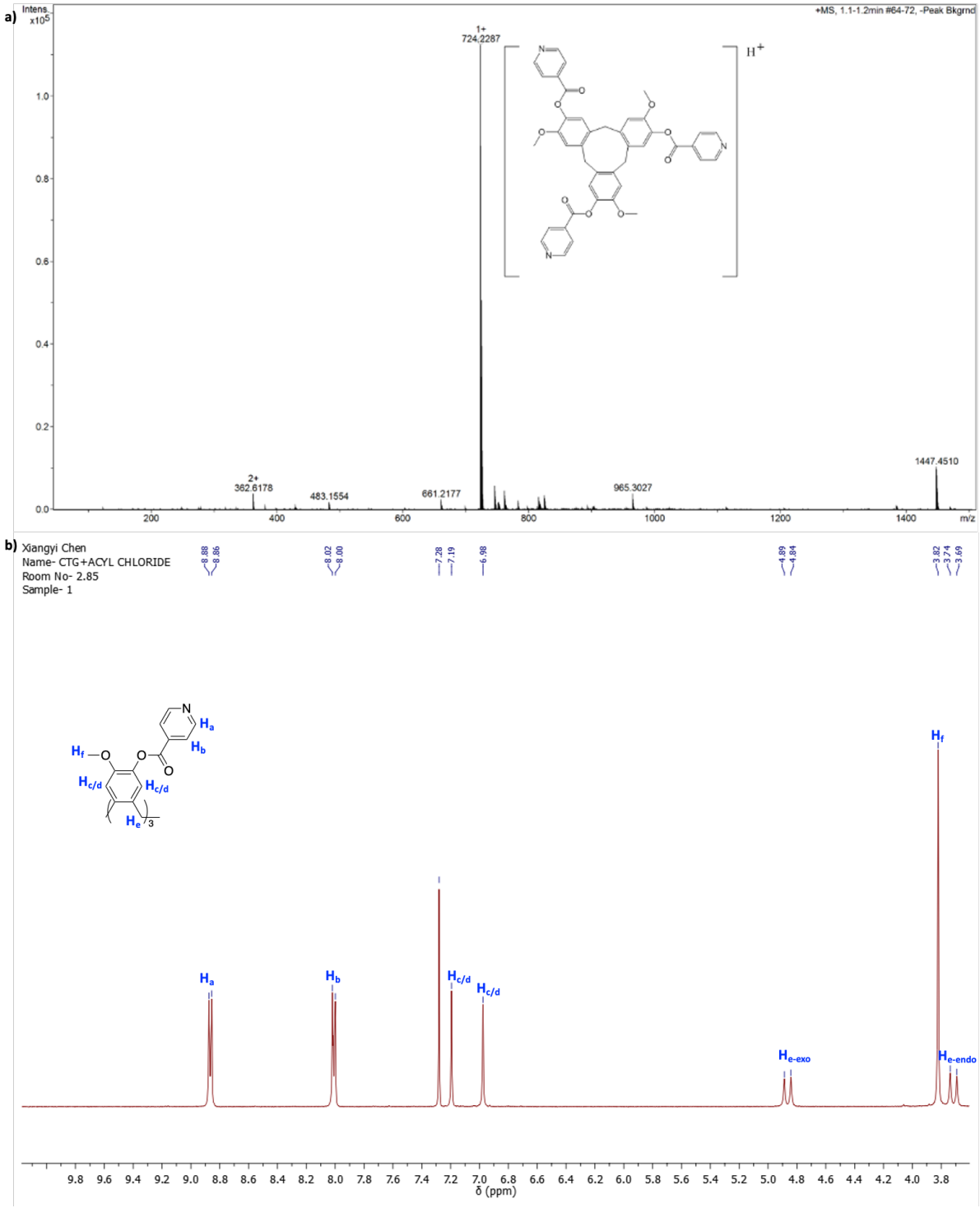

Figure 3.12 a) LC-MS data of the reaction mixture to synthesise **CTG-py**; b) ^{1}H NMR spectrum (400 MHz, $CDCl_3$, δ, ppm) of **CTG-py**.

3.3.2.4 Synthesise tris-fullerene-CTG derivatives, 10

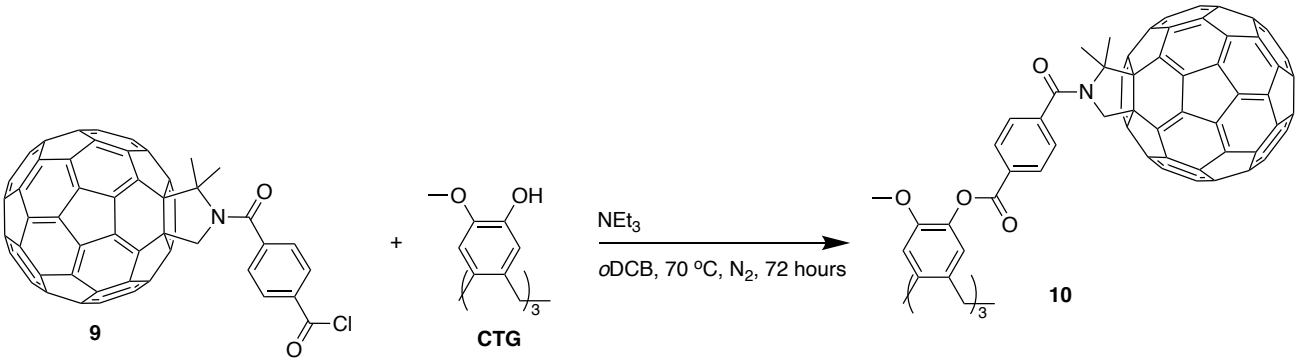

Scheme 3.11 Route to synthesise tris-fullerene-CTG complex, **10**.

CTG (2mg, 0.005 mmol) was added to a degassed RBF that had freshly prepared compound **9** inside, followed by adding with anhydrous *o*DCB and anhydrous triethylamine in order, the resulting mixture was heated at 70 °C under N_2 atmosphere for extended reaction time (72 hours to 3 weeks), and monitored periodically by MALDI ToF ms. Negative mode data showed ion peaks with m/z = 720.4 and 994.6, corresponding to the $[M]^-$ of fullerene and the fullerene dimer fragment respectively. In the results from positive mode, an ion peak at 683.8 m/z appeared, which matches the $[M+2H]^+$ corresponding to the CTG cup binding a fullerene bridge molecule, **9**, in its cavity. At the same time, an ion peak at m/z = 1540 was also detected, however, it cannot be assigned. Unfortunately, the fullerene-CTG complex, **10**, and its intermediates, i.e. a CTG with either one or two fullerene arms, was not observed. The reaction mixture was also analysed by TLC, in which a new spot with R_f = 0.7 was observed.

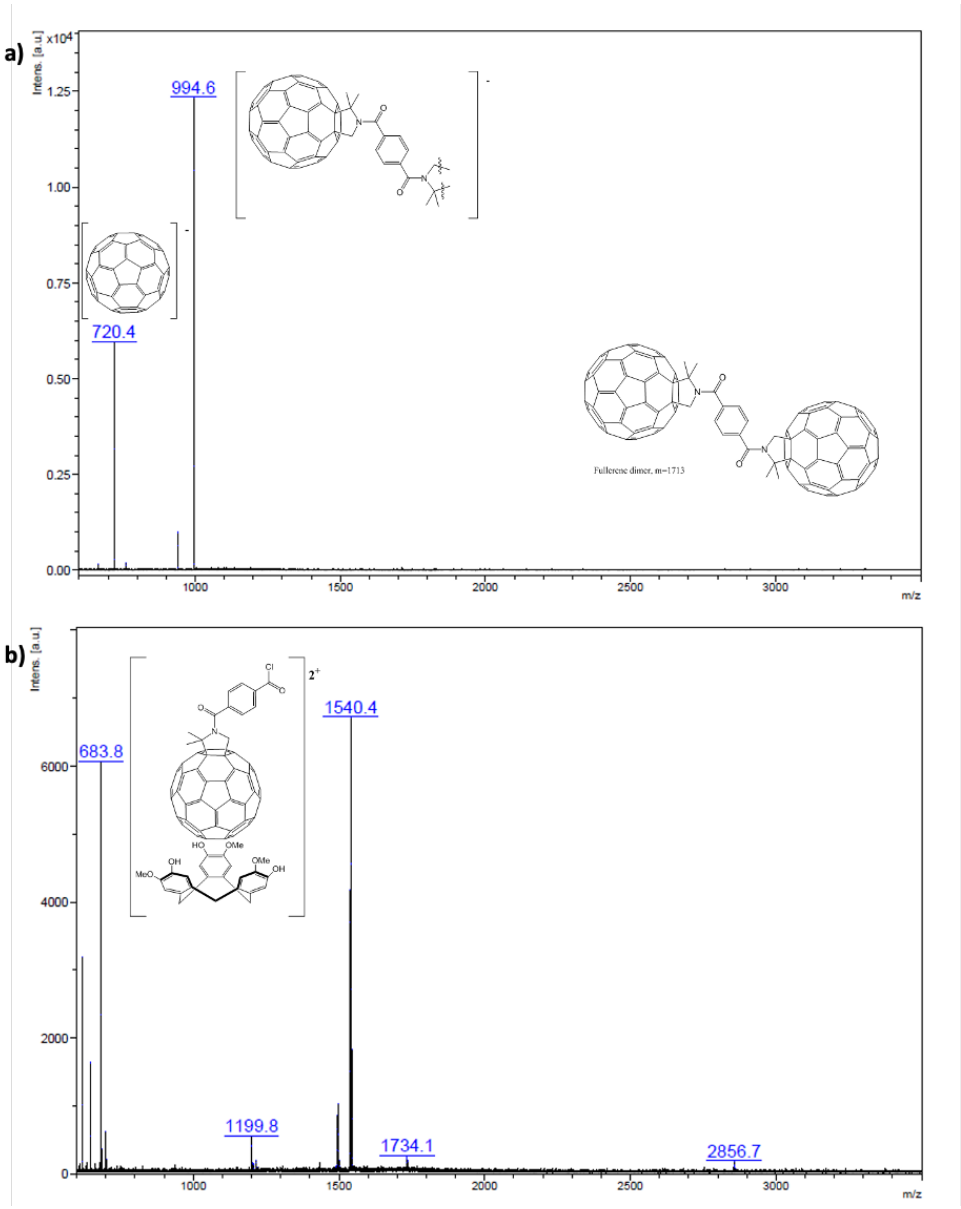

Figure 3.13 **M**ALDI ToF ms (MeCN, DCTB) data of the reaction mixture; a) negative mode with ion peaks, m/z = 720.4, 994.6, found; b) positive mode with ion peaks, m/z = 683.8 and 1540.4, found.

The reaction mixture was added with excess CS_2 to dissolve every fullerene derivative, then the mixture was centrifuged. The precipitate was retained, the soluble layer was then passed through a column chromatography to isolate the newly formed band. The precipitate and the column fractions were both analysed by MALDI ToF ms. As seen in the **Figure 3.14a**, an ion peak with m/z = 938 was detected to match the $[M]^-$ of

fullerene-carboxylic acid **8** as the result of the hydrolysis of the acyl chloride. The new material isolated from the column chromatography was assigned as the fullerene dimer (see **Figure 3.14b**). We proposed the hypothesis that: i) the fullerene dimer was synthesised during the preparation of the **8**, however, there is no evidence to support this as the there was no dimer was detected in any characterisaiton of **8**; ii) the fullerene dimer was generated in the reaction to synthesise molecule **10** via an unknown mechanism.

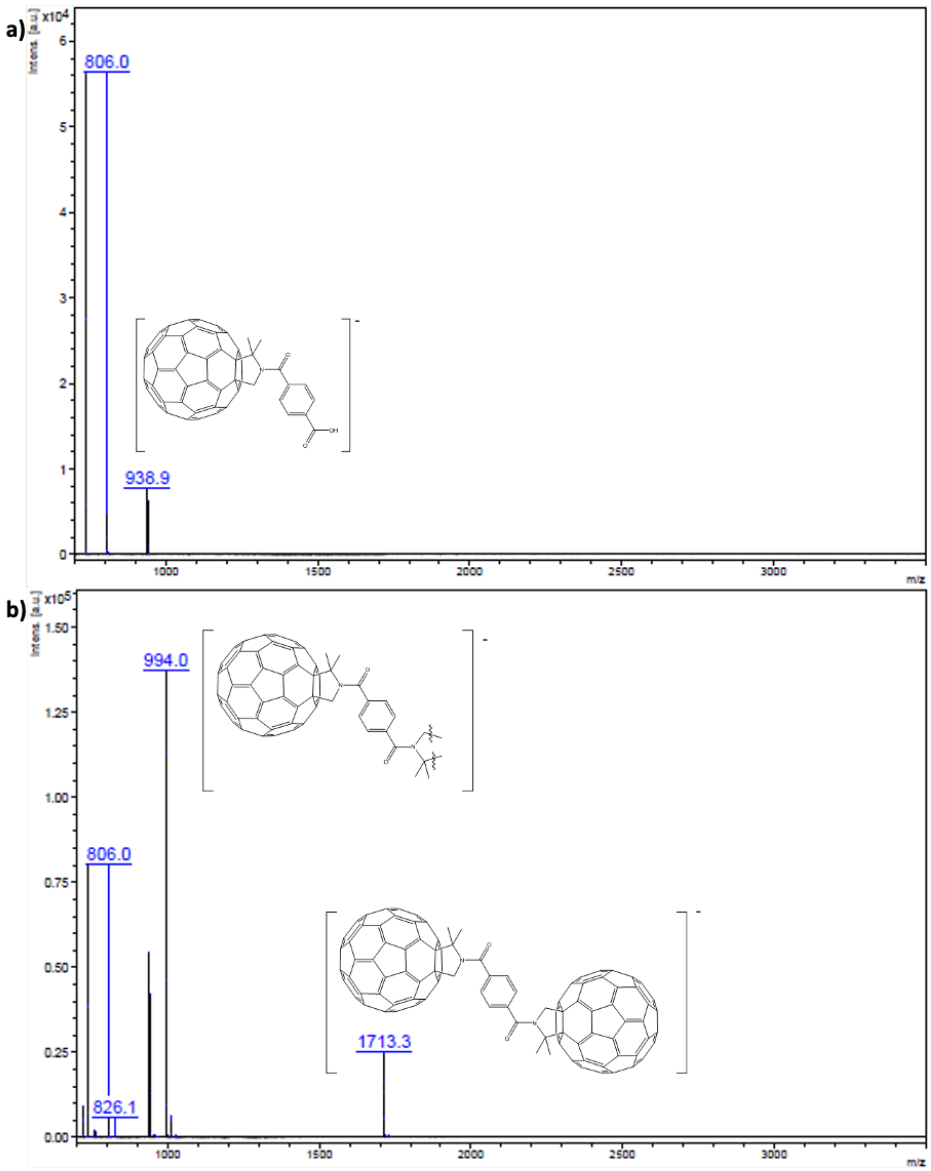

Figure 3.14 MALDI ToF ms (negative mode, MeCN/DCTB) data of a) the precipitate in the centrifuge tube with an ion peak m/z = 938.9 found; and b) the newly formed band isolated from the column chromatography with ion peaks with m/z = 994.0 and 1713.3 found.

Due to the large quantity of fullerene derivatives required for this route and the unknown mechanism occurring via which fullerene dimer is formed, this route was not judged appropriate to carry out the synthesis of the tris-fullerene-CTG. Therefore, the

route 2: one-pot Prato reaction was proposed, as it shows the potential to yield the target molecule well due to the reasons below:

1. It uses the fullerene C_{60} as the starting material to make the target molecule directly, which avoids the low yielding, small scale and repetitive nature of the fullerene bridge synthesis.
2. The functionalisation of CTG can be performed on large scale with decent yields so large quantities of starting material for the Prato reaction are readily available.
3. The high reaction temperature used for Prato reaction can increase the reaction rate to form the target molecule and keep the CTG and the subsequent CTG-C_{60} species dissolved in *o*DCB.

3.3.3 Molecules synthesised from Route 2

3.3.3.1 Synthesis of the CTG tris-aldehyde, 11

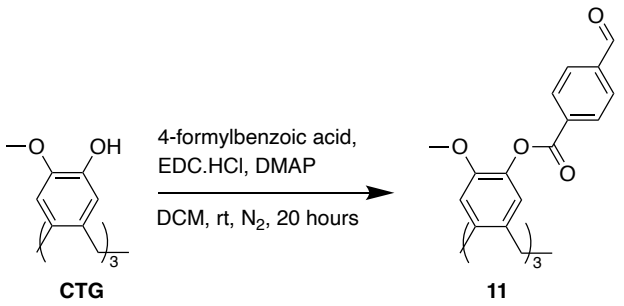

Scheme 3.12 Route to synthesise CTG tris-aldehyde with ester linker, **11**.

The reaction to synthesise compound **11** was shown in **Scheme 3.12**. In this reaction, a carbodiimide derivatives, EDC.HCl was used as the carboxylic acid activating agent, which reacts with the carboxylic acid group forming the *O*-acylisourea intermediate (see **Scheme 3.13**).[14] The lone pair on the oxygen of the CTG alcohol serves as a nucleophile to react with the *O*-acylisourea intermediate giving the ester as the product. Within the *O*-acylisourea, the acyl migration has the possibility to happen giving a *N*-

acylurea side product when there is a lack of a strong nucleophile. As alcohols are typically weak nucleophiles, the use of DMAP is crucial to avoid the formation of the *N*-acylurea and yield esters efficiently. DMAP as a strong nucleophile can react with the *O*-acylisourea intermediate initially, resulting in the acyl group being transferred to the DMAP, forming a reactive amide, which will then react with alcohol giving the ester product. The reaction to synthesise **11** was successfully performed, which was monitored by TLC. A new spot with R_f = 0.4 was observed on the TLC (1%methanol/DCM) plate and assigned to the presence of **11**. The reaction mixture was washed with water to get rid of the excess EDC.HCl and the ureas by-products. The organic layer was collected and concentrated under reduced pressure, followed by passing through column chromatography (SiO_2, 1%methanol/DCM) giving yellow solid (45.7%) as product. The formation of the **11** was proved by NMR spectroscopy. In the ^{1}H NMR spectrum (see **Figure 3.15a**), the aldehyde peak at δ = 10.07 ppm and two doublets at 8.32 and 7.96 ppm were detected as the result of the benzaldehyde being attached to the CTG scaffold. In the ^{13}C NMR spectrum (see **Figure 3.15b**), two peaks at δ = 191.65 and 163.79 ppm were detected, which were assigned to the aldehyde carbon and the ester carbon respectively.

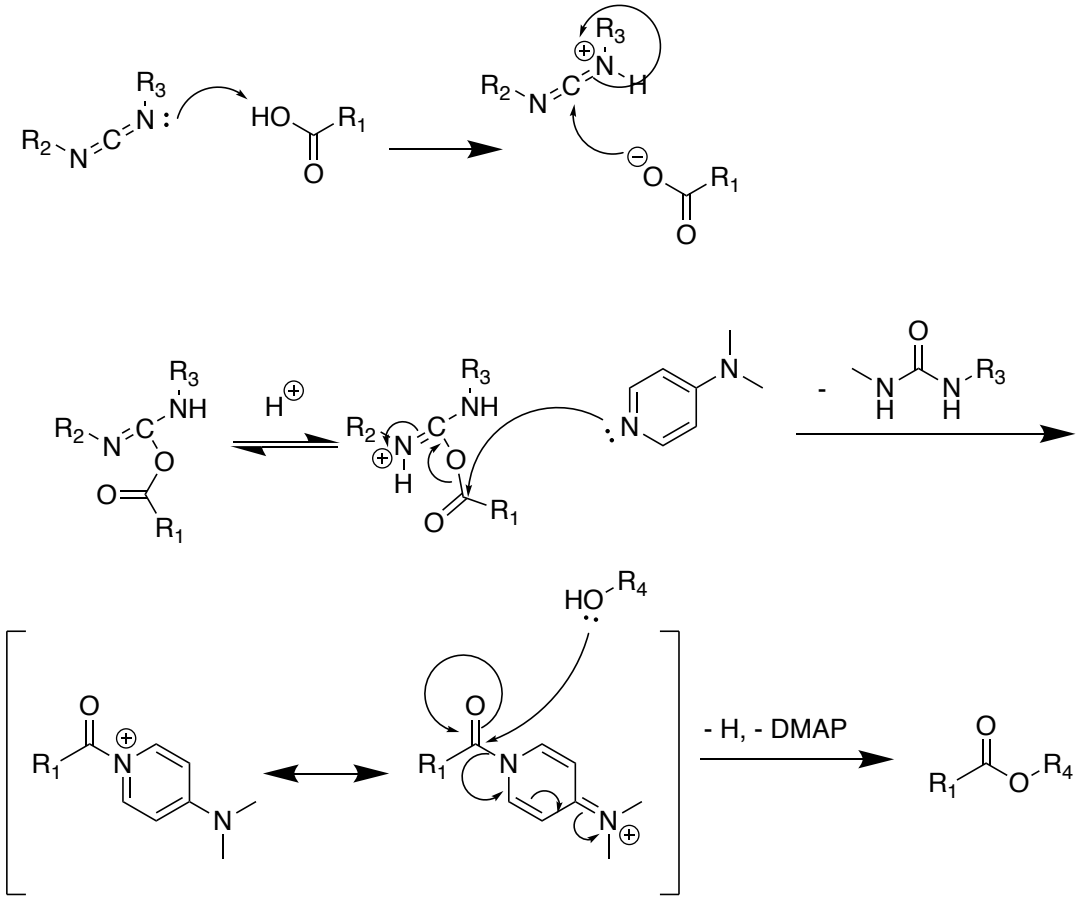

Scheme 3.13 Mechanism of Steglich Esterificatoin that uses carbodiimide as carboxylic acid activating agent.

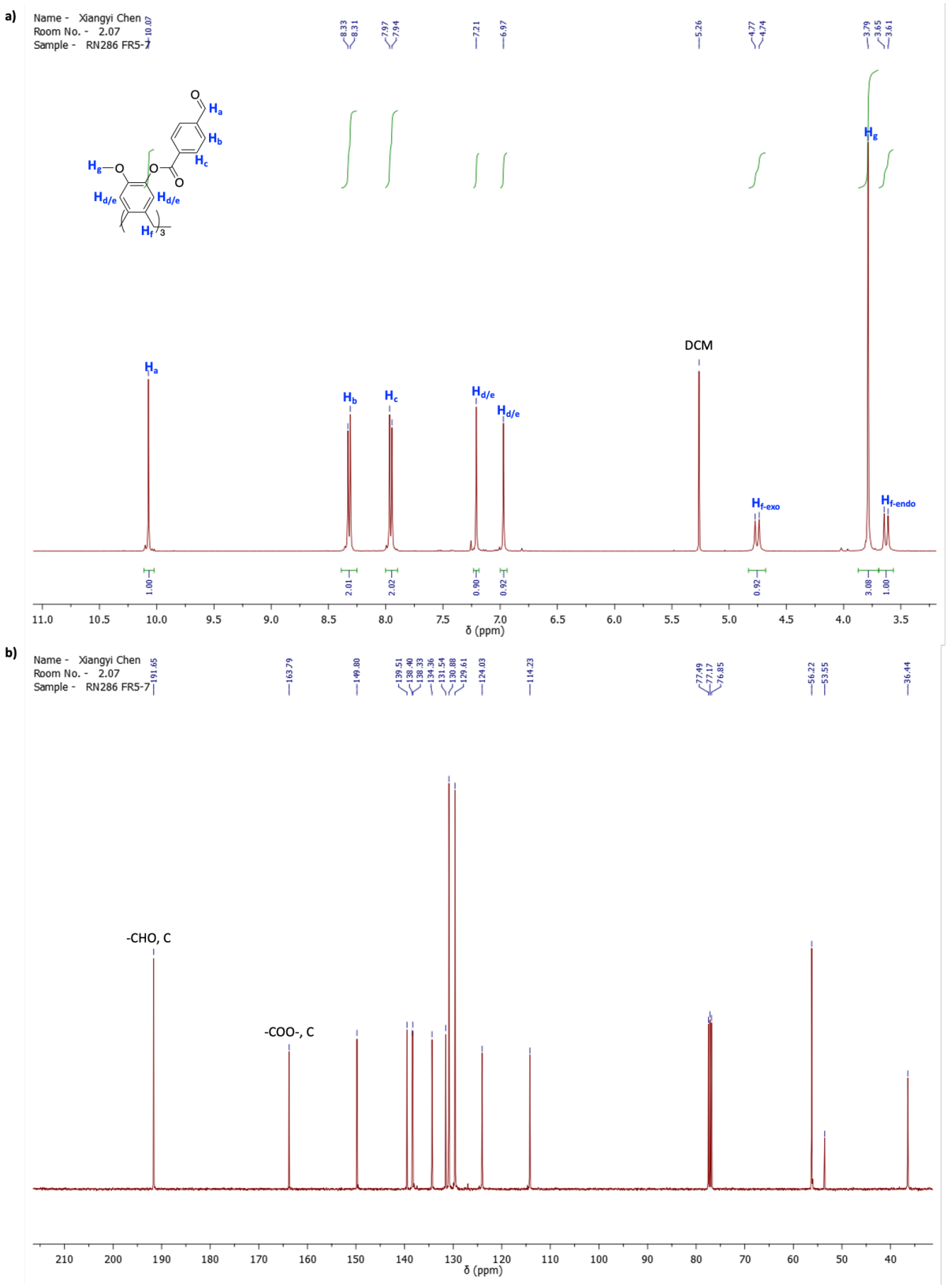

Figure 3.15 a) ^{1}H NMR and b) $^{13}C\{^{1}H\}$ NMR spectra (400 MHz, $CDCl_3$, δ, ppm) of compound **11**.

3.3.3.2 Synthesis of tris-fullerene-CTG, 12

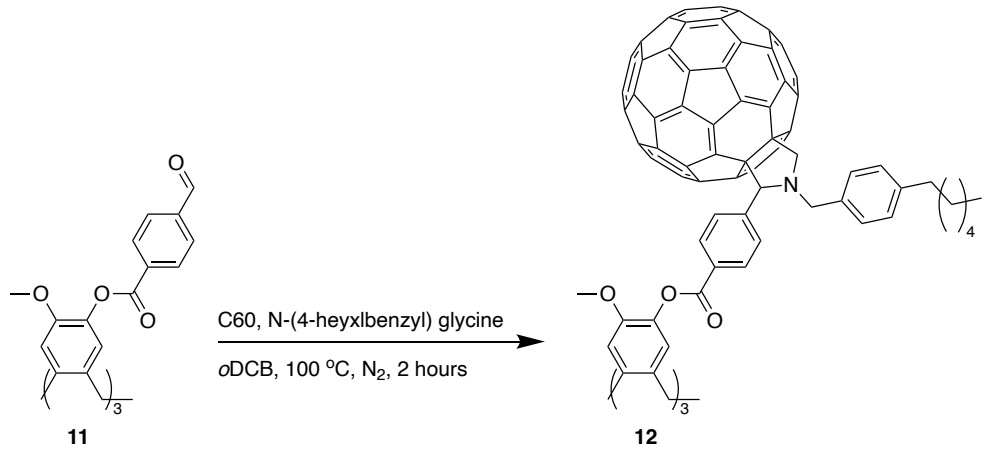

Scheme 3.8 Route to synthesise tris-fullerene-CTG, **12**.

CTG trisaldehyde, **11**, was used to perform the one-pot Prato reaction with 4.5 equivalents of C_{60} and the 15 equivalents of amino acid, *N*-(4-hexylbenzyl) glycine (which has been discussed in the C_{60}Fc RFB chapter) to synthesise molecule **12**. The reaction mixture was monitored by TLC (1%ethylacetate/*o*DCB). A new spot with brown colour was observed on the TLC plate with of an R_f = 0.3 (see **Figure 3.16a**), which indicated that there were some fullerene derivatives formed in the reaction. The solvent was removed, the residue was redissolved with CS_2, the resulting mixture was passed through a column chromatography (SiO_2, 1%ethylacetate/*o*DCB). The column fraction was collected and analysed by MALDI ms and NMR spectroscopy. In the MALDI ms data (see **Figure 3.17**), the fullerene peak was observed at m/z = 720.76, which means the fractions collected were the fullerene related species. A peak at m/z = 3527.38 was observed, which was really close to the calculated mass of molecule [**12**]$^-$, 3525.74. A peak at m/z = 2807.34 was also observed and the mass difference between two peaks was exactly 720, which suggests that it could be due to fragmentation of the compound **12**, i.e. having lost one fullerene cage. To get a better MALDI data, the MALDI acquisition conditions need to be optimised, such as matrix,

power and the calibrants. In the ^{1}H NMR spectrum (see **Figure 3.18**), all the peaks were attempted to be assigned, including the two CTG aromatic peaks at δ = 7.03 and 6.79 ppm, two aromatic peaks from the linker of the CTG and the fulleropyrrolidine at δ = 8.17 and 7.47 ppm, and two aromatic peaks from the phenyl group of the hexylbenzene at δ = 7.37 and 7.16 ppm. The four peaks that are assigned to the hexyl groups were also observed at δ = 2.63, 1.64, 1.30 and 0.88 ppm. There are several doublets were observed from 3.5-5.5 ppm, indicating the formation of the fulleropyrrolidine, in which the geminal couplings occurred at H_h and H_j (see **Figure 3.18**). At the same time, a singlet at δ = 5.22 ppm was assigned as the proton on the pyrrolidine carbon that is attached to the benzene linker. Moreover, this pyrrolidine carbon shows chirality, which means multiple isomers can be formed together when one CTG binds three fullerene cages. However, the integral of the peaks does not match the correct value and a small aldehyde proton peak was also observed at δ = 9.90 ppm, which indicated that the fractions that were collected from the column chromatography were probably a mixture of **12**, and the corresponding one- and two-armed intermediates. The TLC results of the column fraction also suggest a mixture as multiple spots were observed (see **Figure 3.16b**). The fractions were combined and attempts to pass the mixture through column chromatography with different eluents, such as CS_2, 2-5%ethylacetate/*o*DCB, 0.5-2%methanol/*o*DCB, 0.5-4%ethylacetate/toluene, 0.5-1%methanol/toluene, 0.5-2%ethylacetate/DCM and 0/5-2%ethylacetate/$CHCl_3$ were made. However, it proved impossible to separate the mixture. It is concluded that the silica gel chromatography is not able to isolate this mixture of CTG-fullerene isomers and a HPLC with a fullerene specialised column, i.e. Buckyprep M, is required to perform the isolation properly, which is a future work. Due to the formation of the isomers via this route, the compound **12** not is a promising

candidate to develop supramolecular arrays as the clockwise (*P*) and counterclockwise (*M*) isomers can be hard to yield and isolate. Therefore, finding a route that can generate the non chiral product is required. Using the CTG-aminoacid derivatives for the Prato reaction can solve this problem, in which the linker will not attach to the pyrrolidine carbon instead to the N atom of the pyrrolidine. The synthesis of CTG-tris-aminoacid will be discussed in the following section.

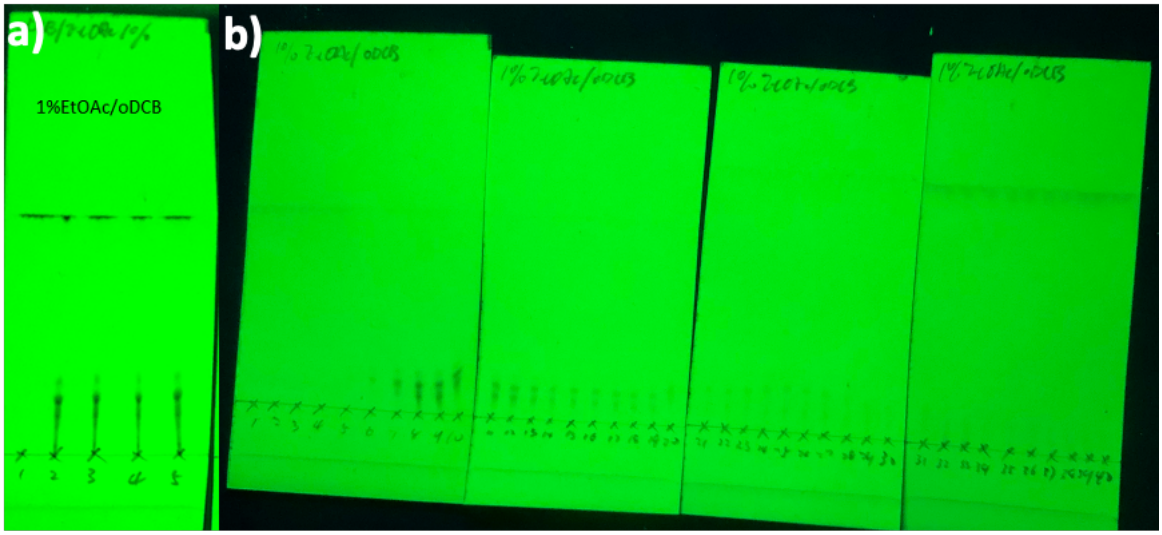

Figure 3.16 TLC results of a) the reaction mixture to synthesise molecule **12** and b) the column fractions.

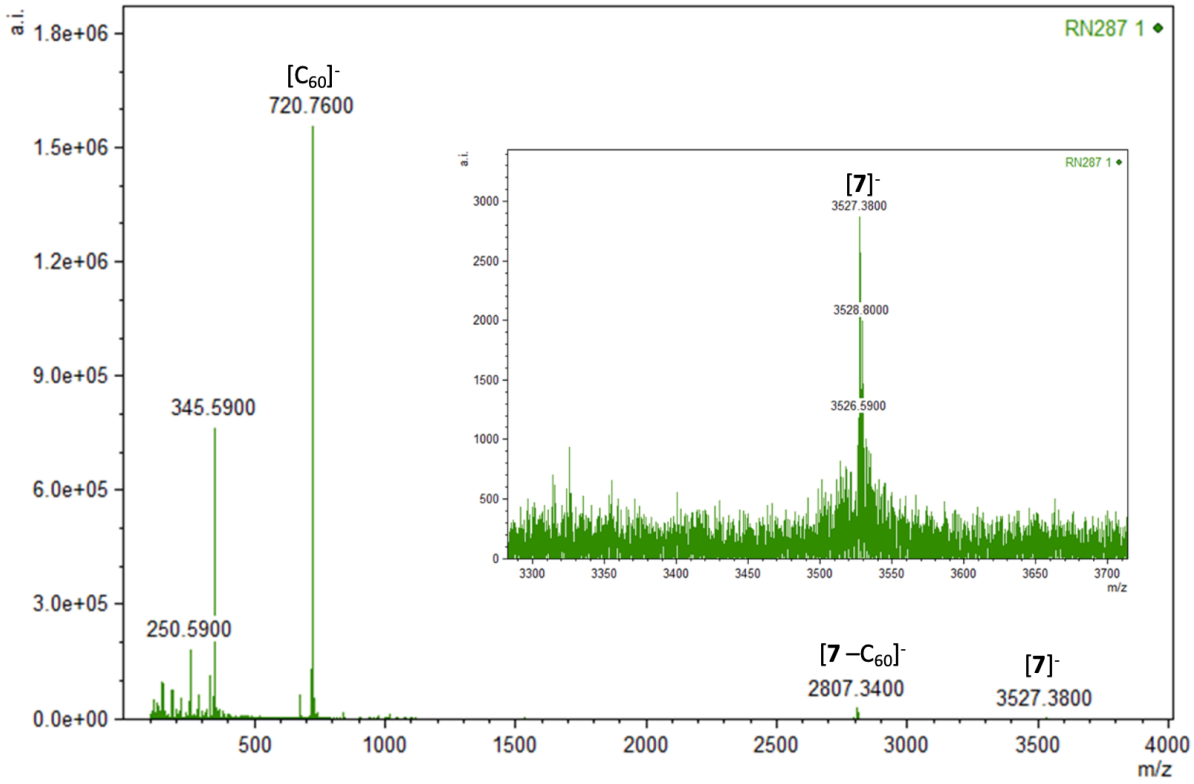

Figure 3.17 MALDI ToF ms spectra (negative mode, MeCN/DCTB) of the of the column fractions of **12**. The calculated mass of [**12**] and [**12**-C_{60}] is 3525.74 and the 2805.74.

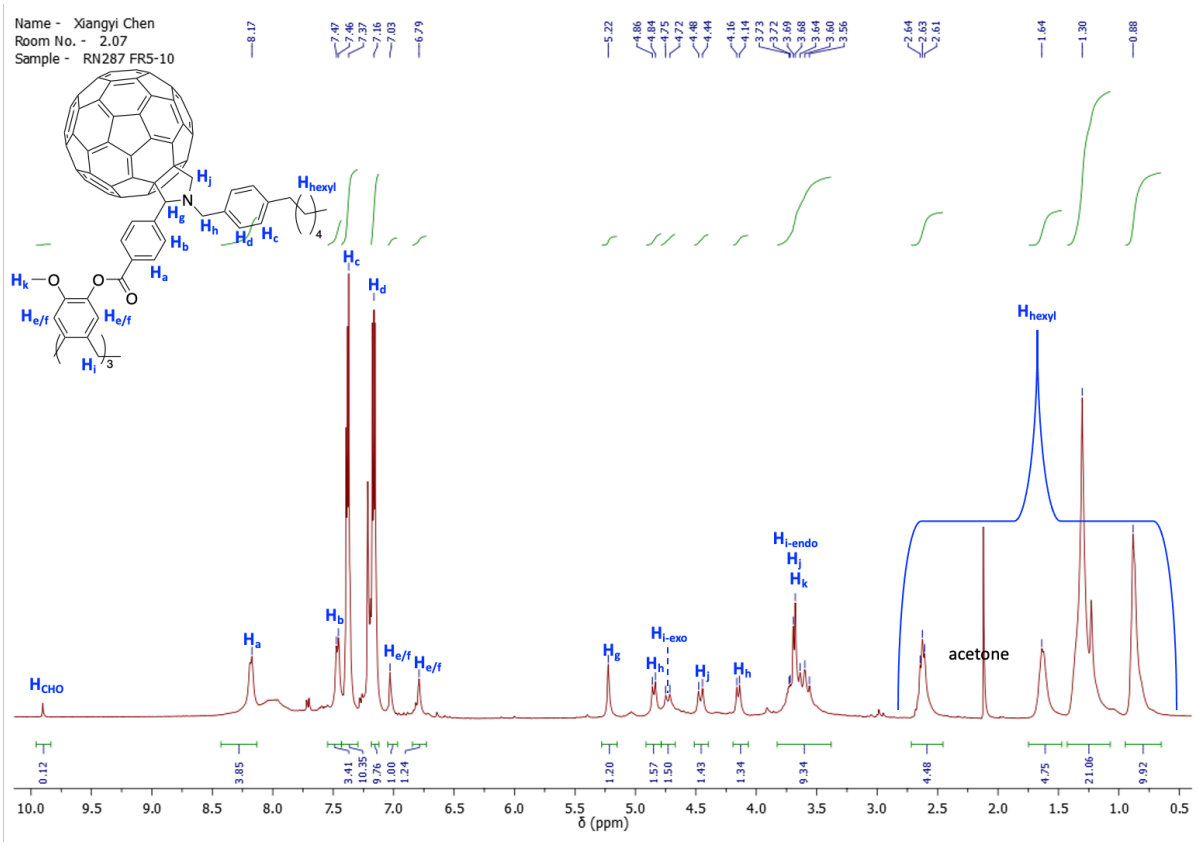

Figure 3.18 ^{1}H NMR spectrum (400 MHz, $CDCl_3$, δ, ppm) of column fraction of the reaction mixture to synthesise molecule **12**.

3.3.3.3 Synthesis CTG tris-aldehyde with ether linker, 13

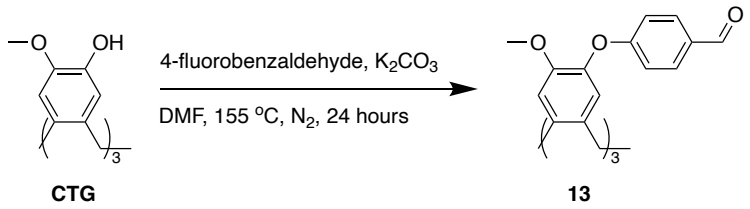

CTG **13**

Scheme 3.14 Route to synthesise CTG tris-aldehyde with ether linker, **13**.

The route we designed for synthesis of the CTG-tris-aminoacid includes the reductive amination between the CTG-tris-aldehyde and glycine methyl ester to give the product CTG-tris-methyl ester and the following ester deprotection to give CTG tris-aminoacid. Due to the incompatibility of the ester linker in **11** for the synthesise of the amino acid,

tris-aldehyde CTG ,**13**, with ether linker was proposed to synthesise via the aromatic substitution, which was shown in **Scheme 3.14**. CTG (1 *equiv*), 4-fluorobenzaldehyde (3.3 *equiv*) and K_2CO_3 (*3.3 equiv*) were added in anhydrous DMF (10 mL), the resulting mixture was heated to 155 ^oC for 24 hours. The solvent was removed using Schlenk line technique due the toxicity of the DMF, followed by washing the residue with brine and extract with large amount of DCM (details see experimental). The organic layer was collected and dried with $MgSO_4$. The solvent was removed and added with minimal amount of chloroform forming a suspension, which was filtered to give the white solid as the product, **13**, on 72% yield. NMR spectrometry and LC-MS spectrometry were used to provide the evidence for the formation of the **13**. In ^1H NMR spectrum (see **Figure 3.19a**), a distinct singlet at δ = 9.90 ppm and two doublets at δ =7.80 and 6.98 ppm were detected corresponding to the aldehyde proton and the phenyl protons respectively. In LC-MS data (see **Figure 3.19b**), ion peaks at m/z = 720 and 743 were found, which are corresponded to $[M+H]^+$ and $[M+Na]^+$ ions of **13** respectively.

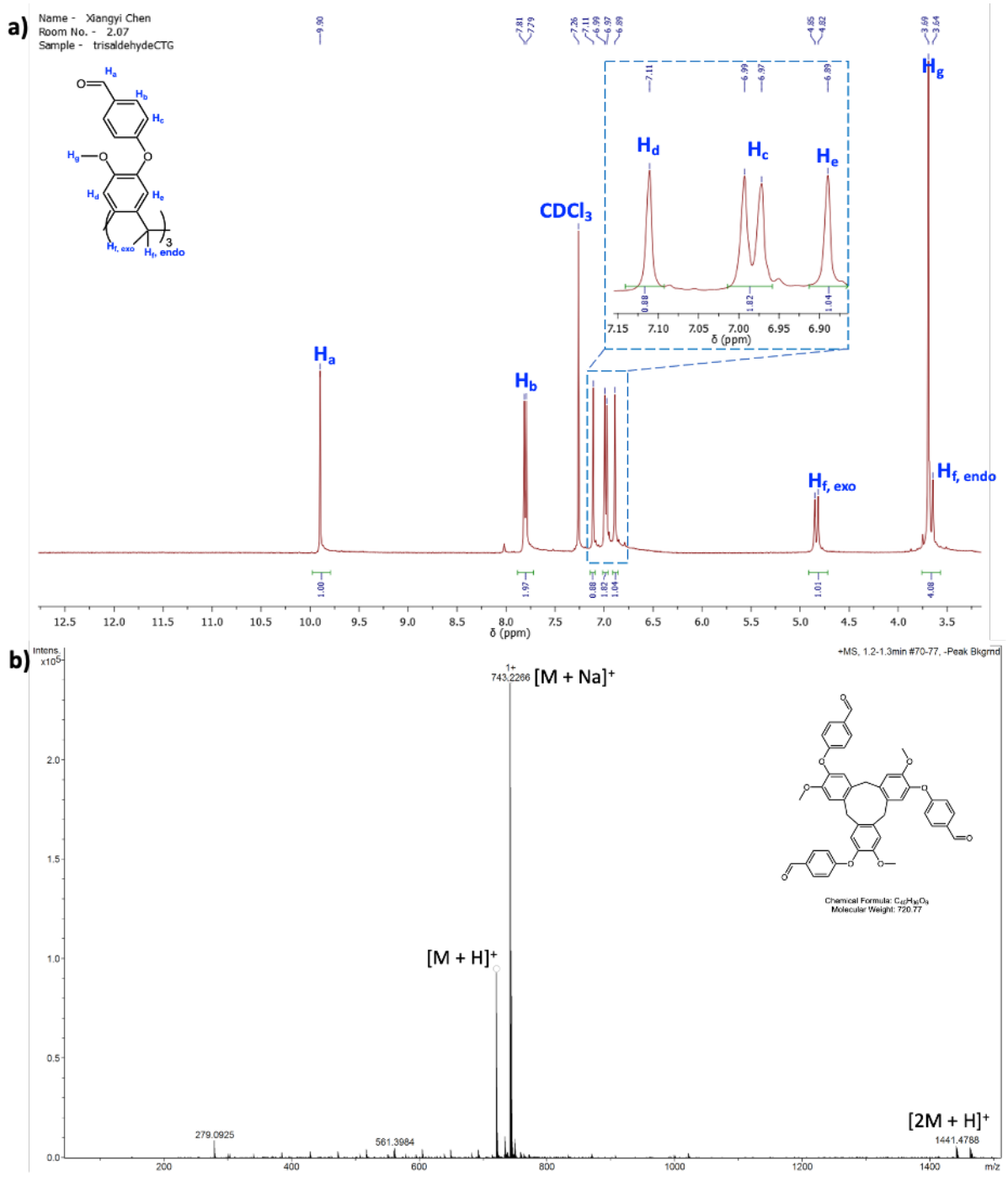

Figure 3.19 a) ^{1}H NMR spectrum (400 MHz, $CDCl_3$, δ, ppm) of compound 8; b) LC-MS data of the compound **13**.

3.3.3.4 Synthesis CTG tris-methyl ester, 14

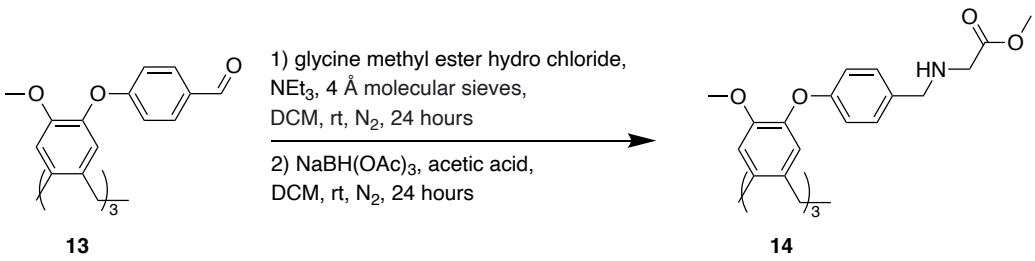

Scheme 3.15 Route to synthesise CTG tris-methyl ester, **14**.

The reaction to synthesise CTG tris-methyl ester, **14**, has been shown in **Scheme 3.15**, which includes two steps, 1) aldehyde and amine coupling reaction to give imine intermediate and 2) the imine reduction. The reaction mixture was monitored by ^{1}H NMR spectrometry (see **Figure 3.20a**). After 24 hours, the imine peak at δ = 8.22 ppm was detected successfully. By following the standard procedures (see fullerene RFB chapter), the reduction step was performed. In the ^{1}H NMR spectrum (see **Figure 3.20b**), the imine peak disappeared, which indicated that the reduction worked. After the pre work up, the crude product was purified by column chromatography (SiO_2, 1->4%methanol/DCM) giving sticky solid (51%) as the product that were characterised by NMR spectrometry. In ^{1}H NMR (see **Figure 3.21**) spectrum, two methylene singlets at δ = 3.74 and 3.40 were found as the evidence for the formation of the compound **14**. In the LC-MS (see **Figure 22**) results, an ion peak at m/z = 940 was observed corresponding to the $[M+H]^+$ ion of compound **14**.

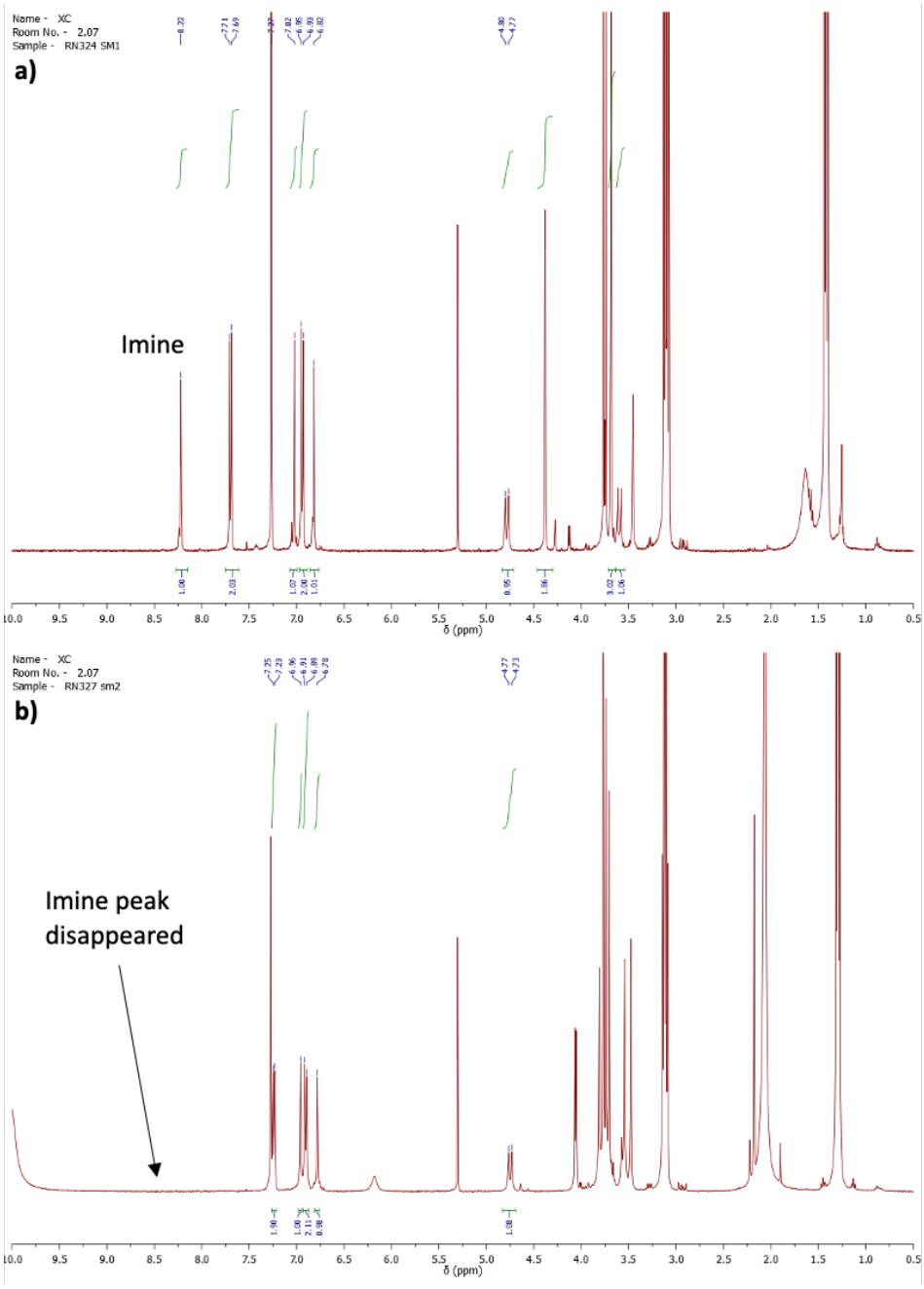

Figure 3.20 ^{1}H NMR (400 MHz, $CDCl_3$, δ, ppm) spectrum of the reaction mixture a) step 1, aldehyde and amine coupling reaction; b) step 2, imine reduction.

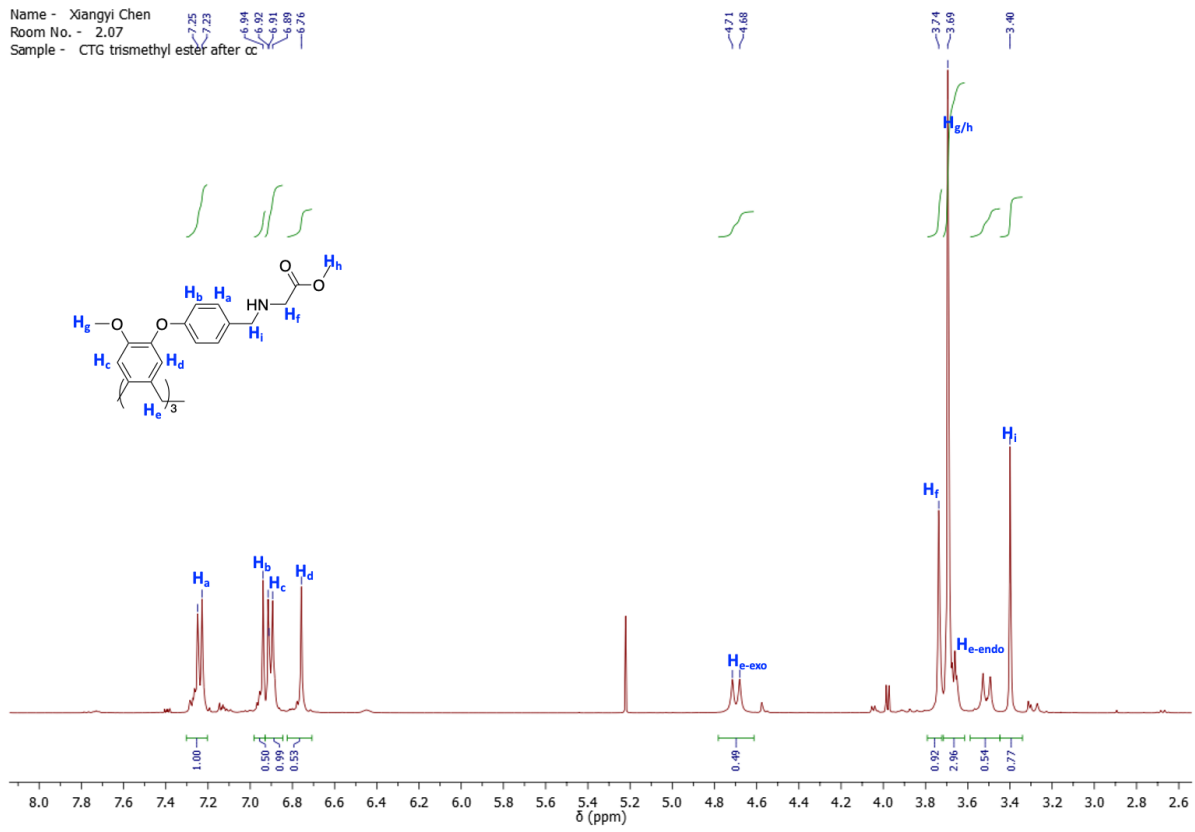

Figure 3.21 ^{1}H NMR (400 MHz, $CDCl_3$, δ, ppm) spectrum of compound **14.**

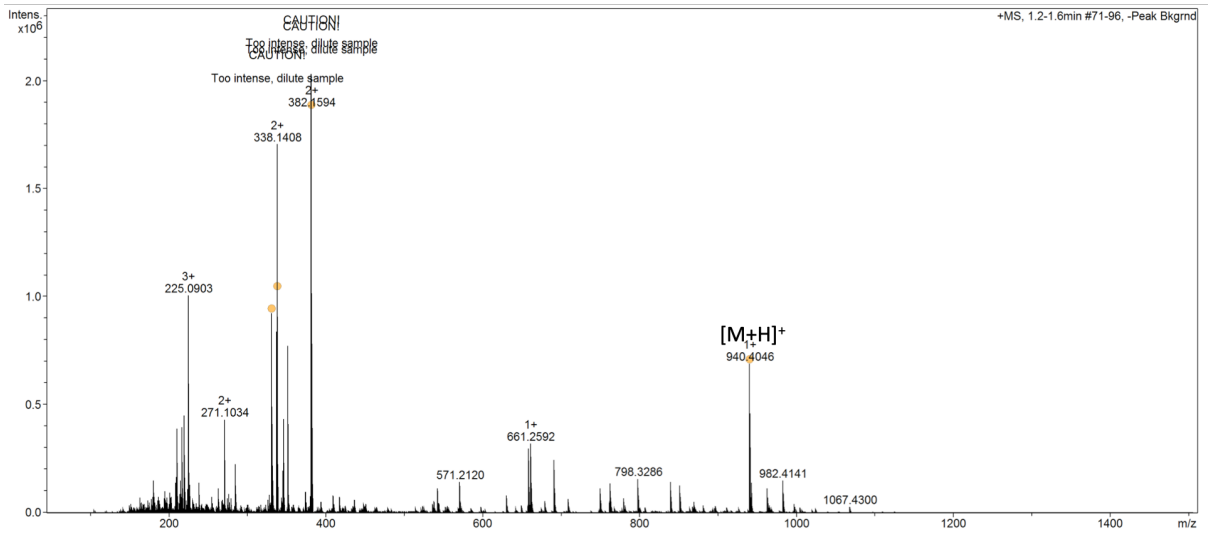

Figure 3.22 LC-MS spectra of the compound **14**.

3.3.3.5 Synthesis CTG tris-amino acid, 15

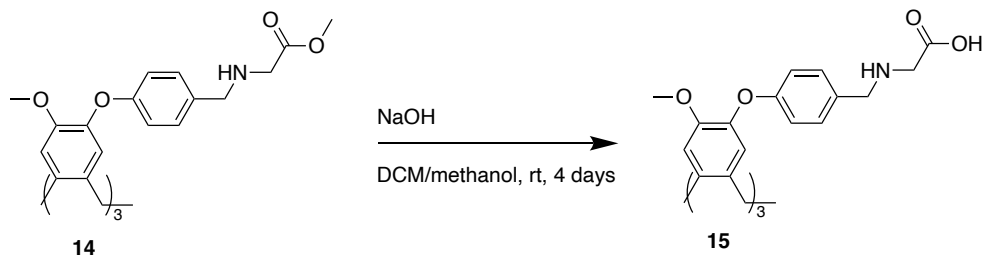

Scheme 3.16 Route to synthesise CTG tris-amino acid, **15**.

NaOH (6.5 equivalent) was dissolved in methanol, then added to the DCM solution of **14**, the resulting mixture was stirred at room temperature for 4 days. The reaction mixture changed from the solution to a white suspension. The solvent was removed, and added with water (2 mL), then adjusted the pH to 6.7 using HCl (1 M). The mixture was centrifuged three times (H_2O, 10000 rpm x 5 min), the precipitate was filtered and dried in the oven for 24 hours giving white solid as product, **15**. The product was analysed by NMR spectrometry using different solvent ($CDCl_3$ D4-methanol, D6-DMSO; see **Figure 3.23**), however, none of them can dissolve the solid properly and give a clear ^1H NMR spectrum. The formation of the product was proved by the LC-MS results (see **Figure 3.24**), in which an ion peak at m/z = 898 was observed and corresponded to the $[M+H]^+$ ion of **15**.

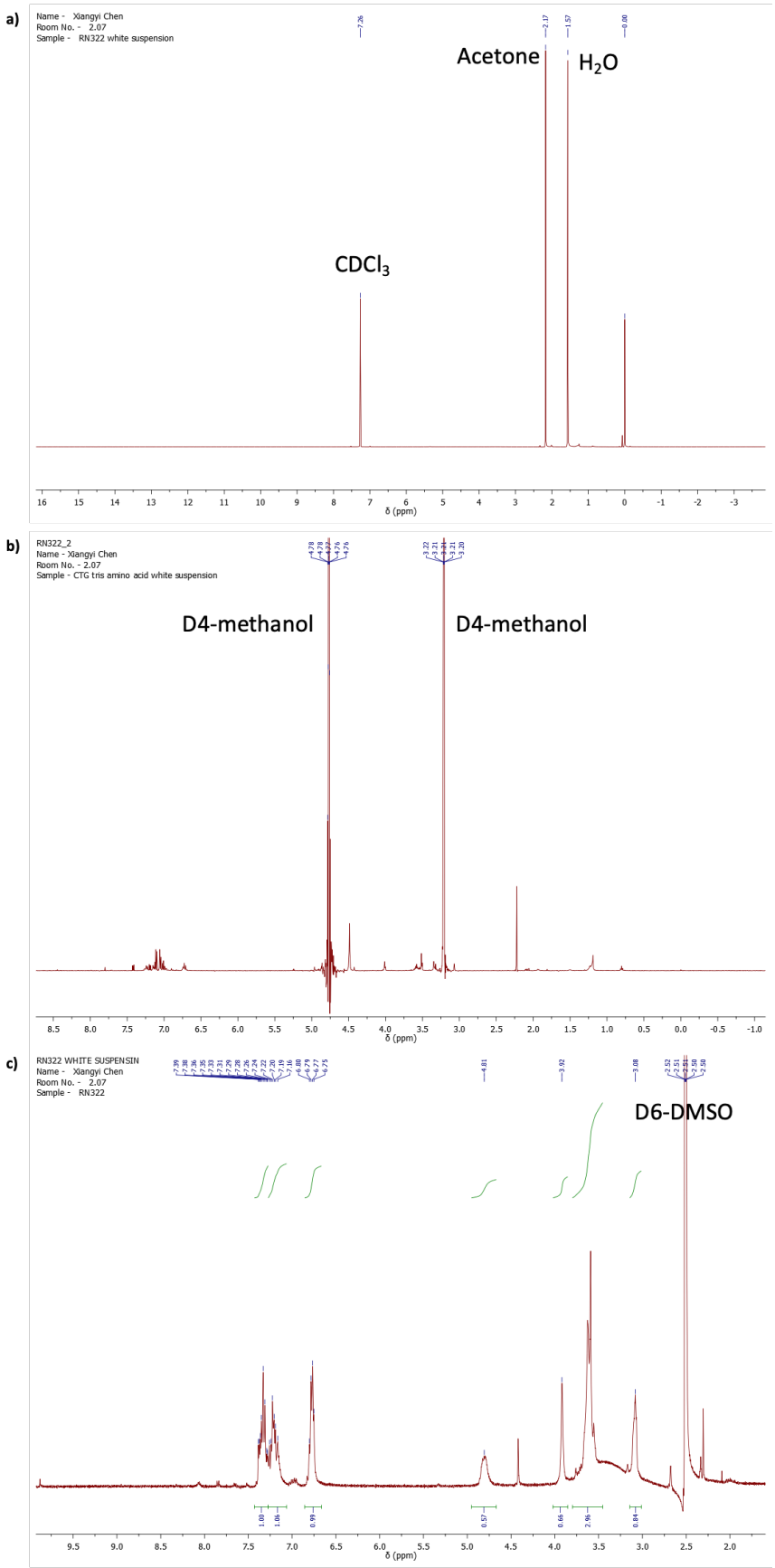

Figure 3.23 ^{1}H NMR spectrumof white solid in $CDCl_3$, D4-methanol, D6-DMSO.

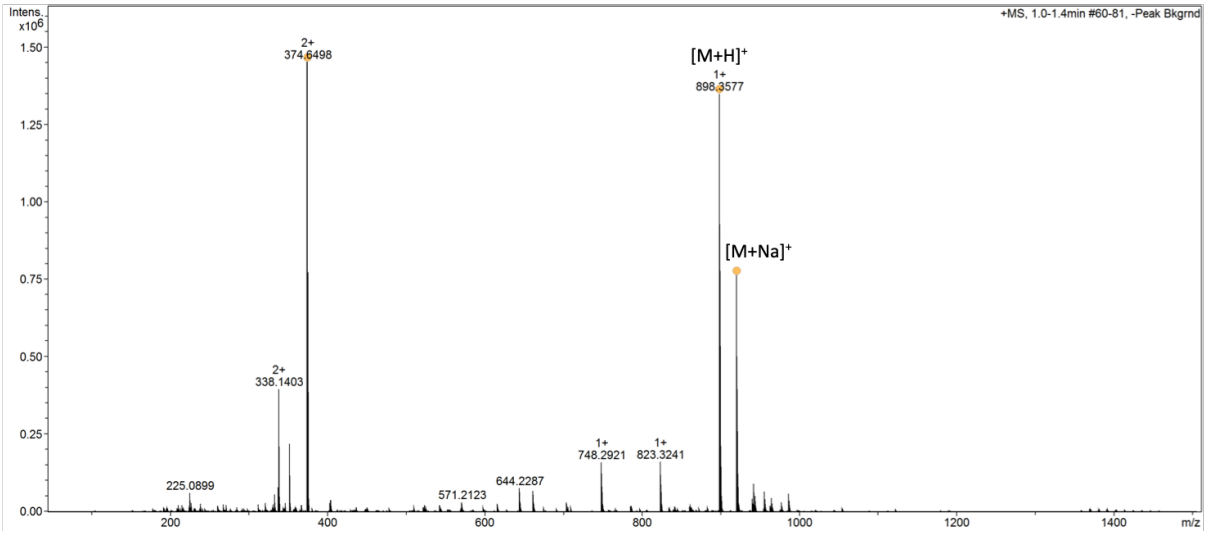

Figure 3.24 LC-MS results of compound **15**.

3.3.3.6 Synthesise tris-fullerene-CTG, 11

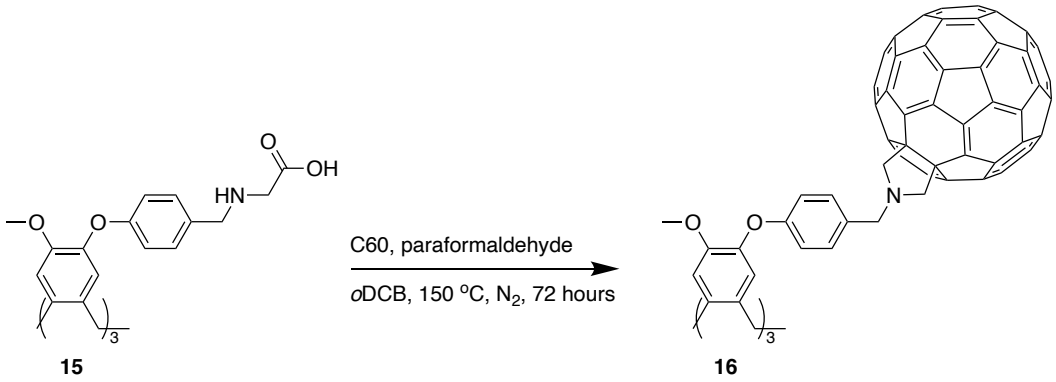

Scheme 3.17 Route to synthesise tris-fullerene-CTG, **16**.

The reaction to synthesise molecule, **16**, was performed, with 1 equivalent of CTG, 6 equivalent of C_{60} and 10 equivalent of paraformaldehyde (which was added every day due to the formaldehyde that formed from paraformaldehyde is a gas and escapes from the reaction mixture). The reaction mixture was analysed by TLC (see **Figure 3.25**) and MALDI ms (see **Figure 3.26**). With all the solvent system tried so far, no discrete spot was observed on the TLC plate. In the MALDI ms results, a peak with m/z = 2965.62 was observed, which was close to the $[M]^-$ ion peak of **16**. However,

the target molecule does not fly well in the current current acquisition conditions, i.e. matrix and the power. For future work, MALDI ms experiment optimisation is required to monitor the formation of the molecule **16**. Currently, the target molecule hasn't been isolated from the reaction mixture, which should also be performed in the future.

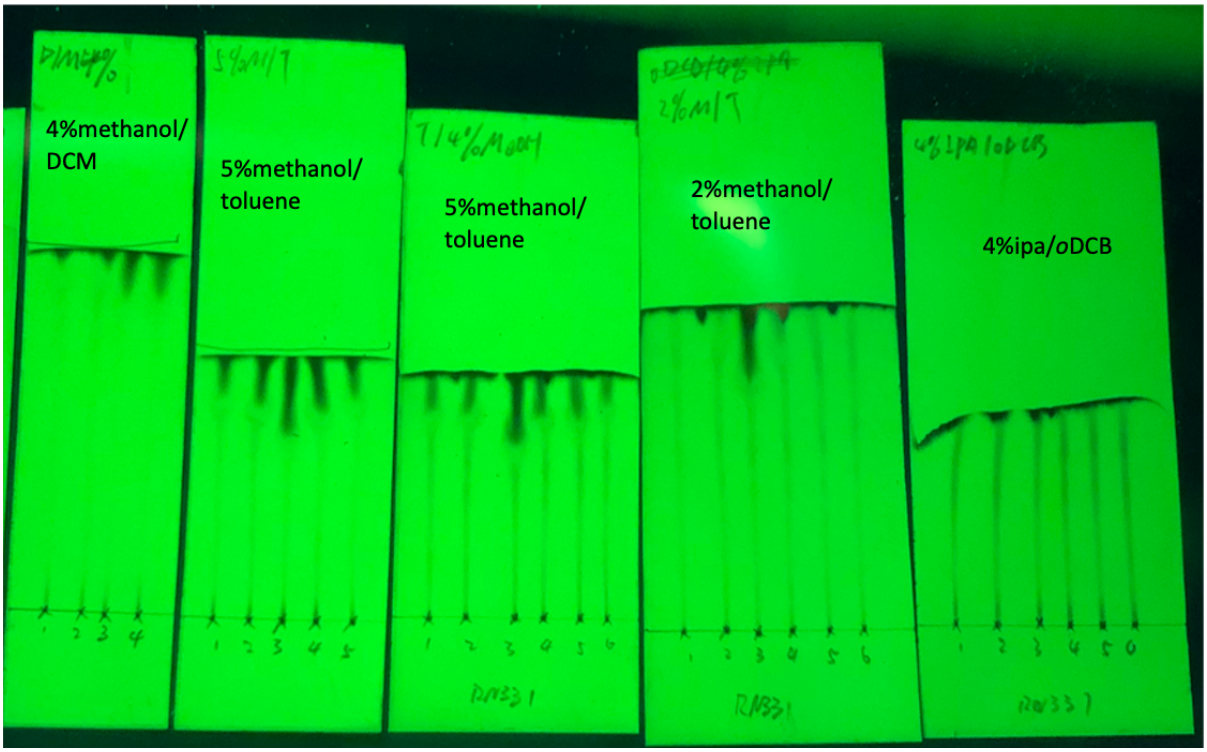

Figure 3.25 TLC results of the reaction mixture to synthesise compound **16** with different solvent system.

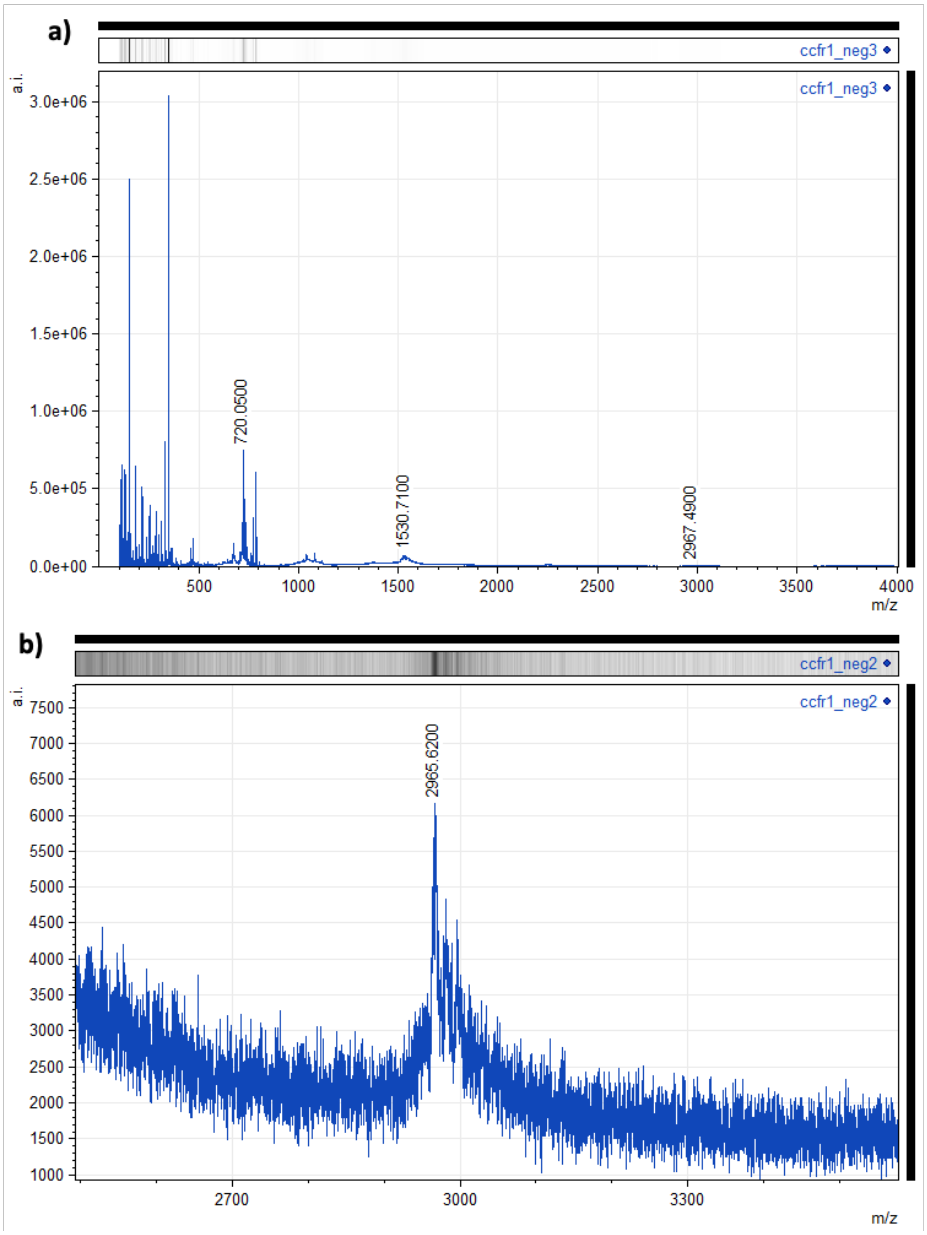

Figure 3.26 MALDI ms (MeCN/DCTB, negative mode) data of the reaction mixure to synthesis molecule **16**, a) whole spectrum and b) zoomed in spectrum.

3.4 Conclusion

In this study, a synthetic route to synthesise CTG tris-fullerene complex based on a one-pot Prato reaction has been proposed and proved to be viable. A trisfullerene CTG molecule, **12**, synthesised from the CTG tris-aldehyde was successfully formed, which could be used to develop the supramolecular arrays when *P* or *M* isomers is

available. The CTG tris-fullerene, **16**, that has no isomers, synthesised from the CTG-tris-aminoacid has yet to be isolated and characterised, but it shows potential to be successful. Future works that can facilitate the synthesise of CTG tris-fullerene is as follows;

1. Using the longer linkers between fullerene and CTG, e.g. a biphenyl linker, or a linker with substituents, which can increase the solubility of the one-, two-fullerene armed intermediate and thus increase the conversion.
2. It's worth exploring replacing the paraformaldehyde species with other ketone derivatives due to the fact that paraformaldehyde decomposes to formaldehyde gas rapidly, which reduces the possibility of the reaction. At the same time, the other ketone species, i.e. acetone, can introduce extra substituents on to the pyrrolidine, which is of benefit for increasing the solubility of the intermediates.

3.5 Experimental

C_{60} (99.5%) was purchased from SES Research Corporation. All other reagents and solvents were purchased from Aldrich and were used without further purification. Infrared spectra were measured using Bruker ALPHA FT-IR spectrometer over the range 400-4000 cm^{-1}. $^{1}H\{^{13}C\}$ and $^{13}C\{^{1}H\}$ NMR were obtained using Bruker AV(III) 400 or Bruker AV(III) 500 spectrometers. Mass spectrometry was carried out using a MALDI ToF spectrometer (Shimadzu AXIMA performance). UV-Vis spectra were measured using an Agilent Technologies Cary Series Spectrometer.

3.5.1 Preparation of the CTG

3.5.1.1 Synthesis of 3-Methoxy-4-propenyloxybenzylalcohol, 6

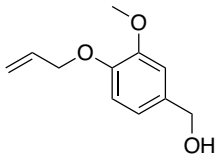

3-Methoxy-4-hydroxybenzyl alcohol (25.0 g, 158 mmol) was dissolved in acetone (125 ml). Potassium carbonate (21.8 g, 176 mmol) and allyl bromide (15.1 ml, 158 mmol) were added to the solution and heated at reflux overnight. The reaction mixture was dried under reduced pressure to remove the excess allyl bromide. The product was extracted with DCM (3 × 200 ml) and combined organics washed with water (2 × 200 ml). The organic layer was dried with MgSO4. After the filtration, the solution was dried under the reduced pressure to yield (24.07 g, 123.5 mmol, 78 %) as cream solid.

^{1}H NMR (300 MHz, $CDCl_3$, *δ*, ppm): 6.94 (s, 1H, Ar H); 6.86 (s, 2H, Ar H); 6.15-6.02 (m, 1H, CH); 5.40 (dd, 1H, CH_2, J=9.3 Hz); 5.29 (dd, 1H, CH_2, J=9.3 Hz); 4.62 (m, 4H, CH_2), 3.89 (s, 3H, OCH_3).

^{13}C{^{1}H} NMR (125.67 MHz, $CDCl_3$, *δ*, ppm): 149.37, 147.30, 133.88, 133.17, 119.11, 117.90, 113.13, 110.62, 69.79, 65.06, 55.1

3.5.1.2 Synthesis of (±)-2,7,12-trimethoxy-3,8,13-tris(propenyloxy)-10,15-dihydro-5H-tribenzo[a,d,g] cyclononatriene, 7

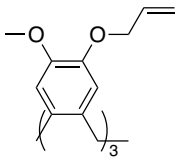

Compound **6** (24 g, 123.5 mmol) was heated in a round bottom flask is heated to the molten state (100 °C) with the heat gun. One spatula tip of Super phosphoric acid was added stirring overnight. After overnight reaction, a brown solid formed, which was triturated in 100 + 50 ml methanol, sonicated and then filtered to produce a fine white powder. The white powder was washed with methanol (50 ml) followed by diethyl ether

(50 ml) and then dried under water driven vacuum filtration to yield the product (6.05 g, 11.5 mmol, 9.3 %).

^{1}H NMR (300 MHz, $CDCl_3$, δ, ppm): 6.85 (s, 3H, Ar H), 6.79 (s, 3H, Ar H), 6.12-5.99 (m, 3H, CH), 5.37 (dd, 3H, CH_2, J= 9, 3 Hz), 5.24 (dd, 3H, CH_2, J= 9, 3 Hz), 4.74 (d, 3H, CH_2, J=12 Hz), 4.59 (m, 6H, CH_2), 3.84 (s, 9H, OCH_3), 3.52 (d, 3H, CH_2, J=12 Hz).

^{13}C NMR (125.67 MHz, $CDCl_3$, *δ*, ppm): 148.06, 146.60, 133.65, 132.22, 131.59, 117.47, 115.37, 113.38, 70.08, 55.16, 36.45.

3.5.1.3 Synthesis of (±)-2,7,12-trimethoxy-3,8,13-tris(hydroxy)-10,15-dihydro-5H-tribenzo[a,d,g] cyclononatriene, CTG

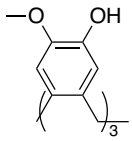

Compound **7** (3.00 g, 5.67 mmol) and triphenylphosphine (0.28g, 1.07 mmol) was dissolved in a mixture of dry THF (150 ml), water (30 ml) and diethylamine (27 ml) under an atmosphere of N_2. The solution was refluxed overnight and then filtered through celite. The solvent was removed under reduced pressure to give a brown residue which was triturated in methanol (10 ml) and then filtered to yield the product (1.505 g, 2.16 mmol, 65.45 %). As a grey /white powder.

^{1}H NMR (300 MHz, $CDCl_3$, δ, ppm): 8.59 (bs, 3H, OH), 6.85 (s, 3H, Ar H), 6.83 (s, 3H, Ar H), 4.59 (d, 3H, CH_2, J=12 Hz), 3.73 (s, 9H, OCH_3), 3.37 (d, 3H, CH_2, J=12 Hz).

^{13}C{^{1}H} NMR (125.67 MHz, $CDCl_3$, *δ*, ppm): 145.18, 144.07, 132.40, 131.18, 115.39, 112.19, 55.0, 36.27.

3.5.2 Preparation of fullerene bridge molecule

3.5.2.1 Synthesis of 4-(2,2-dimethyl fulleropyrrolidinyl carbonyl) benzoic acid, 8

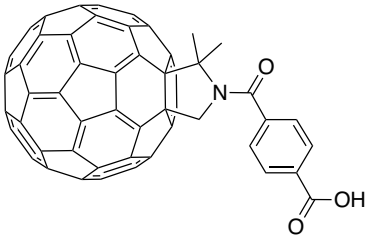

2,2-Dimethyl fulleropyrrolidine (50 mg, 0.065 mmol) was suspended in anhydrous DCM (50 ml), then DMAP (25 mg) and pyridine (0.75 ml) were added, and the reaction mixture was stirred for 10 min at room temperature. Then terephthaloyl chloride (150 mg, 0.75 mmol) was added and stirred for 18 h at room temperature. The solvent was removed under the reduced pressure, the residue was redissolved with CS_2 (CS_2) and passed through a silica gel pad (toluene/methanol 4:1), All fractions were collected and washed with water (20 ml), collected the organic layer, and extracted water layer with CS_2 (10 ml) three times. All the organic fractions were combined and purified by column chromatography (silica gel, ODCB/IPA 99.5:0.5 followed by 97:3). Further purification was carried out by washing with methanol (50 ml) and petroleum ether (50 ml) to yield the product (24 mg, 21%) as a brown solid.

^{1}H NMR (300 MHz, 297 K, CS_2/$CDCl_3$ 7:1 v/v, *δ*, ppm): 8.30 (d, 2H, Ar H), 7.97 (d, 2H, ArH), 5.35 (s, 2H, CH_2), 2.54 (s, 6H, CH_3).

^{13}C{^{1}H} NMR (500 MHz, 297 K, CS_2/$CDCl_3$ 7:1 v/v, *δ*, ppm): 170.39, 169.27, 154.10, 152.74, 147.53, 146.53, 146.65,146.26, 146.23, 146.14, 145.74, 145.64, 145.59, 145.48, 145.37,145.29, 144.62, 144.59, 143.32, 142.90, 142.85, 142.37, 142.35,142.18, 142.03, 142.00, 141.98, 141.90, 140.43, 139.97, 136.30, 136.16, 131.12, 130.99,128.44, 127.97, 79.70, 70.54, 67.94, 60.60, 26.70

MALDI-TOF MS (DCTB/CS_2, m/z): 938.9 $[M]^-$.

3.5.2.2 Synthesis of 4-(2,2-dimethyl fulleropyrrolidinyl carbonyl) benzoyl chloride, 9

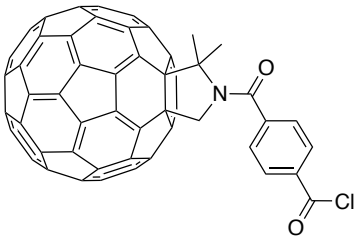

4-(2,2-Dimethyl fulleropyrrolidinyl carbonyl) benzoic acid (24 mg, 0.0254 mmol) was added to thionyl chloride (2 mL), degassed with N_2 and heated to 60 °C for 1 hour. The excess thionyl chloride was removed under reduced pressure, giving brown solid as product (25 mg, 100%). The product was used for without further purification.

3.5.3 (±)-2,7,12-trimethoxy-3,8,13-tris(isonicotinoyl)-10,15-dihydro-5H-tribenzo[a,d,g] cyclononatriene, CTG-py

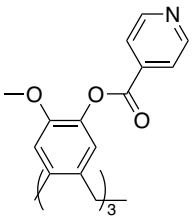

The isonicotinoyl chloride hydrochloride was first dissolved in THF (30 mL) or ODCB (30 mL), CTG (0.2 g, 0.49 mmol) was added to another round bottom flask and dissolved with THF (30 mL) or ODCB (30 mL). The flask with CTG was cooled to 0°C in an ice bath and triethylamine (1.06 mL) was added and stirred for 15 min. The mixture of the CTG and triethylamine was transferred to the flask with isonicotinoyl chloride hydrochloride. The white suspension was allowed to stir at 0 °C at the beginning then warmed up to room temperature (the reaction mixture was heated to 70 °C in ODCB directly) and stirred for three days. The solvent was removed on rotary evaporator to give a cream residue. This crude product was triturated in ethanol (100

mL), filtered and washed with ethanol (50 mL) and diethyl ether (20 mL) before drying in vacuum to yield the product (0.1805 g, 0.261 mmol, 54.4 %) as a white powder.

^{1}H NMR (400 MHz, D6-DMSO, *δ*, ppm): 8.87 (d, 6H, Ar H, J=8 Hz), 8.01 (d, Ar H, J=8 Hz), 7.19 (s, 3H, Ar H), 6.98 (s, 3H, Ar H), 4.87 (d, 3H, CH_2, J=16 Hz), 3.82 (s, 9H, OCH_3), 3.72 (d, 3H, CH_2, J=16 Hz).

^{13}C{^{1}H} NMR (400 MHz, D6-DMSO, *δ*, ppm): 163.31, 150.78, 149.74, 138.35 138.24, 136.68, 131.45, 123.82, 123.35, 114.20, 56.22, 36.51, 30.92.

ESI-MS (DMSO, m/z): 724.23 $[M+H]^+$.

3.5.4 Fullerene-CTG complex, 10

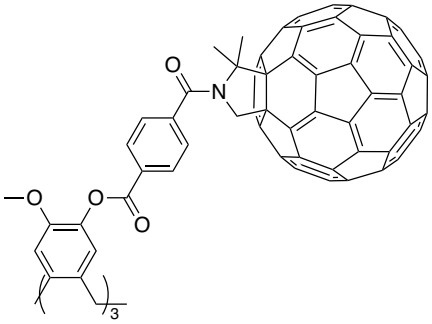

CTG (2 mg, 0.0049 mmol) and 4-(2,2-dimethyl fulleropyrrolidinyl carbonyl) benzoyl chloride were added to anhydrous *o*DCB (2 mL). Then trimethylamine was added to the reaction mixture, stirred at room temperature for 15 min, then the reaction mixture was heated to 70 °C and stirred for three weeks.

3.5.5 Preparation of CTG-trisaldehyde, 6, and fullerene-CTG complex, 12.

3.5.5.1 Synthesis of (±)-2,7,12-trimethoxy-3,8,13-tris(4-benzaldehyde ester)-10,15-dihydro-5H-tribenzo[a,d,g] cyclononatriene, 11

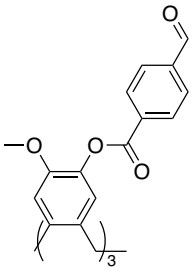

The suspension of CTG (250 mg, 0.61 mmol, 1 *equiv.*) in DCM (anhydrous, 100 mL) was added with 4-formylbenzoic acid (550 mg, 3.68 mmol, 6 *equiv.*), EDC.HCl (1400 mg, 7.32 mmol, 12 *equiv.*) and DMAP (450 mg, 3.68 mmol, 6 *equiv.*), the resulting mixture was sonicated and stirred under room temperature for 20 hours. After reaction, the mixture was washed with water (100 mL), organic layer was collected, the aq layer was washed with DCM (10 mL x 3), and organic layer was combined, concentrated and purified by column chromatography (SiO_2, 1%methanol/DCM) giving yellow solid as product (235 mg, 48%)

^{1}H NMR (400 MHz, $CDCl_3$, *δ*, ppm): 10.14 (s, 3H, CHO), 8.35 (d, 6H, Ar H, J=8 Hz), 8.01 (d, Ar H, J=8 Hz), 7.19 (s, 3H, Ar H), 6.97 (s, 3H, Ar H), 4.86 (d, 3H, CH_2, J=12 Hz), 3.81 (s, 9H, OCH_3), 3.71 (d, 3H, CH_2, J=12 Hz).

^{13}C{^{1}H} NMR (400 MHz, $CDCl_3$, *δ*, ppm): 191.65, 163.79, 149.80, 139.51, 138.40 138.33. 134.36, 131.54, 130.88, 129.61, 124.03, 114.23, 56.22, 53.55, 36.44.

3.5.5.2 Synthesis of fullerene-CTG complex, 12

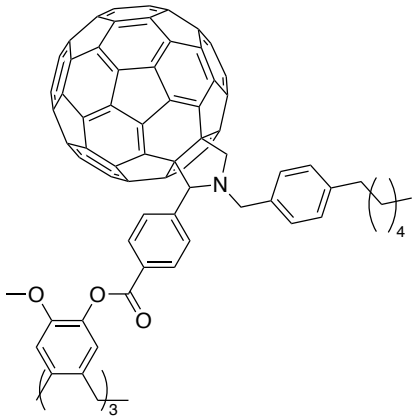

Molecule **11** (5 mg, 0.00622 mmol, 1 equiv.), C_{60} (20 mg, 0.0280 mmol, 4.5 *equiv.*) and hexylbenzylaminoacid (23.3 mg, 0.0933 mmol, 15 *equiv.*) were added to a degassed RFB, anhydrous oDCB (7.2 mL) were added, the resulting mixture was sonicated for 30 min, then heated to 100 °C for 2 hours.

MALDI ToF ms (DCTB/MeCN): 3527.38 $[M]^{-}$.

3.5.6 Synthesis of (±)-2,7,12-trimethoxy-3,8,13-tris(4-benzaldehyde ether)-10,15-dihydro-5H-tribenzo[a,d,g] cyclononatriene, 13

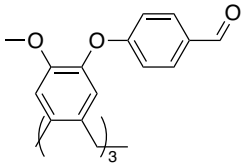

CTG (0.5 g, 1.23 mmol, 1 *equiv.*), 4-fluorobenzaldehyde (0.44 mL, 4.04 mmol, 3.3 *equiv.*) and K_2CO_3 (0.56 g, 4.04 mmol, 3.3 *equiv.*) were added with anhydrous DMF (10 mL). The mixture was heated to reflux condition for 24 hours. The DMF was removed using Schlenk line technique, followed by adding with 50 mL of brine. The resulting mixture was extracted with DCM (50 mL x 4). The organic layer was combined and dried with $MgSO_4$, DCM was removed, then added with 10 mL of chloroform. The suspension was filtered, giving white solid (0.64 mg, 0.89 mmol, 72%) as product.

^{1}H NMR (400 MHz, $CDCl_3$, *δ*, ppm): 9.90 (s, 1H, CHO), 7.80 (d, 2H, Ar H, *J*=8 Hz), 7.11 (s, 1H, Ar H), 6.98 (d, 2H, Ar H, *J*=8 Hz), 4.84 (d, 1H, CH_2, *J*=12 Hz), 3,69 (s, 3H, OCH_3), 3.66 (d, 1H, CH_2, *J*=12 Hz).

^{13}C{^{1}H} NMR (400 MHz, $CDCl_3$, *δ*, ppm): 190.72 (CHO), 163.45, 150.43, 141.74, 137.44, 132.08, 131.84, 131.04, 123.64, 116.34, 114.53 (Ar C), 56.13, 36.47

LC-MS (m/z): 721.24 $[M+H]^+$, 743.23 $[M+Na]^+$.

IR (*v*, cm^{-1}): 2832, 2746, 1680.

3.5.7 Synthesis of (±)-2,7,12-trimethoxy-3,8,13-tris(4-benzyl-(N-glycine methyl ester) ether)-10,15-dihydro-5H-tribenzo[a,d,g] cyclononatriene, 14

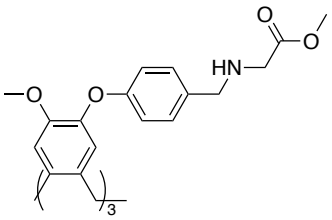

Compound **13** (300 mg, 0.42 mmol, 1 *equiv*.), glycine methyl ester hydrochloride (203 mg, 1.62 mmol, 3.87 *equiv*.) and 4 Å molecular sieves were added in anhydrous DCM (10 mL), followed by adding with triethylamine (0.23 mL, 1.62 mmol, 3.87 *equiv*.), the mixture was stirred for 24 hours. The reaction mixture was filtered, the filtrate was added with $NaBH(OAc)_3$ (343 mg, 1.62 mmol, 3.87 *equiv*.) and AcOH (1.1 mL), the resulting mixture was concentrated to 5.5 mL, then stirred at room temperature, under N_2 for 24 hours. The solvent was removed, 1 mL of methanol was added, the resulting mixture was cooled down to 0°C, then, $NaHCO_3$ (1 M) was used to adjust pH to 7. The resulting mixture was extracted with DCM (50 mL x 3), the organic layer was combined, dried with $MgSO_4$. Further purification was carried out by column chromatography (4% methanol/DCM), giving product (166 mg, 42%) as white solid.

^{1}H NMR (500 MHz, $CDCl_3$, *δ*, ppm): 7.24 (d, 2H, Ar H, *J*=10 Hz), 6.93 (s, 1H, Ar H), 6.91 (d, 2H, Ar H, *J*=10 Hz), 6.75 (s, 1H, Ar H), 4,72 (d, 1H, CH_2, *J*=15 Hz), 3.73 (s,

2H, CH_2), 3.71 (s, 3H, $COOCH_3$), 3.70 (s, 3H, OCH_3), 3.52 (d, 1H, CH_2, *J*=15 Hz), 3.41 (s, 2H, CH_2).

$^{13}C\{^1H\}$ NMR (500 MHz, $CDCl_3$, *δ*, ppm): 172.81 (C=O), 156.90, 149.73, 143.86, 135.62, 133.67, 131.85, 129.47, 121.52, 117.54, 114.09 (Ar H), 56.01, 52.63, 51.78, 49.79, 36.24.

LC-MS (m/z): 940 $[M+H]^+$

3.5.8 Synthesis of (±)-2,7,12-trimethoxy-3,8,13-tris(4-benzyl-(N-glycine) ether)-10,15-dihydro-5H-tribenzo[a,d,g] cyclononatriene, 15

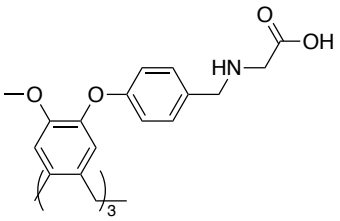

Compound **14** (140 mg, 0.15 mmol, 1 *equiv*.) was dissolved in DCM (1.7 mL), then 1 mL methanol with NaOH (42 mg, 1.05 mmol, 7 *equiv*.) dissolved was added. The resulting mixture was stirred under room temperature for 4 days. The solvent was removed, the residue was added with water (2 mL), HCl (1 M) was used to adjust the pH to 6.4, the mixture was sonicated occasionally. Further purification was carried out by centrifuge (H_2O, 11000 rpm x 5 min x 3), the residue was washed with water, giving product (67 mg, 35%) as white solid.

LC-MS (m/z): 896.34 $[M-H]^-$; 898.36 $[M+H]^+$.

IR (*v*, cm^{-1}): 1602 ($v_{C=O}$), 1217 (v_{c-o}).

3.5.9 Synthesis of fullerene-CTG complex, 16

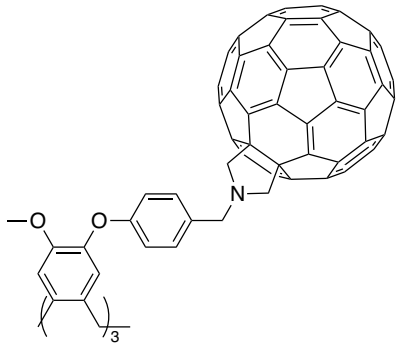

Compound **15** (5 mg, 0.0056 mmol, 1 *equiv.*), C_{60} (24 mg, 0.0336 mmol, 6 *equiv.*) and paraformaldehyde (5 mg, 0.168 mmol, 30 *equiv.*) were added to anhydrous *o*DCB, the resulting mixture was sonicated for 15 min, and thorogphy degassed with N_2. Then, the reaction mixture was heated to reflux for 7days. A portion of paraformaldehyde (5 mg, 0.168 mmol, 30 *equiv.*) was added every 24 hours.

3.6 References

1. Fuertes-Espinosa, C. *et al.* Supramolecular Fullerene Sponges as Catalytic Masks for Regioselective Functionalization of C60. *Chem* **6**, 169–186 (2020).
2. Hahn, U., Cardinali, F., Chemistry, J. N.-N. J. of & 2007, undefined. Supramolecular chemistry for the self-assembly of fullerene-rich dendrimers. *pubs.rsc.org*.
3. Boyd, P. D. W. *et al.* Selective supramolecular porphyrin/fullerene interactions. *Journal of the American Chemical Society* **121**, 10487–10495 (1999).
4. Lu, D. *et al.* The Supramolecular Chemistry of Cycloparaphenylenes and Their Analogs. *Frontiers in Chemistry* **7**, (2019).
5. Martin, N. & Nierengarten, J. *Supramolecular chemistry of fullerenes and carbon nanotubes*. (2012).
6. Zhao, Y. & Chen, G. C60 fullerene amphiphiles as supramolecular building blocks for organized and well-defined nanoscale objects. *Structure and Bonding* **159**, 23–53 (2014).
7. Lebedeva, M. A. *et al.* Stabilising the lowest energy charge-separated state in a {metal chromophore-fullerene} assembly: A tuneable panchromatic absorbing donor-acceptor triad. *Chemical Science* **7**, 5908–5921 (2016).
8. Richards, V. Molecular machines. *Nature Chemistry 2016 8:12* **8**, 1090–1090 (2016).
9. Hirao, T., Iwabe, Y., Fujii, N. & Haino, T. Helically Organized Fullerene Array in a Supramolecular Polymer Main Chain. *J. Am. Chem. Soc* **143**, 4339–4345 (2021).
10. Caballero, R. *et al.* Self-Assembly-Directed Organization of a Fullerene−Bisporphyrin into Supramolecular Giant Donut Structures for Excited-State Charge Stabilization. *J. Am. Chem. Soc* **143**, 57 (2021).

11. Henkelis, J. J., Fisher, J., Warriner, S. L. & Hardie, M. J. Solvent-Dependent Self-Assembly Behaviour and Speciation Control of Pd6L8 Metallo-supramolecular Cages. *Chemistry – A European Journal* **20**, 4117–4125 (2014).

12. Huerta, E., Cequier, E. & Mendoza, J. de. Preferential separation of fullerene[84] from fullerene mixtures by encapsulation. *Chemical Communications* 5016–5018 (2007) doi:10.1039/B711993C.

13. Lebedeva, M. A., Chamberlain, T. W., Schröder, M. & Khlobystov, A. N. An efficient route to the synthesis of symmetric and asymmetric diastereomerically pure fullerene triads. *Tetrahedron* **68**, 4976–4985 (2012).

14. ESTERIFICATION OF CARBOXYLIC ACIDS WITH DICYCLOHEXYLCARBODIIMIDE/4-DIMETHYLAMINOPYRIDINE: tert-BUTYL ETHYL FUMARATE. *Organic Syntheses* **63**, 183 (1985).

Chapter 4 Fullerene-platinum Complex as Lithographic Resists for Developing Nanoscale Patterning

4.1 Introduction

Nanoscale patterning is considered as a fundamental step in various of advanced solid-state devices for example integrated electronics, chemical and biological sensors, nanoelectromechanical systems (NEMS), on-chip energy storage units and etc.[1–4]. The recent developments in lithography techniques have induced the prosperity of device fabrication and resulted in diverse demands for patterning materials, i.e. the resists. The integrated circuit (IC) manufacturing as the most important application of nanoscale patterning requires the stringent targets of resolution and sensitivity for pushing the miniaturisation forward without losing throughput. In other non-electronics applications, the resist pattern can act as an active component that can achieve functionality enhancement, which is commonly pursued as it reduces the process complexity.[5,6]

In the photolithography of IC manufacturing, the sensitivity of the resists is a key factor that directly impacts the throughput. Traditional photoresists adopt a chemical amplification strategy, in which the reactions is initiated by each absorbed photon that matches the critical sensitivity requirements.[7,8] With the continuous shrinkage of feature size, novel high-resolution extreme ultraviolet (EUV), electron beam (e-beam) and charged particle lithography utilise photons, electrons or ions with energies significantly above the ionisation threshold and the exposure is thus driven by secondary electrons rather than photochemistry.[7,9] In this case, the energy deposition efficiency is considerably decreased and the exposure sites are more widely scattered. In addition, the resist film thinning for nanoscale patterns (to avoid pattern collapse)

makes the situation worse due to the further reduced energy absorption in a thinner film. This combined with the random distribution of resist molecules and additional photo-acid diffusion, induces both sensitivity and shot noise problems for the traditional polymeric chemically amplified resists.[8,10,11] One promising solution is utilisation of small molecular materials with high-absorption elements incorporated (typically metals), which may simultaneously enhance the energy deposition efficiency, i.e. the sensitivity, and the ultimate patterning resolution.[12] In addition, metal incorporation may also enhance the plasma etch resistance, which is highly desirable for the pattern transfer in a thinned film. [13] Inspired by this, several metal-based resists such as metal halides,[14] oxides,[15] naphthenates, [16] and metal oxoclusters[17] have been reported, showing promising progress in sensitivity and resolution enhancement. However, integration of these highly inorganic resists into the semiconductor manufacturing process is challenging due to compatibility considerations. [18,19]Alternatively, complexing of metal ions into organic resist systems might be the optimised strategy, but has been rarely reported. [20]

In our previous work, several fullerene derivatives were integrated (as a molecular component) into CA resist systems and led to an enhanced performance in e-beam and EUV lithography.[21,22]Some fullerene derivatives also exhibited negative-tone-resist behaviour on their own in e-beam lithography, demonstrating flexible exposure mechanisms and good compatibility as a candidate of novel molecular resists.[23,24] Inspired by this, a fullerene-platinum complex that was reported previously by Chamberlain group is proposed as a resists material for developing the high-resolution lithography.

4.2 Aims and objectives

The aim of this study is to synthesise and characterise the fullerene-bipyridine ligand and the fullerene-bipyridine-Pt complex, which are used as patternable resists material for high-resolution charged particle lithography (i.e. e-beam and helium ion beam lithography). This will be achieved via completion of the following objectives:

1. Using the reported procedure to synthesise and characterise the C_{60}-bipy ligand and C_{60}-bipy-Pt complex.[25]
2. Evaluating the response of C_{60}-bipy ligand and C_{60}-bipy-Pt complex to electron beam (e-beam) exposure.
3. Using C_{60}-bipy ligand and C_{60}-bipy-Pt complex to develop the fine pattern

Importantly, this is a collaborated study with researchers in China. My contribution to this study is the synthesis of C_{60}-bipy ligand and C_{60}-bipy-Pt complex, objective 1. The following lithographic performance tests were carried out by our collaborator, Dongxu Yang in University of Electronic Science and Technology of China.

4.2.1 Synthetic strategy

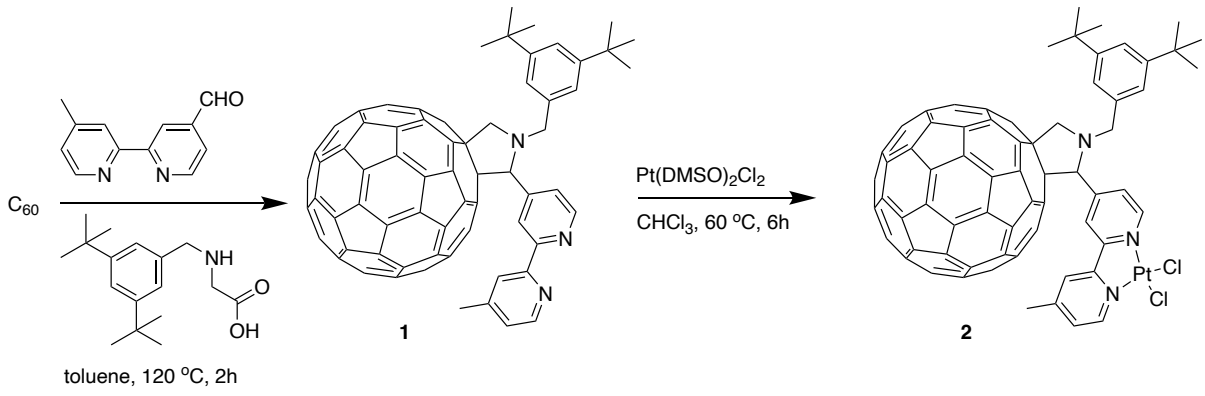

Scheme 4.1 Route to synthesise compound **1** (C_{60}-bipy) and **2** (C_{60}-bipy-Pt).

The fullerene ligand, **1**, was synthesised from a Prato reaction that uses the 4'-methyl-2,2'-bipyridine-4-carboxaldehyde and N-((3,5-di-tert-Butylphenyl)methyl)glycine as

starting material to react with C_{60}. Bipyridine is a well-known bidentate chelating ligand that serves to allow facile complexation of the C_{60}-bipy with a number of transition metals, i.e. Pt. The target platinum complex was formed from the reaction between C_{60}-bipy ligand and $Pt(DMSO)_2Cl_2$. The detailed experimental and characterisation can be found in Experimental section.

4.3 Results and discussion

4.3.1 The preparation of compound 1 (C_{60}-bipy) and 2 (C_{60}-bipy-Pt)

4.3.1.1 The synthesis of compound 1

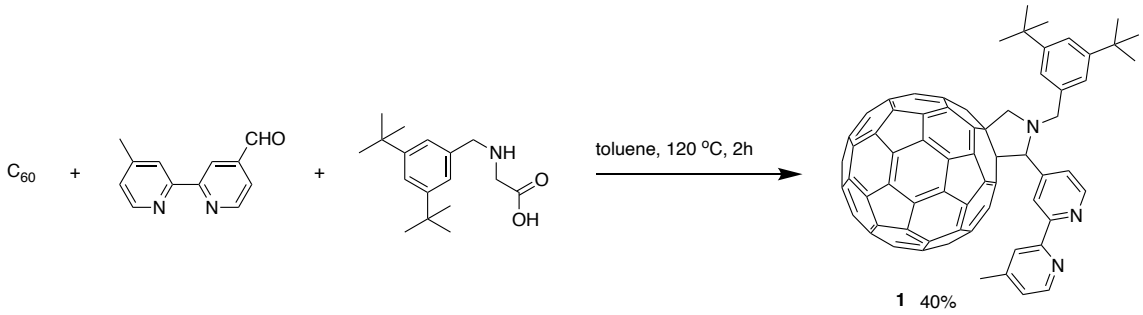

Scheme 4.2 Route to synthesis compound **1**.

The reaction to synthesie compound **1** was performed was sussessfully performed by following the reported procedures. The reaction mixture was purified by column chromatography (SiO_2, toluene->toluene/ethyl acetate 99/1), giving black solid as product on 43% yield. The formation of the compound **1** was indicated by NMR spectroscopy. In the ^1H NMR spectrum (see **Figure 4.1**), six bipyridine proton peaks were observed at the chemical shift of 8.90, 7.77, 8.56, 8.27, 7.96 and 7.14 ppm, whilst the pyrrolidine proton peaks were also observed at 53.3 49.8 42.5 ppm. The other characterisation data can be found in the Experimental section.

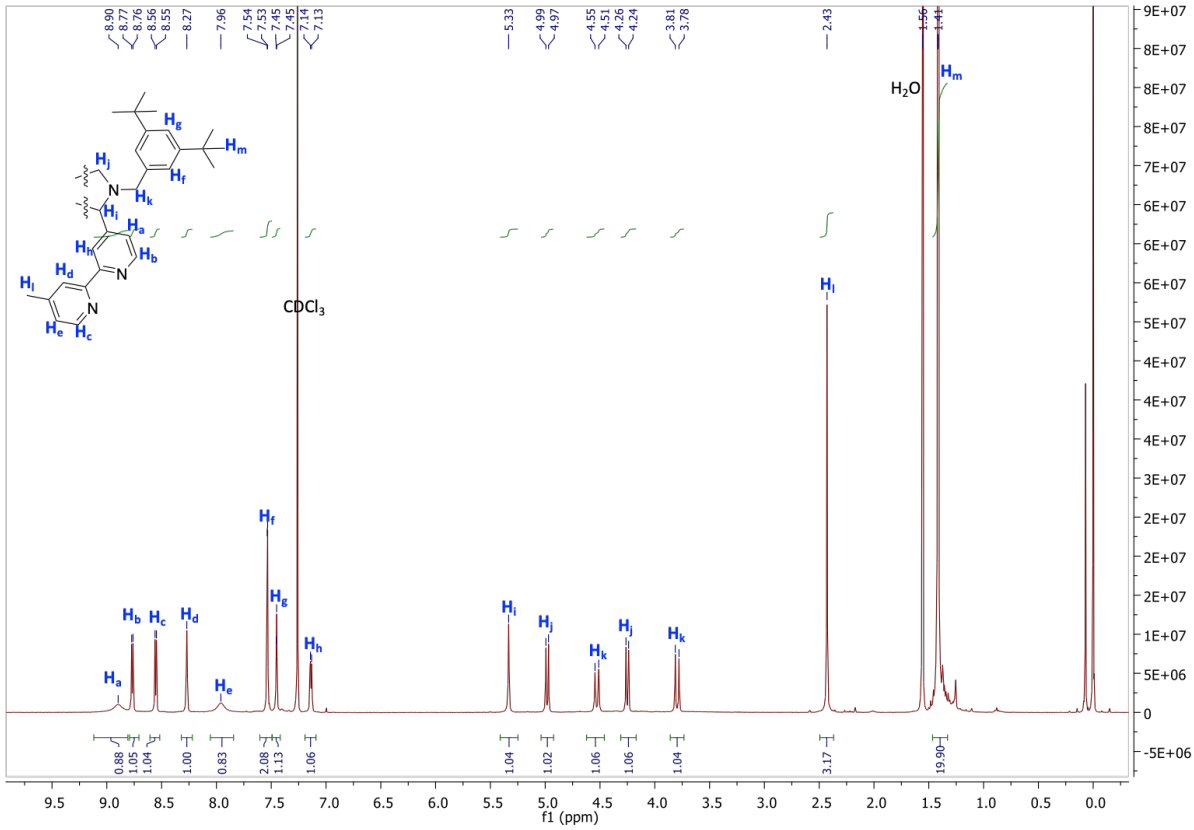

Figure 4.1 ^{1}H NMR spectrum (500 MHz, $CDCl_3$, δ, ppm) of compound **1**.

4.3.1.2 The synthesis of compound 2

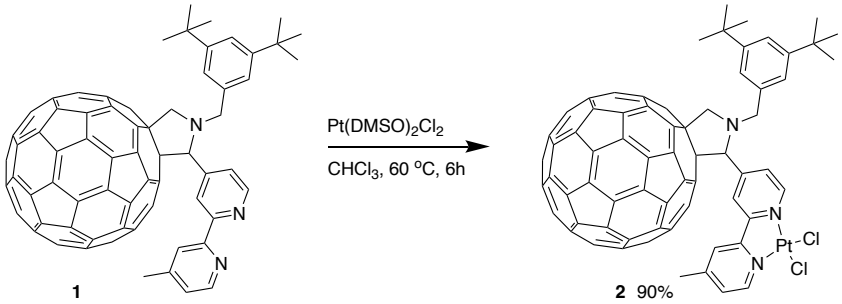

Scheme 4.3 Route to synthesise compound, **2**.

The reaction to synthesise compound **2** was successfully performed (detailed procedures can be found in the experimental section). The reaction mixture was concentrated under reduced pressure, followed by passing through a column chromatography (SiO_2, CH_2Cl_2 -> CH_2Cl_2/MeOH 99.5/0.5) giving black solid (yield:

90%) as product. NMR spectroscopy was used to characterise compound **2**. In the ^{1}H NMR spectrum (see **Figure 4.2**), due to the coordination of the platinum a deshelling effect was observed on the two aromatic protons next to N atoms, δ = 9.85 and 9.58 ppm, which were 8.77 and 8.56 ppm in the ^{1}H NMR spectrum of compound **1**. In MALDI ToF ms data, a peak with m/z = 1398.1 was found corresponding to the $[M]^{-}$ peak of compound **2**.

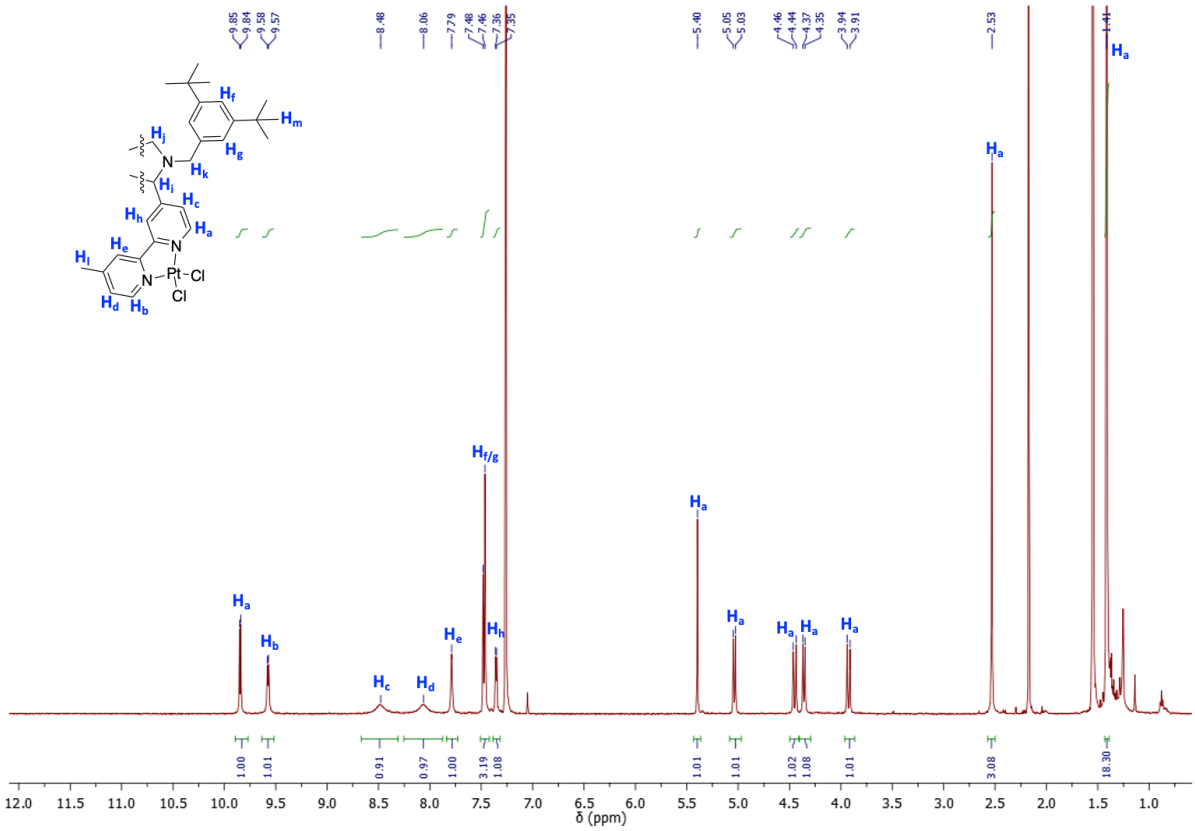

Figure 4.2 ^{1}H NMR spectrum (500 MHz, $CDCl_3$, δ, ppm) of compound **2**.

4.3.2 Response of fullerene resists materials to electron beam

To study the response of compound **1** and **2** to e-beam, the chloroform solution of the materials was spun-coated onto a piece of silicon chip (detailed methods can be found in Experimental section). The power of 20 kV was selected to test the sensitivity of materials using a dose matrix of 30 x 30 μm square array. Without post-exposure bake,

the patterns were developed in either monochlorobenzene (MCB) or cyclohexanone (CYH). As seen in **Figure 4.3a**, the residual thickness of the patter was plotted against does. The sensitivity and contrast of the materials were attained from fitting a sigmoidal function to the response curves (detailed methods can be found in Experimental section). In comparison of compound **1** and **2**, it is observed that the introduction of the platinum metal centre is beneficial for improving the sensitivity to e-beam from 10.1 (8.9) mC cm^{-2} to 2.7 (4.3) mC cm^{-2} in MCB (CYH), which is explained by that the presence of the Pt atoms can enhance the secondary electron scattering and thus increased energy deposition efficiency. Whilst slow in comparison to chemically amplified resists,[21] the near order of magnitude improvement seen for the C_{60}-Bipy-Pt sensitivity, over the control C_{60}-Bipy, gives a speed comparable to the common high-resolution e-beam resist hydrogen silsesquioxane (HSQ).[26,27] This result demonstrates the feasibility of organic-metal complex to improve the resist sensitivity. Interestingly, a higher contrast was observed in CYH development (2.3) than in MCB (1.4), which is explained by that the CYH is better in mop off the residues with low exposure dosage.

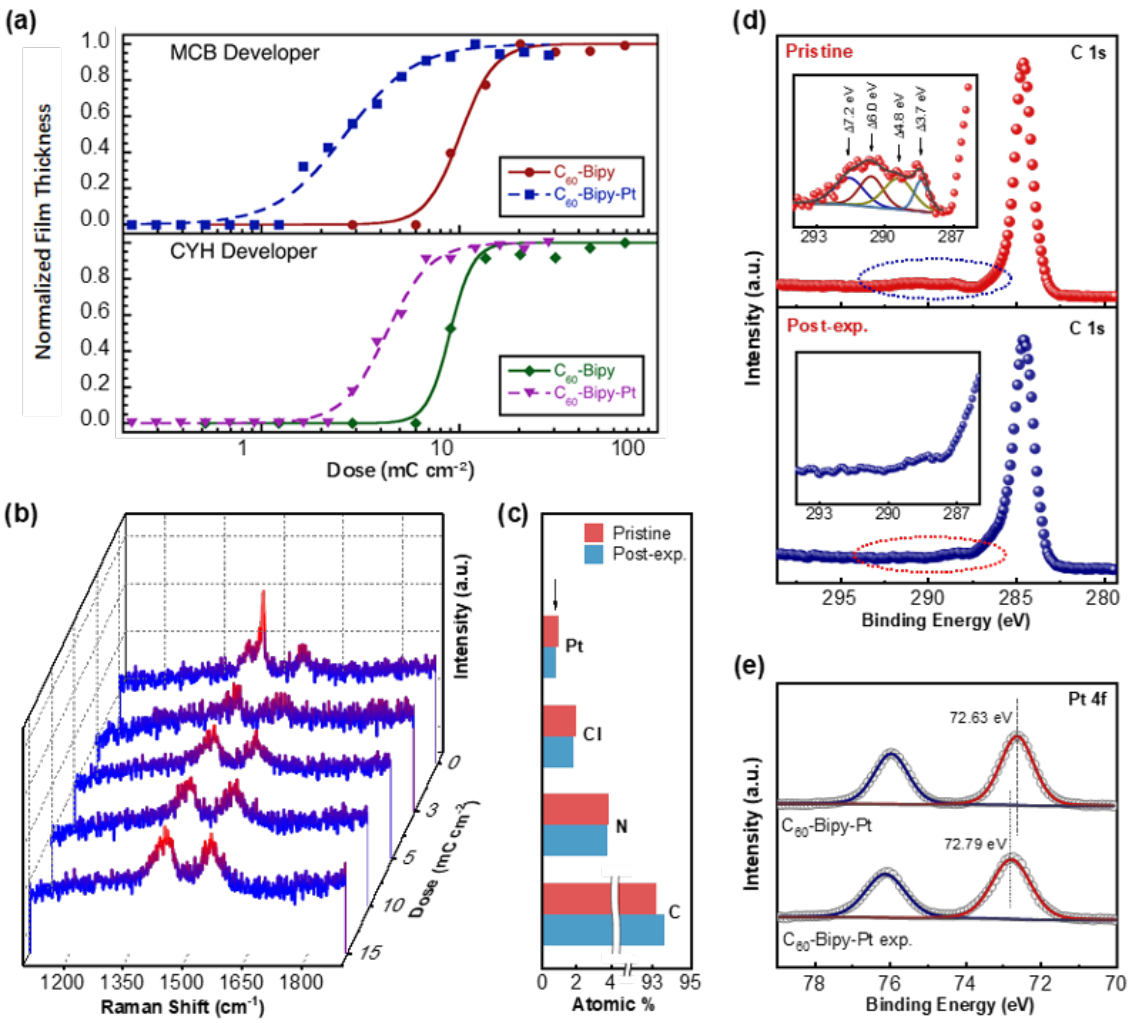

Figure 4.3 (a) Response curves of C_{60}-Bipy and C_{60}-Bipy-Pt films exposed to electrons at 20 kV and developed in monochlorobenzene and cyclohexanone; (b) *Ex-situ* Raman spectra of the as-prepared film and lithographically processed (various-dose exposure and development) films of C_{60}-Bipy-Pt; XPS spectra of C_{60}-Bipy-Pt before and after electron beam exposure (7 mC cm^{-2}) in (d) C 1s and (e) Pt 4f regions, with (c) the correspondingly calculated element ratios (the position of the arrow mark represents the theoretical value of Pt concentration in the targeted molecule).

Raman spectroscopy and X-ray photoelectron spectroscopy (XPS) were used to investigate the mechanism of the lithographic behaviour. *Ex-situ* Raman analysis was

performed on a set of the above-mentioned square patterns with different dosages. In the Raman spectrum of pristine compound **2** (see **Figure 4.3a**), a distinct moiety of the C_{60} with a sharp peak at 1464 cm^{-1} is observed corresponding to the double-bond stretching pentagonal pinch mode, which drops significantly upon e-beam exposure at 3 mC cm^{-2} and vanishes completely at higher exposure doses with only the D and G bands of the resultant carbon structures left. The Raman spectra indicate a fragmentation of the fullerene cage upon e-beam, followed by the formation of the crosslinked network of graphite-like structure, giving the lithographic behaviour. Notably, the increased peak intensity at higher exposure dosage is probably caused by the thicker residual film of the micro-meter patterns. XPS was used to compare the film of **2** before and after exposure (see **Figure 4.4**). The change of the carbon structure is revealed in the C 1s region of the XPS spectrum. As seen in **Figure 4.3d**, the pristine C_{60}-Bipy-Pt film shows a range of π-type shake-up satellites at the high binding energy side of the carbon main line, which matches well with the reported fullerene feature.[28] Whereas, no these characteristic peaks are observed in the exposed film, which indicates the decomposition of fullerene cage. As seen in **Figure 4.3e**, the Pt 4f spectra of before and after exposure film were also compared, in which the $4f_{7/2}$ of C_{60}-Bipy-Pt of **2** is located at 72.63 eV and close to the chemical state of Pt(II). The calculated weight ratio of Pt from the peak intensity is 13.0 wt%, agreeing with the theoretical value 13.9 wt% (see **Figure 4.3c**). The binding energy of the Pt showed a 0.16 eV positive shift after exposure. From the XPS data, no evidence of the formation of Pt(0) was found. The binding energy shift of N 1s and Cl 2p were also revealed, which is probably due to the decomposition of the fullerene cage. The results indicated that the coordination environment of Pt centre should be unaffected. So, the mechanism of the negative-tone lithographic behaviour of **2** is the e-beam induced

fullerene cage fragmentation and the subsequent formation of insoluble graphitised film, in which the bipyridine-Pt moiety tends to remain after exposure and development process.

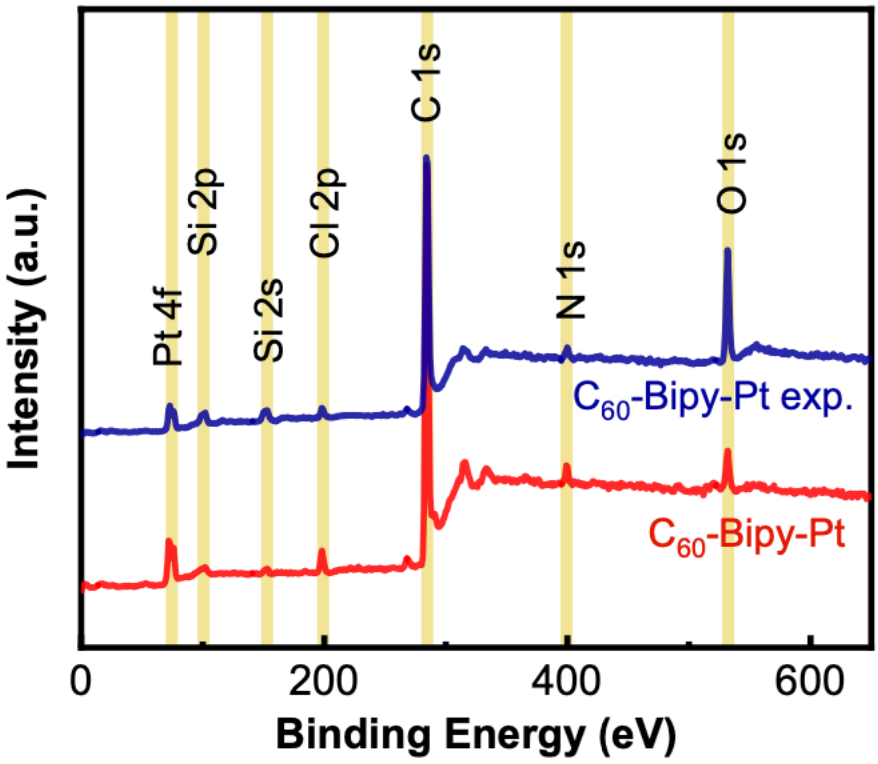

Figure 4.4 XPS survey spectra of compound 2 on silicon chip before and after e-beam exposure (7 mC cm^{-2}).

4.3.3 Fine patterning by electron and helium ion beam

As seen in **Figure 4.5**, Compound **1** and **2** was subsequently used for a resolution test, in which a series of line patterns with various pitch sizes (the period of a line and space pattern) were exposed using a 30 kV electron beam. The unexposed material is removed using the appropriate developer, leaving the exposed pattern on the substrate. Using MCB developer, both **1** and **2** are capable to achieve ~40 nm pitch dense and ~15.4 nm isolated lines (see **Figure 4.6**). Using CYH as developer, a high contrast was expected and observed. Line-and-space patterns with pitch size from 50

nm down to 28 nm are achieved in both C_{60}-Bipy (40 nm pitch at a line dose of 71 nC cm^{-1} – **Figure 4.7b**; 30 nm pitch, line dose: 52 nC cm^{-1} – **Figure 4.7c**) and in C_{60}-Bipy-Pt (40 nm pitch at a line dose of 47 nC cm^{-1} – Figure 3e; 30 nm pitch, line dose: 42 nC cm^{-1} – **Figure 4.7f**). Both material are able to form clearly resolved fine lines down to 30 nm pitch and tart showing a slight bridging at pitch 28 nm. Line edge roughness (LER) at 30 nm pitch is 2.78 nm for C_{60}-Bipy and 2.83 nm for C_{60}-Bipy-Pt. Further images and measurements for other pitch sizes are shown in Appendix and **Table 4.1**, respectively. Interestingly, C_{60}-Bipy shows a limited resolution of >14 nm, while C_{60}-Bipy-Pt is capably of sub-13 nm resolution. The improved ultimate resolution after Pt incorporation can be attributed to the shot noise reduction resulted from the enhanced energy deposition.[12] Consistent results were also observed in isolated line patterns, as shown in **Figure 4.7d** and **g**. The narrowest linewidths achieved are ~12 nm (line dose: 63 nC cm^{-1}) and ~10 nm (line dose: 42 nC cm^{-1}) for the C_{60}-Bipy and C_{60}-Bipy-Pt, respectively. Due to the significantly improved pattern quality by CYH development compared to the MCB development, the former was used in subsequent lithography-related tests unless otherwise noted. The resolution capability of this resist family is among the best compared with other advanced e-beam resists under similar exposure conditions.[10,12,13] The profile of C_{60}-Bipy-Pt pattern was also observed through cross-sectional SEM imaging. As shown in **Figure 4.7h**, the patterns exhibit a good line profile with near vertical sidewalls, which is beneficial for high-quality pattern transfer from resist to substrate. Combining both the high etch selectivity and the vertical line profile, high-resolution patterns were successfully transferred from the C_{60}-Bipy-Pt patterns to the silicon substrate using fluorine ICP (inductively coupled plasma) etching (as schematically illustrated in **Figure 4.7a**). **Figures 4.7i** and **j** respectively show the top-down and tilted images of the transferred 40 nm pitch lines

on silicon with high aspect ratio of ~10. The absence of silicon grass formation or surface roughening suggests that no platinum or other resist residue was present in the space between the lines.

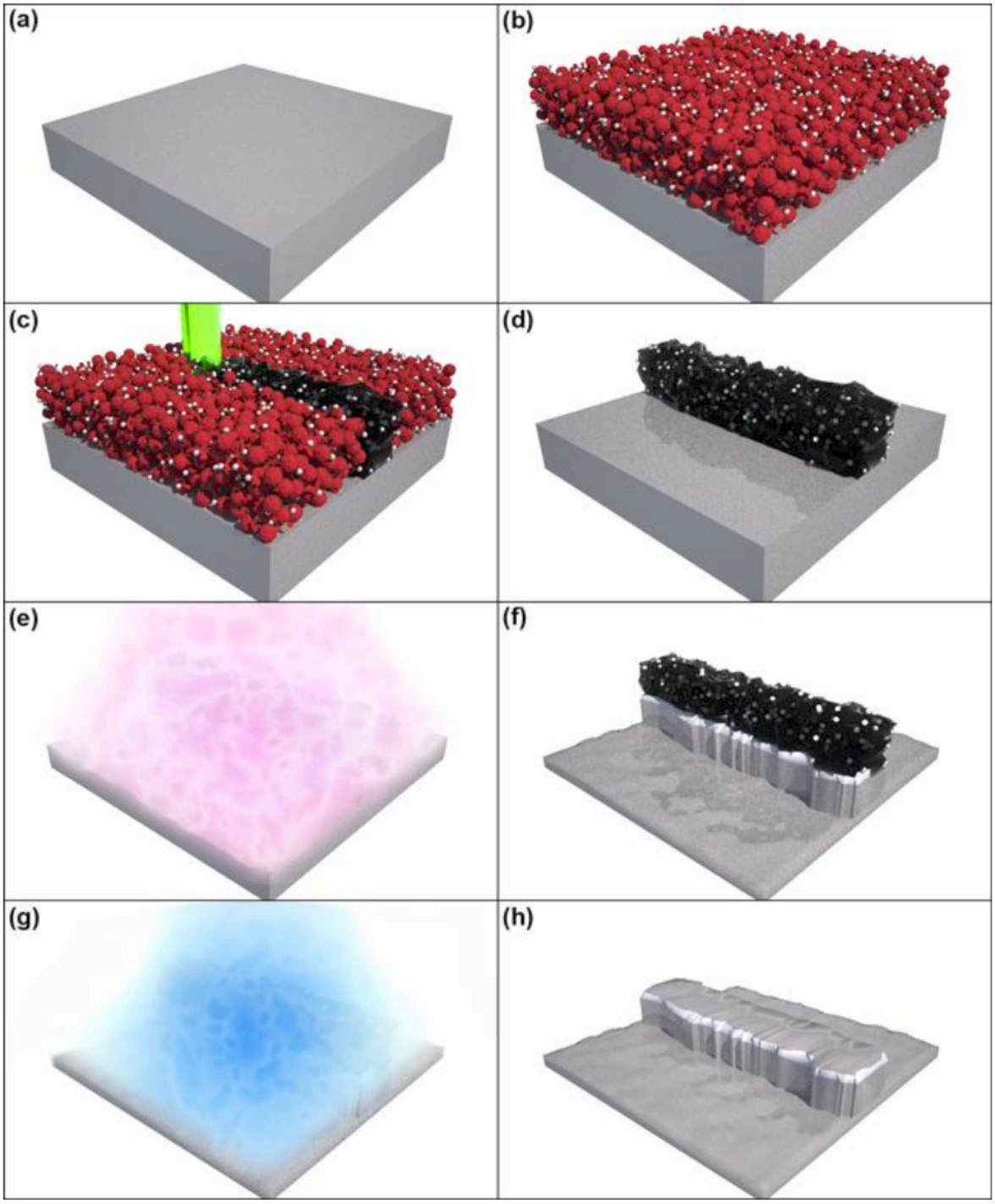

Figure 4.5 (a) A silicon substrate is cleaned and the fullerene compound deposited by spin coating to give (b) a thin smooth film of the material. (c) The

fullerene derivative is exposed using an electron beam, rendering the irradiated areas insoluble. (d) The unexposed material is removed using a suitable solvent such as cyclohexanone leaving a resist pattern on the substrate.

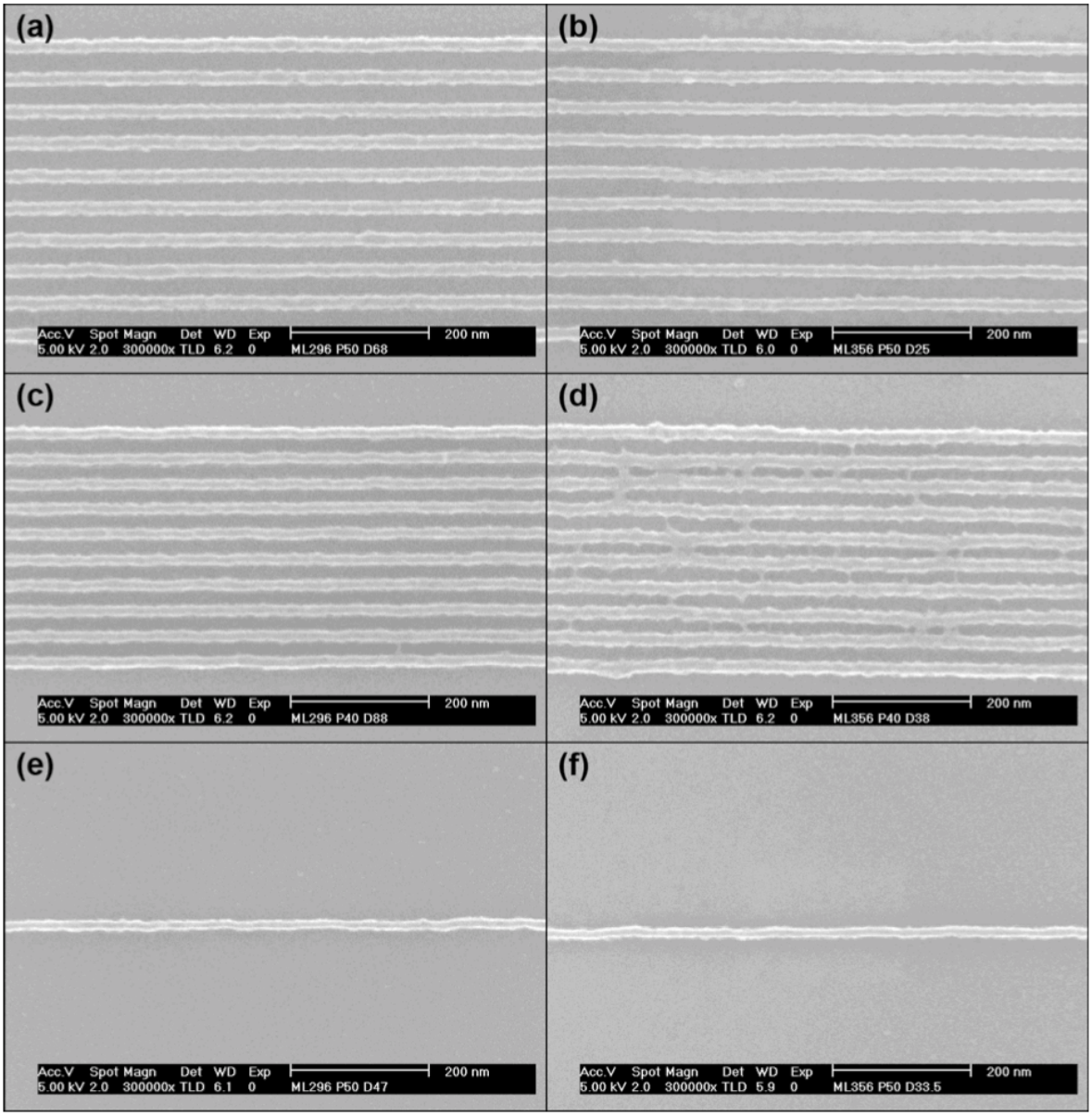

Figure 4.6 High-resolution line and space patterns and isolated lines produced in the control **1**, C_{60}- Bipy (left column: a,c,e), and the **2**, complex C_{60}-Bipy-Pt (right column: b,d,f), using 30 kV electron beam irradiation and development in MCB without post exposure bake. (a) Pitch is 50 nm (line dose is 68 nC/cm); (b) pitch is 50

nm (line dose is 25 nC/cm); (c) pitch is 40 nm (line dose is 88 nC/cm); (d) pitch is 40 nm (line dose is 38 nC/cm); (e) linewidth is 15.6 nm (line dose is 47 nC/cm); and (f) linewidth is 15.5 nm (line dose is 34 nC/cm).

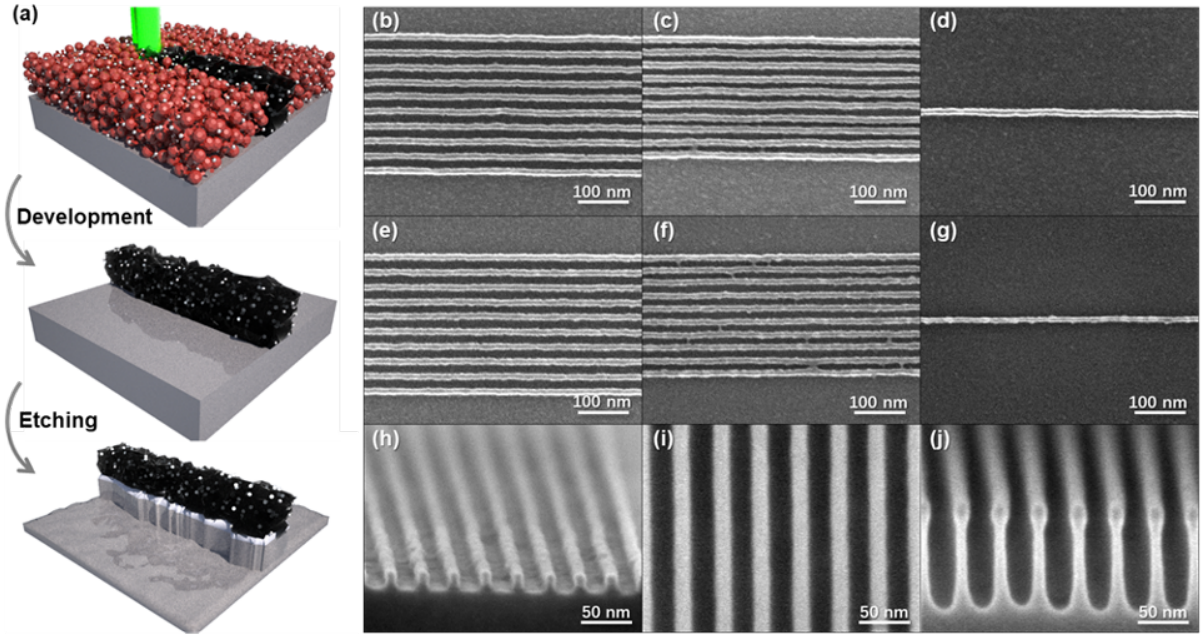

Figure 4.7 (a) Schematic illustration of the electron beam patterning and etching of the fullerene-metal complex resists; (b) - (d) show SEM micrographs of 32 nm pitch lines and spaces, 28 nm pitch lines and space, and ~12 nm isolated lines, respectively, exposed in the 1, C_{60}-Bipy, control material, whilst (e) – (g) show 32 nm and 28 nm pitch lines and spaces, and ~10 nm isolated lines, respectively, in the 2, C_{60}-Bipy-Pt complex. All samples were developed in CYH; (h) The resist profile of C_{60}-Bipy-Pt, seen here at an ~80° tilt and in 32 nm pitch lines and spaces shows good clearance between the lines and vertical resist walls; (i) ~45° tilted and (j) ~85° tilted images of the 40 nm pitch line-space patterns transferred to silicon by ICP etching.

Table 4.1 Linewidths measured with, and line width roughness/line edge roughness calculated by SuMMIT for patterns produced lithographically in number of samples of the control and the complex material at three nominal pitches and developed in CYH.

Compound	Nominal Pitch (nm)	Measured Linewidth (nm)	LWR (nm)	LER (nm)
C_{60}-Bipy	32	14.2	2.61	2.41
C_{60}-Bipy	30	14.4	3.36	2.78
C_{60}-Bipy	28	14.7	4.17	3.07
C_{60}-Bipy-Pt	32	14.0	2.81	2.16
C_{60}-Bipy-Pt	30	13.2	3.62	2.83
C_{60}-Bipy-Pt	28	12.8	3.68	2.75

4.4 Conclusion

In conclusion we have demonstrated that the incorporation of platinum atoms into a fullerene derivative resist via complexation leads to a significant enhancement in the electron beam sensitivity without concomitant reduction in the high-resolution patterning or etching capabilities. The metal atoms are found to be highly stable against aggregation or leaching even under extreme irradiation doses or with aggressive solvents. This work may pave way for a fundamentally new strategy for both fields of metal-organic resists and carbon functional patterning.

4.5 Experimental

C_{60} (99.5%) was purchased from SES Research Corporation. All other reagents and solvents were purchased from Aldrich and were used without further purification. Infrared spectra were measured using Bruker ALPHA FT-IR spectrometer over the range 400-4000 cm^{-1}. ^{1}H and $^{13}C\{^{1}H\}$ NMR were obtained using Bruker AV(III) 400 or

Bruker AV(III) 500 spectrometers. Mass spectrometry was carried out using a MALDI ToF spectrometer (Shimadzu AXIMA performance).

4.5.1 Synthesis of 4-methyl,4'-(2-(N-(3,5-di-tert-butylphenylmethyl))fulleropyrrolidino)-bipyridine, 1

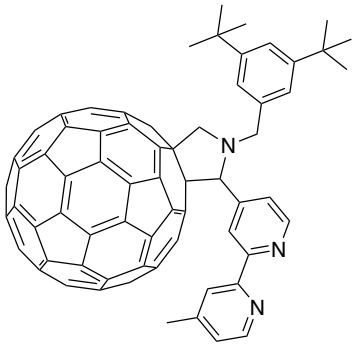

C_{60} fullerene (100 mg, 0.139 mmol), N-((3,5-di-tert-butylphenyl)methyl)glycine (46 mg, 0.167 mmol) and 4'-methylbipyridine-4-carboxaldehyde (33 mg, 0.167 mmol) were degassed with Ar and dissolved in dry toluene (60 mL). The resultant mixture was sonicated for 15 min, degassed with bubbling N_2 for 15 minutes and then heated at reflux for 2 hours. The solvent was then removed under reduced pressure, and the resulting solid was purified by column chromatography (silica gel, toluene, then toluene/ethyl acetate 99:1). Further purification was carried out by suspending the solid in MeOH (20 mL), filtering, washing with MeOH (30 mL) and drying under vacuum to give the desired product as a black solid (68 mg, 40 %).

^{1}H NMR (500 MHz, 297 K, $CDCl_3$, δ, ppm): 8.90 (s, 1H, Ar H), 8.77 (d, 1H, Ar H, J=5.0 Hz), 8.56 (d, 1H, Ar H, J=5.0 Hz), 8.27 (s, 1H, Ar H), 7.96 (s, 1H, Ar H), 7.54 (s, 2H, Ar H), 7.45 (s, 1H, Ar H), 7.14 (d, 1H, Ar H, J=5 Hz), 5.33 (s, 1H, CH), 4.98 (d, 1H, CH_2, J=10.0 Hz), 4.53 (d, 1H, CH_2, J=15 Hz), 4.25 (d, 1H, CH_2, J= 10.0 Hz), 3.85 (d, 1H, CH_2, J=15 Hz), 2.43 (s, 3H, CH_3), 1.41 (s, 18H, $C(CH_3)_3$).

^{13}C{^{1}H} NMR (400 MHz, 297 K, CDCl3, δ, ppm): 156.11, 153.51, 152.36, 152.03, 151.23, 149.40, 147.38, 147.33, 146.33, 146.30, 146.27, 146.23, 146.14, 146.02,

146.00, 145.77, 145.71, 145.60, 145.54, 145.43, 145.39, 145.34, 145.32, 145.20, 144.74, 144.51, 144.46, 144.38, 143.13, 143.03, 142.73, 142.62, 142.55, 142.30, 142.27, 142.21, 142.16, 142.13, 142.07, 142.04, 141.94, 141.86, 141.75, 141.69, 140.25, 140.23, 140.19, 139.51, 137.91, 137.22, 136.54, 136.29, 136.13, 135.91, 129.06, 128.25, 125.32, 122.86, 121.60, 79.83, 76.04, 68.91, 66.46, 56.80, 34.98, 31.61, 21.73, 21.50.

MALDI-TOF ms (DCTB/MeCN, m/z): 1133.1 [M^-].

4.5.2 Synthesis of 4-methyl,4'-(2-(N-(3,5-di-tert-butylphenylmethyl))fulleropyrrolidine)-bipyridine Pt dichloride, 2

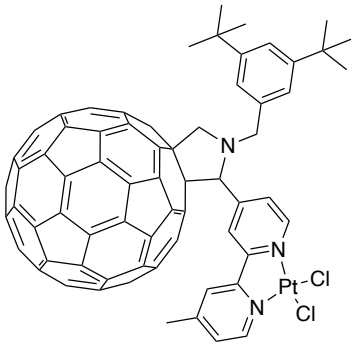

Compound **1** (20 mg, 0.018 mmol) and $Pt(DMSO)_2Cl_2$ (8 mg, 0.019 mmol) were degassed together with N_2 and dissolved in degassed $CHCl_3$ (15 mL). The resultant mixture was then heated to reflux under N_2 atmosphere for 6 hours. The solvent was then removed under reduced pressure and the resulting solid was purified by column chromatography (silica gel, under N_2 pressure, CH_2Cl_2, then CH_2Cl_2/MeOH 99.5:0.5) and dried under vacuum to give the product (22 mg, 90 %) as a brown solid.

^{1}H NMR (500 MHz, 297 K, $CDCl_3$, δ, ppm): 9.85 (d, 1H, Ar H, J=5 Hz), 9.58 (d, 1H, Ar H, J=5 Hz), 8.48 (s, 1H, Ar H), 8.06 (s, 1H, Ar H), 7.79 (s, 1H, Ar H), 7.48 (s, 1H, Ar H), 7.46 (s, 2H, Ar H), 7.36 (d, 1H, Ar H, J=5 Hz), 5.40 (s, 1H, CH pyrrolidine), 5.04 (d, 1H, CH_2, J= 10 Hz), 4.45 (d, 1H, CH_2, J=15 Hz), 4.36 (d, 1H, CH_2, J= 10 Hz), 3.93 (d, 1H, CH_2, J=15 Hz), 2.53 (s, 3H, CH_3), 1.41 (s, 18 H, $C(CH_3)_3$).

$^{13}C\{^{1}H\}$ NMR (400 MHz, 297 K, CDCl3, δ, ppm): 162.65, 159.24, 157.32, 156.26, 155.32, 152.99, 152.04, 151.54, 151.24, 150.60, 149.79, 149.17, 147.48, 147.41, 146.43, 146.31, 146.25, 146.12, 146.09, 145.99, 145.85, 145.63, 145.60, 145.52, 145.47, 145.36, 145.27, 145.13, 144.77, 144.70, 144.50, 144.29, 143.24, 143.13, 142.88, 142.78, 142.74, 142.64, 142.21, 142.17, 142.10, 142.00, 141.95, 141.84, 141.77, 141.74, 136.59, 135.80, 135.47, 129.21, 128.91, 128.05, 127.34, 124.17, 122.77, 122.02, 79.16, 75.43, 68.76, 66.62, 56.94, 35.01, 31.65, 31.33, 29.72, 29.58, 22.01.

MALDI-TOF ms (DCTB/MeCN, m/z): 1398.1 [M^-].

4.5.3 Lithography Sample Preparation

All samples prepared for electron beam lithography were coated on to silicon tokens produced from 100 mm wafers (Si-Mat, n-type, <100>, 1-10Ωcm) using a Disco DAD 321 wafer dicer. The tokens were cleaned with a 15 min ultrasonic wash in acetone followed by another 15 min in IPA. The substrates were subsequently dried with nitrogen before spin coating. The fullerene derivatives were dissolved in chloroform with a concentration of 5 g L^{-1}. By adjusting the spin speed a 40-50 nm resist film was prepared for sensitivity tests (500 RPM for 1 second, then ramp to 1200 RPM in 3 s and spin for 45 s) while a 30-40 nm film for high-resolution tests (ramp immediately to 1500 RPM and spin for 45 s). A 70 °C post-application bake (PAB) of ten minute duration was applied after spin coating. For EUV open frame exposures the high-resolution film coating procedure was adopted.

4.5.4 Electron Beam Lithography and SEM Characterisation.

An XL30 SFEG field emission scanning electron microscope with ELPHY Plus pattern generator was used for electron beam patterning. After exposure, a dip development

in cyclohexanone or monochlorobenzene for 20 s was applied, followed by a rinse in isopropyl alcohol for several seconds. Samples were then dried with nitrogen. For high-resolution patterning a 30 kV acceleration voltage was used with ~50 pA beam current. Single pixel lines were used and dosage is described as a line dose (nC cm^{-1}). The high-resolution structures on silicon substrate were imaged using the same SEM with 5 kV acceleration voltage. Levels have been adjusted to enhance contrast, and images cropped for clarity but they are otherwise unprocessed (raw images are shown in the supplementary information). The line width roughness (LWR) of line patterns was measured using SuMMIT (EUV Technology Corp). Cross-sections were prepared by patterning lines across an area of the substrate that had been pre-scribed on the back of the substrate prior to resist spinning, and then snapping the sample along the scribe line after development.

4.6 Reference

1. Tseng, A., Chen, K., … C. C.-I. T. on & 2003, undefined. Electron beam lithography in nanoscale fabrication: recent development. *ieeexplore.ieee.org*.
2. Cui, Y., Wei, Q., Park, H. & Lieber, C. M. Nanowire nanosensors for highly sensitive and selective detection of biological and chemical species. *Science* **293**, 1289–1292 (2001).
3. Chen, H., Zhang, W., Li, M., He, G. & Guo, X. Interface Engineering in Organic Field-Effect Transistors: Principles, Applications, and Perspectives. *Chemical Reviews* **120**, 2879–2949 (2020).
4. Palmer, R., Robinson, A., nano, Q. G.-A. & 2013, undefined. How nanoscience translates into technology: the case of self-assembled monolayers, electron-beam writing, and carbon nanomembranes. *ACS Publications* **7**, 6416–6421 (2013).
5. He, Q. & Zhang, H. Nanoscale patterning hots up. *Nature Electronics* **2**, 13–14 (2019).
6. Elder, B., Neupane, R., Tokita, E., … U. G.-A. & 2020, undefined. Nanomaterial patterning in 3D printing. *Wiley Online Library* **32**, (2020).
7. Ito, H. Chemical amplification resists for microlithography. *Advances in Polymer Science* **172**, 37–245 (2005).
8. Kozawa, T., Physics, S. T.-J. J. of A. & 2010, undefined. Radiation chemistry in chemically amplified resists. *iopscience.iop.org* **49**, (2010).
9. Macdonald, M., Harrison, R., … M. W.-T. J. of & 1994, undefined. Ototoxicity of carboplatin: comparing animal and clinical models at the Hospital for Sick Children. *europepmc.org*.
10. Robinson, A. & Lawson, R. *Materials and processes for next generation lithography*. (2016).
11. Thackeray, J. W. Stochastic exposure kinetics of extreme ultraviolet photoresists: simulation study. *Journal of Micro/Nanolithography, MEMS, and MOEMS* **10**, 033019 (2011).

12. Prewett, P. D. *et al.* Charged particle single nanometre manufacturing. *Beilstein Journal of Nanotechnology* **9**, 2855–2882 (2018).

13. Gangnaik, A., Georgiev, Y., Materials, J. H.-C. of & 2017, undefined. New generation electron beam resists: a review. *ACS Publications* **29**, 1898–1917 (2017).

14. Muray, A., Isaacson, M., Adesida, I. & Scheinfein, M. RADIOLYSIS AND RESOLUTION LIMITS OF INORGANIC HALIDE RESISTS. *Journal of Vacuum Science & Technology B: Microelectronics Processing and Phenomena* **3**, 367–372 (1984).

15. Krysak, M., Trikeriotis, M., … E. S.-A. in R. & 2011, undefined. Development of an inorganic nanoparticle photoresist for EUV, e-beam, and 193nm lithography. *spiedigitallibrary.org* **7972**, 79721C (2011).

16. Nedelcu, M., Saifullah, M., … D. H.-A. F. & 2010, undefined. Fabrication of Sub-10 nm Metallic Lines of Low Line-Width Roughness by Hydrogen Reduction of Patterned Metal–Organic Materials. *Wiley Online Library* **20**, 2317–2323 (2010).

17. Wu, L. *et al.* Unravelling the effect of fluorinated ligands in hybrid EUV photoresists by X-ray spectroscopy. *Journal of Materials Chemistry C* **8**, 14757–14765 (2020).

18. Ashby, P., Olynick, D., … D. O.-A. & 2015, undefined. Resist Materials for Extreme Ultraviolet Lithography: Toward Low-Cost Single-Digit-Nanometer Patterning. *Wiley Online Library* **27**, 5813–5819 (2015).

19. Li, L. *et al.* Extreme ultraviolet resist materials for sub-7 nm patterning. *Chemical Society Reviews* **46**, 4855–4866 (2017).

20. Haller, I., Feder, R., Hatzakis, M. & Spiller, E. Copolymers of Methyl Methacrylate and Methacrylic Acid and Their Metal Salts as Radiation Sensitive Resists. *Journal of The Electrochemical Society* **126**, 154–161 (1979).

21. Frommhold, A., Yang, D., … A. M.-J. of M. & 2013, undefined. Performance of negative tone chemically amplified fullerene resists in extreme ultraviolet lithography. *spiedigitallibrary.org* **12**, 033010 (2013).

22. Yang, D. X., Frommhold, A., Xue, X., Palmer, R. E. & Robinson, A. P. G. Chemically amplified phenolic fullerene electron beam resist. *Journal of Materials Chemistry C* **2**, 1505–1512 (2014).

23. Gibbons, F., Manickam, M., Preece, J., small, R. P.- & 2009, undefined. Direct Electron-Beam Writing of Highly Conductive Wires in Functionalized Fullerene Films. *Wiley Online Library* **5**, 2750–2755 (2009).

24. Robinson, A., Palmer, R., … T. T.-A. physics & 1998, undefined. A Fullerene derivative as an electron beam resist for nanolithography. *aip.scitation.org* **72**, 1302 (1998).

25. Lebedeva, M. A. *et al.* Stabilising the lowest energy charge-separated state in a {metal chromophore-fullerene} assembly: A tuneable panchromatic absorbing donor-acceptor triad. *Chemical Science* **7**, 5908–5921 (2016).

26. Kim, J., Chao, W., Griedel, B., … X. L.-J. of V. & 2009, undefined. Understanding the base development mechanism of hydrogen silsesquioxane. *avs.scitation.org* **27**, 2628 (2009).

27. Manfrinato, V. R. *et al.* Resolution limits of electron-beam lithography toward the atomic scale. *Nano Letters* **13**, 1555–1558 (2013).

28. Leiro, J. A., Heinonen, M. H., Laiho, T. & Batirev, I. G. Core-level XPS spectra of fullerene, highly oriented pyrolitic graphite, and glassy carbon. *Journal of Electron Spectroscopy and Related Phenomena* **128**, 205–213 (2003).

4.7 Appendix

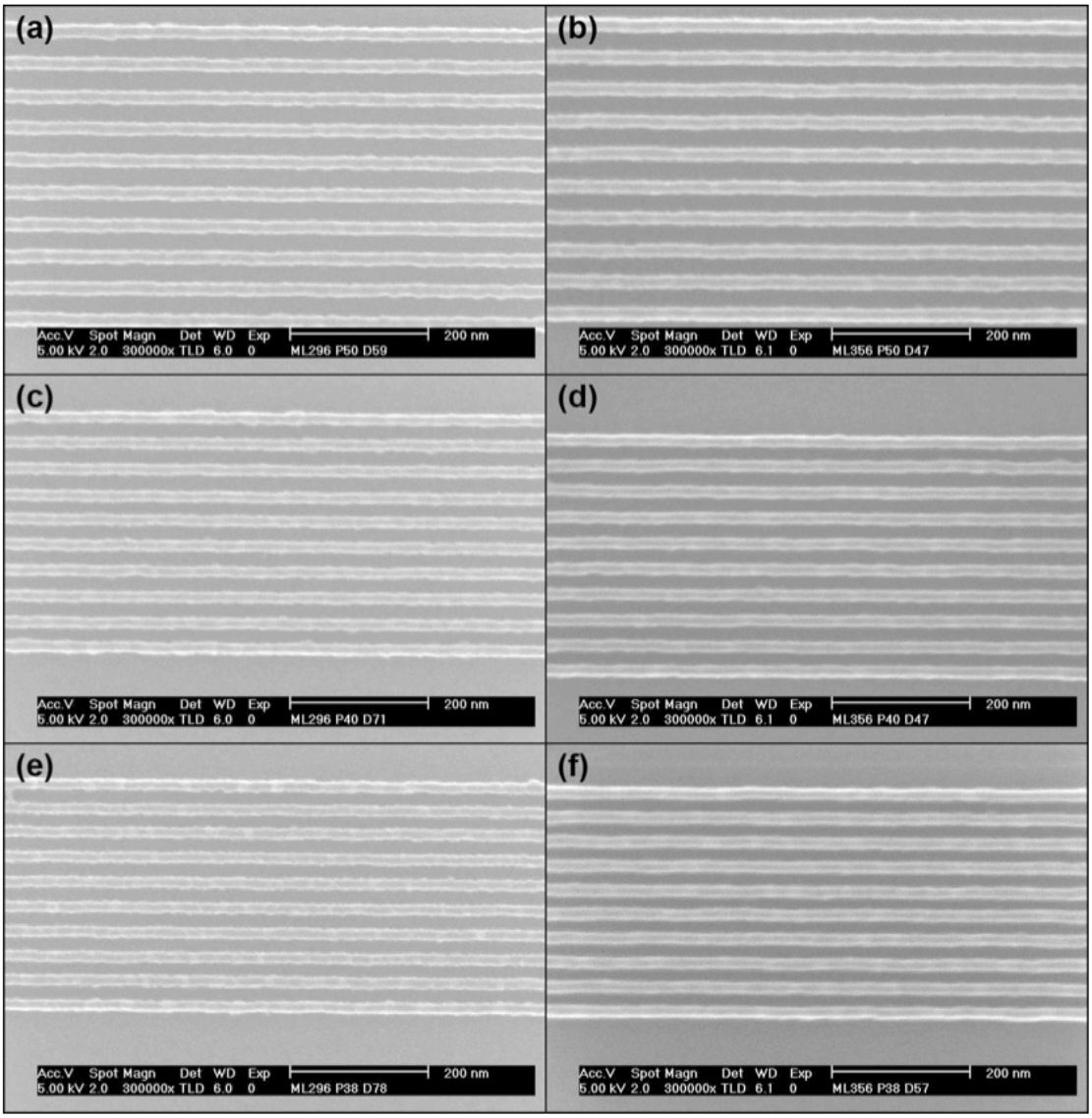
(a)
Acc.V Spot Magn Det WD Exp 200 nm
5.00 kV 2.0 300000x TLD 6.0 0 ML296 P50 D59
(b)
Acc.V Spot Magn Det WD Exp 200 nm
5.00 kV 2.0 300000x TLD 6.1 0 ML356 P50 D47
(c)
Acc.V Spot Magn Det WD Exp 200 nm
5.00 kV 2.0 300000x TLD 6.0 0 ML296 P40 D71
(d)
Acc.V Spot Magn Det WD Exp 200 nm
5.00 kV 2.0 300000x TLD 6.1 0 ML356 P40 D47
(e)
Acc.V Spot Magn Det WD Exp 200 nm
5.00 kV 2.0 300000x TLD 6.0 0 ML296 P38 D78
(f)
Acc.V Spot Magn Det WD Exp 200 nm
5.00 kV 2.0 300000x TLD 6.1 0 ML356 P38 D57

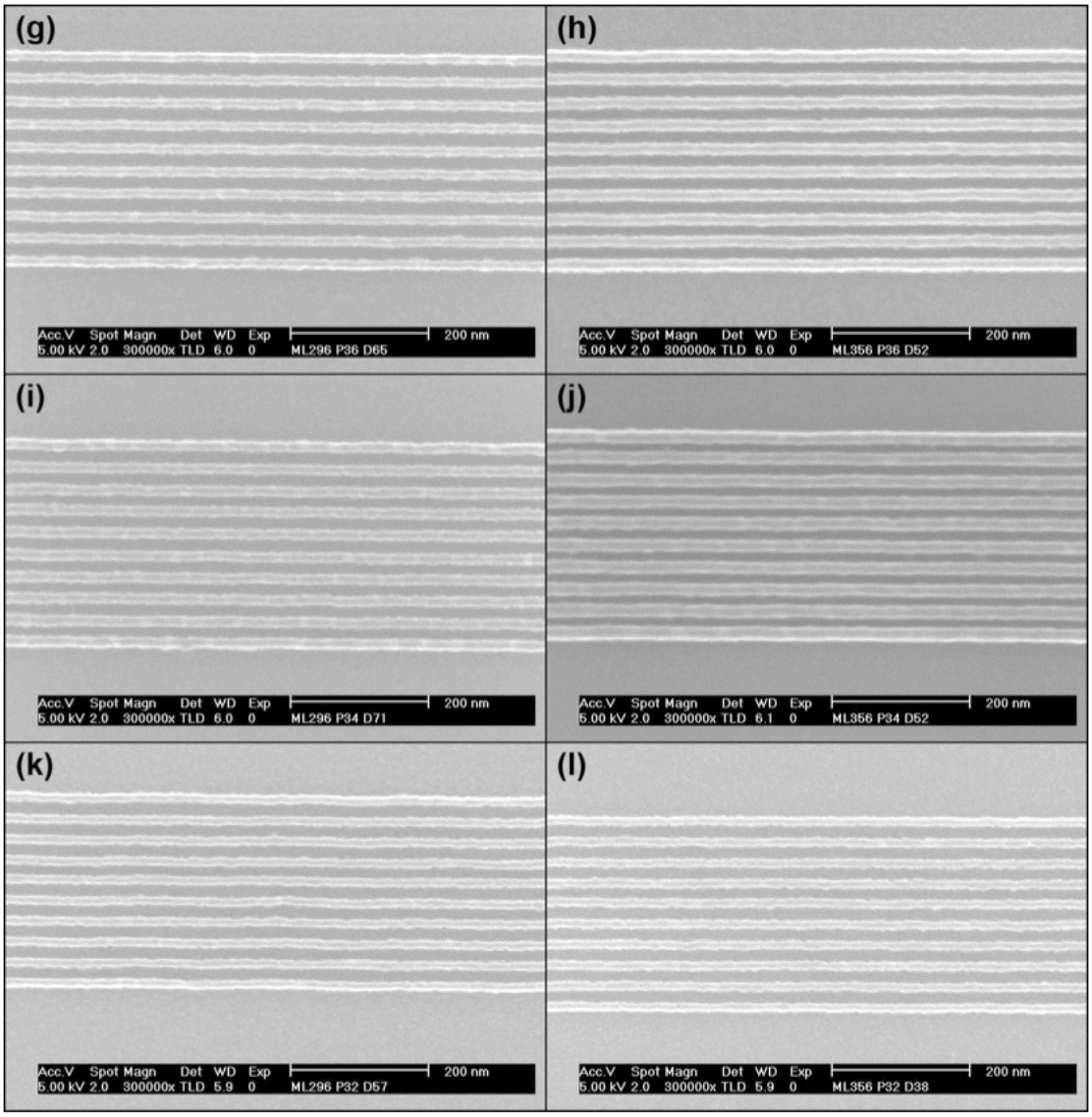
(g)
Acc.V Spot Magn Det WD Exp 200 nm
5.00 kV 2.0 300000x TLD 6.0 0 ML296 P36 D65
(h)
Acc.V Spot Magn Det WD Exp 200 nm
5.00 kV 2.0 300000x TLD 6.0 0 ML356 P36 D52
(i)
Acc.V Spot Magn Det WD Exp 200 nm
5.00 kV 2.0 300000x TLD 6.0 0 ML296 P34 D71
(j)
Acc.V Spot Magn Det WD Exp 200 nm
5.00 kV 2.0 300000x TLD 6.1 0 ML356 P34 D52
(k)
Acc.V Spot Magn Det WD Exp 200 nm
5.00 kV 2.0 300000x TLD 5.9 0 ML296 P32 D57
(l)
Acc.V Spot Magn Det WD Exp 200 nm
5.00 kV 2.0 300000x TLD 5.9 0 ML356 P32 D38

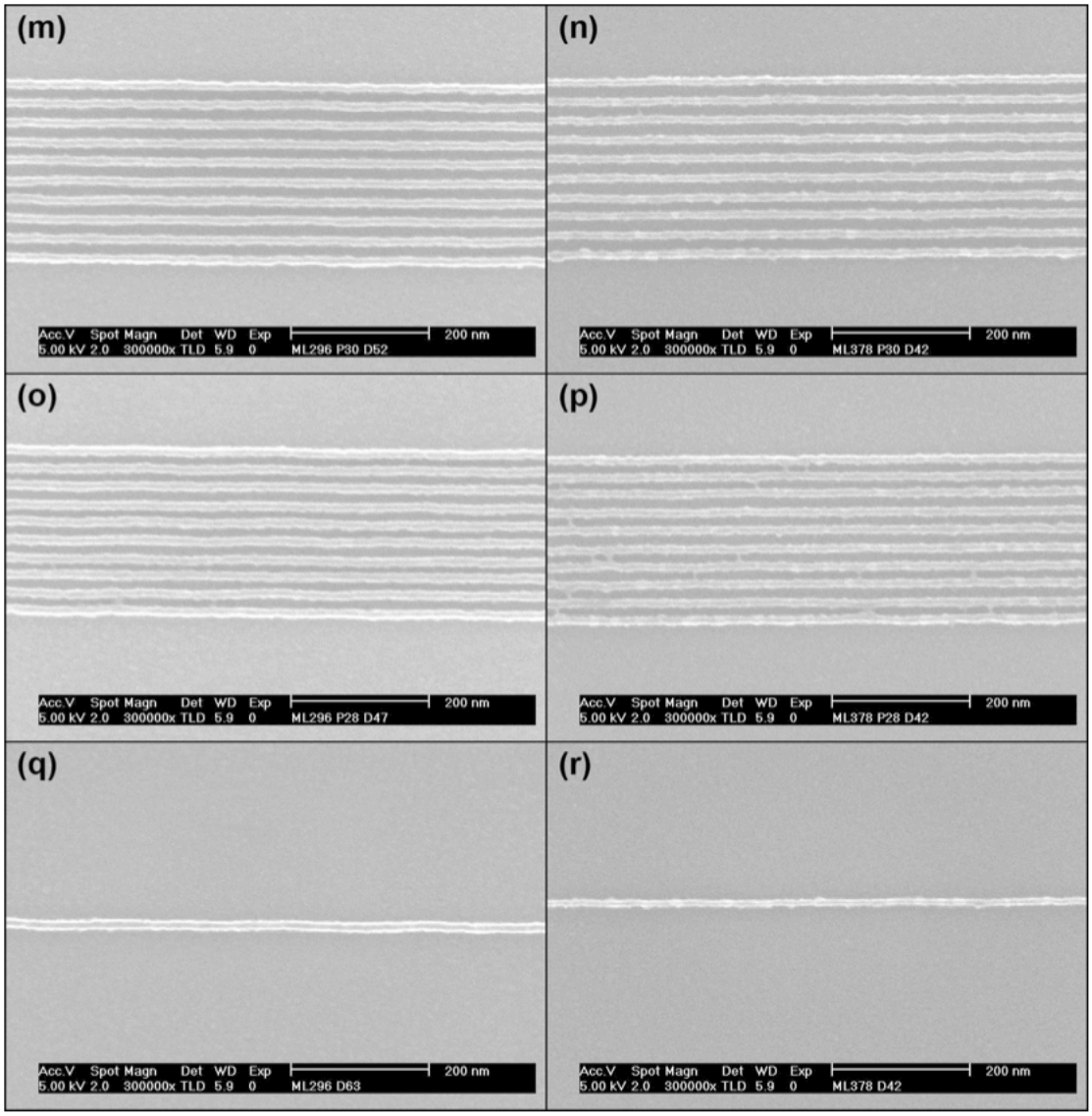

Figure A1. High-resolution line and space patterns produced in the control **1**, C60-Bipy (left column: a,c,e), and the complex **1**, C60-Bipy-Pt (right column: b,d,f), using 30 kV electron beam irradiation and development in CYH without post exposure bake. (a) Pitch is 50 nm (line dose is 59 nC/cm); (b) pitch is 50 nm (line dose is 47 nC/cm); (c) pitch is 40 nm (line dose is 71 nC/cm); (d) pitch is 40 nm (line dose is 47 nC/cm); (e) pitch is 38 nm (line dose is 78 nC/cm); and (f) pitch is 38 nm (line dose is 57 nC/cm);

Chapter 5 Conclusion

Fullerene has been discovered for almost 40 years and has been a popular research direction in multiple disciplines with numerous applications suggested. However, the practical application of fullerene-based systems are still infrequently reported and evenly more rarely adopted. In my work, I have explored the synthesis of fullerene derivatives for three applications; 1) fullerene-based charge carriers for redox flow batteries, 2) tris-fullerene CTG molecules for developing supramolecular arrays, and 3) a fullerene-platinum complex for use as a resist material for lithographic patterning.

The reaction that I used to functionalise fullerene is the Prato reaction. In comparison with other fullerene chemistries, such as the Bingel and Diels-Alder reactions, the Prato reaction can give a stabler pyrrolidine ring product and shows the potential to introduce up to three functional groups on the same pyrrolidine ring (two pyrrolidine carbons and N atom). Two types of synthetic strategy were adopted through my study; 1) step-by-step functionalisation, which initially forms a pyrrolidine ring with a secondary amine and then adds a group to the N via a coupling reaction, and 2) a one-pot Prato reaction, which uses pre-functionalised amino-acids as the starting material to perform the reaction. The first strategy has the advantage of using easily accessible staring materials, the choice of the glycine derivatives and ketone/aldehyde can be more flexible, and thus more diverse molecule design is feasible. I recommend this strategy when the fullerene moiety is expected to bind other functional species in a 1 to 1 ratio. However, this strategy can suffer from low overall yields, which makes it unsuitable for working on large quantities and for coupling reactions with other species with larger than 1 to 1 ratios. The second strategy is advantageous for yielding fullerene derivatives with multiple groups on one pyrrolidine ring, however, it involves

tricky amino acid synthesis prior to fullerene addition and there is a relatively limited choice of the groups that can be attached to the N atom, which could be more difficult when poly-amino acid scaffolds are needed (i.e. the tris-amino acid CTG).

I explored amino acid synthesis via reductive amination, which introduced a methylene linker between the N and the appended groups. Further, diverse amino acid synthesis is encouraged to enable expansion of the breadth of novel structures and functionality in terms of fullerene derivatives. This strategy is particularly good for the large quantities of material required for real world applications and the synthesis of well controlled poly-C_{60} complexes.

In Chapter 2 fullerene-ferrocene charge carriers for redox flow batteries have been thoroughly investigated with 21 novel fullerene derivatives made. The main problem encountered in the work was the synthesis of the two hexafluoro C_{60}-Fc derivatives with carbonyl linked solubilising groups on the N atom via the step-by-step synthetic strategy as the large steric hindrance inhibits in the system. However, this was solved using the one-pot Prato reaction synthetic strategy. The best of the derivatives exhibited good solubility, a wide potential window, and strong performance in cell cycling tests in actual flow cells.

Covalently linked multi-fullerene host molecules have yet to be reported, which I believe represents an opportunity to develop interesting supramolecular arrays with the potential to find application in catalysis, novel electronic devices etc. In Chapter 3, my study of tris-fullerene CTG molecules, the strategy of using tris-amino acid derivatised CTG molecule to perform the one-pot reaction with C_{60} was proposed,

performed and evaluated. This revealed the possibility of making the synthetically challenging and structurally complex tris-C_{60} CTG and with further work, such as trying different linkers between CTG and C_{60} and improving the MALDI ToF ms data acquisition, the goal of synthesising and isolating workable quantities of this materials is not far away.

The fullerene-Pt complex, synthesised successfully in Chapter 4, shows good sensitivity to the electron beam revealing excellent lithographic behavior and high-resolution patterning. This opens a new door for organometallic resists and carbon patterning. In the future, the combination of different fullerene ligands and metal centres (i.e. Fe, Ru, Au) will be explored and is expected to further push the boundaries of this new field.

In conclusion, it is possible to envisage that fullerene derivatives, as an active compound or as a building blocks, can find real world applications, e. g. energy storage and 2D electronic devices. I believe that the development of a large scale use, coupled with the abundance and sustainable nature of carbon as an element, will drive the price of fullerene down to an industrially viable level and make it a key molecular building block of materials in the future. As a chemist, the challenges therefore lie in efficient and flexible routes to fullerene functionalisation enabling; 1) facile molecular design and 2) high yielding synthetic routes. I believe that in this thesis I have contributed to the progression of both of these areas of fullerene science.